# Novel Ruthenium Complexes and their Application in Dye Sensitised Solar Cells

**Keri Laura McCall**


**Thesis submitted for the degree of PhD**

**The University of Edinburgh**

**October 2008**

# Declaration

I hereby declare that this thesis has been entirely composed by myself and that the work described herein is my own except where clearly mentioned either in acknowledgement, reference or text. It has not been submitted in whole or in part for any other degree, diploma or other qualification.

Keri L. McCall

October 2008

***For Rob, my thanks for you being bearded.***

# Acknowledgements

There are so many people to thank for helping me get through the last three years and completing this work that I could probably write a good few pages, but I've had quite enough of writing so I'll keep it short and sweet.

First and foremost, my supervisor Neil Robertson deserves much praise for his guidance, general wisdom and support (and the occasional pint of lager). I've really enjoyed my time working on this project so thanks for the opportunity.

I have to thank the groups of Laurie Peter (University of Bath) and James Durrant (Imperial College London) for their fantastic welcome and much help in deciphering results when I visited. A special mention needs to go to James Jennings from Bath, who helped with DSSC measurements, and Ana Morandeira from London, who helped with TAS measurements. They deserve praise for both giving up their time to help me and also answering all of my many questions. I wouldn't understand half of what I've written if it weren't for them. In addition, the other members of the Supergen consortium have been very encouraging and many a helpful discussion has been had at meetings.

Computational work could not have even been started without the supreme knowledge and teachings of Andy Turner. Other fine computational chemists who have helped along the way are also greatly acknowledged for their time and advice – Tricia, Sarah, Carole and Lynsey.

Praise be to the Yellowlees group for their help with the numerous equipment problems and complex electrochemistry/EPR questions! The Robertson group has certainly grown since I joined it and overall it's definitely been an enjoyable few years working with everyone. Cheers for the numerous strong coffees and just general banter (good and bad). Special mention to the solar girls (past and present), "in sun we trust", and have fun in/with the sun Charlotte! So long office chums and thanks for all the coffee.

Thanks definitely need to go to my parents for their continued support throughout the last three years. I promise to stop being a student now and get a real job.

Finally, the one person who has stuck by me through crankiness and despair deserves much praise. To my bearded Rob I owe my sanity and I only hope I can repay him with a lifetime of tea and biscuits.

## Abstract

This work focuses on the design, synthesis and characterisation of novel ruthenium bipyridyl complexes and their use in dye sensitised solar cells (DSSCs). Four series of dyes have been synthesised with the general formula $Ru(R\text{-}bpy)_2L$, where R = H, $CO_2Et$, $CO_2H$ and L represents four different bidentate ligands; cyanodithioimidocarbonate (**L1**), ethyl xanthate (**L2**), 2,3-bis(2-cyanoethylthio)-6,7-bis(methylthio) tetrathiafulvalene (**L3**) and Cu(*exo*$O_2$-cyclam) (**L4**). These have been chosen to investigate two key aims: firstly, the increase of the light-harvesting ability of the dye and secondly, the retardation of the recombination of the injected electron with the oxidised dye. Each complex was characterised using electrochemistry, absorption spectroscopy, spectroelectrochemistry and hybrid-DFT calculations. In addition the performance of the acid derivatives in a DSSC was also investigated using IPCE and IV measurements, as well as transient absorption spectroscopy.

Two different S-donor ligands, **L1** and **L2,** have been used to investigate the effect of these strongly electron-donating systems on the light-harvesting ability of the dye. Complexes utilising the di-anionic **L1** were shown to exhibit significantly increased absorption range and higher extinction co-efficients, relative to the high efficiency dye N719. This dye series also showed a large degree of S-donor ligand character to the HOMO, deduced via spectroelectrochemical and computational studies. Despite these advantageous features the dye performed very poorly in a DSSC, which was attributed

to fast recombination. This was a result of the cyano group of **L1** coordinating to the $TiO_2$ in addition to the acid groups of the bipyridine ligands. The complexes synthesised with the mono-anionic **L2** on the other hand showed only a slightly increased light-harvesting ability relative to N719 and no significant ligand character to the HOMO. However, the performance of this dye in a DSSC was more promising, with efficiencies of up to ~ 2 % achieved.

The control of the loss mechanism via recombination of the injected electron with the oxidised dye in a DSSC was investigated by incorporating redox-active ligands, **L3** and **L4**. The series of dyes synthesised with **L3** showed significant ligand character to the HOMO orbital, as deduced by spectroelectrochemical, emission and computational studies. Upon adsorption of the acid derivative to $TiO_2$ an extremely long-lived charge-separated state of 20 ms was observed via transient absorption spectroscopy. Despite this unique long-lived charge-separated state, the dye yielded extremely low DSSC efficiencies. This was attributed to the poor regeneration of the neutral dye by iodide, which in turn was thought to be the result of a stable intermediate formation between the dye cation and the iodide anion.

The complexes synthesised with **L4** showed the highest light-harvesting efficiency of all the series studied with a wide absorption range and large molar extinction co-efficients. Whilst the maximum efficiency of the dye in a DSSC was nearly 3 %, the performance was found to vary under prolonged irradiation. This was attributed to the degradation of the dye by either exchange of the counter ions with the electrolyte or loss of **L4**.

# Contents

## Chapter 3: S-Donor Ligand Dyes



## Chapter 4: TTF Ligand Dyes

## Chapter 5: Cu(exo$O_2$-cyclam) Ligand Dyes



## Chapter 6: Conclusions and Future Work



## Appendix



## Publications

# Abbreviations

| | |
|---|---|
| bpy | 2,2'-bipyridyl |
| CIGS | Copper indium gallium diselenide |
| CT | Charge transfer |
| dcbpy | 4,4'-$(CO_2H)_2$-2,2'-bipyridyl |
| DCM | Dichloromethane |
| decbpy | 4,4'-$(CO_2Et)_2$-2,2'-bipyridyl |
| DFT | Density functional theory |
| DMF | Dimethylformamide |
| DSSC | Dye sensitised solar cell |
| ECP | Effective core potential |
| EPR | Electron paramagnetic resonance |
| eT | Electron transfer |
| ET | Energy transfer |
| ff | Fill factor |
| FTO | Fluorine doped tin oxide |
| HF | Hartree-Fock |
| HOMO | Highest occupied molecular orbital |
| IL | Intraligand |
| IPCE | Incident photon-to-current efficiency |
| $I_{sc}$ | Short circuit current |
| LLCT | Ligand to ligand charge transfer |
| LUMO | Lowest unoccupied molecular orbital |
| MLCT | Metal to ligand charge transfer |
| MMLL'CT | Mixed metal ligand to ligand charge transfer |
| MO | Molecular orbital |
| NMR | Nuclear magnetic resonance |
| OTTLE | Optically transparent thin layer electrode |
| PMII | Propylimidazoliumiodide |
| PTZ | Phenothiazine |
| PV | photovoltaics |
| RTIL | Room temperature ionic liquids |
| SCE | Saturated calomel electrode |
| SOMO | Singly-occupied molecular orbital |
| spiro-OMeTAD | 2,2',7,7'-tetrakis(*N*,*N*-di-*p*-methoxyphenyl-amine) 9,9'-spirobifluorene |
| TAS | Transient absorption spectroscopy |
| TBP | Tert-butyl pyridine |
| TD-DFT | Time-dependent density functional theory |
| TPA | Triphenylamine |
| TTF | Tetrathiafulvalene |
| $V_{oc}$ | Open circuit voltage |
| XRD | X-ray Diffraction |

## Structures

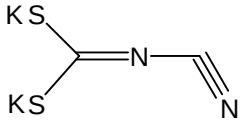


**L1**: potassium cyanodithioimidocarbonate

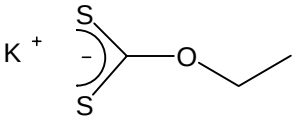


**L2**: potassium ethyl xanthate

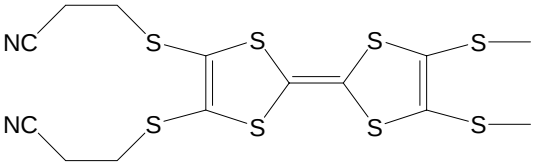


**L3**: 2,3-bis(2-cyanoethylthio)-6,7-bis(methylthio)tetrathiafulvalene

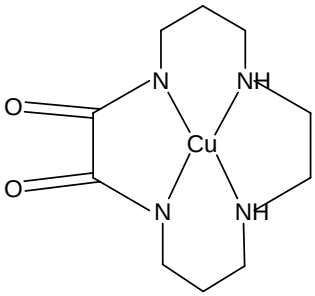


**L4**: Cu(*exo*$O_2$-cyclam)

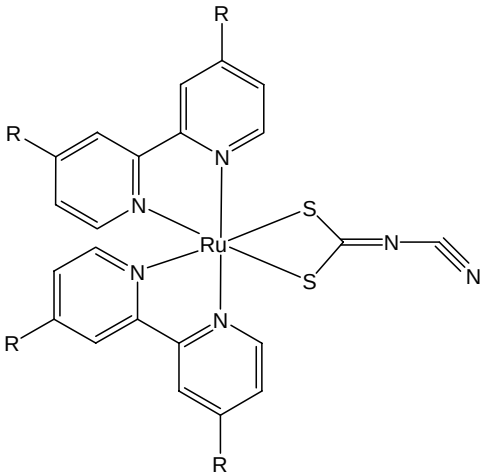


**1**: Ru(bpy)$_2$**L1**
**2**: Ru((C$O_2$Et)$_2$-bpy)$_2$**L1**
**3**: Ru((C$O_2$H)$_2$-bpy)$_2$**L1**

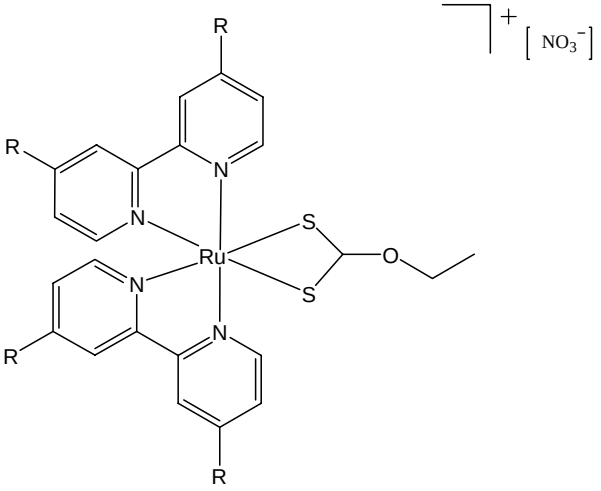


**4**: Ru(bpy)$_2$**L2**
**5**: Ru((C$O_2$Et)$_2$-bpy)$_2$**L2**
**6**: Ru((C$O_2$H)$_2$-bpy)$_2$**L2**

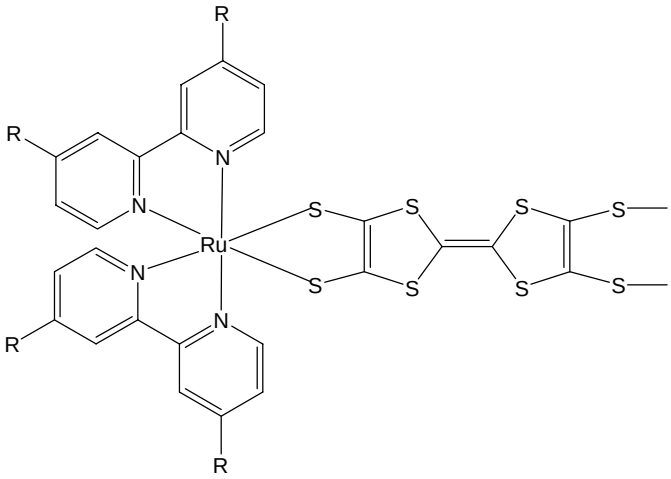


**7**: Ru(bpy)$_2$**L3**
**8**: Ru((CO$_2$Et)$_2$-bpy)$_2$**L3**
**9**: Ru((CO$_2$H)$_2$-bpy)$_2$**L3**

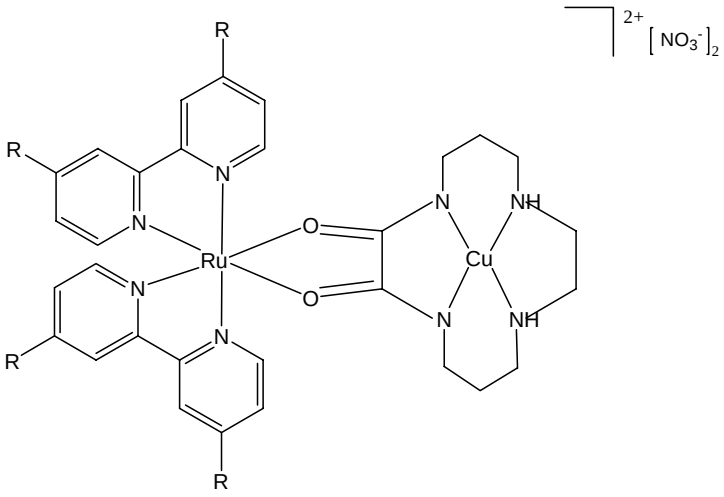


**10**: Ru(bpy)$_2$**L4**
**11**: Ru((CO$_2$Et)$_2$-bpy)$_2$**L4**
**12**: Ru((CO$_2$H)$_2$-bpy)$_2$**L4**

# Chapter 1:

# Introduction

# 1. Introduction

This thesis presents work carried out in the area of Dye Sensitised Solar Cells (DSSCs), and in particular, the design, synthesis and characterisation of novel ruthenium bipyridyl dyes for use in this field. This chapter provides a brief review of the development of DSSCs, as well as a summary of existing dyes used for this application.

## 1.1. Global Energy Demand

One of the most urgent and greatest challenges to face the scientific community today is the need to meet the growing global energy demand for the future. In 2001, the global energy consumption for the entire year was estimated to be 13.5 TW and of that amount, 86% was generated by fossil fuels.[1] Concerns arising from the increase in carbon dioxide in the Earth's atmosphere, widely attributed to the burning of fossil fuels, has provoked public discussion of how the world can decrease these emissions. However, the global energy consumption is set to more than double to an estimated 30 TW by 2050 due in large part to the industrialisation of India and China.[2] Therefore there is a real need for the development and instigation of additional energy sources.

Combining the two problems of increasing energy production and decreasing carbon emissions is a significant challenge but one which needs to be addressed in the near future. For this reason a great deal of research is being carried out on a number of different methods for the production of 'clean' energy.

## 1.2. Renewable Energies

The most commonly known renewable energy sources include wind, wave, hydroelectric, biomass, nuclear and solar energy. There has been significant interest in the advantages, disadvantages, capacity and cost of energy from each of these sources, and the findings of one review are briefly summarised in Table 1.[3] However, solar energy is seen by some to be an ideal solution to the increasing energy demand with the possibility of carbon neutrality, i.e. no carbon emissions resulting from manufacture or application, as well as the widespread availability of an infinite fuel source with no political repercussions.[4,5] For these reasons it is very likely that solar energy will feature in future energy production. Whether it is in conjunction with other sources or as the major method of electricity generation is yet to be established. Some reports have even suggested that photovoltaics (PV) could provide a significant proportion of Europe's energy from 2025 onwards if the growth in the sector continues to grow at a similar speed to recent years (an average annual growth of 35 % since 1998).[6]

| Energy Source | Advantages | Disadvantages | Cost / kWh |
|---|---|---|---|
| Solar | Unlimited energy source; publically accepted technology. | Fluctuation of energy production due to daylight hours and cloudy weather. | $ 0.25 – 0.40 |
| Nuclear | Low fuel costs; uranium sufficiently widespread globally. | Nuclear waste disposal; poor public opinion following high profile accidents; global security issues regarding production of weapons grade plutonium; large subsidies required for resulting low energy costs. | $ 0.025 – 0.07 |
| Hydropower | Cheap and mature technology. | Can have substantial environmental costs; not available in areas with low water reserves. | $ 0.03 – 0.10 |
| Biomass | Possibility of carbon negativity; mature and efficient technologies available. | Availability of land for fuel growth; changing climate may result in less land suitable for agriculture. | $ 0.02 – 0.09 |
| Wind | No fuel required. | Intermittent nature of wind; windiest places tend to be less populated; wind unequally distributed globally; public acceptance of wind farms is varied. | $ 0.05 – 0.09 |
| Wave | Tidal patterns predictable. | Coastline not available to every country; environmental impacts of large installations. | $ 0.20 – 0.90 |

**Table 1.** Summary of various attributes of renewable energy sources. [3]

Currently the use of solar energy is limited by the high cost of the resultant electricity, accepted to be $ 0.25 - 0.90 / kWh depending on the location, relative to $ 0.05 / kWh for current wholesale electricity. As well as this the intermittent nature of the energy source requires new technologies to be developed for the storage/conversion of the generated energy, e.g. solar thermal conversion or solar fuel production.

A comparison of the development and maximum efficiencies achieved for a range of photovoltaic cell technologies can be found in a recent review, which also outlines the best module efficiencies (up to 2007) as measured by a recognised test centre.[7] This shows the best single-junction cell, *i.e.* one semiconductor component, and module efficiencies are achieved by the crystalline silicon cells. This is one of the reasons why 90 % of commercially available solar cells tend to be crystalline silicon devices. In this discussion the results for multi-junction cells, which are stacks of several different semiconductors with varying band gaps, will not be considered further as they are not governed by the same maximum efficiency limits and are prohibitively expensive for both large-scale and commercial use.

In a conventional photovoltaic *p*-*n* junction cell, made from silicon for example, the semiconductor assumes both the role of light harvester and charge carrier conductor. In order to function with good efficiency the photons should be absorbed close to the *p*-*n* interface. Any electron-hole pairs formed away from the junction must diffuse to the *p*-*n* contact where the electrostatic field separates the charges. To avoid charge carrier recombination during diffusion the concentration of defects in the solid must

be small and therefore the purity of the semiconductor high. This makes the manufacture of such devices somewhat expensive.[8]

This technology does offer the advantages of high efficiencies (15 – 22 %) and excellent durability, but owing to the energy intensive manufacturing process and high expense of purified silicon the resultant cost of energy is currently too high to compete with wholesale electricity from fossil fuels. There is however a number of alternative solar cells which offer an easier and cheaper method of mass production, such as reel-to-reel processing or screen printing, which should allow solar energy to become more cost-competitive.[9]

Thin film technologies incorporate less expensive materials such as amorphous silicon, cadmium telluride (CdTe) and copper indium gallium diselenide (CIGS). The lower cost, thought to be $ 0.15 – 0.20 / kWh, comes at the expense of a lower efficiency, relative to crystalline silicon cells. This trade off is one of the key driving forces for research into these technologies, as with a relatively small increase in efficiency the cost of the resultant energy can be significantly reduced.[10]

CIGS and CdTe devices are attractive due to the relatively high efficiencies (9 – 15 %). There is concern however about whether these technologies can support large-scale production due to the shortage of indium, tellurium and selenium available, and if demand increases this may also lead to large increases in price for these materials.[11] The toxicity of cadmium may also become a problem in the commercialisation of these cells with European legislation banning the sale of some

CdTe modules. In addition there are existing problems with the disposal of NiCd batteries after their lifetime.[10]

## 1.3. Dye Sensitised Solar Cells

The DSSC represents an exciting class of devices, broadly known as bulk heterojunctions due to their 3-dimensional structure, which offer fresh challenges and hope for solar energy research. The main advantages of this system are the ease of manufacture, non-toxicity of the constituents, and the compatibility with several supporting materials, meaning that they can potentially be incorporated into domestic devices, buildings and even decorative applications.

The first high efficiency DSSC was reported by Grätzel and O'Regan in 1991[12] and has since received significant attention as a commercially viable low-cost, high efficiency solar cell. The main difference between this technology and other solar cells is the separation of the light-harvesting and charge-carrier transport, mimicking the natural process of photosynthesis. This separation means that there is no longer the requirement for high purity materials with controlled defect levels and hence the cost of these cells can be foreseen to be substantially lower than those described above.

The DSSC has five main components (Figure 1); (i) a conductive mechanical support, typically fluorine doped tin oxide (FTO) coated glass, (ii) a nanocrystalline

semiconducting oxide, typically titanium dioxide ($TiO_2$), (iii) a dye (D) such as a ruthenium bipyridyl complex, (iv) an electrolyte, generally containing the iodide/triiodide ($I^-/I_3^-$) redox couple and (v) an FTO coated glass counter electrode with a platinum catalyst coating.

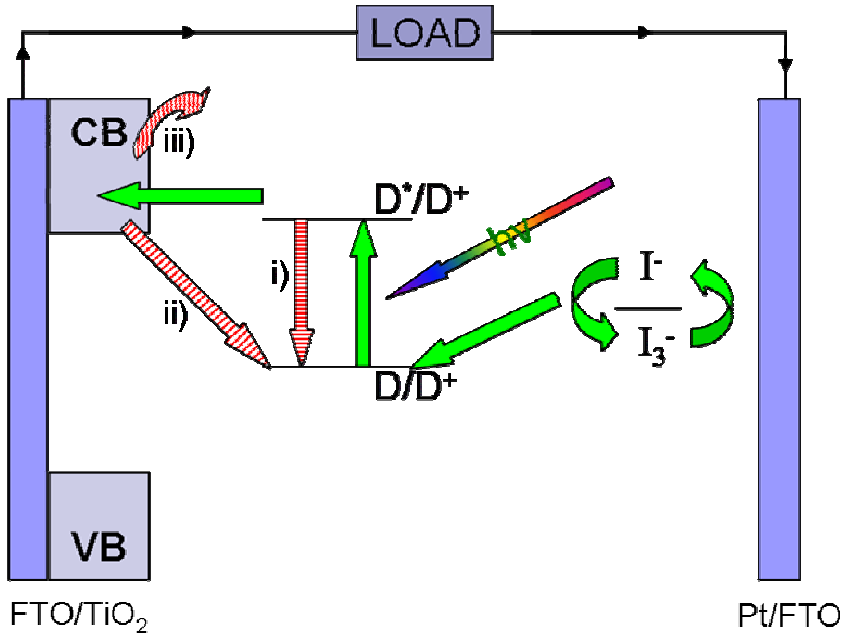


**Figure 1.** Diagram showing the main components and electron transfer processes of a DSSC. Green solid arrows represent key electron transfer processes involved in the function of the cell and red striped arrows represent loss mechanisms.

The absorption of incident sunlight by the dye results in excitation of an electron from the ground state to the excited state of the dye. Following this the electron is rapidly injected, on the pico to femtosecond timescale,[13,14] into the conduction band of the $TiO_2$, where it is transported to the back electrode and enters the external circuit. The oxidised dye is reduced back to the neutral state by the redox electrolyte, generally in microseconds, which is itself regenerated at the counter electrode, completing the circuit. The main loss processes in a DSSC (represented by the striped red arrows in Figure 1) are i) the relaxation of the excited electron back to the

ground state of the dye, ii) the recombination of the injected electron with the oxidised dye and finally iii) the loss of the injected electron in the conduction band to the triiodide in the electrolyte (also known as the dark current). The efficiency of charge separation and energy conversion depends on the kinetic competition between the various forward steps and the charge-recombination processes.

Currently the record cell efficiency for a DSSC stands at 11.1 %, [15] incorporating a ruthenium polypyridyl dye known as N719 (cis-bis(isothiocyanato)bis(2,2'-bipyridyl-4,4'-dicarboxylato)-ruthenium(II)bis-tetrabutylammonium) (Figure 2). The fully protonated version of this dye will also be mentioned in this thesis and is more commonly referred to as N3. Ruthenium polypyridyl complexes are the most commonly used class of dyes for this application, although much research is devoted to other classes which are further discussed in Section 1.4.2.3.

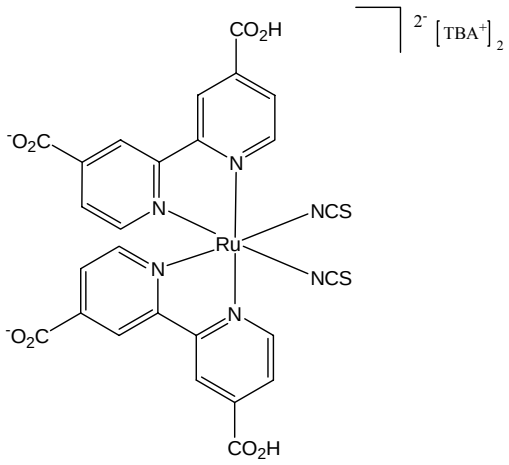


**Figure 2.** Chemical structure of the ruthenium bipyridyl complex N719.

The potential of DSSCs to be low-cost, high efficiency solar cells has gained significant commercial interest, with several companies now developing prototypes for commercial applications. These include Toyota who have demonstrated

integrated DSSC panels in the walls of their 'dream house'; Konarka[16] are developing DSSCs on flexible substrates for 'smart clothing' and portable charger applications; Dyesol[17] are investigating large area systems including building integrated panels; and G24i[18] are the first company to build a manufacturing plant for DSSCs with the hope that a variety of products will be on the market for the end of 2008.

## 1.4. Cell Optimisation

For commercialisation of DSSCs to be successful a number of key issues need to be investigated and improved upon. Some recent reviews discuss these in detail,[19,20] however the main concerns are outlined briefly in the following sections and a broad overview of the research to date is discussed.

### 1.4.1. Redox Electrolyte

The function of the redox electrolyte is the regeneration of the resultant oxidised dye and the transport of holes to the counter electrode. The most commonly used electrolyte in DSSCs is iodide/triiodide in an organic solvent e.g. acetonitrile, which also yields the highest efficiency cells. The high efficiencies of these cells are thought to be a result of the superior dye regeneration by the iodide and also the slow electron transfer from the $TiO_2$ to triiodide making the dark current loss mechanism unfavourable.

The use of the iodide/triiodide liquid electrolyte in a DSSC is however a significant disadvantage when it comes to large-scale manufacture. The main issue is that the sealing method currently used is not resistant to the organic solvents and this can result in solvent leakage and corrosion, which will ultimately limit device stability and performance. Therefore a significant breakthrough in replacing this electrolyte with a more practical electrolyte, yet still as efficient, may lead to higher manufacturability and a longer lifetime device. This prospect has lead to significant research in this area,[21,22,23] and is summarised briefly in this section.

Ionic liquids (also referred to as molten salts) are liquids that are entirely comprised of ions that are fluid at temperatures around 100 °C or below. Room-temperature ionic liquids (RTIL) have good thermal and chemical stability, negligible vapour pressure and high ionic conductivity. In addition as a redox electrolyte in a DSSC they can be both the solvent and iodide source combined. For these reasons RTIL have received significant interest in this area with the resulting DSSCs commonly referred to as quasi-solid-state.

It has been known for some time that DSSCs employing RTIL show excellent stability. [24] The main issue with their use has been the resultant low short-circuit current of the devices due to slow diffusion of the iodide species in high viscosity RTIL. However, significant advances have been made through research into low-viscosity RTIL resulting in DSSCs with efficiencies of around 7 %. [25,26,27] Most recently the efficiency of these cells increased to a maximum of 8.2 % through the use of a eutectic melt containing three imidazolium iodide salts.[28] In addition these

cells showed excellent stability with 93 % conversion efficiency retained after 1000 hours light soaking.

Fully solid-state DSSCs are also attracting significant attention. These employ p-type semiconductors as the hole transport material, which can be inorganic or organic. This semiconductor must be i) able to transfer holes from the oxidised dye after injection, ii) be able to be deposited within the pores of the $TiO_2$ by a deposition technique that is non-destructive to the dye/$TiO_2$ layer, and iii) transparent in the visible spectrum.

Copper based inorganic p-type semiconductors meet all of the above requirements, and have received significant interest in this field. CuI has been shown to yield efficiencies of 3.8 %,[29] however the stability of the cell is greatly reduced under extended illumination due to crystallite formation. [30] An alternative is CuSCN which has shown much greater stability [31] and excellent pore filling, although the maximum efficiency achieved has been only 2 %.[32] The low efficiency is thought to derive from fast charge recombination leading to poor fill factors and low photocurrents.

Organic p-type semiconductors have the advantage of low cost and ease of film formation. 2,2',7,7'-tetrakis(*N*,*N*-di-*p*-methoxyphenyl-amine) 9,9'-spirobifluorene (more commonly known as spiro-OMeTAD) is a system which has been thoroughly investigated. [33,34] The main disadvantages of the use of spiro-OMeTAD are the low conductivity, high probability of charge recombination from $TiO_2$, poor electronic contact between the dye molecules and the semiconductor and finally poor pore penetration. These issues lead to the optimum thickness of the spiro-OMeTAD films

to be ~ 2 μm,[35] rather than the typical 10 μm thick $TiO_2$ used for efficient absorption over a wide spectral range. The requirement of the thin film means that the use of dyes with increased molar extinction co-efficients is needed to maintain significant light absorption. This point is further discussed below. The maximum efficiency for cells made with spiro-OMeTAD is 4 %. [35]

Polymer electrolytes in DSSCs fall into two categories: polymer-gel and pure polymer electrolytes. These polymeric materials are less expensive, lighter and consume less energy in their production giving them the potential to be more environmentally friendly.

Polymer gel electrolytes are polymer gels that contain ionic species (such as iodide/triiodide) dissolved in an organic solvent, however above a specific temperature the electrolyte is liquid and below this it thickens to form a gel. This means that a high degree of pore-filling can be achieved at elevated temperatures but after cooling a solid film is formed, leading to advantages in manufacturability and stability. In addition they can exhibit ionic conductivities similar to liquid electrolytes. The highest efficiency achieved for these quasi-solid-state DSSCs currently stands at 6.1 %, [36] however in combination with ionic liquids the efficiency can be increased to 7 %. [25]

Pure polymer electrolytes are generally deposited via casting or spin-coating techniques to form a thin film and a solid-state DSSC. The main issue with polymer electrolytes is the lower ionic mobility which affects the kinetics of all processes

involved in the cell operation. The highest efficiency recorded for polymer electrolyte DSSCs is 5.6 % using a poly(*N*-methyl-4-vinyl-pyridine) polymer doped with *N*-methyl pyridine iodide and iodine.[37]

It is important to note that for all these variations of electrolytes there is also the requirement to alter the dye used for sensitisation, as N719 no longer achieves the highest efficiencies in these DSSCs. For example, with the spiro-OMeTAD cells the efficiency can be increased via the introduction of amphiphilic dyes containing long hydrocarbon chains. These chains are thought to form a blocking layer on the surface of the $TiO_2$, effectively suppressing recombination loss processes between the $TiO_2$ and the spiro-OMeTAD.,[38] They also improve the contact between the polar dye and the non-polar semiconductor. In addition organic indoline based dyes with very high molar extinction co-efficients have been shown to perform promisingly in spiro-OMeTAD cells, due to the greater light harvesting ability of the dye in a thin film. [39,40] Finally, long-lived charge-separated states in dyes used for spiro-OMeTAD cells have been shown to yield an increased efficiency due to decreased charge recombination.[41]

These examples for just one type of solid-state DSSC show the potential advantages that can be acquired through dye design. Hence, the design of new dyes needs to be carried out in conjunction with solid and quasi-solid state electrolyte development if higher efficiencies are to be achieved.

## 1.4.2. Dye Design

Dyes used in this application need to meet a number of requirements if they are to function efficiently. Firstly, to achieve efficient and rapid electron injection into the conduction band of the $TiO_2$ it is necessary to achieve strong adsorption of the dye to the semiconductor surface. This is generally achieved via carboxylic acid or phosphonic acid groups, although several others have been investigated.[42] The redox levels of the dye need to be sufficient for electron injection, i.e. the excited state more negative than the conduction band, and regeneration of the oxidised dye by the redox electrolyte requires the ground state to be more positive than the redox couple. Ideally the dye would have panchromatic sensitisation, i.e. an absorption spectrum that spans the entire visible range and extends into the near-IR region with sufficiently high molar absorption co-efficients, thereby harvesting the majority of the solar spectrum (Figure 3). Finally a highly stable dye is essential for a long lifetime commercial DSSC and therefore the dye should be able to sustain $10^8$ redox turnovers under illumination, corresponding to 20 years exposure to sunlight.[43]

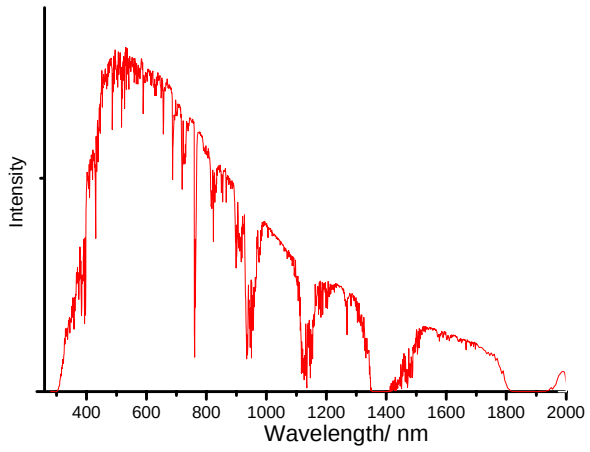


**Figure 3.** Standard intensity AM 1.5 spectrum for light incident on the Earth's surface, more commonly known as the solar spectrum.[44]

As discussed previously, the role of the dye is to absorb the incident sunlight and inject an electron into the semiconductor, resulting in efficient charge-separation. N719 has been shown to perform extremely well in DSSCs, however there is potential for significant improvement in efficiency through variation of the dye used. One of the main drawbacks to N719 is the absorption range resulting in no significant absorption beyond 700 nm, whilst for a maximum efficiency single-junction solar cell the ideal absorption range should be up to 900 nm. This is based on the Shockley-Queisser limit which states the maximum achievable efficiency as ~30 %.[45] In addition, increasing the molar extinction co-efficient of the dye can lead to the use of thinner $TiO_2$ films which in turn can lead to lower dark current and hence a higher efficiency. Therefore it can be seen that there is much room for improvement regarding the light-harvesting efficiency of sensitisers. In addition the stability of N719 under long-term use has been called into question with significant degradation occurring in accelerated testing.[46,47] One of the main degradation mechanisms is thought to be the loss of the isothiocyanate ligands via exchange with the electrolyte.[48,49]

These issues, and the development of new quasi-solid-state and solid-state electrolytes, have led to much work in the area of dye design, with high efficiency, long-term stability, low-cost and ease of manufacture the main aims.[50] The following section reviews a number of different types of dyes and the various advantages and disadvantages for each system.

### 1.4.2.1. Organic Dyes

Organic dyes offer the advantages of being readily available, cheap, and the resultant DSSCs have excellent manufacturability. These dyes have larger molar extinction co-efficients than metal complexes, the variety in their structures allows for simple molecular design to alter the properties and there are no limitations with resource availability as there are for the platinum group metals. In addition, due to the high molar extinction co-efficients, ultra-thin flexible devices may be manufactured and integrated into appliances or building materials.

Coumarin dyes (Figure 4) have received much interest, with Arakawa *et al.* showing that systematic variation and extension of the π-conjugation in the dye can result in a wide absorption range and a high efficiency DSSC of 7.7 %.[51,52,53] Thiophene containing dyes have recently shown efficiencies of 6-7 %, with this functional group commonly used to increase the π-conjugation and hence the efficiency of a system.[54,55,56,57,58] Several other classes of dye have been investigated for this application, including unsymmetrical squaraines,[59] hemicyanine[60] and polyene dyes[61,62] generally achieving 6-7 % efficiencies. Even natural dyes extracted from black rice, various flowers, fruits and seaweed have been investigated. These dyes are extremely cheap to produce, however no significant efficiency has been achieved to date.[63,64] The current highest efficiency reached using an organic dye is 9 % for an indoline dye (Figure 4); the stability of cells utilising this dye is however limited.[65] This class of dye has also achieved efficiencies of 4.1 % in a solid-state device using spiro-

OMeTAD as the electrolyte.[40] Recently a highly stable and 7 % efficient DSSC has been reported by Grätzel *et al.* using a fused dithienothiophene dye.[66]

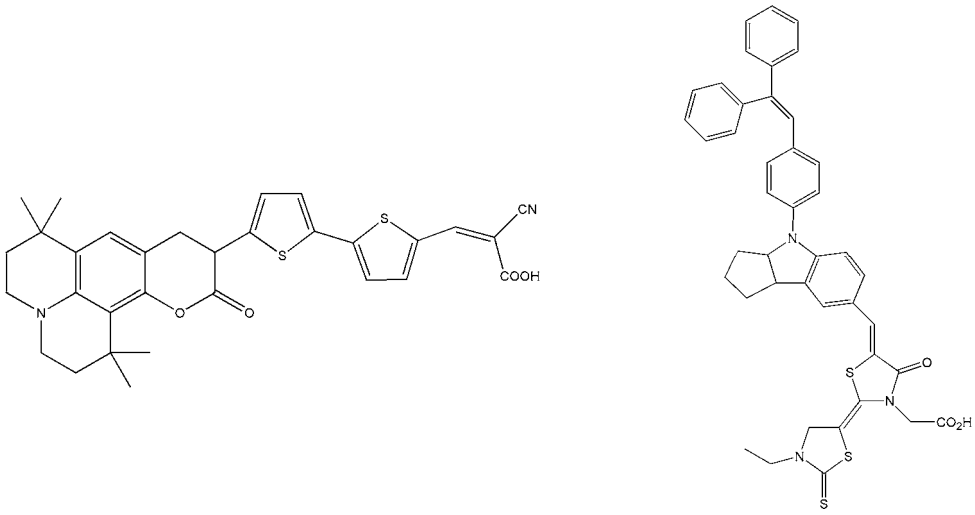


**Figure 4.** Chemical structures of the highest efficiency coumarin (left) and indoline (right) dyes.

One of the key issues that still remains with organic dyes, despite their superior light-harvesting abilities, is the increased dark current when used with an iodide/triiodide electrolyte. This is thought to be a consequence of dye/$I_3^-$ complex formation leading to a higher concentration of $I_3^-$ nearer the $TiO_2$ surface and hence increased capture of injected electron by the electrolyte.[67] This observation exemplifies the need for redox electrolyte research in conjunction with the development of new dyes.

### 1.4.2.2. Porphyrins and Phthalocyanines

Porphyrins have naturally received much attention for use in DSSCs due to their light-harvesting and charge-separation role in photosynthesis.[68] The delocalised macrocyclic structure results in very strong absorption in the visible region, generally

between 400 and 500 nm, as well as significant intensity bands in the 500 – 700 nm region. These dyes have been shown to inject electrons efficiently into the conduction band of $TiO_2$ [69] and have exhibited slow recombination rates,[70] however the efficiencies are yet to reach above 7 % (Figure 5).[71] The main reasons for the lower efficiencies are attributed to aggregation of the dyes on the surface and a high probability of exciton annihilation.

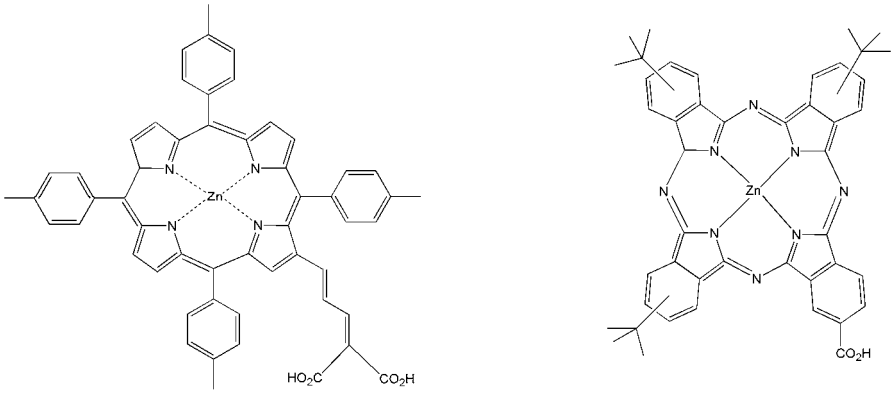


**Figure 5.** Chemical structure of highest efficiency porphyrin (left) and phthalocyanine dyes (right).

The structurally similar phthalocyanines show strong absorption in the UV and red/near IR spectral regions, which can be readily tuned by structural variation. The limit on IPCE has generally been found to be 45 % for these dyes however, resulting in global efficiencies of around 1 % [72,73] with the exception of one system showing an 80 % IPCE and overall efficiency of 3.5 % (Figure 5).[74] This low efficiency has recently been attributed to increased dark current, slow electron injection (nanoseconds)[75,76] and the tendency for aggregation.

Co-sensitisation has become an interesting area of research with respect to organic and phthalocyanine dyes. The fact that many of these systems have narrow absorption bands means that the overall efficiency of the resultant DSSC will

probably be low. However, if two (or more) dyes with narrow absorption bands, in different regions of the visible spectrum, are sensitised on the same $TiO_2$ film then it is possible to increase the absorption range of the film, and hence the overall efficiency of the DSSC. This strategy has achieved efficiencies of nearly 8 % for cells which absorb light efficiently out to near 800 nm.[74,77,78,79,80]

### 1.4.2.3. Ruthenium Polypyridyl Dyes

As stated earlier the ruthenium bipyridyl complex N719 has shown the highest efficiency DSSCs. The high efficiencies achievable using these dyes has encouraged much research into the design of new ruthenium polypyridyl sensitisers that attempt to improve upon the absorption range and/or increase the stability of the dye. This section attempts to review the most significant and relevant studies, focusing on the key areas of absorption range extension and higher stability dyes, whilst studies relevant to the dye series studied in this work are detailed at the beginnings of each chapter.

Ruthenium polypyridyl dyes are of particular interest as they have been found to have appropriate redox potentials for use in a DSSC. These are estimated to be -0.9 V for the first reduction (of the LUMO) and 0.5 V (vs. SCE) for the first oxidation (of the HOMO) based on comparison of hundreds of ruthenium complexes.[81] These levels can be tuned in ruthenium complexes by systematic variation of the attached ligands, for example either by destabilisation of the metal $t_{2g}$ orbital by using a strong

donor ligand, or secondly by using a ligand with a low-lying $\pi^*$ MO. These strategies are further discussed in Chapter 3, Section 3.1.

The majority of work in ruthenium polypyridyl dye design has focused on variation of one of the bipyridyl ligands, with numerous studies focusing on retaining two bipyridyl ligands and two NCS ligands, as used for N3, or alternatively using a tris-bipyridyl complex. The variation comes in replacing one 4,4'-dicarboxy-2,2'-bipyridyl ligand with another functionalised bipyridyl ligand yielding heteroleptic complexes. It should be noted that one acid functionalised bipyridyl ligand must remain to allow adsorption to the $TiO_2$ surface. Introducing electron donating groups onto the bipyridyl ligands has been shown to destabilise the $t_{2g}$ orbital more than the ligand $\pi^*$ resulting in a decrease in energy between the two, and hence a red-shift in the absorption spectrum. As there have been a significant number of studies carried out using this approach, they will not all be reviewed here and have been discussed in more detail in several reviews.[50,81,82] Discussed below are several areas of particular interest, which help to put the work carried out in this thesis into more context.

Incorporation of amphiphilic groups into the dye is of much interest as the presence of the hydrophobic groups can greatly increase stability, wettability with solid-state organic electrolytes, and may also decrease the dark current in liquid electrolytes. The simplest groups incorporated have been alkyl chains of varying lengths in place of the carboxylic acid groups on one bipyridyl ligand.[83] The effect of the chain length has been thoroughly investigated and was found to increase the efficiency of

the DSSC up to a C13 length chain, after which the efficiency dropped.[38,84] The increase was attributed to the chains forming a blocking layer between the $TiO_2$ and the electrolyte, effectively reducing the dark current loss process. The decrease in efficiency with longer chains was attributed to the longer alkyl chains not swelling to their full length and instead collapsing, thereby no longer blocking the recombination process. The presence of alkyl chains was also found to have a profound effect in solid-state cells where an organic hole transport material was used (e.g. spiro-OMeTAD). Here the chains are expected to be interacting strongly with the spiro-OMeTAD, enabling efficient charge transfer and also increasing the wetting of the $TiO_2$ surface by the spiro-OMeTAD. Finally it is also believed that the hydrophobic moiety reduces the susceptibility of the dye to water induced desorption thereby increasing the stability.[85] The most commonly used dye in this class is Z907 (Figure 6) which tends to be the dye of choice for solid-state cells as efficiencies with this dye are greater than cells made with N719.

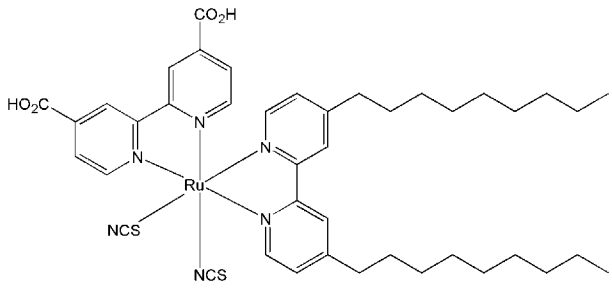


**Figure 6.** Chemical structure of highest efficiency hydrophobic dye, Z907.

Multiple pyridyl ligands have also been investigated with a number of examples of terpyridyl complexes[86,87,88] as well as one example of a quaterpyridyl.[89] The terpyridyl analogue of N3 is commonly referred to as 'the black dye' (Figure 7), due to its very broad absorption range with efficient sensitisation of $TiO_2$ up to 900 nm.[90]

It should be noted however that the molar extinction co-efficient of the low energy band is only 7000 $M^{-1}$ $cm^{-1}$. Despite this DSSC efficiencies have been very promising with this dye having a maximum of 10.4 %, although the synthetic challenges of making multiple pyridyl ligand complexes may prevent their widespread commercial use in DSSCs.

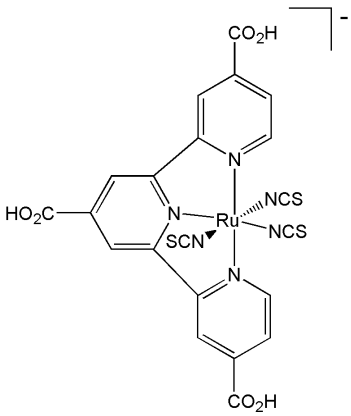


**Figure 7.** Chemical structure of the ruthenium terpyridyl complex known as 'the black dye'.

Maximising the light harvested by a sensitiser is a key priority in increasing the overall DSSC efficiency and many studies have achieved higher molar extinction coefficients by increasing the conjugation in the dyes. Several examples incorporate thiophene groups onto the bipyridyl ligands, e.g. C104 (Figure 8), yielding molar extinction coefficients of approximately 21000 $M^{-1}$ $cm^{-1}$ at 550 nm, a significant improvement on N719.[91,92,93,94] These dyes have also yielded DSSCs with very high efficiencies (8 - 10.5 %). A second class of dyes investigated incorporate alkyloxystyryl groups onto the bipyridyl ligand, e.g. K-19 (Figure 8), yielding molar extinction coefficients of approximately 18000 $M^{-1}$ $cm^{-1}$ at 540 nm.[95] The corresponding DSSC efficiencies were also as high as 10 %. These studies show the potential of increasing the conjugation on the bipyridyl ligands to enhance light harvesting ability, and it is highly likely that this is an area that will be further

investigated in the future. It should also be noted that these dyes additionally incorporate alkyl chains and are likely to be very compatible for use in solid-state DSSCs utilising organic hole transport materials.

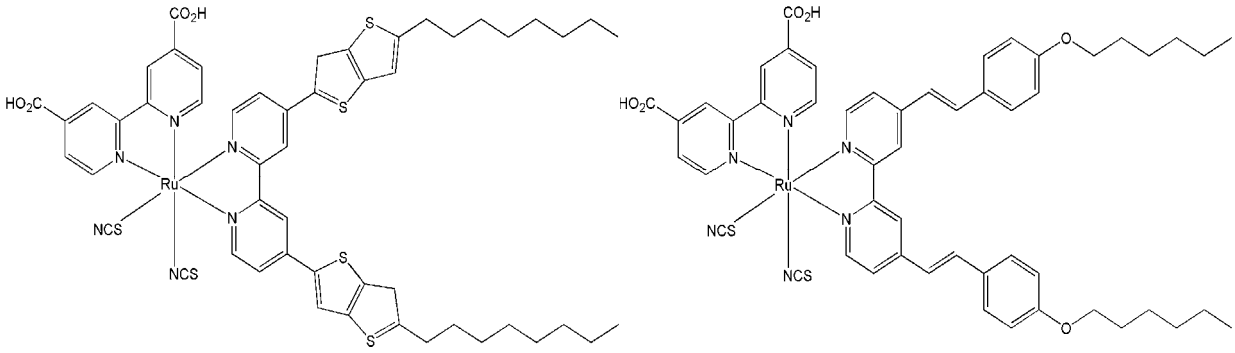


**Figure 8.** Chemical structures of C104 (left) and K-19 (right).

Overall there has been no significant improvement in the efficiency of DSSCs sensitised with any of these novel dyes and/or redox electrolytes, with the best tending to have 8 – 10 % efficiency. This means that no major breakthroughs have been made in the last 10 years regarding improving DSSC efficiency and the highest efficiency devices are essentially unchanged from its conception, i.e. utilising N719, or an analogue thereof such as Z907, as the sensitiser. Hence there is a real need for a much more focused effort on truly alternative and novel dye design if there is to be any large increase in overall efficiency.

## 1.5. Aims of Project

This project involves the synthesis and characterisation of four series of novel ruthenium bipyridyl complexes, and investigates their performance in a DSSC. Two of these series are based on the introduction of S-donor bidentate ligands to enhance both the light-harvesting ability and the long-term stability of the dye in a DSSC. The final two series are investigating the extension of the lifetime of the charge-separated state by incorporation of redox-active ligands, aiming to decrease recombination of the injected electron with the oxidised dye. In one case a mononuclear dye was investigated, with an appended functionalised tetrathiafulvalene moiety, and in the other a polynuclear dye with a copper macrocycle covalently bound to the ruthenium centre. A detailed introduction into the background literature and a more detailed discussion of the aims of each of the dye series are given at the start of each chapter.

## 1.6. Conclusion

Whilst there are now many options other than fossil fuels for energy production, solar energy remains an important yet under used resource. This is widely believed to be due to the high cost of the currently available solar modules, largely based on silicon technology. DSSCs represent a significant opportunity for development of a low cost, high efficiency solar cell. However, the main issue with DSSCs is currently the relatively low efficiency versus other solar technology such as silicon,

CIGS and CdTe based cells. Whilst their main advantage is the low overall cost and ease of manufacture. Therefore providing the efficiency of the system can be improved, solar energy utilising DSSC technology could potentially become one of the main energy resources.

In order to increase the efficiency and long term stability of DSSCs all of the key components are undergoing a large degree of research. This includes the redox electrolyte and the sensitiser used as the light harvester, as discussed in this chapter. With DSSCs undergoing the initial stages of commercialisation and with several key areas still requiring full optimisation, studies into dye design and investigation of their function as a sensitiser in a DSSC are essential.

## 1.7. References


[1] N.S. Lewis, D.G. Nocera, *PNAS*, 2006, **103**, 15729-15735.

[2] R. Eisenberg, D.G. Nocera, *Inorg. Chem.*, 2005, **44**, 6799-6801.

[3] Q. Schiermeier, J. Tollefson, T. Scully, A. Witze, O. Morton, *Nature*, 2008, **454**, 816-823.

[4] N. Armaroli, V. Balzani, *Angew. Chemie. Int. Ed.*, 2007, **46**, 52-66.

[5] K.W.J. Barnham, M. Mazzer, B. Clive, *Nature Mat.*, 2006, **5**, 161-164.

[6] Solar Generation, European Photovoltaics Industry Association/Greenpeace Publication, September 2006.

[7] M.A. Green, K. Emery, Y. Hisikawa, W. Warta, *Prog. Photovolt.: Res. Appl.*, 2007, **15**, 425-430.

[8] M. Grätzel, *Phil. Trans. R. Soc. A*, 2007, **365**, 993-1005.

[9] J.A. Maine, G. Phani, J.M. Bell, I.L. Skryabin, *Sol. Energy Mater. Sol. Cells*, 2005, **87**, 133-148.

[10] M.A. Green, *Prog. Photovolt.: Res. Appl.*, 2006, **14**, 383-392.

[11] D. Butler, *Nature*, 2008, **454**, 558-559.

[12] B. O'Regan, M. Grätzel, *Nature*, 1991, **353**, 737-739.

[13] B. Wenger, M. Grätzel, J-E. Moser, *J. Am. Chem. Soc.*, 2005, **127**, 12150-12151.

[14] S.A. Haque, E. Palomares, B.M. Cho, A.N.M. Green, N. Hirata, D.R. Klug, J.R. Durrant, *J. Am. Chem. Soc.*, 2005, **127**, 3456-3462.

[15] Y. Chiba, Y. Islam, Y. Watanabe, R. Komiya, N. Koide, L. Han, *Jpn. J. Appl. Phys.*, 2006, **45**, 24-28.

[16] www.konarka.com

[17] www.dyesol.com

[18] www.G24i.com

[19] T.W. Hamann, R.A. Jensen, A.B.F. Martinson, H. Van Ryswyk, J.T. Hupp, *Energy Environ. Sci.*, 2008, **1**, 66-78.

[20] F-T. Kong, S-Y. Dai, K-J. Wang, *Advances in Optoelectronics*, 2007, 1-13.

[21] B. Li, L. Wang, B. Kang, P. Wang, Y. Qiu, *Sol. Energy Mater. Sol. Cells*, 2006, **90**, 549-573,

[22] A.F. Nogueira, C. Longo, M-A. De Paoli, *Coord. Chem. Rev.*, 2004, **248**, 1455-1468.

[23] H.J. Snaith, L. Schmidt-Mende, *Adv. Mater.*, 2007, **20**, 3187-3200.

[24] N. Papageorgiou, Y. Athanassov, M. Armand, P. Bonhote, H. Pettersson, A. Azam, M. Grätzel, *J. Electrochem. Soc.*, 1996, **143**, 3099-3108.

[25] P. Wang, S.M. Zakeeruddin, P. Comte, I. Exnar, M. Grätzel, *J. Am. Chem. Soc.*, 2003, **125**, 1166-1167.

[26] P. Wang, S.M. Zakeeruddin, J-E. Moser, M. Grätzel, *J. Phys. Chem. B*, 2003, **107**, 13280-13285.

[27] P. Wang, S.M. Zakeeruddin, J-E. Moser, R. Humphry-Baker, M. Grätzel, *J. Am. Chem. Soc.*, 2004, **126**, 7164-7165.

[28] Y. Bai, Y. Cao, J. Zhang, M. Wang, R. Li, P. Wang, S. M. Zakeeruddin, M. Grätzel, *Nature Mater.*, 2008, **7**, 626-630.

[29] G.R.A. Kumara, S. Kaneko, M. Okuya, K. Tennakone, *Langmuir*, 2002, **18**, 10493-10495.

[30] G.R.A. Kumara, A. Konno, K. Shiratsuchi, J. Tsukahara, K. Tennakone, *Chem. Mater.*, 2002, **14**, 954-955.

[31] V.P.S. Perera, K. Tennakone, *Sol. Energy Mater. Sol. Cells,* 2003, **79**, 249-255.

[32] B. O'Regan, F. Lenzmann, R. Muis, J. Wienke, *Chem. Mater.*, 2002, **14**, 5023-5029.

[33] U. Bach, D. Lupo, P. Comte, J-E. Moser, F. Weissörtel, J. Salbeck, H. Spreitzer, M. Grätzel, *Nature*, 1998, **395**, 583-585.

[34] C.S. Karthikeyan, M. Thelakkat, *Inorg. Chim. Acta*, 2008, **361**, 635-655.

[35] L. Schmidt-Mende, S.M. Zakeeruddin, M. Grätzel, *Appl. Phys. Lett.*, 2005, **86**, 013504.

[36] P. Wang, S.M. Zakeeruddin, J-E. Moser, Md.K. Nazeeruddin, T. Sekiguchi, M. Grätzel, *Nature Mater.*, 2003, **2**, 402-407.

[37] J. Wu, S. Hao, Z. Lan, J. Lin, M. Huang, Y. Huang, P. Li, S. Yin, T. Sato, *J. Am. Chem. Soc.*, 2008, **130**, 11568-11569.

[38] L. Schmidt-Mende, J.E. Kroeze, J.R. Durrant, Md.K. Nazeeruddin, M. Grätzel, *Nano Lett.*, 2005, **5**, 1315-1320.

[39] G. Boschloo, T. Marinado, K. Nonomura, T. Edvinsson A.G. Agrios, D.P. Hagberg, L. Sun, M. Quintana, C.S. Karthikeyan, M. Thelakkat, A. Hagfeldt, *Thin Solid Films*, 2008, **516**, 7214-7217.

[40] L. Schmidt-Mende, U. Bach, R. Humphry-Baker, T. Horiuchi, H. Miura, S. Ito, S. Uchida, M. Grätzel, *Adv. Mater.*, 2005, **17**, 813-815.

[41] C.S. Karthikeyan, H. Wietasch, M. Thelakkat, *Adv. Mater.*, 2007, **19**, 1091-1095.

[42] E. Galoppini, *Coord. Chem. Rev.*, 2004, **248**, 1283-1297.

[43] M. Grätzel, *C.R. Chimie*, 2006, **9**, 578-583.

[44] Figure courtesy of Garry Rumbles from the National Renewable Energy Laboratory.

[45] W. Shockley, H.J. Queisser, *J. Appl. Phys.*, 1961, **32**, 510-519.

[46] H. Tributsch, *Coord. Chem. Rev.*, 2004, **248**, 1511-1530.

[47] A. Hinsch, J.M. Kroon, R. Kern, I. Uhlendorf, J. Holzbock, A. Meyer, J. Ferber, *Prog. Photvolt.: Res. Appl.*, 2001, **9**, 425-438.

[48] H.G. Agrell, J. Lindgren, A. Hagfeldt, *Solar Energy*, 2003, **75**, 169-180.

[49] O. Kohle, M. Grätzel, A.F. Meyer, T.B. Meyer, *Adv. Mater*, 1997, **9** 904-906.

[50] N. Robertson, *Angew. Chemie Int. Ed.*, 2006, **45**, 2338-2345.

[51] K. Hara, K. Sayama, Y. Ohga, A. Shinpo, S. Suga, H, Arakawa, *Chem. Commun.*, 2001, 569-570.

[52] K. Hara, Y. Tachibana, Y. Ohga, A. Shinpo, S. Suga, K. Sayama, H. Sugihara, H. Arakawa, *Sol. Energy Mater. Sol. Cells,* 2003, **77**, 89-103.

[53] K. Hara, M. Kurashige, Y. Dan-oh, C. Kasada, A. Shinpo, S. Suga, K. Sayama, H. Arakawa, *New J. Chem.*, 2003, **27**, 783-785

[54] N. Koumura, Z-S. Wang, S. Mori, M. Miyashita, E. Suzuki, K. Hara, *J. Am. Chem. Soc.*, 2006, **128**, 14256-14257.

[55] S-L. Li, K-J. Jiang, K-F. Shao, L-M. Yang, *Chem. Commun.*, 2006, 2792-2794.

[56] Y-S. Yen, Y-C. Hsu, J.T. Lin, C-W. Chang, C-P. Hsu, D-J. Yin, *J. Phys. Chem. C,* 2008, **112**, 12557-12567.

[57] G. Li, K-J. Jiang, Y-F. Li, S-L. Li, L-M. Yang, *J. Phys. Chem. C*, 2008, **112**, 11591-11599.

[58] K.R.J. Thomas, Y-C. Hsu, J.T. Lin, K-M. Lee, K-C. Ho, C-H. Lai, Y-M. Cheng, P-T. Chou, *Chem. Mater.*, 2008, **20**, 1830-1840.

[59] S. Alex, U. Santhosh, S. Das, *J. Photochem. Photobiol. A: Chem.*, 2005, **172**, 63-71.

[60] Y-S. Chen, C. Li, Z-H. Zeng, W-B. Wang, X-S. Wang, B-W. Zhang, *J. Mater. Chem.*, 2005, **15**, 1654-1661.

[61] K. Hara, M. Kurashige, S. Ito, A. Shinpo, S. Suga, K. Sayama, H. Arakawa, *Chem. Commun.*, 2003, 252-253.

[62] K. Hara, T. Sato, R. Katoh, A. Furube, T. Yoshihara, M. Murai, M. Kurashige, S. Ito, A. Shinpo, S. Suga, H. Arakawa, *Adv. Funct. Mater.*, 2005, **15**, 246-252.

[63] S. Hao, J. Wu, Y. Huang, J. Lin, *Solar Energy*, 2006, **80**, 209-214.

[64] N.J. Cherepy, G.P. Smestad, M. Grätzel, J.Z. Zhang, *J. Phys. Chem. B*, 1997, **101**, 9342-9351.

[65] S. Ito, S.M. Zakeeruddin, R. Humphry-Baker, P. Liska, R. Charvet, P. Comte, Md.K. Nazeeruddin, P. Péchy, M. Takata, H. Miura, S. Uchida, M. Grätzel, *Adv. Mater.*, 2006, **18**, 1202-1205.

[66] H. Qin, S. Wenger, M. Xu, F. Gao, X. Jing, P. Wang, S.M. Zakeeruddin, M. Grätzel, *J. Am. Chem. Soc.*, 2008, **130**, 9202-9203.

[67] K.E. Splan, A.M. Massari, J.T. Hupp, *J. Phys. Chem. B*, 2004, **108**, 4111-4115.

[68] W.M. Campbell, A.K. Burrell, D.L. Officer, K.W. Jolley, *Coord. Chem. Rev.*, 2004, **248**, 1363-1379.

[69] Y. Tachibana, S.A. Haque, I.P. Mercer, J.R. Durrant, D.R. Klug, *J. Phys. Chem. B*, 2000, **104**, 1198-1205.

[70] J.N. Clifford, G. Yahioglu, L.R. Milgrom, J.R. Durrant, *Chem. Commun.*, 2002, 1260-1261.

[71] W.M. Campbell, K.W. Jolley, P. Wagner, K. Wagner, P.J. Walsh, K.C. Gordon, L. Schmidt-Mende, Md.K. Nazeeruddin, Q. Wang, M. Grätzel, D.L. Officer, *J. Phys. Chem. C*, 2007, **111**, 11760-11762.

[72] Md.K. Nazeeruddin, R. Humphry-Baker, M. Grätzel, D. Wöhrle, G. Schnurpfeil, G. Schneider, A. Hirth, N. Trombach, *J. Porphyrins Phthalocyanines*, 1999, **3**, 230-237.

[73] J. He, G. Benkö, F. Korodi, T. Polívka, R. Lomoth, B. Åkermark, L. Sun, A. Hagfeldt, V. Sundström, *J. Am. Chem. Soc.*, 2002, **124**, 4922-4932.

[74] J-J. Cid, J-H. Yum, S-R. Jang, Md.K. Nazeeruddin, E. Martínez-Ferrero, E. Palomares, M. Grätzel, T. Torres, *Angew. Chemie Int. Ed.*, 2007, **46**, 8358-8362.

[75] B.C. O'Regan, I. López-Duarte, M.V. Martínez-Díaz, A. Forneli, J. Albero, A. Morandeira, E. Palomares, T. Torres, J.R. Durrant, *J. Am. Chem. Soc.*, 2008, **130**, 2906-2907.

[76] A. Morandeira, I. López-Duarte, M.V. Martínez-Díaz, B. O'Regan, C. Shuttle, N.A. Haji-Zainulabidin, T. Torres, E. Palomares, J.R. Durrant, *J. Am. Chem. Soc.*, 2007, **129**, 9250-9251.

[77] N. Robertson, *Angew. Chemie Int. Ed.*, 2008, **47**, 1012-1014.

[78] Y. Chen, Z. Zeng, C. Li, W. Wang, X. Wang, B. Zhang, *New J. Chem.*, 2005, **29**, 773-776.

[79] D. Kuang, P. Walter, F. Nüesch, S. Kim, J. Ko, P. Comte, S.M. Zakeeruddin, Md.K. Nazeeruddin, M. Grätzel, *Langmuir*, 2007, **23**, 10906-10909.

[80] J-H. Yum, S-R. Jang, P. Walter, T. Geiger, F. Nüesch, S. Kim, J. Ko, M. Grätzel, Md.K. Nazeeruddin, *Chem. Commun.*, 2007, 4680-4682.

[81] Md.K. Nazeeruddin, M. Grätzel, *Comp. Coord. Chem. II*, 2003, **9**, 719-758.

[82] A.S. Polo, M.K. Itokazu, N.Y.M. Iha, *Coord. Chem. Rev.*, 2004, **248**, 1343-1361.

[83] C. Sahin, C. Tozlu, K. Ocakoglu, C. Zafer, C. Varlikli, S. Icli, *Inorg. Chim. Acta*, 2008, **361**, 671-676.

[84] J.E. Kroeze, N. Hirata, S. Koops, Md.K. Nazeeruddin, L. Schmidt-Mende, M. Grätzel, J.R. Durrant, *J. Am. Chem. Soc.*, 2006, **128**, 16376-16383.

[85] Md.K. Nazeeruddin, S.M. Zakeeruddin, J-J. Lagref, P. Liska, P. Comte, C. Barolo, G. Viscardi, K. Schenk, M. Grätzel, *Coord. Chem. Rev.*, 2004, **248**, 1317-1328.

[86] S.M. Zakeeruddin, Md.K. Nazeeruddin, P. Péchy, F.P. Rotzinger, R. Humphry-Baker, K. Kalyanasundaram, M. Grätzel, V. Shklover, T. Haibach, *Inorg. Chem.*, 1997, **36**, 5937-5946.

[87] A. Islam, F.A. Chowdhury, Y. Chib, R. Komiya, N. Fuke, N. Ikeda, L. Han, *Chem. Lett.*, 2005, **34**, 344-345.

[88] Md.K. Nazeeruddin, E. Müller, R. Humphry-Baker, N. Vlachopoulos, M. Grätzel, *Dalton Trans.*, 1997, 4571-4578.

[89] T. Renouard, R-A. Fallahpour, Md.K. Nazeeruddin, R. Humphry-Baker, S.I. Gorelsky, A.B.P. Lever, M. Grätzel, *Inorg. Chem.*, 2002, **41**, 367-378.

[90] Md.K. Nazeeruddin, P. Péchy, T. Renouard, S.M. Zakeeruddin, R. Humphry-Baker, P. Comte, P. Liska, L. Cevey, E. Costa, V. Shklover, L. Spiccia, G.B. Deacon, C.A. Bignozzi, M. Grätzel, *J. Am. Chem. Soc.*, 2001, **123**, 1613-1624.

[91] C-Y. Chen, S-J. Wu, C-G. Wu, J-G. Chen, K-C. Ho, *Angew. Chemie Int. Ed.*, 2006, **45**, 5822-5825.

[92] K-J. Jiang, N. Masaki, J-B. Xia, S. Noda, S. Yanagida, *Chem. Commun.*, 2006, 2460-2462.

[93] C-Y. Chen, H-C. Lu, C-G. Wu, J-G. Chen, K-C. Ho, *Adv. Func. Mater.*, 2007, **17**, 29-36.

[94] F. Gao, Y. Wang, J. Zhang, D. Shi, M. Wang, R. Humphry-Baker, P. Wang, S.M. Zakeeruddin, M. Grätzel, *Chem. Commun.*, 2008, 2635-2637.

[95] P. Wang, C. Klein, R. Humphry-Baker, S.M. Zakeeruddin, M. Grätzel, *J. Am. Chem. Soc.*, 2005, **127**, 808-809.

# Chapter 2:

# Experimental Techniques

A number of different techniques were used in this study to characterise the synthesised dyes, allowing a clear understanding of the properties of the dyes as well as a rationalisation of their performance in a DSSC. These techniques are outlined in detail, with theoretical basis and experimental set-up, in this chapter. The synthetic procedure and basic analysis of the bipyridyl ligands (R-bpy) and ruthenium bipyridyl bis-chloride ($Ru(R\text{-}bpy)_2Cl_2$) starting materials are also detailed, where R = H and $CO_2Et$.

## 2.1 Electrochemistry

This technique allows the study of redox reactions of a species *via* measurement of current as a function of the potential applied to the system. The set-up used in this work involves three electrodes (Figure 1); the working electrode, where the reaction takes place, the reference electrode and the counter electrode. A potential is applied to the working electrode, this is held relative to the reference electrode. The reference electrode is a half cell with a known redox potential and is used as a reference to measure and control the working electrode potential. The reference electrode is placed in a salt bridge to prevent any products formed from entering the reaction cell. The counter electrode is made of an inert material that will not produce any electrochemical products which will interfere with reactions at the working electrode. It controls the applied potential at the working electrode by supplying sufficient current and hence should have a surface area larger than that of the working electrode so as not to limit the cell. A potentiostat is used to control the

electrodes, ensuring that current flows only between the working and counter electrodes.

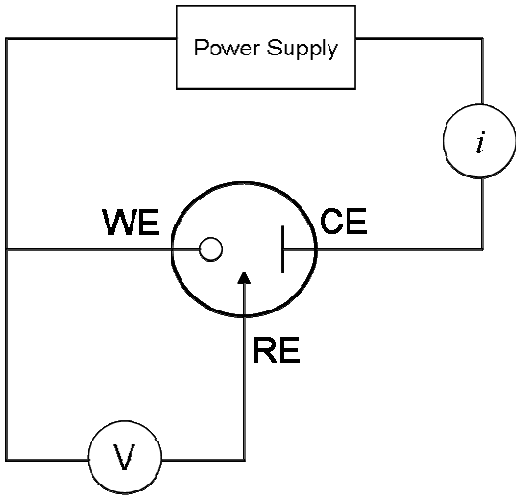


**Figure 1.** Electrochemical cell diagram (WE = working electrode, CE = counter electrode and RE = reference electrode).

### 2.1.1 Cyclic Voltammetry

In this technique the potential applied to the working electrode is scanned linearly from an initial potential $E_1$ to a second potential $E_2$, and at this point the scan is reversed and the potential scanned back to $E_1$. The current measured is plotted as a function of the potential (Figure 2).

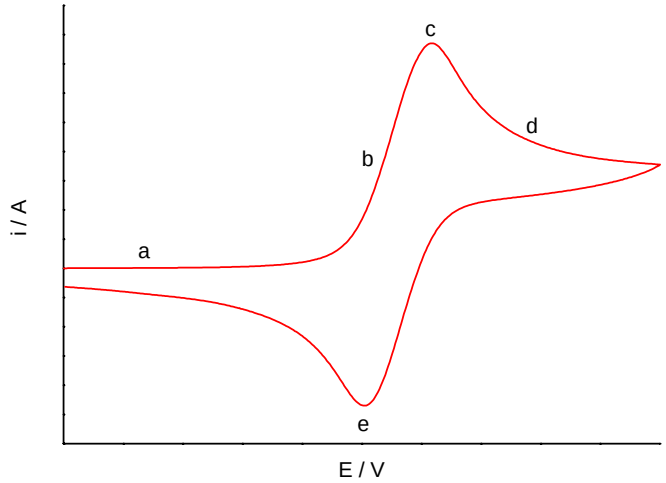


**Figure 2.** Cyclic voltammogram of an ideal reversible one electron oxidation.

Initially no current is measured as the potential is not sufficient to induce an oxidation of the dissolved species in the cell (region a in Figure 2). As the potential is scanned further, the current begins to increase as the potential is now adequate to oxidise the species in the cell (region b). At first this rise in current with potential is exponential but this leads to depletion of the compound under study at the surface of the electrode and hence the reactant must diffuse to the electrode. This mass transport is slow and therefore the concentration of the compound at the electrode decreases. The maximum point in the cyclic voltammogram indicates a balance between the increasing rate constant and the decreasing concentration of the compound, this point is known as the peak current (region c). The decrease in current is caused by the concentration decrease and is mass transport limited (region d). On reversing the scan to the initial potential $E_1$ a negative current is observed due to reduction of the resultant oxidised product (region e). This behaviour is analogous for a reduction process showing the reverse signs for the potential and current.

The peak potential and the peak height reflect the electrochemical reversibility of the redox reaction. To be deemed reversible a scan must meet a number of requirements. Firstly, the height of the forward and reverse peaks must be equal, with the separation of the peaks being approximately 59 mV (for a one electron transfer). There should also be no variation in the peak position with scan rate, and the peak current should increase linearly as a function of the square root of the scan rate. An electrochemically irreversible redox reaction shows a larger than 59 mV peak separation, which increases with increasing scan rate. In addition there is no linear relationship between the scan rate and peak current, indicating that the kinetics of the reverse reaction are slow. A chemically irreversible reaction on the other hand will show no reverse peak at all as the electrochemically produced species has reacted to form a secondary species and therefore cannot be returned to the original state.

An electrolyte is added to the solution of interest so as to increase the conductivity of the ions in solution. This eliminates migration as a mode of mass transport and enables study of only diffusion controlled processes.[1]

The electrochemical studies were carried out in a glass cell, with a Teflon cover (Figure 3). The electrodes were placed through holes in this cover along with a nitrogen bubbler, used to remove oxygen from the solution, and a stopper. Before commencing the study the solution was thoroughly mixed, using a magnetic stirrer bar and degassed using nitrogen.

A type III μAutolab potentiostat, controlled *via* a PC using General Purpose Electrochemical System (GPES) software, was used to carry out all electrochemistry experiments. A 0.5 mm diameter Pt working electrode, Pt rod counter electrode and a Ag/AgCl (sat. KCl) reference electrode were used. In all cases tetrabutyl ammonium tetrafluoroborate ($TBABF_4$) was used as the supporting electrolyte.

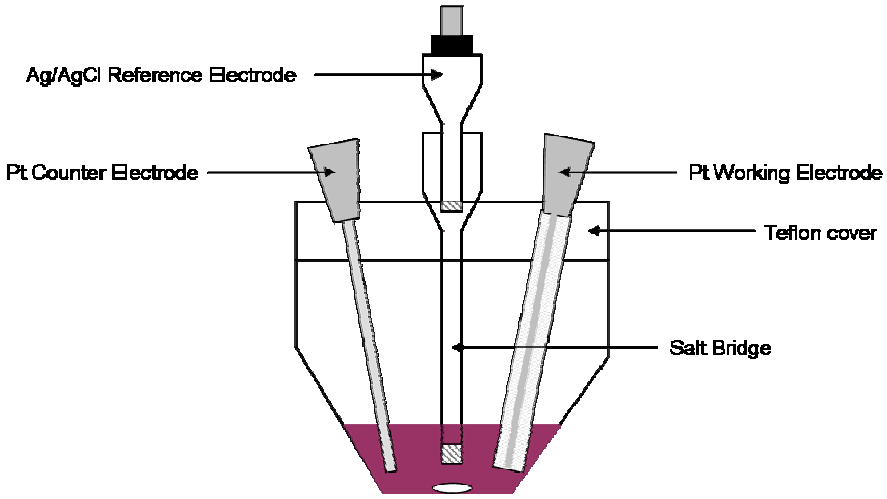


**Figure 3.** Diagram of electrochemical cell used for cyclic voltammetry and differential pulse experiments.

### 2.1.2 Differential Pulse Voltammetry

This technique uses a series of discrete potential steps rather than a linear increase, as in cyclic voltammetry (Figure 4). Each potential step has the same amplitude, and the return potential after each pulse is slightly negative for an oxidation and slightly positive for a reduction, of the potential prior to the step. The voltammogram is obtained by measuring the current immediately before the potential step and again just before the end of the step. The analytical current is therefore the difference

between the current at the end of the step and the current before the step, and this is plotted versus the average potential, *i.e.* the average of the potential before the step and the step potential. This technique allows for greater sensitivity to be achieved as it measures a difference current. For example it will often distinguish between two peaks, of very similar potential, which are only seen as one in cyclic voltammetry.[1]

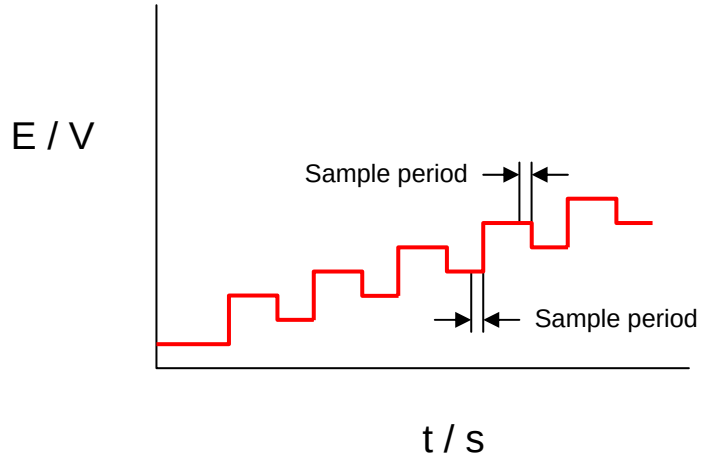


**Figure 4.** Graph showing the variation of potential with time in a differential pulse experiment.

The differential pulse voltammetry measurements were carried out using the same set-up as for cyclic voltammetry.

## 2.2 Spectroelectrochemistry

Electrochemistry can yield information about the potential at which a redox reaction occurs and its reversibility, but it is not possible to identify the electrogenerated species by cyclic voltammetry alone. By combining electrochemistry with various

other detection techniques it is possible to infer the identity of the oxidised/reduced species more readily.

The Optically Transparent Thin Layer Electrode (OTTLE) technique combines electrochemistry with UV/Vis/n-IR spectroscopy. This allows the detection and identification of an electrogenerated product by observing changes in absorption bands, such as position and intensity, as well as observation of new bands, after the application of a potential. With this information the character of the frontier orbitals of a complex can be inferred.

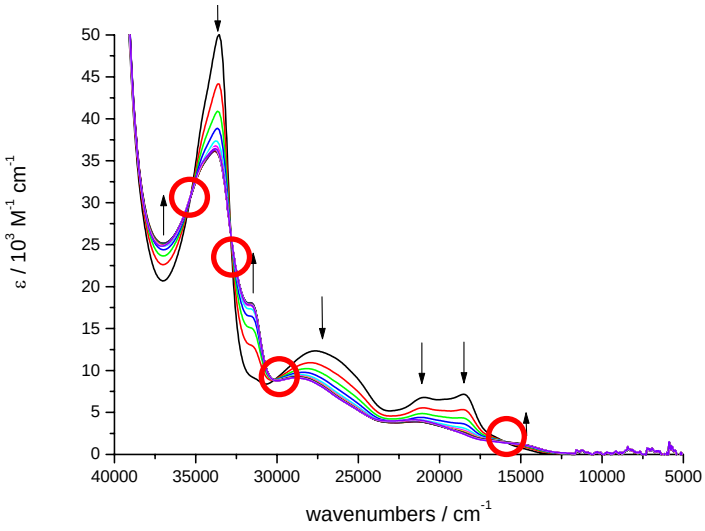


**Figure 5.** Example OTTLE spectrum showing typical growth and collapse of absorption bands upon oxidation of the solution. Arrows indicate whether the band is growing or collapsing upon oxidation and isosbestic points are circled.

Figure 5 shows a typical OTTLE study for the oxidation of a ruthenium bipyridyl complex. The original neutral complex absorption spectrum is shown in black. Following application of a suitable potential to the OTTLE cell the absorption bands may grow or reduce in intensity depending on the nature of the absorption transition

and the nature of the oxidised species being produced. The applied potential is usually chosen to be slightly past the peak potential of the redox process of interest. Each successive scan takes ten minutes and scans are continually taken until the absorption spectra cease to change. At this point the potential is reversed and the reversibility of the study investigated. The original neutral spectrum should be reproduced indicating a fully reversible redox process, if the neutral spectrum is not reproduced then this indicates an irreversible redox process. Isosbestic points (indicated in Figure 5 by red circles) are important features in OTTLE spectra as they show a clean conversion between the two chemical species in the study. If there is a third species involved, *i.e.* an irreversible redox process resulting in a third species, then the point at which the absorption spectra overlap will no longer be at a single wavenumber but will vary over progressively changing wavenumbers. Conclusions about the nature of the oxidised species being studied are drawn by comparison to spectroelectrochemical studies of similar complexes or ligands carried out elsewhere in this thesis or to literature studies.

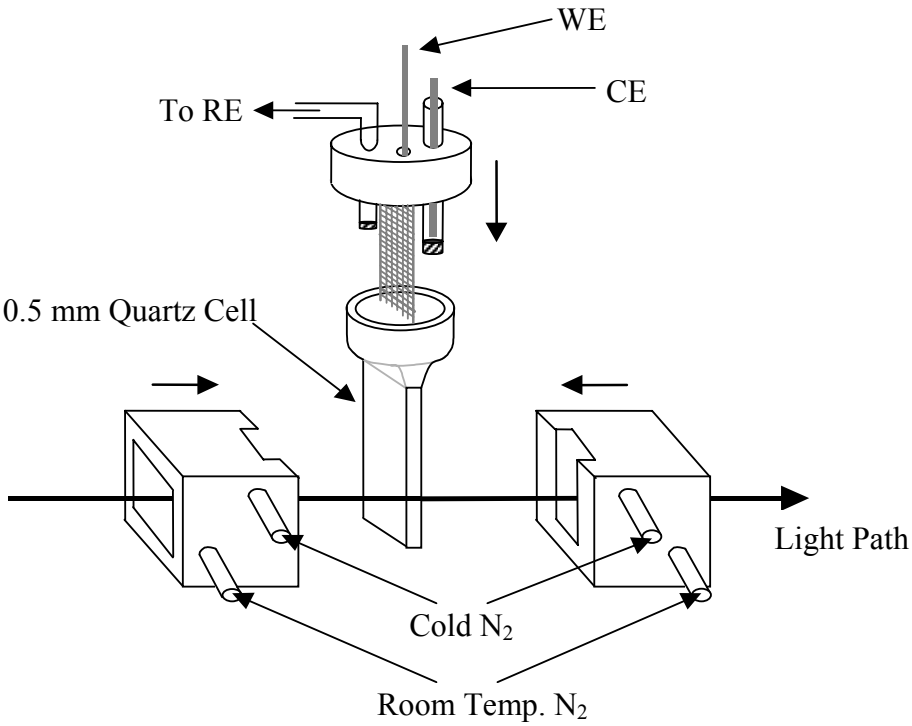


**Figure 6.** Diagram of OTTLE cell experimental set-up.

A quartz cell containing a Pt/Rh gauze working electrode was placed in a Teflon block with a quartz window (Figure 6). The working electrode wire that extends into the cell reservoir was covered by a Teflon coat to prevent bulk electrolysis. The reservoir was itself covered with a Teflon cap and the electrodes fitted through this. Both the reference and the counter electrode were placed in salt bridges. The temperature of the cell was monitored using a thermocouple and reduced to -40 °C using pre-cooled nitrogen gas. To prevent frosting of the cell, room temperature nitrogen was also passed through the cell. UV/Vis/n-IR spectra were recorded repeatedly before, during and after application of a potential to the cell. After application of a potential the true spectrum of the electrogenerated species is obtained when no further change in the spectrum was observed after numerous scans.

The original non-oxidised/reduced species was regenerated by returning the potential to a suitable value: in this work a potential of -0.2 V for an oxidative study and +0.1 V for a reductive study were used.

The quartz cell used was 0.5 mm thick, the working electrode a Pt/Rh gauze, the counter electrode was a Pt wire and the reference electrode Ag/AgCl. A Perkin-Elmer Lambda 9 spectrophotometer, linked to a PC running UV/Winlab software was used to record the spectra. All samples were studied at 253 K in either 0.1 M $TBABF_4$/DMF or 0.3 M $TBABF_4$/DCM .

## 2.3 In-situ Electron Paramagnetic Resonance (EPR)

EPR is a very sensitive technique for the study of species with unpaired electrons, and can be used in conjunction with other techniques to investigate the nature of oxidations or reductions. In this work EPR is combined with electrochemistry to investigate EPR-active species before and after oxidation or reduction.

EPR is based on the principle that an electron spin will align parallel or anti-parallel to an applied magnetic field and that the energy difference between these two states is defined by Equation 1. When the sample is exposed to electromagnetic radiation of frequency $\nu$, absorption will occur when the energy of the magnetic field is equal to the energy difference between the two states (Equation 1, Figure 7). An EPR spectrum is recorded by scanning the magnetic field incident on a sample whilst keeping the frequency constant, and the absorption of energy is recorded.

$$\Delta E = h\nu = g\mu_B B_0 \qquad \text{Equation 1}$$

**Equation 1.** Definition of the energy difference between parallel and anti-parallel spins in an applied magnetic field. Where $\Delta E$ is the difference in energy, g is a constant which is characteristic to the species under study (known as the g-factor), $\mu_B$ is the Bohr magneton and $B_0$ is the applied magnetic field strength.

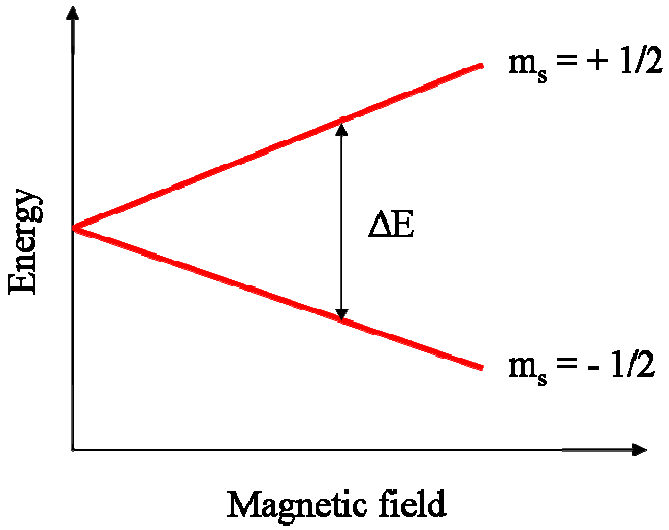


**Figure 7.** Energy level diagram showing the energy splitting in an applied magnetic field.

The variation of EPR spectra between systems arises from the differing g-factor values and the hyperfine structure. The g-factor for a free electron ($g_e$) is 2.0023, but for a given system the g-factor will depend on the ability of the applied field to induce local magnetic fields in the system. For organic radicals the g-factor will vary very little from $g_e$, however inorganic complexes tend to show large variations from $g_e$ due to spin-orbit coupling.

Hyperfine structure refers to the splitting of the resonance lines in a spectrum. This is a result of the magnetic interaction between the electron spin and the magnetic dipole moments of the nuclei present. Therefore when a nucleus with non-zero spin (where I is the spin of the magnetic nuclei) is present this gives rise to an additional magnetic field which will interact with the unpaired electron. This results in 2nI+1 different values at which $h\nu = \Delta E$, (where n is the number of nuclei with spin I) and hence 2nI+1 lines in the EPR spectrum. The size of the hyperfine splitting constant (A) depends on the proximity of the unpaired electron to the magnetic nucleus. This means that one can gain an experimental picture of the location of the unpaired electron, *e.g.* the degree of delocalisation of the electron over a particular ligand. [2,3]

In this work the general procedure has been to generate an EPR-active species *via* oxidation or reduction of a solution of the system under study. This allows the nature of the resultant singly-occupied molecular orbitals (SOMOs) to be investigated after removal/addition of an electron to the HOMO or LUMO respectively.

EPR spectra were recorded using an X-band Bruker ER200D-SCR spectrometer, which was controlled using EPR Acquisition System software, version 2.42. A BAS CV-27 potentiostat was used to electrogenerate the species and the temperature controlled using a Bruker ER111VT variable temperature unit. All experiments were carried out at -40 °C in solvent containing $TBABF_4$ electrolyte.

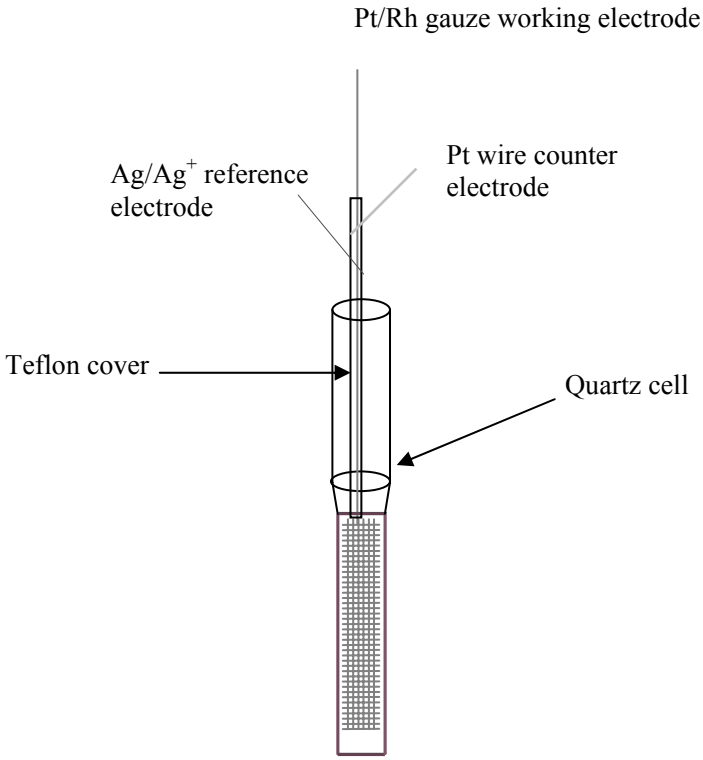


**Figure 8.** Experimental setup for *in-situ* EPR.

The cell used was a high grade quartz flat cell containing a Pt gauze working electrode (with the wire covered by a Teflon jacket to prevent bulk electrolysis), and wrapped around the Teflon were the Ag reference electrode wire and the Pt counter electrode wire both extending down to the top of the flat cell containing the gauze (Figure 8).

## 2.4 Absorption and Emission Spectroscopy

The movement of an electron from the ground state electronic level to the excited state (higher in energy) after absorption of a photon is called a transition and is the basis of absorption spectroscopy. The relaxation (downward transition) of this

excited electron back to the ground state may be accompanied by a release of energy, *e.g.* a photon, and this is the basis of emission spectroscopy.

These transitions are governed by selection rules that determine whether a transition is 'allowed' or 'forbidden'. The spin selection rule states that the transition must occur between two states of the same spin multiplicity. Laporte's selection rule states that there must be a change in parity in the transition *i.e.* the symmetry. Transitions which are allowed are likely to be very intense, *i.e.* the molar extinction co-efficients will be large. Those that are forbidden by these selection rules can still occur, however the intensity will be much lower.

An important forbidden transition in transition metal photochemistry is the intersystem crossing from the singlet excited state to a triplet excited state. This breakdown in the spin selection rule is a result of spin-orbit coupling, a phenomenon which is very active for transition metals. Spin-orbit coupling is an interaction between the electron spin magnetic moment and the magnetic moment due to the orbital motion of the electron. This results in a mixing of states of different multiplicity. Hence the transition between states of different multiplicities can occur more readily.

Figure 9 demonstrates the various processes which can occur during absorption and emission of a photon for a typical ruthenium bipyridyl complex. The solid green arrows represent radiative transitions, those which result in absorption or emission of a photon. Emission from an excited state the same multiplicity as the ground state

(in this case singlet) is called fluorescence. The luminescence lifetime for systems which radiatively relax via fluorescence is typically nanoseconds as the decay process is spin-allowed. If the excited state is a different multiplicity (*e.g.* triplet) from the ground state then the decay process is called phosphorescence. This typically results in luminescence lifetimes of milli to microseconds. This is due to the fact that the transition back to the ground state is spin forbidden. It also results in a significantly lower energy photon (relative to that absorbed) being emitted. This shift in energy is called the Stokes shift and can be an indicator for emission from a triplet state.

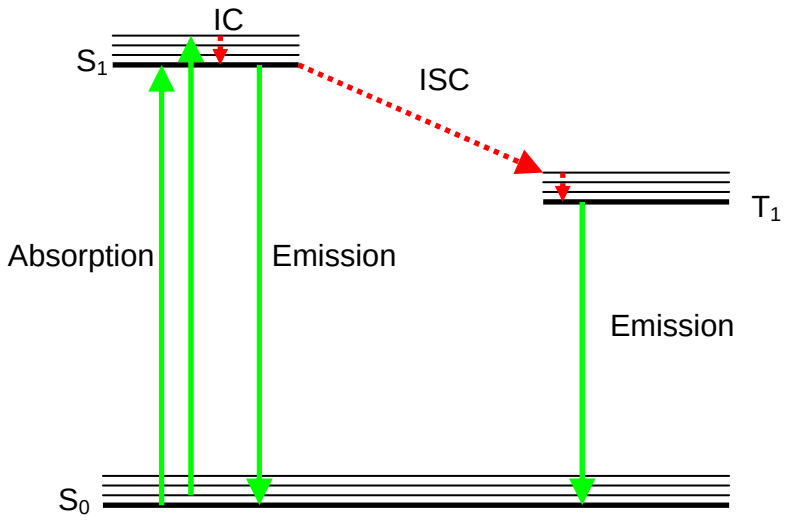


**Figure 9.** Jablonski Diagram showing the possible electronic transitions for a typical ruthenium bipyridyl complex.

The dashed red lines represent non-radiative transitions, such as internal conversion (IC), *e.g.* a relaxation of the electron to the lowest vibrational state, or intersystem crossing (ISC) a transition between two electronic states of different multiplicity. Intersystem crossing allows population of the excited triplet state and results in phosphorescence. Phosphorescence is the dominant emission mechanism for

ruthenium bipyridyl complexes due to the high degree of spin-orbit coupling present in these systems.

Absorption spectra were recorded using a Perkin-Elmer Lambda 9 spectrophotometer, linked to a PC running UV/Winlab software. All spectra were recorded in a 1cm cell in DMF. Emission spectra were recorded using a Fluromax Fluorometer, in a 1 cm cell with ethanol as the solvent. 77 K spectra were recorded by forming a frozen glass of the same solution used for the room temperature study.

## 2.5 Computational Methods

The combination of experimental and theoretical data can deeply enhance our understanding of a system. Recently, with increasing computing power and availability of the relevant software/hardware, computational chemistry is becoming an essential technique to aid chemical research. Density functional theory (DFT) and time-dependent DFT (TD-DFT) are computational techniques that have been used in a number of studies to great effect to investigate the photophysical properties of ruthenium polypyridyl complexes.[4] Here, these techniques have been used to study the energies and composition of the frontier orbitals, as well as to investigate the electronic transitions between these states for the synthesised dyes.

The computational methods used in this work are based on a molecular orbital (MO) theory approach to finding a solution to the Schrödinger equation (Equation 2). As this equation cannot be solved for systems with more than one electron (often termed

the many electron problem), approximations must be made. The level of theory used (*i.e.* Hartree-Fock (HF) or DFT) is used to approximate the Hamiltonian operator. The wavefunction (Ψ) is reproduced using appropriate basis sets for the system under study.

$$\hat{H}\Psi = E\Psi \qquad \text{Equation 2}$$

**Equation 2.** Schrödinger's equation, where $\hat{H}$ is the Hamiltonian operator, E is the energy of the system and Ψ the wavefunction.

In this work the systems being studied are relatively large and contain transition metals, therefore the most accurate and least computationally demanding method to use was Hybrid Density Functional Theory (DFT). Other computational methods often fail to describe these systems accurately due to the wealth of atomic variety, bonding types and lack of experimental data to calibrate terms for transition metal systems.

DFT relies on calculating the electron density to determine the ground-state electronic energy. However, the exchange-correlation function is still unknown and therefore approximations must be used. One such approximation is the generalised gradient approximation (GGA) whereby the gradient of the electron density in the system is considered (*e.g.* PW91). Hybrid DFT functionals include a Hartree-Fock (HF) description of exchange to gain a more accurate description overall. The ratios of HF and DFT are set with respect to a training set of molecules and can give

comparable accuracy to full ab initio calculations. Examples of Hybrid DFT methods commonly used are B3LYP or B3PW91.

To describe the wavefunction (Ψ) a basis set is used to describe each atom. This basis set is the sum of a series of Gaussian functions with varying exponents (Equation 3), with the total function being approximately equal to the atomic radial function.

$$\Psi = \Sigma\, c.\phi \qquad \text{Equation 3}$$

**Equation 3.** Mathematical description of a basis function where c is a weighting co-efficient and ø a Gaussian function.

The values of the weighting co-efficient are varied until a wavefunction is generated that gives rise to the minimum energy for a particular system. For systems with a large number of electrons (*e.g.* Ru) a pseudopotential can be used, such as the Hay-Wadt VDZ (n+1) effective core potential (ECP). This replaces the core electrons with a single function and allows only the valence electrons to be involved in bonding, thus simplifying the calculation.

### 2.5.1 Geometry Optimisation Experimental Details

A geometry optimisation calculation involves the variation of the geometry of a system computationally until a stationary point on the potential energy surface is found.

The calculated geometry was first optimised in the gas phase and then using this structure, solvent was introduced into the system with inclusion of a DMF polarisable continuum model.[5] The reported structures, orbital energies and percentage contributions to the molecular orbitals (MO) in this thesis are those calculated in DMF. This allows a fairer comparison to the experimentally determined results which were also carried out in DMF.

The Gaussian 03 program was used to perform all calculations.[6] The Becke three parameters hybrid exchange and the Perdew-Wang 1991 correlation functionals (B3PW91) level of theory were used.[7,8] For the ruthenium atom a Hay-Wadt VDZ (n+1) ECP was used [9] and all other atoms were described by 6-31G*.[10] The initial structure was inputted using the builder program Arguslab.[11] A frequency calculation was performed to ensure the optimised structure was a minimum on the potential energy surface, verified by the absence of negative imaginary values. The molecular orbital isosurfaces were generated using the cubegen utility in Gaussian 03. The molecular orbital population calculations were carried out using the pop=regular command and the information extracted using a utility written by Dr. Andrew Turner.

### 2.5.2 Time-dependent DFT (TD-DFT)

TD-DFT can be used to generate a theoretical absorption spectrum and identify the nature of the transitions which make up absorption bands. It is based on the response of the ground-state electron density to an oscillating optical field. It should be noted

that it was very important in these studies to include solvent in the calculation, as any TD-DFT calculations carried out using the optimised geometry in the gas-phase resulted in calculated transitions being too low energy. This is an inherent problem in using TD-DFT with charge-transfer complexes and is thought to be due to an over-estimation of the stabilisation of the acceptor orbital by the electron-hole attraction.[4] The inclusion of solvent has been shown to drastically improve the agreement between experimental and calculated spectra for transition metal complexes, relative to calculations carried out in vacuum. [12,13,14] This is attributed to the electrostatic field of the solvent reducing the degree of orbital mixing in polar metal-ligand bonds and reducing the calculated charge-separation upon excitation. However, caution must still be taken for transition metal complexes when comparing these theoretical results to experiment.

TD-DFT was performed in a DMF polarisable continuum model. The number of singlet transitions calculated varied between systems to ensure that a full spectrum could be simulated. The simulated spectra were generated using the GaussSum 2.1 freeware program *via* a Gaussian convolution of the calculated transitions, using a full-width half-maximum value of 3300 $cm^{-1}$. [15]

## 2.6 DSSC Fabrication

The majority of the work carried out on testing the performance of the synthesised dyes in a DSSC was done in collaboration with James Jennings and Dr. Hongxia Wang from Prof. Laurie Peter's group at Bath University. However, preliminary

testing of the dyes performances was achieved using a solar simulator at the University of Edinburgh, set up during the course of this work.

The counter electrode was constructed by first coating fluorine doped tin oxide conductive glass (TEC 8, Pilkington, UK) with $H_2PtCl_4$, followed by heating the slides to 400 °C, leaving a thin layer of platinum (Figure 10, (1)).[16] Two holes were then drilled into the glass to allow injection of the electrolyte at a later stage (2).

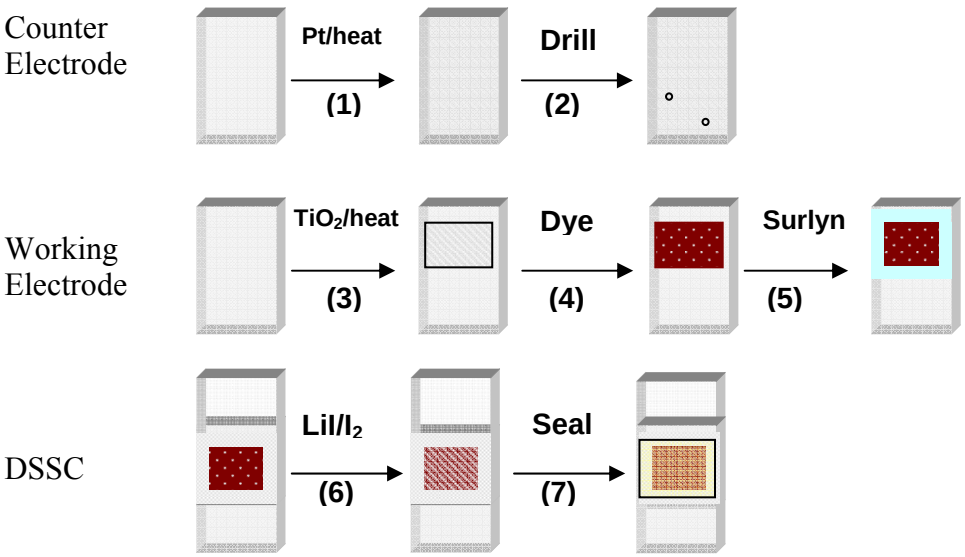


**Figure 10.** Assembly of a DSSC.

To make the working electrodes titanium dioxide paste (Dyesol, DSL-18NR-T) was deposited onto cleaned fluorine doped tin oxide conductive glass by doctor-blading (3). The film was dried at 100 °C for 15 minutes and then sintered at 450 °C for 30 minutes to remove the organics and to form a mesoporous film structure. The thickness of the film was about 12 µm. The films were sensitised with the synthesised dyes using a 0.5 mM solution of the dye in methanol (4). The cell was

completed by sealing the dye coated $TiO_2$ electrode and Pt electrode of a cell together by a thermal plastics spacer (Surlyn 1702, 25 μm, Solaronix) at 120$^oC$ (5). The electrolyte was introduced into the cell through the two holes which were drilled in the counter electrode (6). The holes were subsequently sealed by the thermal plastics (Surlyn 1702, Solaronix), combined with a piece of microscope slide under press (7). The active area of the cell was 1 $cm^2$, except where stated.

The default electrolyte composition used in this study was 0.6 M 1-methyl-3-propylimidazolium iodide (PMII), 0.03 M $I_2$, 0.1 M guanidinium thiocyanate, 0.5 M tert-butyl pyridine (TBP) in acetonitrile/valeronitrile (except where stated). See Section 2.8 for further discussion of the role of the electrolyte in DSSCs.

## 2.7 Incident Photon-to-Current Efficiency (IPCE)

This technique allows the light harvesting efficiency of a dye at a given wavelength to be evaluated *i.e.* the percentage of photons hitting the cell that are being converted to electrons. IPCE spectra of the cells were measured with a spectral resolution of 8 nm using monochromatic light provided by a xenon lamp and monochromator. The incident photon flux was measured with a calibrated Si photodiode.

The current output that was measured from the cell was converted to a voltage signal. A lock-in amplifier then extracted the voltage contribution of the cell, which has the same frequency as the modulated incident light. The IPCE was obtained from the voltage signal as a function of wavelength by comparison with a calibrated

photodiode, where $QE_{photodiode}$ is the external quantum efficiency of this photodiode. The overall IPCE, expressed as a percentage is calculated using Equation 4.

$$IPCE = \frac{V_{cell}}{V_{photodiode}} \times QE_{photodiode} \times 100 \qquad \text{Equation 4}$$

**Equation 4.** Incident photon-to-current efficiency calculation.

## 2.8 I-V Measurements

The overall (or global) efficiency of any solar cell is defined as the ratio of output to input power and is defined by Equation 5. Figure 11 shows a typical I-V curve for a DSSC, and highlights where the following parameters are experimentally obtained. The open circuit voltage ($V_{oc}$) is the voltage recorded when no current is flowing and the short circuit current ($I_{sc}$) is the current output under short circuit conditions. The fill factor (ff) is a ratio of the theoretical (red dot dash line) and measured (blue dashed line) power output. The fill factor is influenced by a number of points including the efficiency of charge extraction from the cell, and so can be hindered by a higher total series resistance of the cell. The inputted power ($P_{in}$) is attained using simulated solar light (commonly known as AM 1.5) which delivers 1000 $Wcm^{-2}$.

$$\eta_{global} = \frac{P_{out}}{P_{in}} = \frac{I_{sc} V_{oc} ff}{P_{in}} \qquad \text{Equation 5}$$

**Equation 5.** Global efficiency calculation.

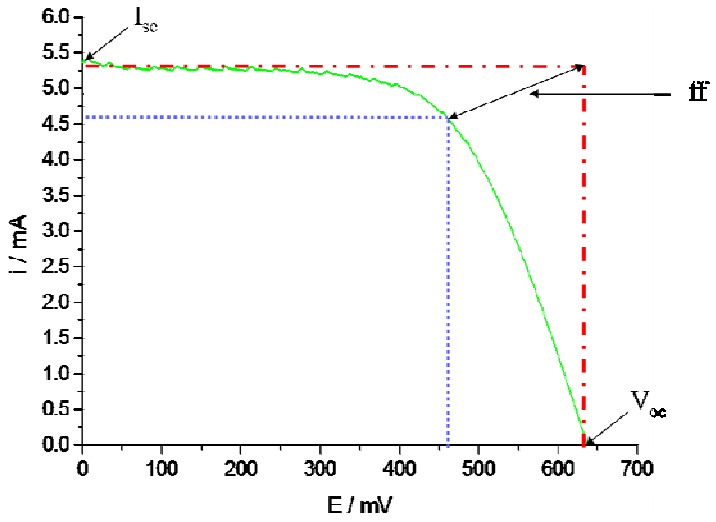


**Figure 11.** Typical IV curve (solid green line) for a DSSC highlighting important parameters obtained from this experiment.

Electrolyte composition is of particular importance in DSSCs as the additives can affect the energy of the conduction band of the $TiO_2$ and therefore the global efficiency of the cell. For example, the addition of TBP pushes the conduction band up in energy, resulting in a larger $V_{oc}$ (Figure 12). A simple measure of the $V_{oc}$ is the difference in energy between the Fermi level of the $TiO_2$ and the redox couple of the electrolyte. Therefore increasing this difference increases the $V_{oc}$. However, this can also result in a lower $I_{sc}$, as the energy of the excited state of the dye may now not be sufficient for high injection yields. In order to optimise the global efficiency of the DSSC the concentration of additives, such as TBP, Li, GuSCN must be empirically altered to maximise both $V_{oc}$ and $I_{sc}$ for a particular dye. Lithium has the opposite effect to TBP and reduces the level of the conduction band (increasing $I_{sc}$ but reducing $V_{oc}$). Guanidinum thiocyanate has been shown to reduce the dark current but has a smaller effect on the energy of the conduction band.

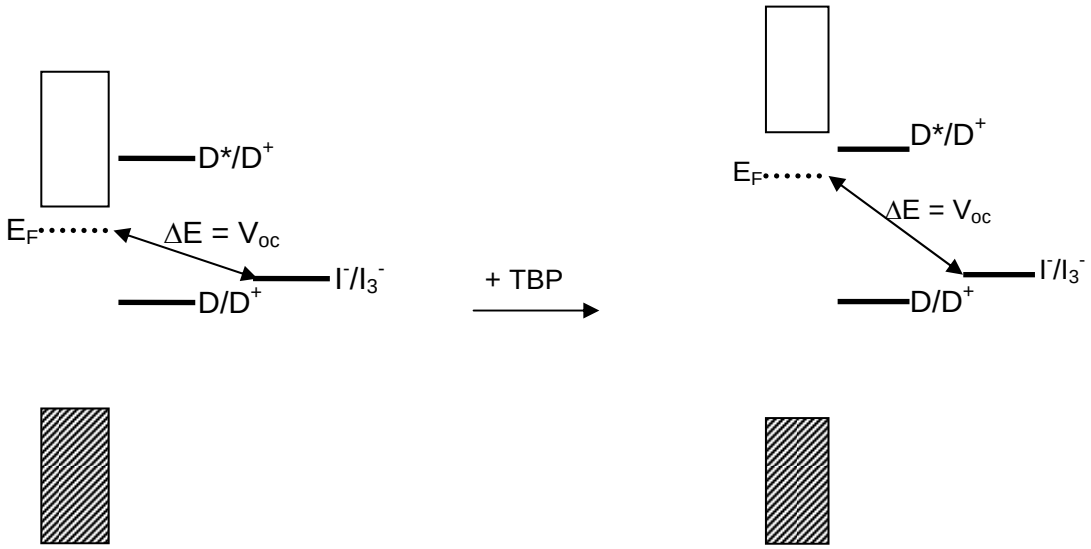


**Figure 12.** Energy level diagram showing effect of TBP addition to conduction band energy and resultant larger $V_{oc}$.

The simulated solar light was generated using AM 1.5 illumination (1000 $Wcm^{-2}$) provided by a solar simulator (1 kW Xe with AM 1.5 filter, Müller) calibrated using a GaAs solar cell. The voltage was scanned and the resulting current output from the cell recorded.

## 2.9 Transient Absorption Spectroscopy

This technique was used to investigate the charge-separated lifetime of the injected electron in the conduction band and the oxidised dye, sensitised on a $TiO_2$ film. This can yield valuable information about the recombination and regeneration rates of the dye/$TiO_2$ system. This work was carried out in collaboration with Dr. Ana Morandeira-Lopez from Prof. James Durrant's group at Imperial College London.

The dye is first sensitised on a film of $TiO_2$ (prepared in the same manner as described in Section 2.6). However in this instance a full cell is not constructed, only the working electrode need be prepared. A few drops of propylene carbonate electrolyte was placed on the film and finally a microscope cover slip placed on top to seal the system. To initiate electron injection from the dye into the $TiO_2$ a pump laser was set to a suitable excitation wavelength and repeatedly pulsed at the film (Figure 13). A second laser (labelled probe laser), was set to a wavelength which measures the absorbance of the dye cation absorption spectrum, and was continuously passed through the dye/$TiO_2$ film with the intensity analysed at a detector. The change in the intensity ($\Delta OD$) of the probe laser was recorded and measured versus time. The longer the signal took to return to its original state ($\Delta OD = 0$) the longer the charge-separated lifetime of the oxidised dye/conduction band electron and hence the slower the recombination.

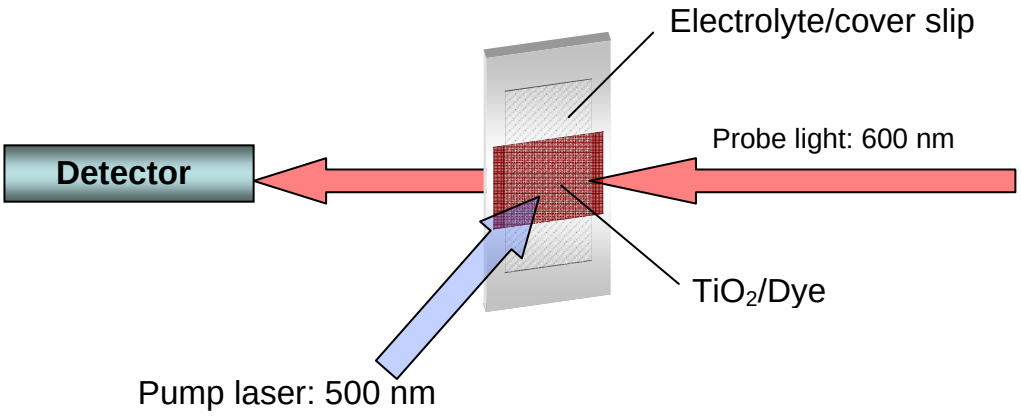


**Figure 13.** Schematic of transient absorption spectroscopy experiment, showing the excitation and measurement of a dye sensitised $TiO_2$ film.

Transient absorption decays were measured using the "flash photolysis" technique. This technique requires that the samples do not absorb or scatter all the incident light.

For this reason, instead of complete DSSCs, thin $TiO_2$ films (about 4 μm) sintered on microscope slides were used. The films were sensitised and covered with a drop of redox inactive electrolyte (0.25 M $LiClO_4$ in propylene carbonate) for dye cation/ $TiO_2$ conduction band $e^-$ recombination measurements, or with a drop of redox active electrolyte (0.25 M LiI/0.05 M $I_2$ in propylene carbonate) for the dye regeneration measurements.

The samples were excited with a dye laser (Photon Technology International Inc., GL-301) pumped by a nitrogen laser (Photon Technology International Inc., GL-3300). The excitation wavelength was 500 nm, the pulse width was 800 ps, the fluence was about 50 $\mu Jcm^{-2}$ and the repetition frequency was 1 Hz. A 100 W tungsten-halogen lamp (Bentham, IL1) with a stabilised power supply (Bentham, 605) was used as a probe light source. The probe light passing through the sample was detected with a silicon photodiode (Hamamatsu Photonics, S1722-01). The signal from the photodiode was pre-amplified and sent to the main amplification system with an electronic band-pass filter to improve the signal to noise ratio (Costronics Electronics). The amplified signal was collected with a digital oscilloscope (Tektronix, TDS 220), which was synchronised with a trigger signal of the laser pulse from a photodiode (Thorlabs Inc., DET210). To reduce stray light, scattered light and emission from the sample, two monochromators and appropriate optical cut-off filters were placed before and after the sample. Owing to the amplification and noise reduction system, the detectable change of absorbance was as small as $10^{-5}$ to $10^{-6}$.

## 2.10 Synthesis of Starting Materials

2,2'-bipyridyl (bpy) and 4,4'-dimethyl-2,2'-bipyridyl were purchased from Aldrich and used as received. Johnson Matthey are gratefully acknowledged for their kind loan of $RuCl_3.2H_2O$. 4,4'-$(CO_2H)_2$-2,2'-bipyridyl (dcbpy),[17] 4,4'-$(CO_2Et)_2$-2,2'-bipyridyl (decbpy),[18] $Ru(bpy)_2Cl_2$ [19] and $Ru(decbpy)_2Cl_2$ [20] were synthesised according to literature procedures, with standard analysis carried out to confirm successful synthesis.

**4,4'-$(CO_2H)_2$-2,2'-bipyridyl. (dcbpy)** CHN Calculated for $C_{12}H_8N_2O_4$: C 59.07, H 3.3, N 11.47, Found: C 55.99, H 3.21, N 11.39.

**4,4'-$(CO_2Et)_2$-2,2'-bipyridyl. (decbpy)** CHN Calculated for $C_{16}H_{16}N_2O_4$: C 63.99, H 5.37, N 9.33, Found: C 63.83, H 5.01, N 9.07. $^1$H-NMR (DMSO, 250 MHz): δ 9.05 (s, 2H), 8.88 (d, $J_{HH}$ = 4.97, 2H), 7.88 (d, $J_{HH}$ = 5, 2H), 4.37 (q, $J_{HH}$ = 7, 4H), 1.39 (t, $J_{HH}$ = 7, 6H).

**$Ru(bpy)_2Cl_2$.** CHN Calculated for $C_{20}H_{16}N_4Cl_2Ru.H_2O$: C 47.82, H 3.60, N 11.29, Found: C 47.49, H 3.22, N 11.01. $^1$H-NMR (DMSO, 250 MHz): δ 9.97 (d, $J_{HH}$ = 5, 2H), 8.63 (d, $J_{HH}$ = 8, 2H), 8.48 (d, $J_{HH}$ = 8, 2H), 8.05 (t, $J_{HH}$ = 8, 2H), 7.73 (t, $J_{HH}$ = 6, 2H), 7.67 (t, $J_{HH}$ = 6, 2H), 7.51 (d, $J_{HH}$ = 6, 2H), 7.10 (t, $J_{HH}$ = 6.5, 2H).

**$Ru(decbpy)_2Cl_2$.** CHN Calculated for $C_{32}H_{32}N_4O_8Cl_2Ru$: C 49.70, H 4.17, N 7.25, Found: C 49.88, H 4.66, N 7.20. $^1$H-NMR (DMSO, 250 MHz): δ 10.09 (d, $J_{HH}$ =6,

2H), 9.12 (s, 2H), 8.94 (s, 2H), 8.25 (d, $J_{HH}$ = 6, 2H), 7.75 (d, $J_{HH}$ = 6, 2H), 7.47 (d, $J_{HH}$ = 6, 2H), 4.51 (q, $J_{HH}$ = 7, 4H), 4.34 (q, $J_{HH}$ = 7, 4H), 1.43 (t, $J_{HH}$ = 7, 6H), 1.29 (t, $J_{HH}$ = 7, 6H).

## 2.11 References


[1] A.C. Fisher, *Electrode Dynamics*, Oxford University Press, 1996.

[2] D.F. Shriver, P.W. Atkins, *Inorganic Chemistry*, Oxford University Press, 2001.

[3] P.W. Atkins, *Physical Chemistry*, Oxford University Press, 2001.

[4] A. Vlček Jr., S. Zális, *Coord. Chem. Rev.*, 2007, **251**, 258-287.

[5] E.S. Boes, P.R. Livotto, H. Stassen, *Chem. Phys.*, 2006, **331**, 142-158.

[6] Gaussian 03, Revision C.02, M. J. Frisch, G. W. Trucks, H. B. Schlegel, G. E. Scuseria, M. A. Robb, J. R. Cheeseman, J. A. Montgomery, Jr., T. Vreven, K. N. Kudin, J. C. Burant, J. M. Millam, S. S. Iyengar, J. Tomasi, V. Barone, B. Mennucci, M. Cossi, G. Scalmani, N. Rega, G. A. Petersson, H. Nakatsuji, M. Hada, M. Ehara, K. Toyota, R. Fukuda, J. Hasegawa, M. Ishida, T. Nakajima, Y. Honda, O. Kitao, H. Nakai, M. Klene, X. Li, J. E. Knox, H. P. Hratchian, J. B. Cross, V. Bakken, C. Adamo, J. Jaramillo, R. Gomperts, R. E. Stratmann, O. Yazyev, A. J. Austin, R. Cammi, C. Pomelli, J. W. Ochterski, P. Y. Ayala, K. Morokuma, G. A. Voth, P. Salvador, J. J. Dannenberg, V. G. Zakrzewski, S. Dapprich, A. D. Daniels, M. C. Strain, O. Farkas, D. K. Malick, A. D. Rabuck, K. Raghavachari, J. B. Foresman, J. V. Ortiz, Q. Cui, A. G. Baboul, S. Clifford, J. Cioslowski, B. B. Stefanov, G. Liu, A. Liashenko, P. Piskorz, I. Komaromi, R. L. Martin, D. J. Fox, T. Keith, M. A. Al-Laham, C. Y. Peng, A. Nanayakkara, M. Challacombe, P. M. W. Gill, B. Johnson, W. Chen, M. W. Wong, C. Gonzalez, and J. A. Pople, Gaussian, Inc., Wallingford CT, 2004.

[7] J.P. Perdew, J.A. Chevary, S.H. Vosko, K.A. Jackson, M.R. Pederson, D.J. Singh, C. Fiolhais, *Phys. Rev. B*, 1993, **48**, 4978-4978.

[8] J.P. Perdew, K. Burke, Y. Wang, *Phys. Rev. B*, 1996, **54**, 16533-16539.

[9] P.J. Hay, W.R. Wadt, *J. Chem. Phys.*, 1985, **82**, 299-310.

[10] M.M. Francl, W.J. Pietro, W.J. Hehre, J.S. Binkley, M.S. Gordon, D.J. Defrees, J.A. Pople, *J. Chem. Phys.,* 1982, **77**, 3654-3665.

[11] Arguslab 4.0, M.A. Thompson, Planaria Software LLC, Seattle, http://www.arguslab.com.

[12] A. Vlček Jr., S. Zális, *J. Phys. Chem. A,* 2005, **109,** 2991-2992.

[13] M-F. Charlot, A. Aukauloo, *J. Phys. Chem. A*, 2007, **111**, 11661-11672.

[14] S.R. Stoyanov, J.M. Villegas, D.P. Rillema, *Inorg. Chem. Commun.,* 2004, **7**, 838-841.

[15] N. M. O'Boyle, A.L. Tenderholt, K.M. Langner, *J. Comp. Chem.*, 2008, **29**, 839-845.

[16] N. Papageorgiou, W.F. Maier, M. Grätzel, *J. Electrochem. Soc.* 1997**, 144**, 876-884.

[17] F.H. Case, *J. Am. Chem. Soc.*, 1946, **68**, 2574-2577.

[18] I. Gillaizeau-Gauthier, F. Odobel, M. Alebbi, R. Argazzi, E. Costa, C.A. Bignozzi, P. Qu, G.J. Meyer, *Inorg. Chem.*, 2001, **40**, 6073-6079.

[19] B.P. Sullivan, D.J. Salmon, T.J. Meyer, *Inorg. Chem.,* 1978, **17***,* 3334-3341.

[20] G. Wolfbauer, A.M. Bond, D.R. MacFarlane, *Inorg. Chem.,* 1999, **38**, 3836-3846.

# Chapter 3:

# S-Donor Ligand Dyes

## 3.1 Introduction

As discussed in Chapter 1, current high efficiency DSSCs utilise the sensitiser N719 (cis-bis(isothiocyanato)bis(2,2'-bipyridyl-4,4'-dicarboxylato)-ruthenium(II)bis-tetrabutylammonium) and have achieved a record efficiency of over 10 %.[1] One of the disadvantages of this dye is the lack of absorption in the red and near-infrared region of the electromagnetic spectrum, with the maximum absorption band found at 530 nm.[2] Another disadvantage of N719 is the potential dissociation of the monodentate NCS ligand and/or dye degradation, which will reduce the life span of the cell. Several conditions have been shown to induce loss of the isothiocyanato ligand, including air, high temperatures, water and UV light illumination.[3]

To counter the problem of low absorption in the red, the absorption spectra of ruthenium polypyridyl systems can be tuned by careful consideration of the HOMO and LUMO energy levels.[4,5] One can tune these levels in a number of ways, either by incorporation of a ligand with a low-lying $\pi^*$ molecular orbital[6] or *via* the use of strongly electron-donating ligands to destabilise the Ru $t_{2g}$ orbitals, both causing a decrease in the HOMO-LUMO gap and hence a red-shift in the absorption spectrum.

The former method has been shown to be effective when incorporating 4,4'-dicarboxy-2,2'-biquinoline, extending the absorption maximum of the dithiocyanato ruthenium complex to 630 nm.[7] The resulting DSSC however shows very inefficient

electron injection (IPCE = 3 %) when the dye is adsorbed to $TiO_2$, but increases when adsorbed to $SnO_2$. $SnO_2$ has a conduction band edge around 0.5 V more positive than $TiO_2$, and hence the injection efficiency increased as the LUMO of the dye is now sufficiently negative to allow electron injection. This study, among others,[8,9,10] shows the disadvantage of tuning the dye absorption spectrum *via* stabilisation of the LUMO as in this case the orbital has been shifted to a level below which charge injection into the $TiO_2$ conduction band can occur.

In this chapter the focus is on the use of bidentate S-donor ligands to increase the long-term stability of the dye in a DSSC and also red-shift the absorption range of the system. Despite a number of studies into tuning the absorption properties of platinum diimine dithiolate complexes by variation of the dithiolate ligands,[11,12,13,14] there are few previous studies which have used this approach for ruthenium polypyridyl complexes.

One such study, however, involves a series of ruthenium complexes incorporating three different mono-anionic dithiocarbamate ligands ($S_2CNR$).[15] The performance of these complexes in a DSSC was investigated in detail and they were indeed found to have the desired increase in absorption range. However, the DSSCs sensitised with these dyes showed a low photocurrent relative to N719. Transient absorption spectroscopy was used to investigate the cause of this poor performance. It was found that the recombination of the injected electron with the oxidised dye occurred on a suitably long timescale (μs) but the regeneration of the oxidised dyes by the

iodide/triiodide electrolyte was slower than that of N719. This resulted in charge recombination competing efficiently with dye regeneration for these systems leading to a lower photocurrent being observed for these cells.

Di-anionic dithiolate ligands have also been studied in this context with the MLCT transition tuned over a 150 nm range by changing the donor strength of the ligands. Despite the increased absorption range low efficiencies were obtained for DSSCs sensitised with these dyes. This was thought to be due to fast charge recombination in the systems and slow dye regeneration, although these points were not investigated in detail.[16]

Other classes of bidentate chelating ligands have also been investigated for use in DSSCs including β-diketonate ligands (such as acetylacetonate, and derivatives thereof) whereby the strong donating nature of the negatively charged oxygen donor destabilises the HOMO. [17,18] These complexes exhibited absorption maxima beyond 600 nm and DSSC efficiencies in the range 6.0-3.9 %. Dioxolene ligands (such as catecholate, alizarin and functionalised coumarins) have also been used to make ruthenium bipyridyl dyes.[19] Although these complexes were used in an electrochromic application, they also show a significant extension of absorption range to beyond 600 nm.

The maximum efficiency of a DSSC utilising a dye which replaces the NCS ligands with a bidentate chelating ligand is 6.9 % for [Ru(dcbpy)$_2$(dipivaloylmethanato)]Cl (Figure 1).[20] This dye shows an absorption maximum at 530 nm ($\varepsilon$ = 11000 $M^{-1}cm^{-1}$), with a significant intensity absorption shoulder at 580 nm.

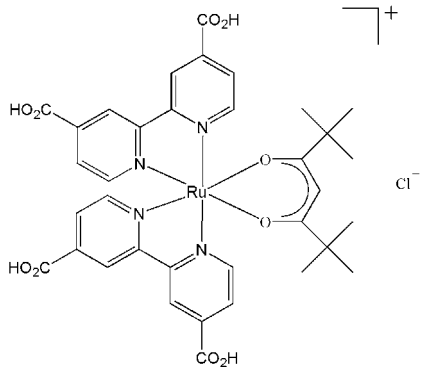


**Figure 1.** Chemical **s**tructure of [Ru(dcbpy)$_2$(dipivaloylmethanato)]Cl.

The present work focuses on the use of two ligands; **L1**, potassium cyanodithioimidocarbonate ($K_2C_2N_2S_2$) and **L2**, potassium ethyl xanthate ($KS_2COEt$), in an attempt to build on the previous work with similar S-donor ligands and to enhance the electronic properties of the dyes. Six complexes (Figure 2) have been synthesised and characterised electrochemically, spectroscopically and computationally using the two S-donor ligands. The unsubstituted and ester bipyridyl derivatives were synthesised to aid the study and rationalisation of the electronic properties of the dye series, in particular due to the poorer solubility of the acid dyes, the electronic properties of these can be conveniently inferred from the ester analogues. The acid derivatives were used as a sensitiser in a DSSC, with the performance and kinetics of these devices investigated.

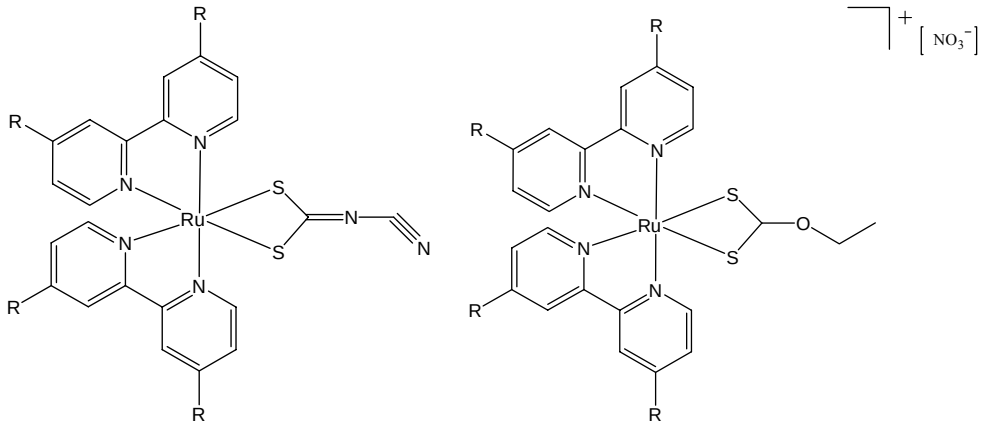


**Figure 2.** Chemical structures of $[Ru(R\text{-}bpy)_2C_2N_2S_2]$ (R = H (**1**), $CO_2Et$ (**2**), $CO_2H$ (**3**)) and $[Ru(R\text{-}bpy)_2(S_2COEt)][NO_3]$ (R = H (**4**), $CO_2Et$ (**5**), $CO_2H$ (**6**)).

## 3.2 Electrochemistry

The redox potentials of all processes for each complex are shown in Table 1. Dyes **1** - **3** all show one reversible oxidation, which increases in potential by around 0.2 V upon inclusion of the electron-withdrawing ester/acid groups on the bipyridines. The oxidation of **1** was fully reversible in 0.1 M $TBABF_4$/DMF as were the two observed reductions (Figure 3).

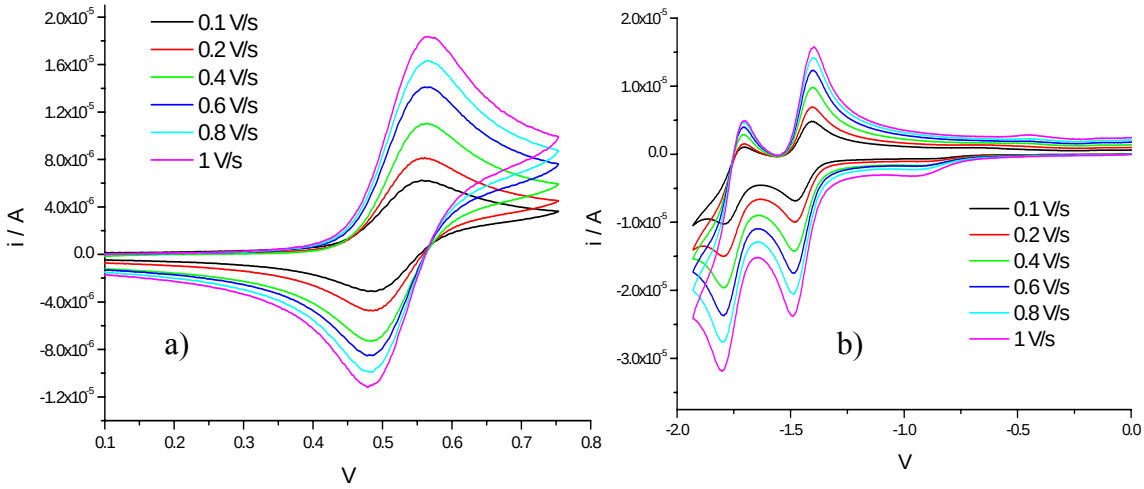


**Figure 3.** Cyclic voltammetry of **1** in 0.1 M $TBABF_4$/DMF, showing a) oxidation and b) reductions.

| Complex | $E_{1/2}^{ox}$ / V | $E_{1/2}^{red}$ / V | | |
|---|---|---|---|---|
| **L1** | -0.1 [a] | -1.92 [a] | | |
| **L2** | 0.49 [a] | -1.9 [a] | | |
| **1** | 0.52 | -1.44 | -1.75 | |
| **2** | 0.73 | -0.98 | -1.21 | -1.77 [a] |
| **3** | 0.71 | -1.08 [a] | -1.34 [a] | |
| **4** | 0.89 | -1.33 | -1.6 | |
| **5** | 1.07 [b] | -0.90 | -1.09 | -1.68 [a] |
| **6** | 1.08 [b] | -0.83 [a] | -1.08 [a] | -1.58 [a] |

[a] Irreversible

[b] Quasi-reversible

**Table 1.** Redox potentials of **L1**, **L2**, and complexes **1** - **6** in 0.1 M $TBABF_4$/DMF (*vs.* Ag/AgCl).

The electrochemistry of complex **2** was studied in both 0.1 M $TBABF_4$/DMF and 0.3 M $TBABF_4$/DCM, with the oxidation of the complex found to be only partially reversible in DMF but fully reversible in DCM (Figure 4). This is likely to arise from DMF coordinating to the oxidised species and further evidence for this was observed during the spectroelectrochemical studies (Section 3.4).

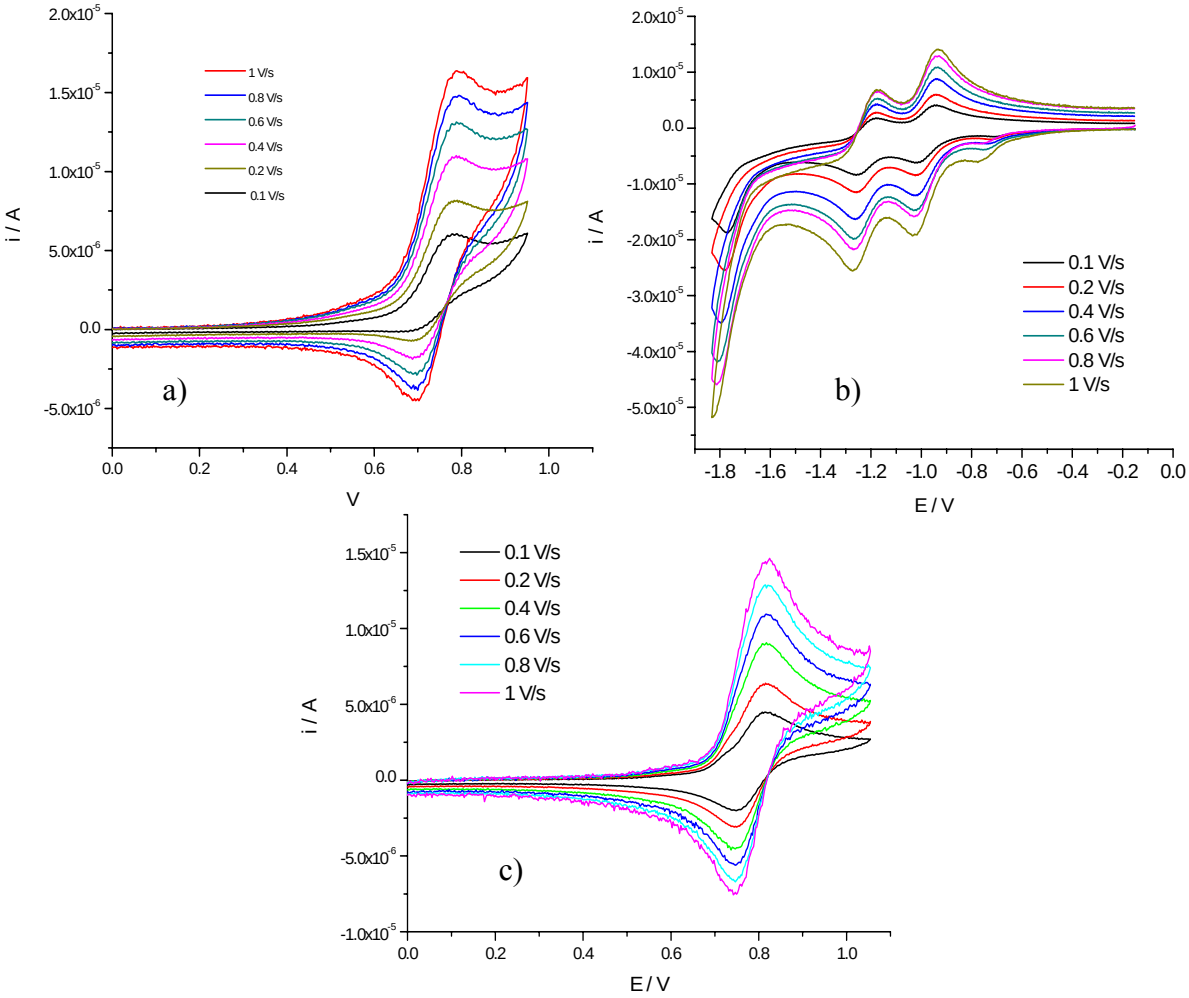


**Figure 4.** Cyclic voltammetry studies of **2** in 0.1 M $TBABF_4$/DMF, showing a) oxidation and b) reductions and c) study carried out in 0.3 M $TBABF_4$/DCM.

The first two reductions for **1** - **3** are assigned to the bipyridyl ligands and are again observed to shift to more positive potential for the acid and ester-substituted complexes relative to the unsubstituted analogue. The third reduction, at -1.77 V, in the study of **2** may be assigned to either the dithiolene ligand, as this was similar to the reduction observed in the electrochemistry of the uncomplexed ligand, or a third bipyridyl based reduction as seen for complexes **5** and **6**.

Complex **4** showed one reversible oxidation and two fully reversible reductions (Figure 5), similar to complex **1**. The electrochemistry of complex **5** was complicated by the presence of a minor impurity (small oxidation peak at 0.46 V), which was not removed *via* a Sephadex column or recrystallisation. The main oxidation process was found to be chemically irreversible in DMF, even at -40 °C, and only partially electrochemically reversible in DCM (Figure 6). Again the oxidation and reduction potentials of the acid analogue **6** were found to be the same as the ester analogue **5**, and it should also be noted that the small impurity peak was not present in the electrochemical studies of **6**.

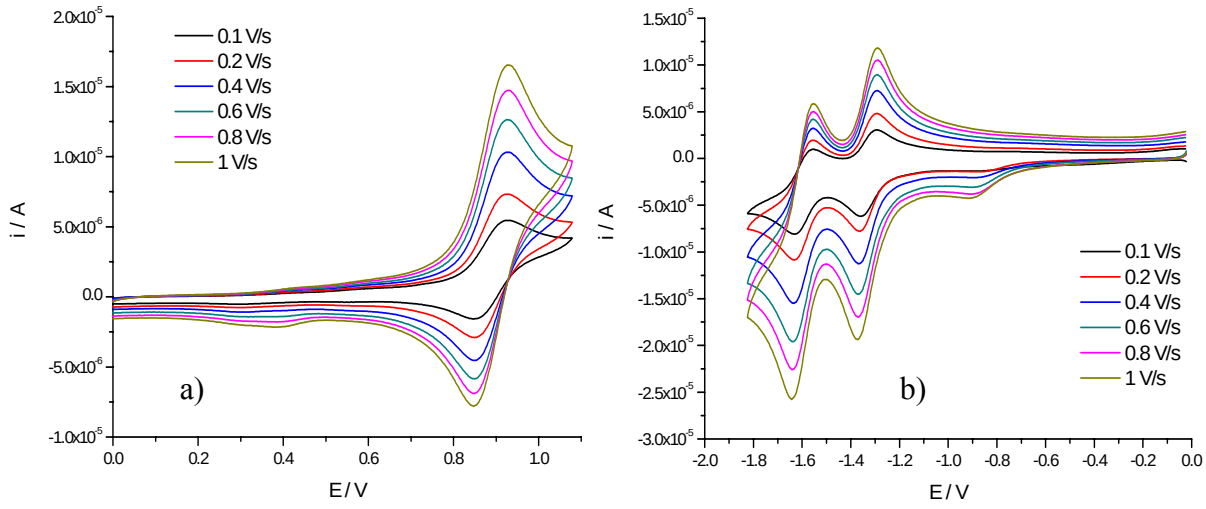


**Figure 5.** Cyclic voltammetry of **4** in 0.1 M $TBABF_4$/DMF, showing a) oxidation and b) reductions.

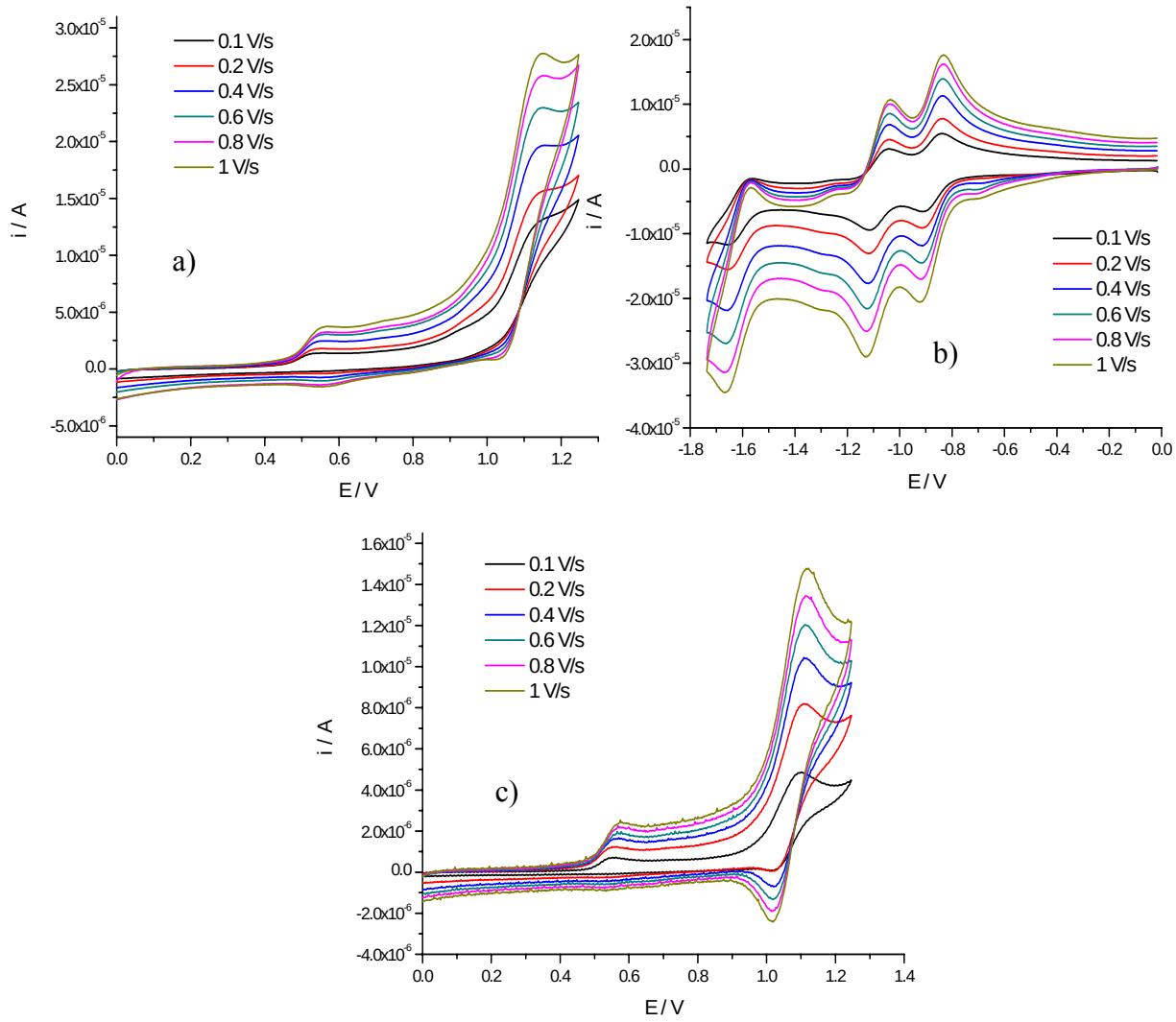


**Figure 6.** Cyclic voltammetry of **5** in 0.1 M $TBABF_4$/DMF at room temperature a) oxidation, b) reductions and c) and at -40 °C (bottom).

The oxidations for **4** – **6** were more positive than for the analogous dyes **1** – **3**, presumably due to the additional positive charge on the former. Importantly, the oxidation and reduction potentials of **3** and **6** are sufficient for both regeneration by the iodide/triiodide redox electrolyte and injection into the conduction band of $TiO_2$, when compared with the expected energies of these components and hence both dyes were expected to function as sensitisers in a DSSC.

## 3.3 Absorption Spectroscopy

Absorption spectra were recorded in DMF (Table 2, Figure 7) and the assignment of these transitions has been further investigated using theoretical computational studies (Section 3.6). **1**, **2** and **3** show a significant red-shift of the absorption maximum, peaking at 548 nm (**1**) and around 580 nm (**2**, **3**) respectively, relative to complexes **4**, **5**, and **6,** with corresponding peaks of around 490 and 530 nm.

In comparison to N3 ($\lambda_{max}$ = 534 nm), dye **3** shows a significantly lower absorption energy and hence a greater absorption range has been achieved, as desired. The molar extinction co-efficients of the acid dyes (**3** and **6**) are both slightly higher than that of N3 ($\varepsilon$ = 14.2 x $10^3$ $M^{-1}$ $cm^{-1}$)[2] which potentially increases their light harvesting efficiency and may also lead to the ability to produce thinner cells, a distinct advantage in a DSSC due to the decreased losses associated with charge transport.[21]

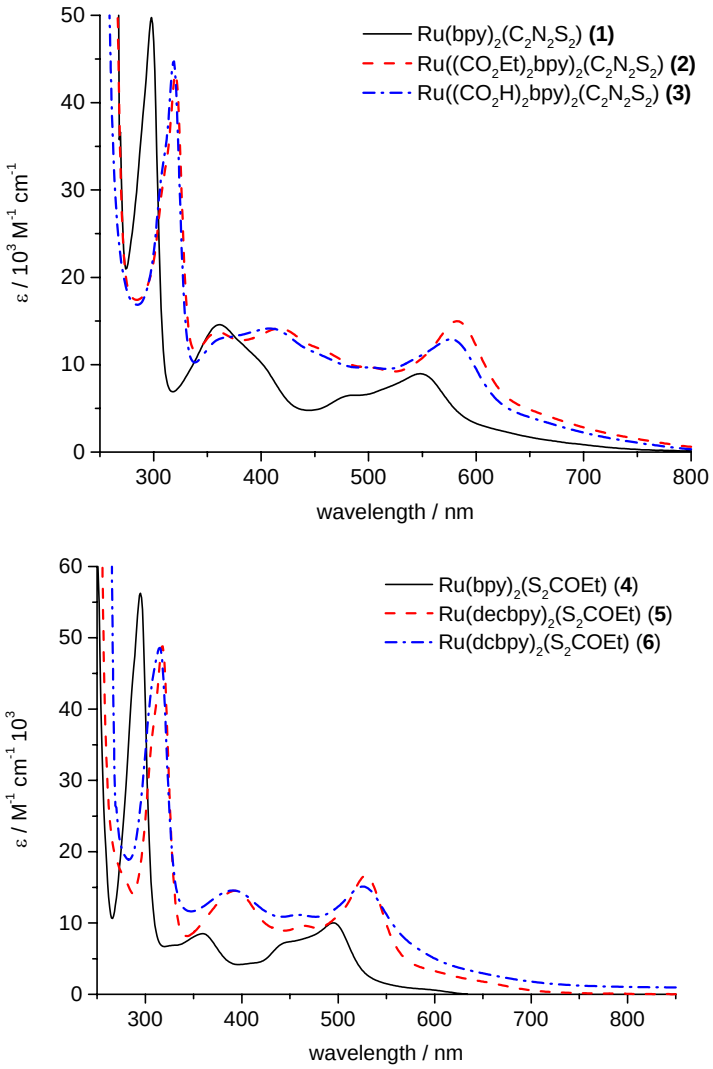


**Figure 7.** Absorption spectra of complexes **1**-**3** (top) and **4**-**6** (bottom) in DMF.

| Complex | $\pi - \pi^*$/nm | MLCT/nm | | |
|---|---|---|---|---|
| **1** | 298 (51.3) | 548 (8.9) | 481 sh (6.4) | 361 (14.6) |
| **2** | 320 (45.2) | 583 (15) | 417 (14.2) | 361 (13.7) |
| **3** | 319 (39) | 578 (13) | 408 (14.3) | 364 (13.2) |
| **4** | 292 (56) | 492 (8.9) | 447 sh (7) | 357 (8.8) |
| **5** | 317 (48.9) | 530 (15.5) | 463 sh (11.6) | 396 (14.5) |
| **6** | 314 (48.6) | 528 (15.2) | 463 (10.1) | 391 (15.0) |

**Table 2.** Summary of absorption spectra maxima for complexes **1** - **6** carried out in DMF. Molar extinction co-efficients / $M^{-1}$ $cm^{-1}$ $10^3$ shown in brackets.

### 3.3.1 Emission Studies

Emission studies showed that **1** – **3** showed no room temperature emission in ethanol, even after de-gassing the solution, whereas **4** – **6** showed weak emission. In contrast, all complexes were found to be emissive at 77 K (Table 3).

The observed emission, and corresponding excitation spectra, for complexes **1** – **3** closely resemble those of the respective tris-bipyridyl complexes [22] (Figure 8, Figure 9) with a large Stokes shift suggesting $^3$MLCT emission. Firstly, the fact that the excitation spectra do not match the observed absorption spectra may be indicative of a significant number of transitions that do not populate emissive states *i.e.* not the typical MLCT seen for ruthenium bipyridyl complexes. The close resemblance of

these studies to the emission and excitation spectra of the corresponding tris-bipyridyl complexes may show that transitions involving any orbital with significant **L1** character populate non-emissive states. These points are further discussed with respect to the hybrid DFT calculations in Section 3.5.

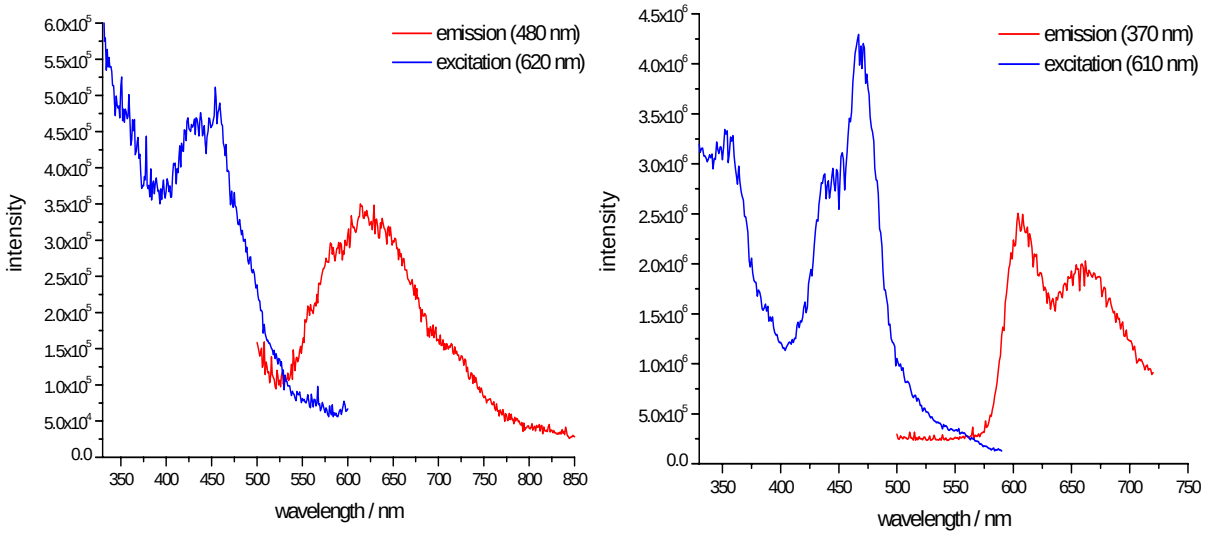


**Figure 8.** Excitation and emission spectra of **1** (left) and **2** (right) in ethanol at 77 K.

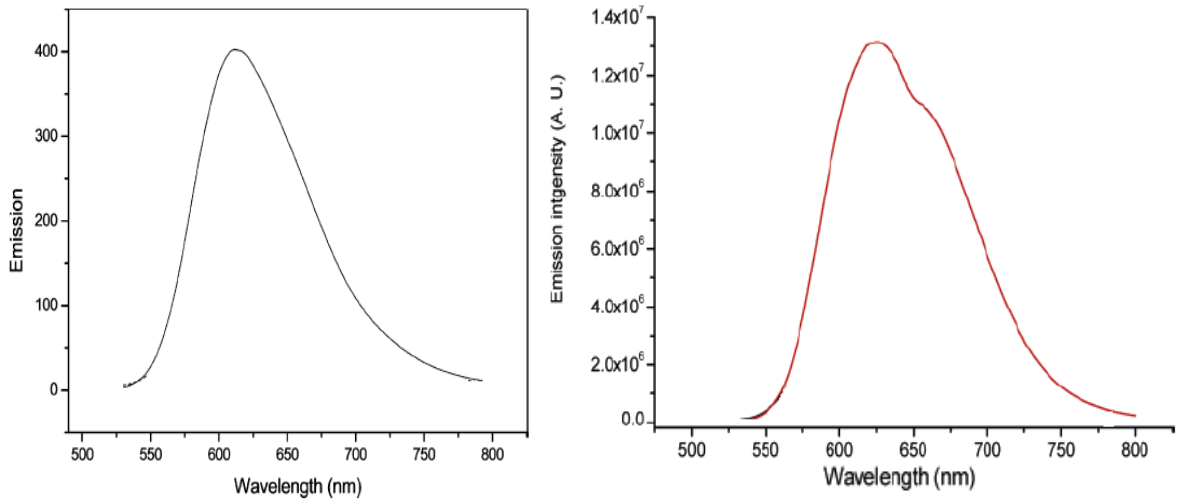


**Figure 9.** Emission spectra of $[Ru(bpy)_3]^{2+}$ (left) and $[(Ru(decbpy)_3]^{2+}$ from literature studies,[22,23] both carried out at room temperature.

The emission spectra of **4** - **6** (Figure 10, Table 3) did not overlap with the excitation spectra also suggesting typical $^{3}$MLCT emission as would be expected for these types of complexes. In addition the excitation spectra of these complexes closely resemble the absorption spectra. The main difference between the room temperature and 77 K studies for **4** was the resolution of the broad band (690 nm) at room temperature to show two sharp bands at 77 K (580 and 640 nm). A similar observation was made for **5** and **6**, with the emission band seen at 760 nm at room temperature resolved as one sharp band at 710 nm at 77 K.

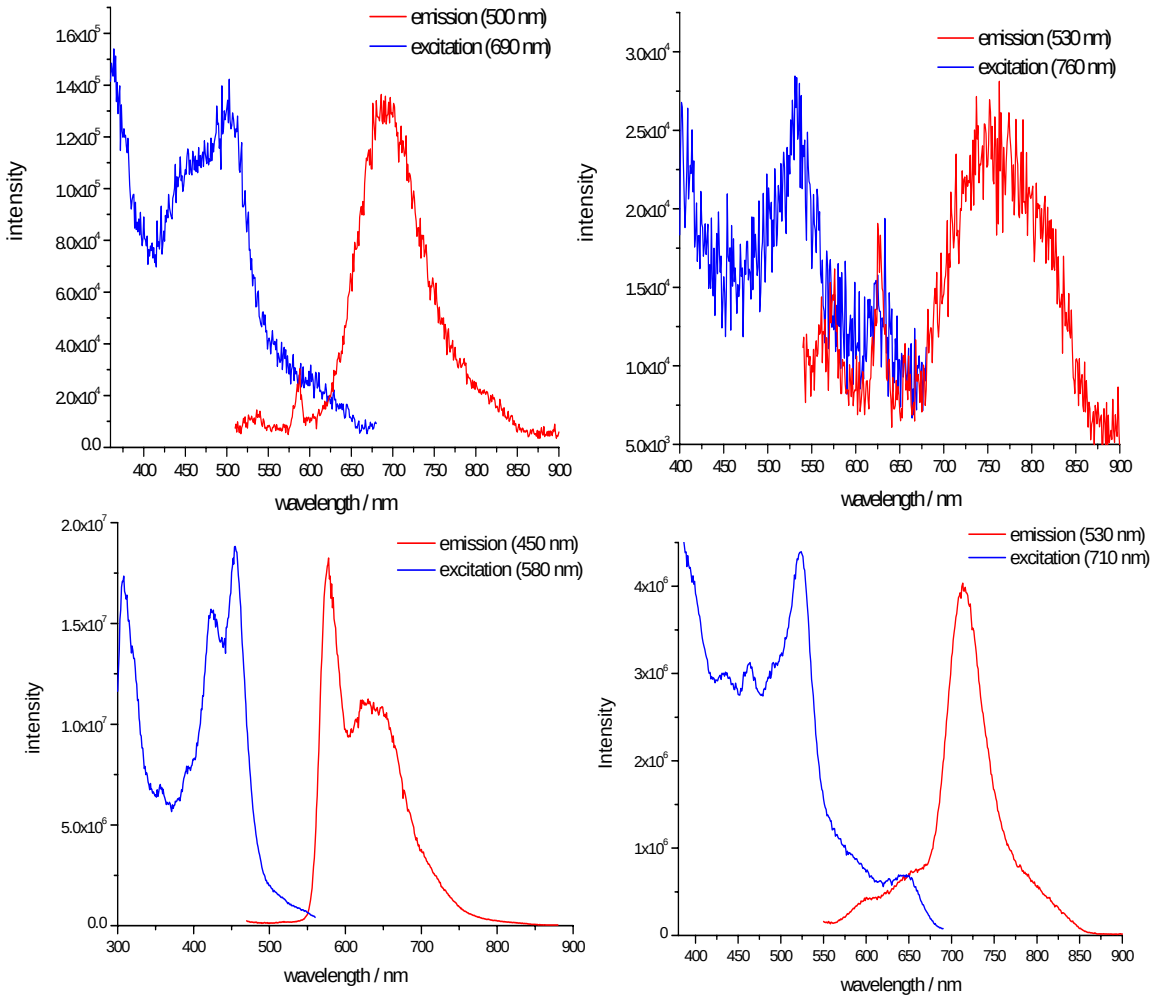


**Figure 10.** Excitation and emission spectra for complexes **4** (left) and **5** (right) at room temperature (top) and 77 K (bottom).

| Complex | Emission max. / nm | |
|---|---|---|
| | 293 K | 77 K |
| **1** | - | 620, 710 |
| **2** | - | 610, 660 |
| **3** | - | 660 |
| **4** | 690 | 580, 640 |
| **5** | 760 | 710 |
| **6** | 750 | 710 |

**Table 3.** Emission spectra maxima for complexes **1 – 6**, at room temperature and 77 K, in ethanol.

## 3.4 Spectroelectrochemistry

Through studying the oxidised and reduced species of these complexes the nature of the frontier orbitals can be further investigated. The change in absorption spectrum of **2** upon oxidation was studied in both 0.1 M $TBABF_4$/DMF and 0.3 M $TBABF_4$/DCM (Figure 11). This was firstly to establish whether the solvent was coordinating to the oxidised complex, as had been hypothesised from the electrochemical studies in the two solvents, and secondly to further characterise the nature of the HOMO. In DMF the CT bands were seen to decrease in intensity and gradually two new bands grew in, however no isosbestic points were observed between the initial and final spectra. This study was not fully reversible to the initial spectrum upon re-reduction, further evidence that the oxidised product is itself forming another species.

In DCM the CT bands also decrease in intensity, however in this case there is no new peak growth. In addition to this, four isosbestic points were observed and the study was fully reversible back to the initial spectrum upon re-reduction. These studies, as well as the electrochemical studies, carried out in the two solvents strongly suggest that solvent coordination is playing a role upon oxidation of **2**. Therefore results in the non-coordinating solvent DCM will be used to discuss the oxidation of **2** in more detail, rather than those obtained in the DMF study.

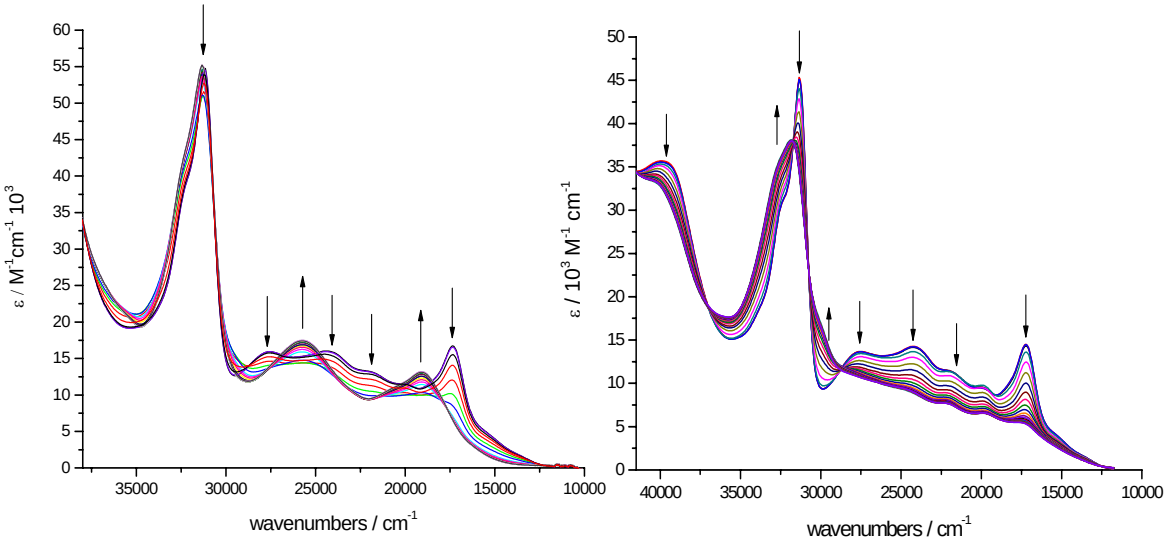


**Figure 11.** Spectroelectrochemical oxidation of **2**. Study carried out in 0.1 M $TBABF_4$/DMF (left) and 0.3 M $TBABF_4$/DCM (right), both at -40 °C, with an applied potential of + 1 V (*vs.* Ag/AgCl). Arrows indicate the growth or reduction of an absorption band with oxidation.

As well as the partial collapse of the CT bands, the study in DCM also shows a broadening of the bipyridyl intraligand band, indicative of a ruthenium based oxidation.[24] The fact that the CT bands do not fully collapse, as would be expected for a complex with a large ruthenium contribution to the HOMO, and also retain their

peak shape suggests that the oxidation is not fully ruthenium based but also has a significant degree of $C_2N_2S_2$ ligand character.

The mono-reduced and di-reduced species of **2** were studied in DMF (Table 4 on Pg. 78, Figure 12) and are very similar to that of the mono-reduced and di-reduced species of $[Ru(decbpy)_2(CN)_2]$, suggesting that the lowest unoccupied orbitals are bipyridyl ligand in nature, as discussed in previous studies.[25] Both studies were fully reversible to the neutral spectrum in this solvent. The mono-reduced species shows collapse of the MLCT bands followed by the growth of new intraligand bands in their place. The $\pi$-$\pi^*$ intraligand band at 31000 $cm^{-1}$ completely collapses after di-reduction, and several of the features observed in the mono-reduced spectrum become more intense (Table 4) as was observed for $Ru(decbpy)_2(CN)_2$.

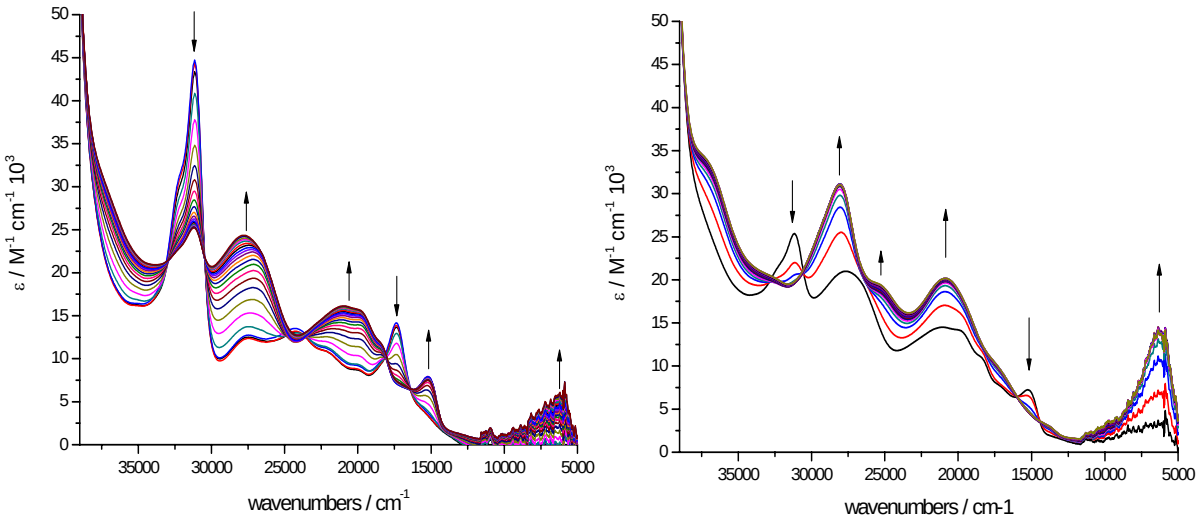


**Figure 12.** Reductive OTTLE studies of **2** in 0.1 M $TBABF_4$/DMF, showing mono-reduced (left) and di-reduced (right), with applied potentials of -1.1 V and -1.49 V (*vs.* Ag/AgCl).

The unsubstituted bipyridyl dye (**1**) in this series showed a similar result upon oxidation (Table 4, Figure 13) with the partial collapse of the CT bands and a broadening of the bipyridyl intraligand band. Again the CT bands retained their peak shape, providing further evidence that the HOMO of the dyes in this series are ruthenium based with a significant degree of $C_2N_2S_2$ character.

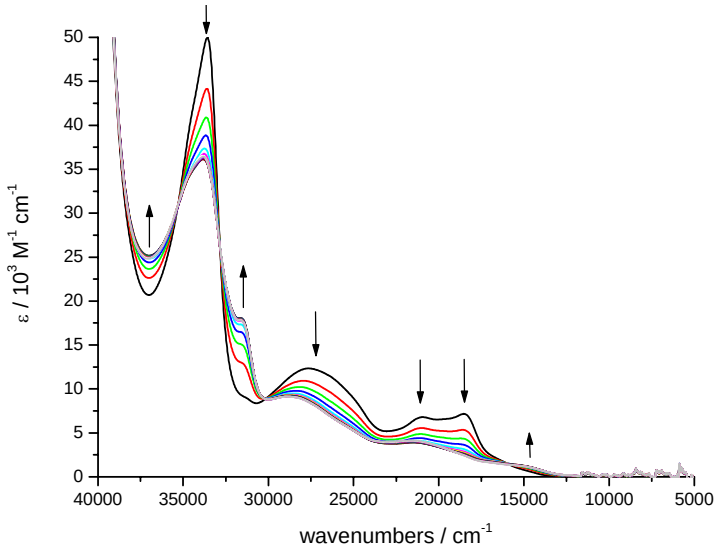


**Figure 13.** Oxidative OTTLE study of **1**, in 0.1 M $TBABF_4$/DMF with an applied potential of +0.5 V (*vs.* Ag/AgCl) at -40 °C.

The oxidative OTTLE experiment for **5** was also found to be solvent dependent, showing no well-defined isosbestic points in DMF and deviations from the original spectrum upon re-reduction. In contrast the study in DCM showed a number of isosbestic points and fully reversible behaviour. The oxidation of **5** in DCM (Table 4, Figure 14) showed an almost complete collapse of the lowest energy CT band and a partial collapse of the second CT band as well as a broadening of the bipyridyl intraligand band. Similar observations were made upon oxidation of

[Ru(decbpy)$_2$Cl$_2$], indicating that the HOMO of **5** is likely to be largely located on the ruthenium centre. The mono-reduced and di-reduced OTTLE studies of **5** closely resemble that of **2**, indicating that the reductions are bipyridyl ligand based (Figure 15)**.**

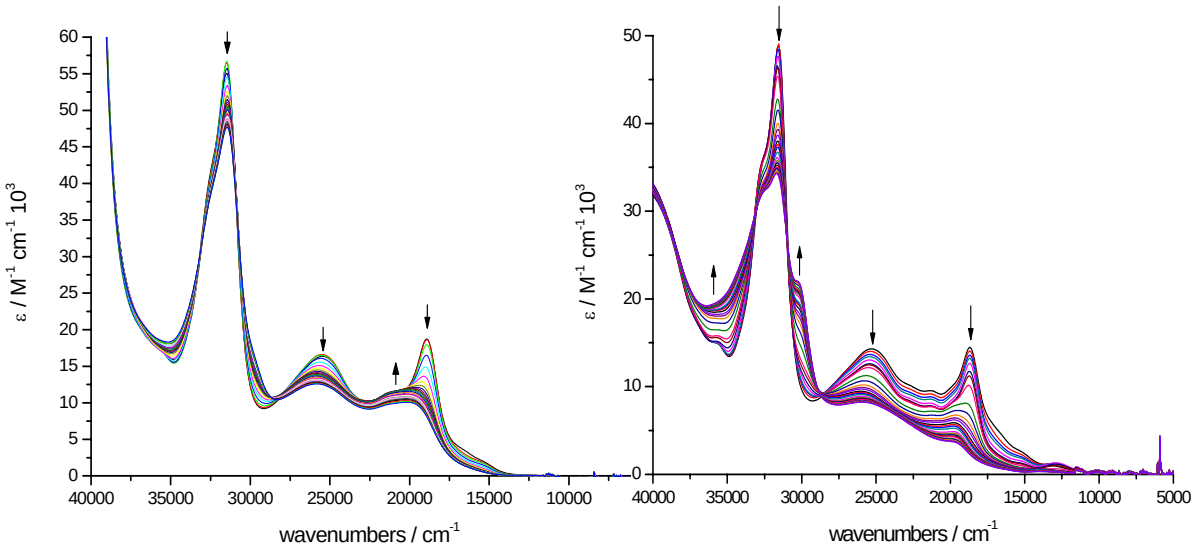


**Figure 14.** Spectroelectrochemical oxidation of **5**. Study carried out in 0.1 M TBABF$_4$/DMF (left) and 0.3 M TBABF$_4$/DCM (right) at -40 °C, with an applied potential of + 1.5 V (*vs.* Ag/AgCl).

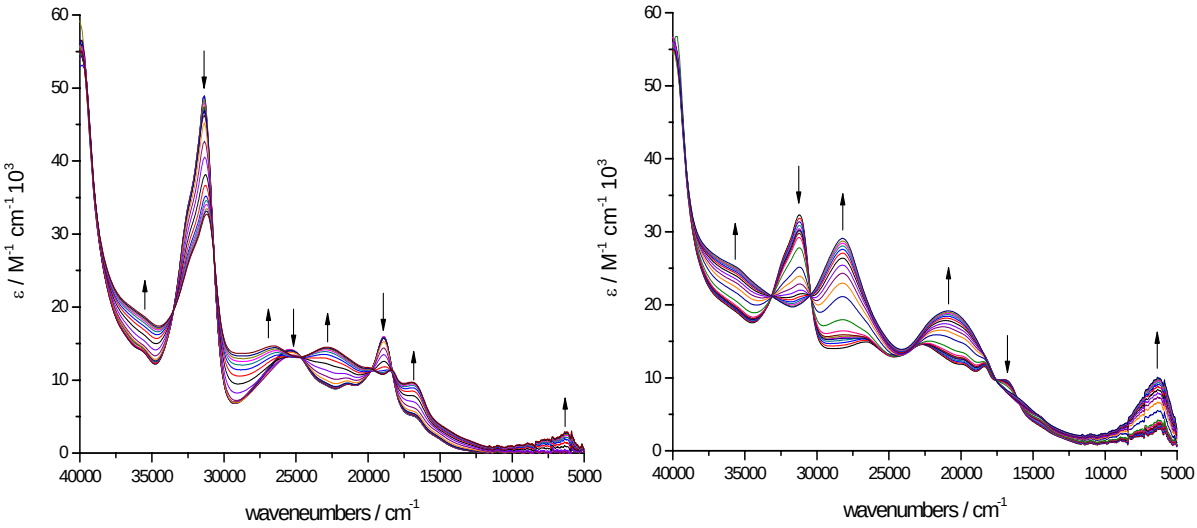


**Figure 15.** Reductive OTTLE Studies of **5**, in 0.1 M TBABF$_4$/DMF showing mono-reduced (left) and di-reduced (right) with applied potentials of -0.99 V and -1.2 V (*vs.* Ag/AgCl) respectively.

Complex **4** showed a similar solvent dependence and also indicated a largely ruthenium centred HOMO, with the complete collapse of the low energy CT band and a partial collapse of the second CT band (Table 4, Figure 16). Also observed in this study was the complete collapse of the bipyridyl intraligand band at 35000 $cm^{-1}$ along with the growth of another band at 31700 $cm^{-1}$. Upon comparison to the oxidation of $[Ru(bpy)_2Cl_2]$ there are distinct similarities indicating a large contribution of the ruthenium to the HOMO.

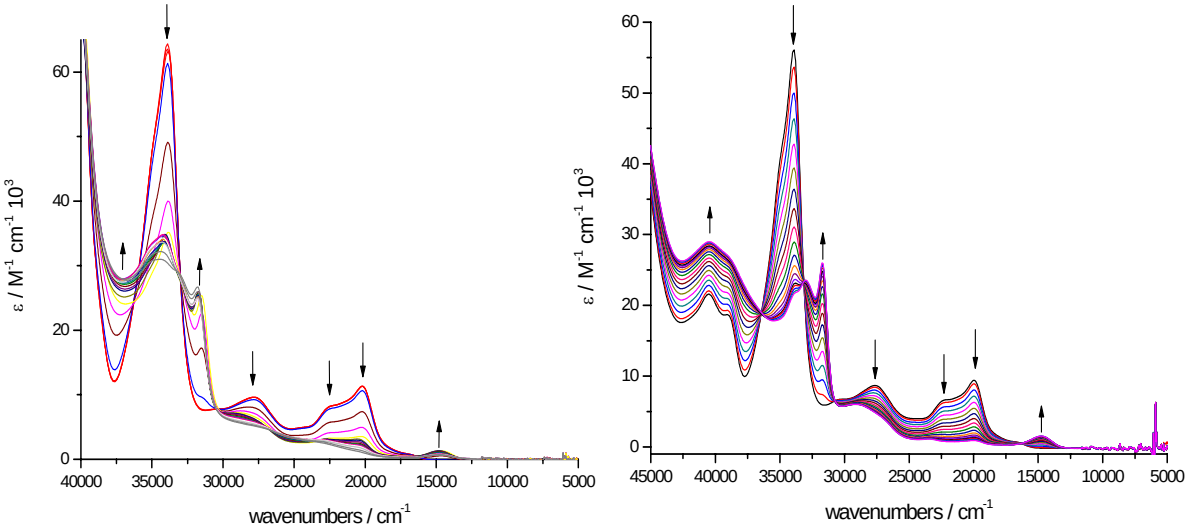


**Figure 16.** Oxidative OTTLE study of **4**, in 0.1 M $TBABF_4$/DMF (left) and 0.3 M $TBABF_4$/DCM (right) with an applied potential of +1.5 V (*vs.* Ag/AgCl).

Interestingly, spectroelectrochemical studies carried out on the ethyl ester analogue of N3 ($Ru((CO_2Et)_2\text{-}bpy)_2(NCS)_2$) found that this dye is not stable in the oxidised state under the conditions in which these OTTLE studies are carried out. In both DMF and DCM the oxidative OTTLE study was found to be irreversible (Figure 17).

Previous stability studies of N3 (and analogues thereof) have been carried out both in solution [26] and in a DSSC [3] and have suggested possible degradation mechanisms for this dye. In a methanolic solution of N3 containing sodium iodide the absorption maximum was observed to red-shift after irradiation, indicating the exchange of the NCS ligands with the stronger donor iodide. NMR studies of this reaction using a model compound with only one thiocyanate also showed the formation of the iodo complex as well as a cyano complex resulting from the loss of sulphur from the NCS ligand. The loss of sulphur is thought to involve the oxidised state of the dye *via* internal charge transfer from the $Ru^{III}$ centre to the NCS ligand. The timescale of this process is 0.1 – 1 second, and so if the dye is reduced back to $Ru^{II}$ by the iodide (which occurs on a timescale of nanoseconds in a DSSC) then the loss of sulphur will not readily occur.

The OTTLE study carried out in DMF in the present work is likely to show the formation of $[Ru(decbpy)_2(DMF)(NCS)]^+$. This is indicated by the clean conversion between the initial and final products with several isosbestic points. This product has also previously been observed for the analogous $Ru(bpy)_2(NCS)_2$ *via* photolysis in DMF. [27] The study in DCM shows a much messier conversion between initial and final spectra, indicating a ligand loss mechanism rather than ligand exchange, presumably due to the low coordinating ability of DCM, with a likely product being the cyano complex discussed above.

It can therefore be concluded that under the conditions used in these studies that the introduction of the bidentate S-donor ligands has indeed increased the stability of the dyes in the oxidised state relative to N3, as desired.

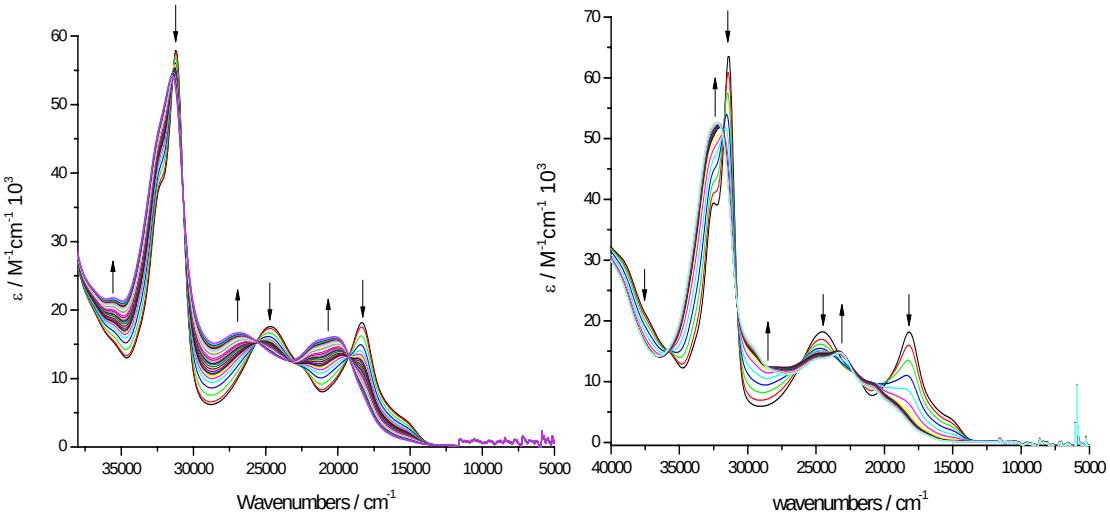


**Figure 17.** Oxidative OTTLE studies of $Ru((CO_2Et)_2\text{-}bpy)_2(NCS)_2$ in 0.1 M $TBABF_4$/DMF (left) and 0.3 M $TBABF_4$/DCM (right) with an applied potential of +1.2 V (*vs.* Ag/AgCl).

| **Complex** | **Absorption / $cm^{-1}$ ($\varepsilon$ / $M^{-1}$ $cm^{-1}$ $10^3$)** |
|---|---|
| $[Ru(decbpy)_2(C_2N_2S_2)]^+$ | 17400 (5.6) 19900 (6.7) 22150 (7.6) 24700 (9.3) 31850 (37.9) 40250 (33.2) |
| $[Ru(decbpy)_2(C_2N_2S_2)]^-$ | 6012 (5.8) 15205 (7.4) 18323 (11.6) 19842 (15.7) 20960 (16.2) 27755 (24.3) 31193 (25.0) |
| $[Ru(decbpy)_2(C_2N_2S_2)]^{2-}$ | 6293 (14.2) 20890 (20.2) 25263 (19.4) 28093 (31.1) |
| $[Ru(bpy)_2(C_2N_2S_2)]^+$ | 15153 (1.3) 21627 (4.1) 28839 (9.1) 31577 (17.8) 33758 (36.4) |
| $[Ru(decbpy)_2(S_2COEt)]^{2+}$ | 19818 (3.67) 25825 (8.3) 30092 (21.8) 31655 (34.2) |
| $[Ru(bpy)_2(S_2COEt)]^{2+}$ | 14750 (1.6) 29100 (6.0) 31700 (26.1) 33000 (23.6) 40500 (29.1) |
| $[Ru(decbpy)_2(S_2COEt)]$ | 6233 (2.9) 16897 (9.7) 18454 (11.1) 22808 (14.4) 26666 (14.6) 31209 (32.7) |
| $[Ru(decbpy)_2(S_2COEt)]^-$ | 6384 (9.7) 20875 (19.5) 28215 (29.3) |

**Table 4.** Absorption spectra maxima of electrochemically mono-oxidised, mono-reduced and di-reduced **2** and **5**, and mono-oxidised **1** and **4**.

## 3.5 Hybrid DFT Calculations

Computational studies of the ester derivatives **2** and **5** were carried out using the same basis sets and level of theory as detailed in Chapter 2, Section 2.4.1.

The HOMO of **2** was found to be largely ruthenium in character (54 %) with partial delocalisation over the $C_2N_2S_2$ ligand (39 %) (Table 5). In addition the HOMO-1 was found to be very close in energy, with only a 0.07 eV difference, and also shows significant delocalisation over the $C_2N_2S_2$ ligand (Figure 18). This suggests that upon oxidation of the dye the resulting hole will be partly delocalised onto the entire ligand. This should be advantageous in a DSSC for regeneration of the oxidised dye by the redox mediator and also for reduced charge recombination.

The large contribution of the $C_2N_2S_2$ ligand to the HOMO may also explain the lack of fluorescence observed with this dye series, as this would mean that the lowest energy excited state which is populated after excitation possesses significant ligand-to-ligand charge-transfer (LLCT) character. This lower-energy state would be expected to undergo more rapid non-radiative decay and hence emission would not be observed. The $^3$MLCT character of the observed emission for this series showed a close resemblance to the emission and excitation spectra of the corresponding tris-bipyridyl complexes. This may be a result of transitions from lower occupied orbitals with a small degree of **L1** and large degree of ruthenium character, such as

the HOMO-2, resulting in typical MLCT transitions, hence the observation of emission similar to that of Ru(R-bpy)$_3$.

| MO | Energy / eV | % Ru | % $C_2N_2S_2$ | % decbpy |
|---|---|---|---|---|
| **LUMO+1** | -2.70 | 11.3 | 2.35 | 86.35 |
| **LUMO** | -2.81 | 6.35 | 1.4 | 92.22 |
| **HOMO** | -5.54 | 53.79 | 38.54 | 7.63 |
| **HOMO-1** | -5.61 | 55.05 | 34.41 | 10.51 |
| **HOMO-2** | -5.93 | 69.36 | 10.58 | 20.02 |
| **HOMO-3** | -6.75 | 24.86 | 58.86 | 16.25 |
| **HOMO-4** | -6.80 | 22.68 | 60.93 | 16.36 |

**Table 5.** Energies and percentage contribution of Ru, $C_2N_2S_2$ and decbpy to selected molecular orbitals for the optimised geometry of **2** in DMF.

The two lowest unoccupied orbitals were found to be very close in energy and located mainly over the two bipyridyl rings with a small degree of ruthenium character, which agrees very well with the reductive spectroelectrochemical studies.

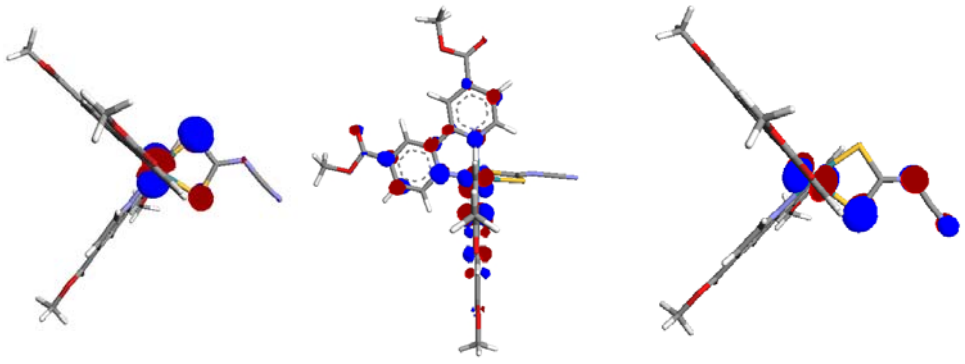

(a) (b) (c)

**Figure 18.** Calculated a) HOMO, b) LUMO and c) HOMO-1 of **2** in DMF.

Complex **5** was also calculated to have significant ruthenium contribution to the HOMO (62 %) however there was less delocalisation over the xanthate ligand in comparison to **2** (Table 6, Figure 19). The HOMO-1 and HOMO-2 energy levels were found to be very close in energy with only a 0.06 eV difference between them. Both of these orbitals have a large degree of ruthenium character and only partial contributions from the bipyridyl and xanthate ligands. Again the LUMO was calculated to be located over the two bipyridyl ligands with a small degree of ruthenium character, which should facilitate efficient injection into the conduction band of the $TiO_2$.

| MO | Energy / eV | % Ru | % $S_2COEt$ | % decbpy |
|---|---|---|---|---|
| **LUMO+1** | -2.83 | 10.56 | 2.32 | 87.13 |
| **LUMO** | -2.91 | 5.86 | 1.45 | 92.69 |
| **HOMO** | -5.88 | 62.43 | 29.35 | 8.2 |
| **HOMO-1** | -6.12 | 73.97 | 12.59 | 13.47 |
| **HOMO-2** | -6.18 | 70.08 | 9.93 | 19.95 |

**Table 6.** Energies and percentage contribution of Ru, $S_2COEt$ and decbpy to selected molecular orbitals for the optimised geometry of **5** in DMF.

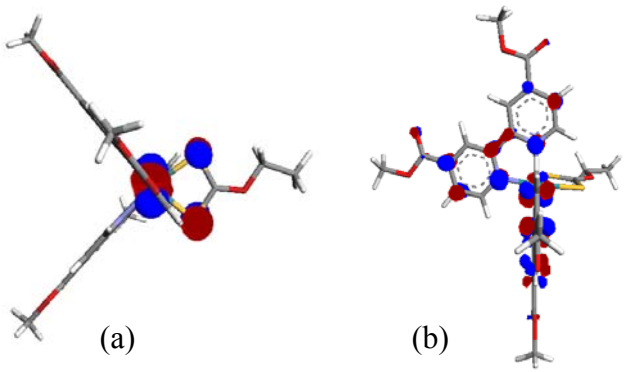


**Figure 19.** Calculated a) HOMO and b) LUMO of **5** in DMF.

## 3.6 TD-DFT

TD-DFT calculations were also carried out for **2** and **5,** with the calculated absorption spectra showing significant similarities to observed. The energies, oscillator strengths and composition of the calculated transitions for these complexes are summarised in Table 7 and Table 8 respectively.

For both systems the bipyridyl intraligand transitions at ~ 300 nm were reproduced, both in energy of transition and intensity relative to other transitions (Figure 20). Interestingly, for both dyes the lowest energy band was found not to be HOMO to LUMO in nature, but rather HOMO-2 to LUMO, making this band an MLCT in both cases, rather than a mixed ruthenium/S-donor ligand to bipyridyl ligand as would be the case for the HOMO to LUMO transitions. For both systems the character of the HOMO-2 is largely on the ruthenium, which leads to a greater degree of overlap with the unoccupied orbitals compared to the HOMO and HOMO-1. Importantly in comparing the two simulated spectra the observed trend of **2** having an extended absorption range was conserved with a calculated absorption maximum at 500 nm versus 470 nm for **5**.

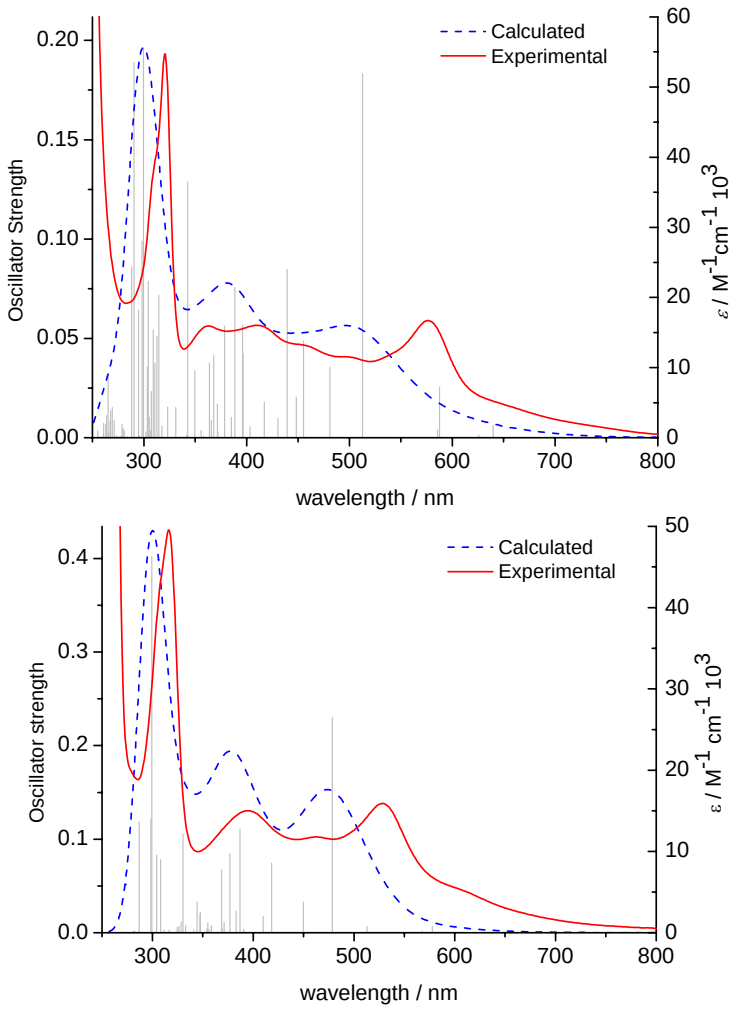


**Figure 20.** Calculated electronic transitions (columns) for (top) **2** and (bottom) **5** relative to observed spectra (red solid line graph) and calculated spectra (blue dashed line graph).

| Complex | Excited State | Energy / nm | | *f* | Composition |
|---|---|---|---|---|---|
| | | Calculated | Observed | | |
| **2** | 5 | 513 | 578 | 0.18 | HOMO-2 to LUMO 64% (MLCT) |
| | | | | | HOMO-1 to LUMO 17% (MMLL'CT) |
| | 9 | 439 | 417 | 0.08 | HOMO-1 to LUMO+2 14 % (MMLL'CT) |
| | | | | | HOMO-1 to LUMO+3 63% (MMLL'CT) |
| | | | | | HOMO to LUMO+2 17% (MMLL'CT) |
| | | | | | HOMO-1 to LUMO+3 16 % (MMLL'CT) |
| | 15 | 389 | 361 | 0.08 | HOMO-2 to LUMO+2 51% (MLCT) |
| | | | | | HOMO-1 to LUMO+5 11% (MMLL'CT) |
| | | | | | HOMO to LUMO+5 44% (MMLL'CT) |
| | 41 | 299 | 320 | 0.2 | HOMO-7 to LUMO+1 58% (bpy intraligand) |
| | | | | | HOMO-5 to LUMO+3 10% (bpy intraligand) |

**Table 7.** Calculated energy, oscillator strength (f) and composition of electronic transitions for **2** in DMF. Only transitions with oscillator strength greater than 0.08 are included for clarity.

| Complex | Excited State | Energy / nm | | *f* | Composition |
|---|---|---|---|---|---|
| | | Calculated | Observed | | |
| **5** | 5 | 479 | 530 | 0.2 | HOMO-2 to LUMO 56% (MLCT) |
| | | | | | HOMO-1 to LUMO+1 36% (MLCT) |
| | 7 | 418 | 463 | 0.07 | HOMO to LUMO+2 68 % (MMLL'CT) |
| | 10 | 387 | 396 | 0.11 | HOMO-1 to LUMO+2 15% (MLCT) |
| | | | | | HOMO-1 to LUMO+3 56% (MLCT) |
| | | | | | HOMO-2 to LUMO+4 30% (MLCT) |
| | 33 | 299 | 317 | 0.4 | HOMO-5 to LUMO+1 59% (bpy intraligand) |
| | | | | | HOMO-3 to LUMO+2 12% (bpy intraligand) |

**Table 8.** Calculated energy, oscillator strength (f) and composition of electronic transitions for **5** in DMF. Only transitions with oscillator strength greater than 0.07 are included for clarity.

These results also relate well to the spectroelectrochemical studies of **2** and **5** carried out in 0.3 M $TBABF_4$/DCM. Upon oxidation of **2** it was observed that the CT bands decrease in intensity but do not fully collapse or shift in energy. This implies that removal of an electron from the HOMO does not affect the energies of the transitions significantly *i.e.* the large contribution of the $C_2N_2S_2$ ligand is evidenced by the fact that the bands do not fully collapse. In contrast the spectroelectrochemistry of **5** showed an almost complete collapse of the lowest energy CT band upon oxidation, reflecting the fact the highest occupied orbitals are all largely ruthenium in character and hence the oxidation of the ruthenium centre greatly alters these transitions.

## 3.7 Solar Cell Measurements.

DSSCs incorporating the acid derivative dyes **3** and **6** were constructed and the performance of the cells investigated by measuring the IPCE (Table 9, Figure 21) and I-V curves, with the results compared to a cell with N719 as the sensitiser for reference. The IPCE curves for the two synthesised dyes show a clear resemblance to the absorption spectra, showing no significant decomposition upon adsorption or in contact with the electrolyte. The characterisation in solution also relates well to that of the dye/$TiO_2$ system.

The maximum IPCE of **3** at 555 nm was unexpectedly low at 11 %, whereas in comparison **6** yielded a value almost three times greater of 29 % at 520 nm. The

possibility that this was due to dye aggregation upon sensitisation was investigated by using a much more dilute dye bath, however this cell gave a comparable low efficiency showing that this is unlikely to be the major cause.

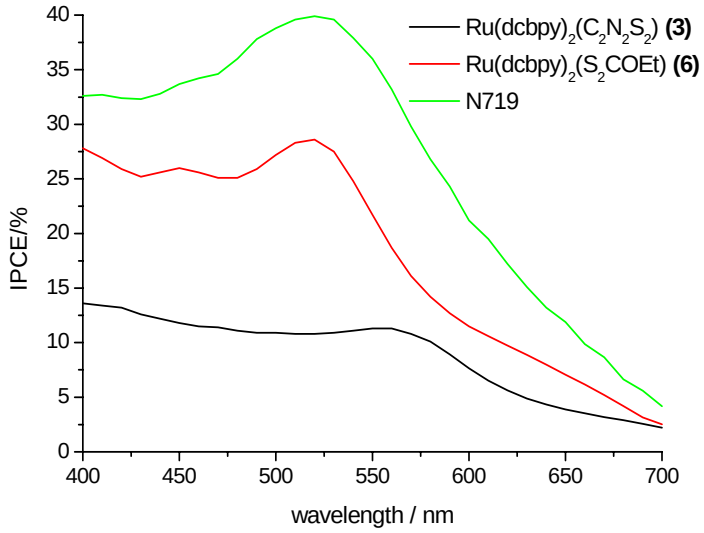


**Figure 21.** IPCE graphs for **3**, **6** and **N719** DSSCs, using the default electrolyte.

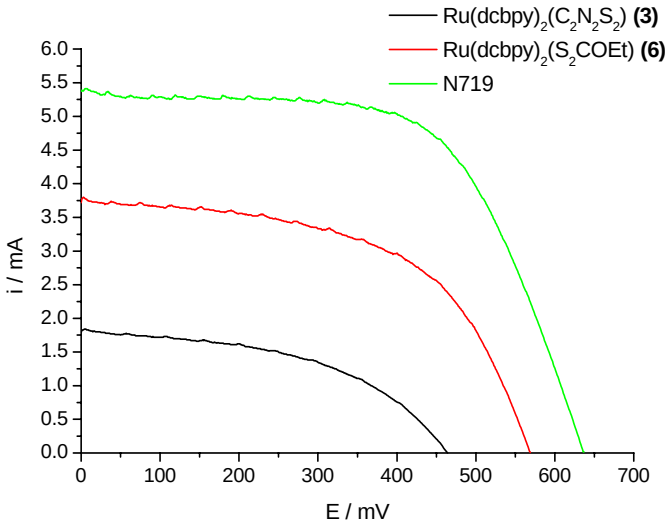


**Figure 22.** AM 1.5 (100 mWcm$^{-2}$) I-V Characteristics for **3**, **6** and **N719** DSSCs.

The I-V curves for the three different dyes are shown in Figure 22 and the resulting values of $I_{sc}$, $V_{oc}$, ff and η obtained, in Table 9. As expected from the IPCE results the cell made with **3** was found to be very low efficiency at 0.4 % and the cell made with **6** three times greater at 1.2 %. For comparison the cell with N719 as the sensitiser gave an efficiency of 2.1 %. These results show that whilst both dyes do function in a DSSC, there is clearly some limiting factor in the case of **3** resulting in a low efficiency cell.

| **Dye** | **IPCE max. / % (λ / nm)** | **$I_{sc}$ / mA** | **$V_{oc}$ / mV** | **ff** | **η / %** |
|---|---|---|---|---|---|
| **3** | 11.3 (555) | 1.79 | 464 | 0.49 | 0.41 |
| **6** | 28.5 (517) | 3.72 | 569 | 0.56 | 1.19 |
| N719 | 39.9 (520) | 5.37 | 637 | 0.62 | 2.12 |

**Table 9.** IPCE maxima, short-circuit current, open-circuit voltage, fill factor and overall AM 1.5 one-sun (1000 $Wcm^{-2}$) efficiency of DSSCs sensitised with **3**, **6** and N719 dyes.

Following the encouraging efficiency of **6**, optimisation of the system was attempted in an effort to enhance the efficiency. Optimisation involved the inclusion of a compact $TiO_2$ blocking layer and reduction of the active area to 0.3 $cm^2$. [28] This was rather disappointing however, with the efficiency using **6** rising to 1.88 % under conditions that gave 6.4 % for N719. It is not clear at present whether this represents a true limit to the efficiency of **6** or whether different optimisation conditions would be needed to reflect its different electronic character (for example the different charge).

## 3.8 Transient Absorption Spectroscopy

In order to rationalise the differing efficiencies of **3** and **6** in a DSSC the kinetics of the $TiO_2$/dye system were investigated using transient absorption spectroscopy. The excitation wavelength was set at 500 nm, a wavelength at which the two sensitised films absorbed approximately the same number of photons. A probe wavelength of 600 nm was chosen, where the ground state bleach recovery of the dyes can be easily monitored and the lifetime of the dye cations inferred. The recombination of the injected electrons with the oxidised dye was investigated using a redox inactive electrolyte (0.25 M $LiClO_4$ in propylene carbonate).

Complex **3** showed very fast recombination kinetics with a half lifetime on the order of 10 μs, which was about 1000 times faster than the recombination dynamics observed for complex **6,** with $t_{1/2}$ in the order of a few ms (Figure 23). From the DFT and spectroelectrochemical studies it would have been expected that the recombination loss process would have been much slower in **3** compared to **6**, as the dye cation hole is thought to be considerably delocalised over the $C_2N_2S_2$ ligand. This would mean that if the dye were binding through the acid groups with the $C_2N_2S_2$ ligand pointing away from the $TiO_2$ surface, the injected electrons would take longer to recombine with the oxidised dye because the hole is located further from the surface, as has been observed previously.[29] The fact that the opposite has been observed suggests that the dye is binding in a mode that facilitates much faster recombination, a simple answer to that being through the terminal cyano group on

the $C_2N_2S_2$ ligand. If there is concerted binding through both the acid and cyano groups then this would account for the low IPCE and low η through fast recombination as the injected electrons will readily recombine with the oxidised dye if the dye cation hole is close to the surface of the $TiO_2$.

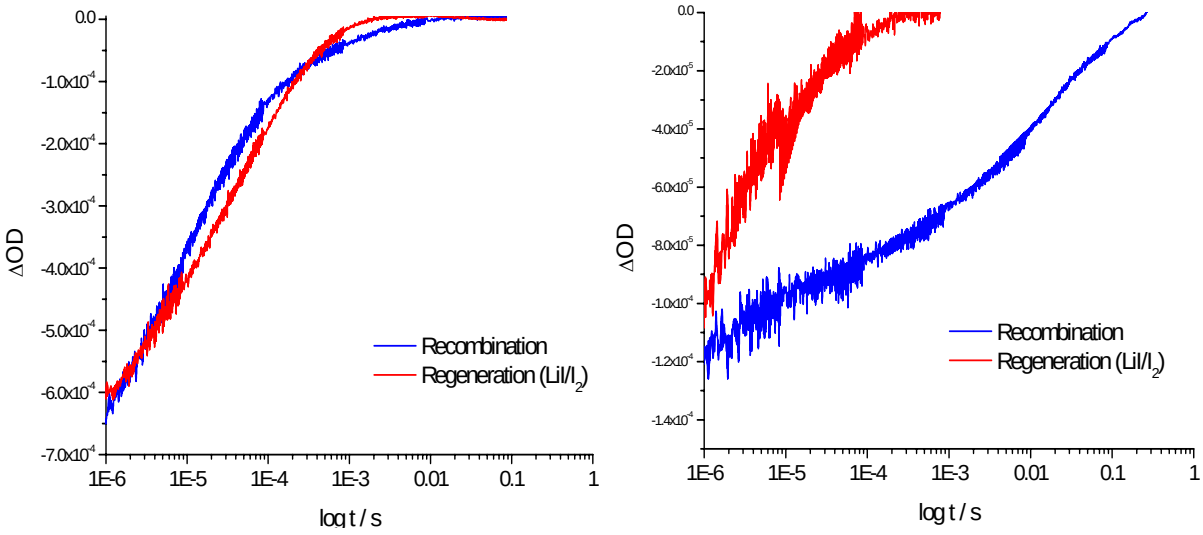


**Figure 23.** Transient absorption decay traces showing recombination and regeneration kinetics for **3** (left) and **6** (right) adsorbed on $TiO_2$ films.

The regeneration of the oxidised dyes was investigated by covering the sensitised films with a redox active electrolyte, 0.25 M LiI/0.05 M $I_2$ in propylene carbonate. As would be expected for a dye that has shown significant efficiencies in a DSSC, dye **6** showed very efficient regeneration dynamics, with a half lifetime for the oxidised dye of only a few microseconds, in the same timescale as the regeneration dynamics of the standard N719,[30] and about 1000 times faster than the recombination kinetics. On the other hand, complex **3** showed regeneration dynamics one order of magnitude slower, with $t_{1/2}$ of tens of μs, which is on the same timescale as the

observed recombination kinetics for this dye. This indicates that recombination with the injected electrons is competing with regeneration of the oxidised dyes by the electrolyte in the DSSC, lowering the efficiency of the device. The faster regeneration dynamics of complex **6** compared to **3** may possibly be attributed to its more positive oxidation potential and therefore, to the larger driving force for the regeneration process.

## 3.9 $TiO_2$/dye Absorption Study

The unsubstituted and ester derivative dyes (**1** and **2**) were used to sensitise $TiO_2$ films to investigate the possibility of the cyano group on the $C_2N_2S_2$ ligand binding to the $TiO_2$ in addition to the acid groups. In addition the unsubstituted and ester derivative bis-chloride complexes and ethyl xanthate dyes (**4** and **5**) were used as further evidence.

The films were soaked overnight in a 1 mM solution in methanol, and rinsed with methanol before absorption spectra were recorded (Figure 24). For the unsubstituted and ester bipyridyl dyes containing the chloride ligands the dye uptake was very low, with a maximum absorbance below 0.1. In the case of the ethyl xanthate series there was no measurable absorbance. This shows these dyes have very little or negligible binding to the $TiO_2$ without the presence of the acid groups on the bipyridyl ligands, as expected. With the $C_2N_2S_2$ series the dye loading was much greater, with the

absorption values of the unsubstituted and ester dyes virtually identical at ~ 0.15, compared to an absorbance of ~0.9 for the acid derivative.

Overall, this study strongly suggests that the cyano group is capable of forming a reasonably strong interaction with the $TiO_2$ surface. This suggests that for the sensitiser **3**, the cyano group may be interacting with the $TiO_2$ in addition to the usual binding through the acid groups, resulting in very fast recombination in a DSSC and a low efficiency cell.

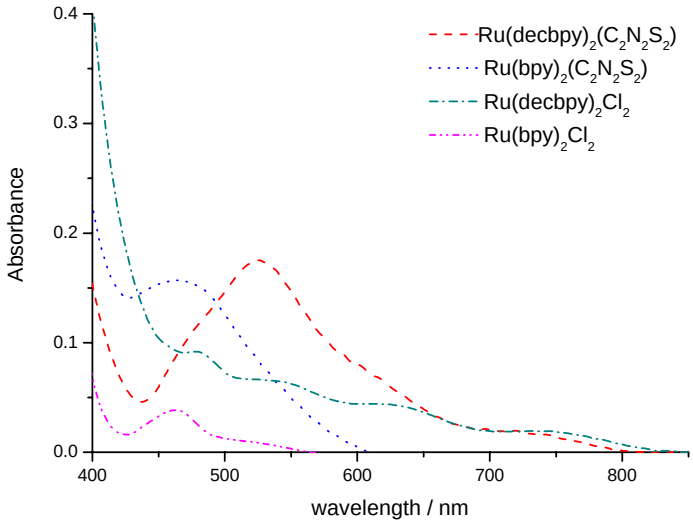


**Figure 24.** Absorption spectra of dye/$TiO_2$ films of $C_2N_2S_2$ series and bis-chloride starting materials.

Chenodeoxycholate (cheno) is known to preferentially adsorb to $TiO_2$ over weakly bound dyes. It was hoped in this case that the cyano bound dyes would be displaced removing the high probability of recombination of the injected electron with the oxidised dye. In an attempt to prevent the cyano binding to the $TiO_2$ surface a study of the effect of co-adsorption of the dye with cheno was undertaken. The cheno was

added to the dye bath and should result in a larger fraction of strongly adsorbed dyes and hence an increase in overall efficiency.[31]

To show proof of concept, a cell was made using dye baths containing no cheno and one with a 1:1 ratio of cheno:**3**. The result of the addition of the co-adsorbent was a dramatic increase in efficiency *via* an increased photocurrent (Figure 25, Table 10). These results also indicate that the cyano group is binding to the $TiO_2$, in addition to the acid groups, and ideally the ratio of cheno:**3** would be further varied to find the optimum conditions for sensitisation of $TiO_2$ with **3**.

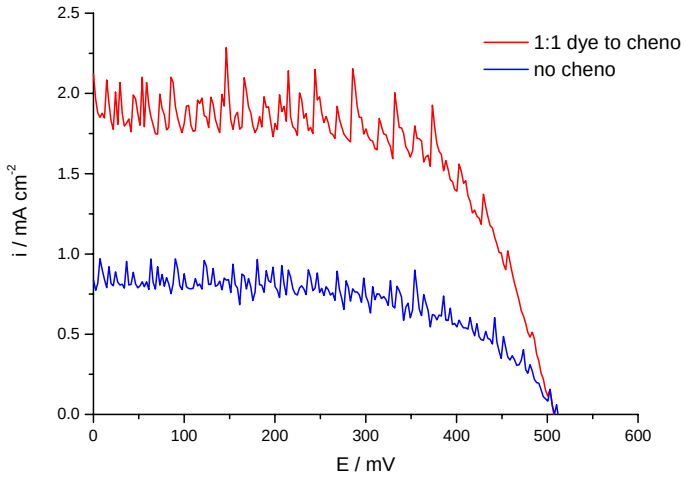


**Figure 25.** I-V curves of DSSCs sensitised with **3**, showing the effect of cheno addition to the dye bath.

| Dye | $I_{sc}$ / mA | $V_{oc}$ / mV | ff | η / % |
|---|---|---|---|---|
| **3** | 0.83 | 511 | 0.55 | 0.24 |
| **3** + cheno | 1.96 | 506 | 0.62 | 0.61 |

**Table 10.** Summary of cell attributes for DSSCs incorporating cheno and **3**.

## 3.10 Conclusions

Two novel series of ruthenium bipyridyl dyes containing S-donor ligands have been synthesised and characterised. The properties of the two series are very distinct, with the $C_2N_2S_2$ series showing significant HOMO contribution from the sulfur-donor ligand and the $S_2COEt$ series having a HOMO largely located on the ruthenium centre. This reflects the greater conjugation across the former ligand. The dianionic $C_2N_2S_2$ ligand also displays greater electron donating capability than the monoanionic $S_2COEt$, resulting in destabilisation of the metal d-orbitals and lower energy MLCT transitions that also possess a high molar extinction coefficient. Thus $Ru(dcbpy)_2(C_2N_2S_2)$ has a number of advantageous properties for a DSSC sensitiser, including an expected higher light harvesting capability in the visible range and delocalisation of the HOMO to enhance charge separation.

Despite these characteristics, it performed worse with respect to $[Ru(dcbpy)_2(S_2COEt)]^+$ in a DSSC, with efficiencies of 0.4 %. This is attributed to the terminal cyano group of the $C_2N_2S_2$ ligand binding to the surface of the $TiO_2$ in addition to the acid groups on the bipyridyl ligands, facilitating fast recombination of the injected electron with the oxidised dye. In contrast, $[Ru(dcbpy)_2(S_2COEt)]^+$ showed an efficiency of 1.2 % in an unoptimised DSSC.

This work shows several key differences to those studies carried out on similar S-donor bidentate ligands such as the dithiocarbamates by Bignozzi and Meyer *et al.* and the dithiolates by Arakawa *et al.* Firstly, the absorption properties of dyes **1** – **6** are more advantageous than both previously studied systems. The maximum absorption wavelengths are at lower energies and the molar extinction co-efficients are higher than all but one literature dye. This theoretically means that dyes **1** – **6** have a greater light harvesting efficiency than the literature dyes. In both previous studies the reported low efficiencies of the DSSCs were attributed to poor dye regeneration by the iodide. For **6** this was shown not to be an issue with fast dye regeneration observed via TAS.

It is apparent that complexes within this family can possess very attractive features for sensitisers in DSSC. Modification of the sulfur-donor ligand has been shown to enable enhanced electronic characteristics and chelating ligands can offer enhanced dye stability. An additional point to note is the possible variation of the alkyl chain length on the $S_2COEt$ ligand, since hydrophobicity in dyes has been associated with enhanced stability,[32] reduction of charge recombination with the electrolyte [33,34] and good interaction with the organic hole-transport materials used in solid-state cells.[35] The challenge for subsequent studies will be the combination of these various positive features into a dye, while avoiding inadvertent detrimental effects such as the rapid recombination observed for **3**.

## 3.11 Synthesis

The dyes were synthesised from the corresponding dichloride precursors by initial abstraction of the chloride ligands through treatment with silver nitrate. This was found to give a better yield and cleaner product compared with simple reflux of the dichlorides with the sulfur-donor ligand, as it allowed a lower temperature and shorter reaction time. Satisfactory purity and yield for the ester and acid-substituted dyes was subsequently obtained through column chromatography. **L1** was synthesised according to the literature [36] and **L2** was purchased from Aldrich.

**Synthesis of cyanodithioimidocarbonate (L1).** Anal. Calc. for $K_2C_2N_2S_2$: C, 12.36; H, 0; N, 14.41; Found: C, 12.54; H, 0; N, 13.61.

**Synthesis of [Ru(bpy)$_2$($C_2N_2S_2$)] (1).** $Ru(bpy)_2Cl_2$ (100 mg, 0.2 mmol) was dissolved in methanol (10 ml) and silver nitrate (71 mg, 0.4 mmol) in water (1 ml) was added. The mixture was refluxed for 1 hour, under $N_2$ and in reduced light, yielding a scarlet red solution and a white precipitate. The precipitate was removed by centrifugation and to the filtrate was added $K_2C_2N_2S_2$ (31 mg, 0.2 mmol) in water (1 ml). The mixture was stirred overnight, under $N_2$ and reduced light. The red precipitate was collected, washed with methanol and dried in vacuo. Yield: 49 mg, 46 %. Anal. Calc. for $C_{22}H_{16}N_6S_2Ru.H_2O$: C, 48.25; H, 3.30; N, 15.35. Found: C, 48.08; H, 2.76; N, 15.11. +ve FAB-MS: m/z 530 ($M^+$). $^1$H-NMR (DMSO, 360

MHz): δ 9.48 (d, $J_{HH}$ = 6, 2H), 8.53 (d, $J_{HH}$ = 8, 2H), 8.44 (d, $J_{HH}$ = 8, 2H), 7.92 (t, $J_{HH}$ = 8, 2H), 7.67 (q, $J_{HH}$ = 8, 4H), 7.50 (d, $J_{HH}$ = 6, 2H), 7.10 (t, $J_{HH}$ = 6.5, 2H).

**Synthesis of [Ru(decbpy)$_2$($C_2N_2S_2$)] (2).** Ru(decbpy)$_2$$Cl_2$ (100 mg, 0.12 mmol) was dissolved in methanol (10 ml) and silver nitrate (44 mg, 0.24 mmol) in water (1 ml) was added. The mixture was refluxed for 1 hour, under $N_2$ and in reduced light, yielding a deep red solution and a white precipitate. The precipitate was removed by centrifugation and to the filtrate was added $K_2C_2N_2S_2$ (30 mg, 0.2 mmol) in water (1 ml). The mixture was stirred overnight, under $N_2$ and reduced light. The dark red precipitate was collected, washed with methanol and dried in vacuo. Yield: 73 mg, 74 %. The product was further purified *via* a Sephadex LH-20 column using a 1:1 methanol:acetonitrile solution as the eluent. Anal. Calc. for $C_{34}H_{32}N_6O_8S_2Ru$.2MeOH: C, 46.31; H, 3.66; N, 9.53. Found: C, 45.09; H, 3.82; N, 9.71. +ve FAB-MS: m/z 818.2 ($M^+$). $^1$H-NMR (DMSO, 360 MHz): δ 10.00 (d, $J_{HH}$ = 6, 2H), 9.29 (s, 2H), 9.19 (s, 2H), 8.47 (d, $J_{HH}$ = 6, 2H), 8.10 (d, $J_{HH}$ = 6, 2H), 7.80 (d, $J_{HH}$ = 6, 2H), 4.68 (q, $J_{HH}$ = 7, 4H), 4.52 (q, $J_{HH}$ = 7, 4H), 1.60 (t, $J_{HH}$ = 7, 6H), 1.48 (t, $J_{HH}$ = 7, 6H).

**Synthesis of [Ru(dcbpy)$_2$($C_2N_2S_2$)] (3).** Ru(decbpy)$_2$$Cl_2$ (100 mg, 0.12 mmol) was dissolved in methanol (10 ml) and silver nitrate (44 mg, 0.24 mmol) in water (1 ml) was added. The mixture was refluxed for 1 hour, under $N_2$ and in reduced light, yielding a deep red solution and a white precipitate. The precipitate was removed by centrifugation and to the filtrate was added 0.1 M aq. KOH (3 ml). The mixture was

stirred for 10 minutes followed by the addition of $K_2C_2N_2S_2$ (30 mg, 0.2 mmol) in water (1 ml). The mixture was stirred overnight, under $N_2$ and reduced light. The product was precipitated with 1 M HCl (1 ml) yielding a dark red precipitate. Yield: 73 mg, 80 %. The crude product was further purified *via* a Sephadex LH-20 column using water as the eluent. Anal. Calc. for $C_{26}H_{16}N_6O_8S_2Ru.5H_2O$ : C, 39.25; H, 3.29; N, 10.56. Found: C, 39.42; H, 2.93; N, 9.50. –ve ESI-MS: m/z 705 ($M^+$) $^1$H-NMR (DMSO, 360 MHz): δ 9.83 (d, $J_{HH}$ = 6, 2H), 9.08 (s, 2H), 8.99 (s, 2H), 8.28 (d, $J_{HH}$ = 6, 2H), 7.92 (d, $J_{HH}$ = 6, 2H), 7.63 (d, $J_{HH}$ = 6, 2H)

**Synthesis of [Ru(bpy)$_2$(S$_2$COEt)][NO$_3$] (4).** $Ru(bpy)_2Cl_2$ (100 mg, 0.2 mmol) was dissolved in methanol (10 ml) and silver nitrate (71 mg, 0.4 mmol) in water (1 ml) was added. The mixture was refluxed for 1 hour, under $N_2$ and in reduced light, yielding a scarlet red solution and a white precipitate. The precipitate was removed by centrifugation and to the filtrate $KS_2COEt$ (30 mg, 0.2 mmol) in water (1 ml). The mixture was stirred overnight, under $N_2$ and reduced light. The reaction mixture was concentrated and loaded onto a Sephadex LH-20 column, using methanol as the eluent. The main scarlet red band was collected. Yield: 102 mg, 85 %. Anal. Calc. for $C_{24}H_{25}N_5O_5S_2Ru.1MeOH$ : C, 45.85; H, 4.01; N, 11.1. Found: C, 45.97; H, 3.34; N, 7.08, +ve FAB-MS: m/z 535 ($M^+$-$NO_3$), $^1$H-NMR (DMSO, 360 MHz): δ 9.43 (d, $J_{HH}$ = 6, 2H), 8.92 (d, $J_{HH}$ = 8, 2H), 8.83 (d, $J_{HH}$ = 8, 2H), 8.35 (t, $J_{HH}$ = 7, 2H), 8.11 (t, $J_{HH}$ = 7.5, 2H), 8.02 (t, $J_{HH}$ = 6.5, 2H), 7.84 (d, $J_{HH}$ = 5.5, 2H), 7.51 (t, $J_{HH}$ = 6.5, 2H), 4.74 (q, $J_{HH}$ = 7, 2H), 1.52 (t, $J_{HH}$ = 7, 3H).

**Synthesis of [Ru(decbpy)$_2$(S$_2$COEt)][NO$_3$] (5).** Ru(decbpy)$_2$Cl$_2$ (100 mg, 0.12 mmol) was dissolved in methanol (10 ml) and silver nitrate (44 mg, 0.24 mmol) in water (1 ml) was added. The mixture was refluxed for 1 hour, under $N_2$ and in reduced light, yielding a deep red solution and a white precipitate. The precipitate was removed by centrifugation and to the filtrate was added KS$_2$COEt (19 mg, 0.12 mmol) in water (1 ml). The mixture was stirred overnight, under $N_2$ and reduced light. The reaction mixture was concentrated and loaded onto a Sephadex LH-20 column using methanol as the eluent, with the main red band collected. The product was further purified by recrystallisation in ethyl acetate. Yield: 24 mg, 23 % Anal. Calc. for $C_{35}H_{37}N_5O_{12}S_2Ru$: C, 47.51; H, 4.21; N, 7.91. Found: C, 46.42; H, 3.45; N, 4.27, +ve FAB-MS: m/z 823 ($M^+$-$NO_3$), $^1$H-NMR (DMSO, 360 MHz): δ 9.49 (d, $J_{HH}$ = 6, 2H), 9.24 (s, 2H), 9.13 (s, 2H), 8.56 (d, $J_{HH}$ = 6, 2H), 7.98 (d, $J_{HH}$ = 6, 2H), 7.69 (d, $J_{HH}$ = 6, 2H), 4.52 (q, $J_{HH}$ = 7, 2H), 4.37 (q, $J_{HH}$ = 7, 2H), 1.38 (t, $J_{HH}$ = 7, 3H).

**Synthesis of [Ru(dcbpy)$_2$(S$_2$COEt)][NO$_3$] (6).** Ru(decbpy)$_2$Cl$_2$ (100 mg, 0.12 mmol) was dissolved in methanol (10 ml) and silver nitrate (44 mg, 0.24 mmol) in water (1 ml) was added. The mixture was refluxed for 1 hour, under $N_2$ and in reduced light, yielding a deep red solution and a white precipitate. The precipitate was removed by centrifugation and to the filtrate was added 0.1 M aq. KOH (3 ml). The mixture was stirred for 10 minutes followed by the addition of KS$_2$COEt (38 mg, 0.12 mmol) in water (1 ml). The mixture was stirred overnight, under $N_2$ and reduced light. The product was precipitated with 1 M $HNO_3$ (2 ml) yielding a dark red precipitate. Yield: 57 mg, 61 %. The crude product was further purified *via* a Sephadex LH-20 column using water as the eluent. Anal. Calc. for

$C_{27}H_{33}N_5O_{18}S_2Ru.6H_2O$: C, 36.82; H, 3.78; N, 7.95. Found: C, 35.19; H, 2.00; N, 8.18, +ve ESI-MS: m/z 711 ($M^+$-$NO_3$), $^1$H-NMR (DMSO, 360 MHz): δ 9.47 (d, $J_{HH}$ = 6, 2H), 9.163 (s, 2H), 9.06 (s, 2H), 8.28 (d, $J_{HH}$ = 6, 2H), 7.94 (d, $J_{HH}$ = 6, 2H), 7.69 (d, $J_{HH}$ = 6, 2H), 4.67 (q, $J_{HH}$ = 7, 2H), 4.57 (q, $J_{HH}$ = 7, 2H), 1.37 (t, $J_{HH}$ = 7, 3H).

## 3.12 References


[1] Md.K. Nazeeruddin, F. De Angelis, S. Fantacci, A. Selloni, G. Viscardi, P. Liska, S. Ito, B. Takeru, M. Grätzel, *J. Am. Chem. Soc.*, 2005, **127**, 16835-16847.

[2] Md.K. Nazeeruddin, A. Kay, I. Rodicio, R. Humphry-Baker, E. Müller, P. Liska, N. Vlachopoulos, M. Grätzel, *J. Am. Chem. Soc.*, 1993, **115**, 6382-6390.

[3] H. Greijer Agrell, J. Lindgren, A. Hagfeldt, *Solar Energy*, 2003, **75**, 169-180.

[4] Md.K. Nazeeruddin, M. Grätzel, *Comp. Coord. Chem. II,* 2003, **9**, 719-758.

[5] K. Kalyanasundaram, Md.K. Nazeeruddin, *Chem. Phys. Lett.,* 1992, **193**, 292-297.

[6] P.A. Anderson, G.F. Strouse, J.A. Treadway, F.R. Keene, T.J. Meyer, *Inorg. Chem.*, 1994, **33**, 3863-3864.

[7] A. Islam, K. Hara, L.P. Singh, R. Katoh, M. Yanagida, S. Murata, Y. Takahashi, H. Sugihara, H. Arakawa, *Chem. Lett.*, 2000, 490-491.

[8] M.K. Nazeeruddin, E. Müller, R. Humphry-Baker, N. Vlachopoulos, M. Grätzel, *Dalton Trans.*, 1997, 4571-4578.

[9] S. Ruile, O. Kohle, P. Péchy, M . Grätzel, *Inorg. Chim. Acta,* 1997, **261**, 129-140.

[10] A. Islam, H. Sugihara, L.P. Singh, K. Hara, R. Katoh, Y. Nagawa, M. Yanagida, Y. Takahashi, S. Murata, H. Arakawa, *Inorg. Chim. Acta*, 2001, **322**, 7-16.

[11] M. Hissler, J.E. McGarrah, W.B. Connick, D.K. Geiger, S.D. Cummings, R. Eisenberg, *Coord. Chem. Rev.,* 2000, **208**, 115-137.

[12] S.D. Cummings, R. Eisenberg, *J. Am. Chem. Soc.*, 1996, **118**, 1949-1960.

[13] E.A.M. Geary, N. Hirata, J. Clifford, J.R. Durrant, S. Parsons, A. Dawson, L.J. Yellowlees, N. Robertson, *Dalton Trans.*, 2003, 3757-3762.

[14] A. Islam, H. Sugihara, K. Hara, L. Singh, R. Katoh, M. Yanagida, Y. Takahashi, S. Murata, H. Arakawa, G. Fujihashi, *Inorg. Chem.*, 2001, **40**, 5371-5380.

[15] R. Argazzi, C.A. Bignozzi, G.M. Hasselmann, G.J. Meyer, *Inorg. Chem.*, 1998, **37**, 4533-4537.

[16] A. Islam, H. Sugihara, K. Hara, L.P. Singh, R. Katoh, M. Yanagida, Y. Takahashi, S. Murata, H. Arakawa, *J. Photochem. Photobiol. A: Chem.*, 2001, **145**, 135-141.

[17] Y. Takahashi, H. Arakawa, H. Sugihara, K. Hara, A. Islam, R. Katoh, Y. Tachibana, M. Yanagida, *Inorg. Chim. Acta*, 2000, **310**, 169-174.

[18] A. Islam, H. Sugihara, M. Yanagida, K. Hara, G. Fujihashi, Y. Tachibana, R. Katoh, S. Murata, H. Arakawa, *New J. Chem*., 2002, **26**, 966-968.

[19] P.F.H. Schwab, S. Diegoli, M. Biancardo, C.A. Bignozzi, *Inorg. Chem.*, 2003, **42**, 6613-6615.

[20] H. Sugihara, S. Sano, T. Yamaguchi, M. Yanagida, T. Sato, Y. Abe, Y. Nagao, H. Arakawa, *J. Photochem. Photobiol. A: Chem.*, 2004, **166**, 81-90.

[21] L. Schmidt-Mende, U. Bach, R. Humphry-Baker, T. Horiuchi, H. Miura, S. Ito, S. Uchida, M. Grätzel, *Adv. Mater.,* 2005, **17**, 813-815.

[22] M. Zhou, G.P. Robertson, J. Roovers, *Inorg. Chem.*, 2005, **44**, 8317-8325.

[23] L. Zhang, B. Liu, S. Dong, *J. Phys. Chem. B,* 2007, **111**, 10448-10452.

[24] G. Wolfbauer, A.M. Bond, D.R. MacFarlane, *Inorg. Chem.*, 1999, **38**, 3836-3846.

[25] G. Wolfbauer, A.M. Bond, D.R. MacFarlane, *Dalton Trans.*, 1999, 4363-4372.

[26] O. Kohle, M. Grätzel, A.F. Meyer, T.B. Meyer, *Adv. Mater.*, 1997, **9**, 904-906.

[27] P.E. Hoggard, G.B. Porter, *J. Am. Chem. Soc.*, 1978, **100**, 1457-1463.

[28] Optimised solar cell conditions: A thin compact layer of titanium dioxide was deposited onto cleaned fluorine doped tin oxide conductive glass (TEC 8, Pilkington, UK) from 0.2 M titanium diisopropoxide bis(acetylacetonate) isopropanol solution by spray pyrolysis deposition technique. Then titanium dioxide paste (Dyesol, DSL-18NR-T) was coated above the compact layer by doctor-blading. The film was dried at 100 $^{o}$C for 15 minutes and then sintered at 450 $^{o}$C for 30 minutes to remove the organics and to form a mesosporous film structure. The thickness of the film was about 13 μm. The $TiO_2$ film was further immersed into 40 mM $TiCl_4$ aqueous solution at 70 $^{o}$C for 30 minutes. The film was washed with pure water (Milli Q), dried at 100 $^{o}$C for 15 minutes and then sintered at 500 $^{o}$C for 30 minutes. After cooling to 120 $^{o}$C, the $TiO_2$ film was immersed into the ethanol solution of the dye $Ru(dcbpy)_2(S_2COEt)$ with the concentration of 0.5 mM overnight. DSSC was made by sealing the dye coated $TiO_2$ electrode and Pt electrode of a cell together by a thermal plastics spacer (Surlyn 1702, 25 μm, Solaronix) at 120 $^{o}$C. The electrolyte was introduced into the cell through the two holes which were drilled in the counter electrode. The holes were subsequently sealed by the thermal plastics (Surlyn 1702, Solaronix) combined with a piece of microscope slide under press. The active area of the cell was 0.3 $cm^2$.

[29] S. Handa, H. Wietasch, M. Thelakkat, J.R. Durrant, S.A. Haque, *Chem. Commun.*, 2007, 1725-1727.

[30] J.N. Clifford, E. Palomares, Md.K. Nazeeruddin, M. Grätzel, J.R. Durrant, *J. Phys. Chem. C,* 2007, **111**, 6561-6567.

[31] N.R. Neale, N. Kopidakis, J. van de Lagemaat, M. Grätzel, A.F. Frank, *J. Phys. Chem. B*, 2005, **109**, 23183-23189.

[32] Md.K. Nazeeruddin, S.M. Zakeeruddin, J-J. Lagref, P. Liska, P. Comte, C. Barolo, G. Viscardi, K. Schenk, M. Grätzel, *Coord. Chem. Rev.,* 2004, **248**, 1317-1328.

[33] S.M. Zakeeruddin, Md.K. Nazeeruddin, R. Humphry-Baker, P. Péchy, P. Quagliotto, C. Barolo, G. Viscardi, M. Grätzel, *Langmuir*, 2002, **18**, 952-954.

[34] L. Schmidt-Mende, J.E. Kroeze, J.R. Durrant, Md.K. Nazeeruddin, M. Grätzel, *Nano Lett.,* 2005, **5**, 1315-1320.

[35] N. Roberston, *Angew. Chem. Int. Ed.,* 2006, **45**, 2338-2345.

[36] C.J. Burchell, S.M. Aucott, H.L. Milton, A.M.Z. Slawin, J.D. Woollins, *Dalton Trans.*, 2004, 369-374.

# Chapter 4:

# TTF Ligand Dyes

## 4.1 Introduction

The study of electron transfer processes within a DSSC is crucial to optimising the efficiency of the system, as with this knowledge the various steps that occur within the cell can be further understood and eventually controlled. This should allow maximisation of the forward processes and reduction of the loss mechanisms. This chapter discusses the molecular design of ruthenium polypyridyl complexes in order to study the interfacial charge recombination dynamics at the dye/$TiO_2$ heterojunction.

The strategy used in this study is that of a donor-acceptor dye (Figure 1). In this system an electron donor moiety is covalently linked to a chromophore unit. Upon excitation of the chromophore by incident light, an electron is injected into the conduction band of the $TiO_2$ (1). This is rapidly followed by the transfer of an electron from the appended electron donor unit (2). This shifts the dye cation hole further from the surface of the $TiO_2$, leading to the recombination loss process (3) being significantly retarded.

There are examples in the literature of this type of donor-acceptor complex, not only for use in a DSSC but also in electrochromic and memory storage applications.[1,2] This chapter will introduce mononuclear complexes whereas chapter 5 discusses polynuclear examples *i.e.* where more than one metal centre is present.

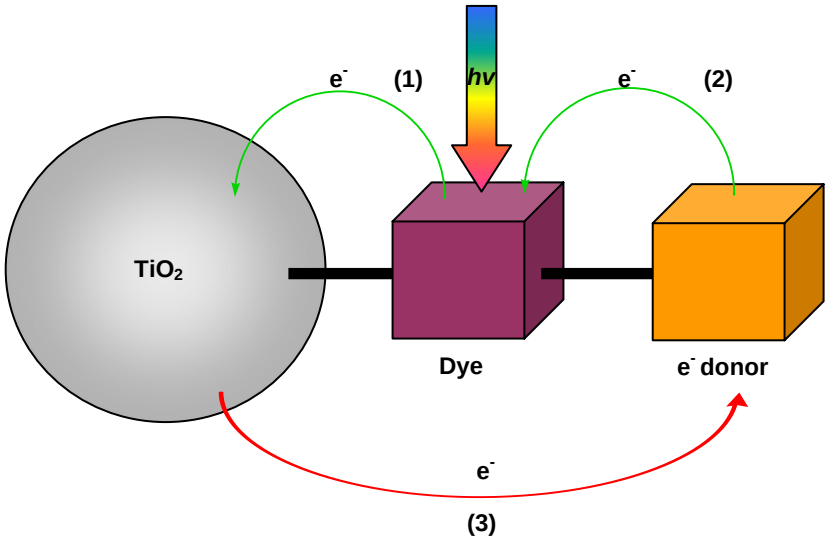


**Figure 1.** Schematic showing the electron transfer processes occurring upon excitation of a donor-acceptor dye sensitised on $TiO_2$.

There are several examples of mononuclear ruthenium polypyridyl dyes with appended secondary electron-donor units that show extended charge-separated state lifetimes in a DSSC. All of these examples utilise the wealth of bipyridyl chemistry by attaching the donor unit to the second or a third bipyridyl ligand. The use of known electron donors such as phenothiazines (PTZ) (Figure 2) has resulted in charge-separated lifetimes of up to 300 μs, with the dye anchored on $TiO_2$. [3,4] Whereas the use of 4-[4-(*N*,*N*-di-*p*-anisylamino)phenoxymethyl]-4'-methyl-2,2'bipyridine (Figure 2) in place of the second dcbpy ligand to yield an N3 derivative (called N845) showed a charge-separated lifetime of 0.7 s.[5] The latter study also investigated the nature of the MOs *via* semiempirical calculations, showing the HOMO to be located on the donor-substituted bipyridyl ligand

hence the extended lifetime. Neither of these studies has reported global efficiency values for a DSSC.

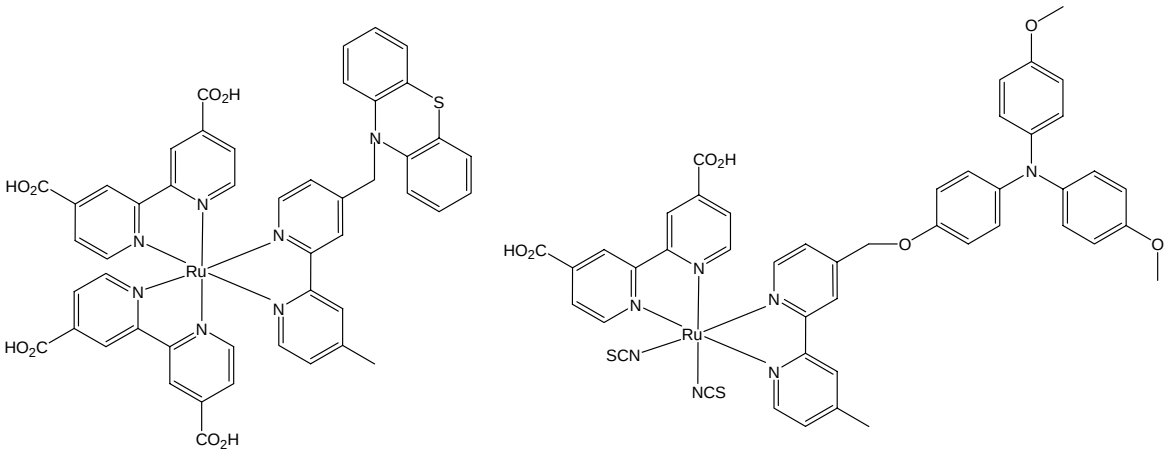


**Figure 2.** Structures of dyes showing long-lived charge-separated states, $Ru(dcbpy)_2(bpy\text{-}PTZ)$ (left) and N845 (right).

A series of dyes which has received significant attention recently is a ruthenium tris-bipyridyl triphenylamine (TPA) series.[6,7,8] By systematic variation of the third functionalised bipyridyl ligand the influence of extended π-conjugation, and also the use of polymeric electron-donating units on the charge-separated state in a DSSC were investigated. N3 analogues have also been investigated, where the functionalised bipyridyl ligand replaces one of the dcbpy ligands and the NCS groups are retained.[9,10,11] It was found that a dye with appended polymeric TPA groups (Figure 3) had an extremely long-lived charge-separated state of 4 s when adsorbed to $TiO_2$, measured *via* transient absorption spectroscopy. This is the longest charge-separated lifetime reported to date for a dye/$TiO_2$ system and was attributed, *via* DFT calculations, to the HOMO

being entirely located over the triphenylamine units rather than on the ruthenium core. In addition these dyes have been found to perform significantly well in solid-state DSSCs, using spiro-OMeTAD as the electrolyte, with a maximum efficiency to date of 3.4 %.

This study relates well to the conclusions of a previous study where the recombination dynamics of a number of ruthenium bipyridyl, phthalocyanine and porphyrin dyes were studied. This concluded that the recombination in these systems was strongly linked to the spatial separation of the dye cation HOMO from the $TiO_2$ surface. Further to this it was calculated that a change in the spatial separation between these two components of just 3 Å results in a 10-fold change in the recombination half-time ($t_{1/2}$).[12]

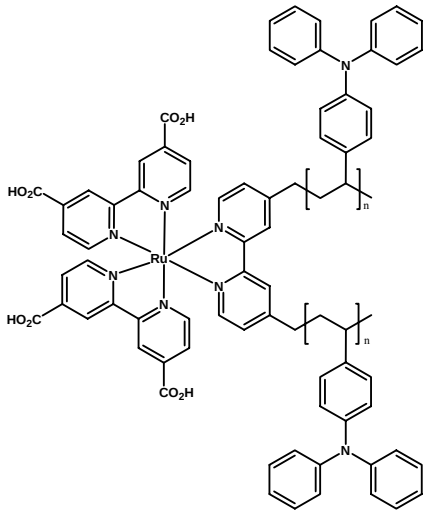


**Figure 3.** Structure of $[Ru(dcbpy)_2(poly\text{-}TPAbpy)]^{2+}$ dye.

With these studies in mind, this work complexes a functionalised tetrathiafulvalene (TTF) unit to a ruthenium bipyridyl moiety (Figure 4). Functionalised TTFs have long been of interest as a functional molecule due to their unique electron donor properties. They are frequently used as building blocks for charge-transfer salts, yielding organic conductors and superconductors.[13] There are a wide variety of other applications that utilise TTF derivatives and are currently under intense investigation, including organic electronics,[14,15] magnetic materials[16] and supramolecular chemistry.[17,18]

With such a large range of applications there are numerous examples of complexes where a transition metal is directly bound to TTF, mainly of Cu,[19,20] Ni,[21,22] and Pt.[23,24,25] There are also examples of TTF-functionalised bipyridyl ligands[19,26,27] and a fused dipyridophenazine-TTF ligand with which ruthenium complexes have subsequently been synthesised.[28,29] The existing ruthenium complexes with appended TTF moieties all show some degree of electronic communication between the TTF and the ruthenium centre often leading to luminescence quenching. Only two examples exist where a TTF unit is directly bound to ruthenium.[30,31] In one case a bis-TTF ruthenium trichloride complex was investigated, however in the other the TTF was bound to a $Ru(bpy)_2$ moiety and primarily investigated for the electrical conductivity of the oxidised species.

This study aims to utilise the electron donating ability of the TTF unit to increase the lifetime of the charge-separated state of the dye in a DSSC, thereby reducing the recombination of the injected electron with the oxidised dye. The structures of the ligand and complexes synthesised and characterised are shown in Figure 4.

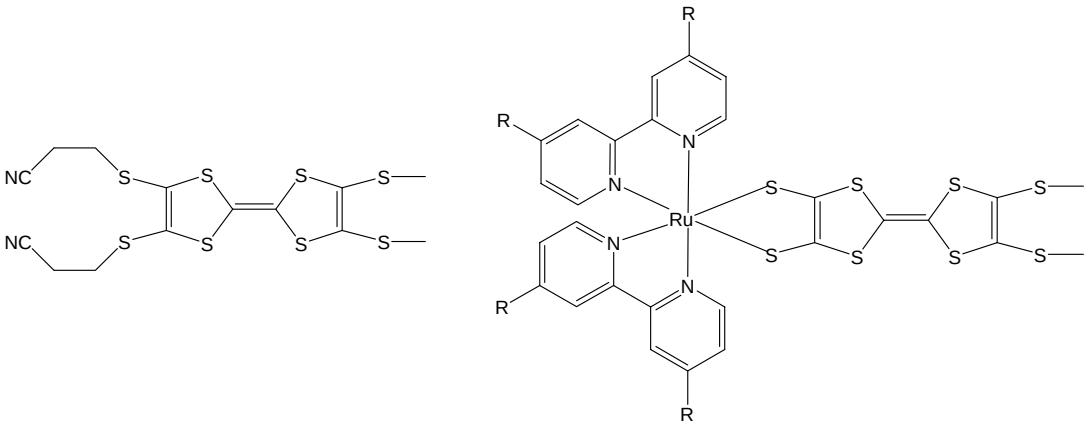


**Figure 4.** Structure of **L3** (left) and dye series with general formula Ru(R-bpy)$_2$(**L3**) (right), where R = H (**7**), $CO_2Et$ (**8**), $CO_2H$ (**9**).

Variation of the peripheral groups from the standard TTF molecule can allow for fine-tuning of the redox properties and also vary the functionality of the system. For **L3,** incorporation of the cyanoethylthio groups allowed a known route to be used for deprotection of the ligand.[32] The deprotection takes place by reaction of **L3** in tetrahydrofuran with tetramethylammonium hydroxide at 0 °C. This removes the cyanoethyl group by nucleophilic substitution leaving a dianionic ligand, allowing a room temperature reaction with the ruthenium bipyridyl complexes. The methylthiol groups on the opposite side of the TTF molecule were chosen to allow variation of the alkyl chain. The lengthening of the alkyl chain should lead to the ability of the dye to form a blocking layer on the surface of the $TiO_2$ in a DSSC, with the advantages of such a functionality already having been discussed in Chapter 3, Section 3.11.

Alkyl chain length variation was investigated during the course of this work with the use of an undecane chain ($C_{11}H_{23}$) in place of the methyl groups. Whilst a pure sample of the unsubstituted bipyridyl complex was obtained, purification of the acid and ester derivatives proved extremely difficult and so this work is not reported here. It should be noted that the preliminary characterisation work (including electrochemistry, absorption spectroscopy and spectroelectrochemistry) with this long alkyl chain series of complexes was identical to the characterisation of **7 - 9**.

## 4.2 Electrochemistry

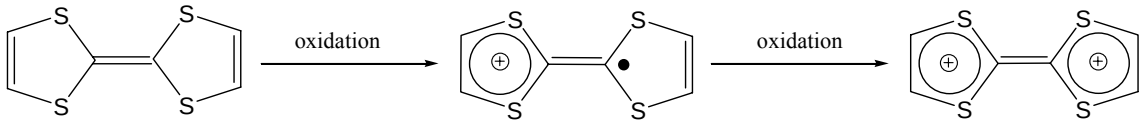


**Figure 5.** Sequential oxidation of a TTF molecule with resulting radical cation and di-cation.

TTF can undergo two reversible oxidations, yielding a stable radical cation and di-cation respectively (Figure 5). The electrochemistry of TTF and derivatives thereof are also known to be solvent-dependent.[33] This variation of oxidation potentials with solvent is thought to be due to solvents with a higher donor number being able to stabilise the dication more readily. (The donor number of a solvent is defined as the negative of the enthalpy of reaction between the solvent and antimony pentachloride.[34]) This effect was observed in the electrochemical study of **L3** (Figure 6), with the difference between oxidation potentials ($\Delta E$) being smaller in DMF ($\Delta E$ = 0.14 V), a solvent with a donor

number of 26.6 kcal/mol, relative to DCM ($\Delta E$ = 0.26 V) which has a negligible donor number.

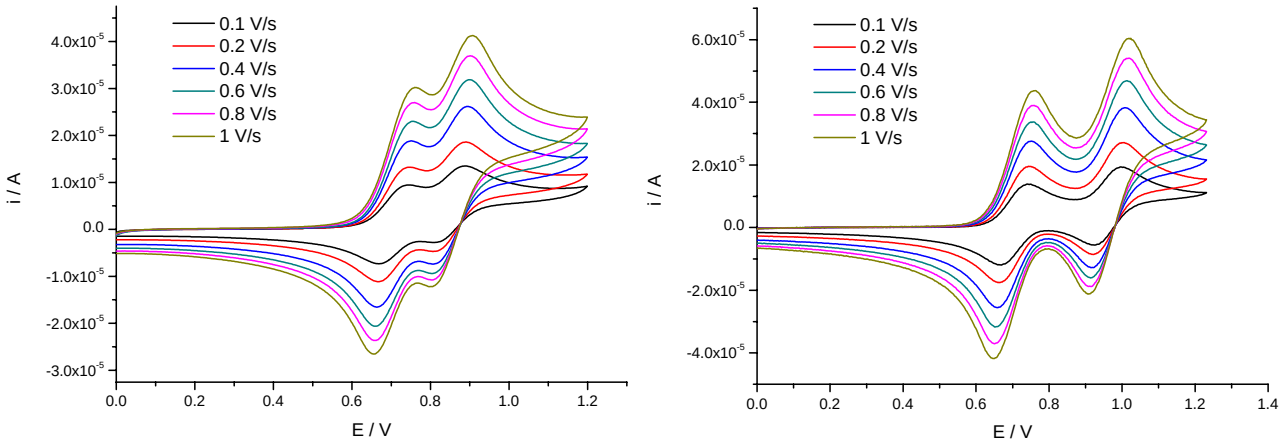


**Figure 6.** CV studies of **L3** in 0.1 M $TBABF_4$/DMF (left) and 0.3 M $TBABF_4$/DCM (right).

Complexes **7 - 9** formed with **L3** all show remarkably similar oxidation potentials (Table 1). This may reflect the similarity in nature of the occupied orbitals, *i.e.* the large contribution of **L3**, this point is further discussed in Sections 4.4 to 4.7. It should be noted that cyclic voltammetry studies of these complexes showed very poorly defined voltammograms, due to the three oxidations occurring at very similar potentials. Therefore in all cases differential pulse voltammetry was used to establish a more accurate description of the redox processes for these systems (Figure 7, Figure 8).

The reduction potentials of the complexes vary according to expectations, with **7** showing the more negative reductions relative to the complexes with the ester and acid derivatives (**8** and **9**). It should be noted that the electrochemical studies were also

carried out in 0.3 M $TBABF_4$/DCM, however the oxidation potentials did not vary from those observed in DMF.

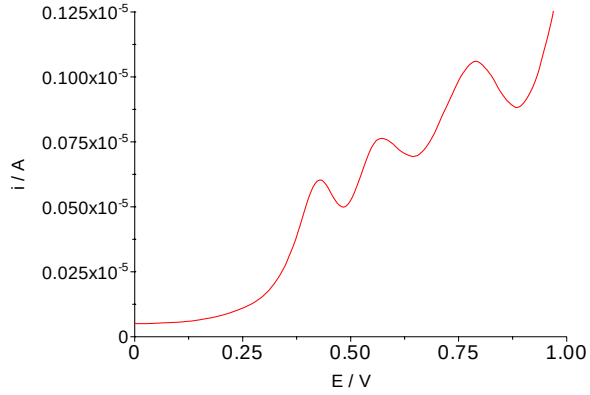


**Figure 7.** Differential pulse study of **7** in 0.1 M $TBABF_4$/DMF.

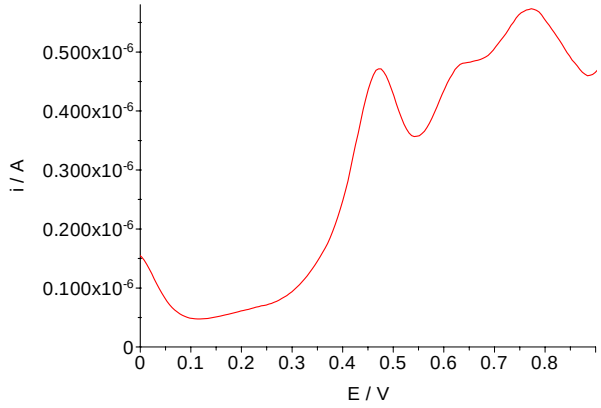


**Figure 8.** Differential pulse study of **8** in 0.1 M $TBABF_4$/DMF.

| **Compound** | **$E_{1/2}^{ox}$ / V** | | | **$E_{1/2}^{red}$ / V** | |
|---|---|---|---|---|---|
| **L3** | 0.85 | 0.71 | | | |
| **7** [a] | 0.79 | 0.56 | 0.42 | -1.41 | -1.49 |
| **8** [a] | 0.79 | 0.65 | 0.47 | -1.01 | -1.3 |
| **9** [a] | 0.78 | 0.64 | 0.46 | -0.98 | |

[a] Obtained *via* differential pulse experiment

**Table 1.** Summary of redox potentials for **7**, **8**, **9** and **L3** in 0.1 M $TBABF_4$/DMF (*vs.* Ag/AgCl).

The nature of the oxidations were of particular interest in this study, as outlined in the introduction to this chapter, and this was further investigated using OTTLE and *in-situ* EPR studies (Sections 4.4 and 4.5).

## 4.3 Absorption Spectroscopy

**L3** shows a number of strong UV transitions and a weak band in the visible region, resulting in a yellow/orange solution (Figure 9, Table 2). The absorption spectra of complexes **7** – **9** (Figure 10, Table 2) are somewhat unusual for ruthenium bipyridyl complexes in that they have very poorly defined bands in the visible region, with a gradual increase in absorption from ~ 800 nm onwards. This broad absorption range would be advantageous, however the molar extinction co-efficients of the lower energy bands are relatively small (less than 9000 $M^{-1}$ $cm^{-1}$). This means that the light harvesting ability of this dye is actually very poor. It is unclear exactly why the absorption spectrum is quite so broad for this series of complexes, however it may be due to the large contribution the TTF moiety makes to the highest occupied orbitals, a point which is further discussed in Section 4.7. It should also be noted that a broad absorption spectrum was observed for both previously studied complexes where TTF was covalently bound to the ruthenium centre.[7]

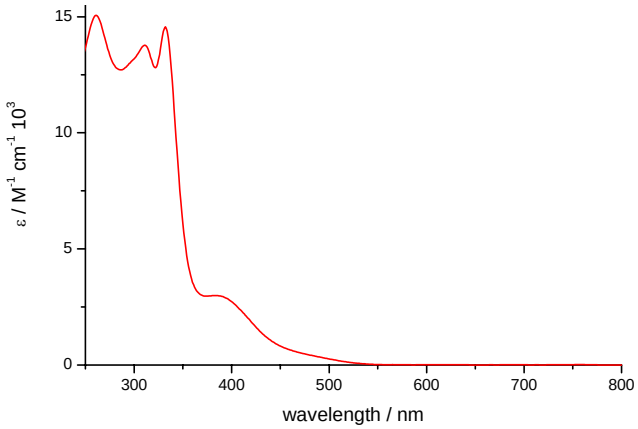


**Figure 9.** Absorption spectrum of **L3** in DCM.

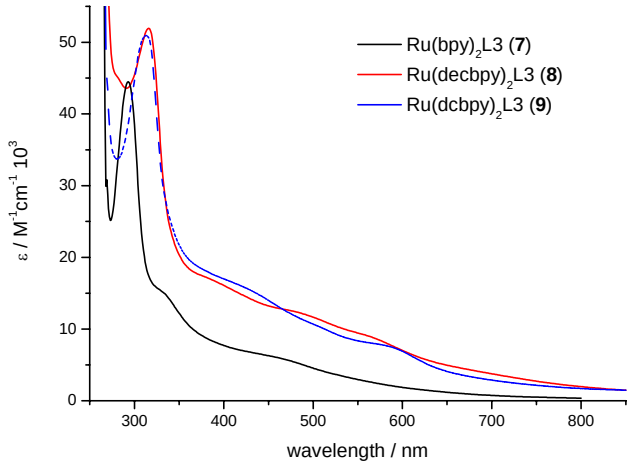


**Figure 10.** Absorption spectra of complexes **7** – **9** in DMF.

| | **π –π*/nm** | | | | **MLCT/nm** | | |
|---|---|---|---|---|---|---|---|
| **L3** | 380 (2.9) | 332 (14.3) | 310 (13.6) | 262 (14.8) | - | | |
| **7** | 293 (44.1) | | | | 334 (15.2) | 450 (6.4) | |
| **8** | 317 (53.0) | | | | 400 (16.4) | 484 (12.6) | 563 (8.9) |
| **9** | 312 (51.0) | | | | 420 (16.1) | 500 (10.5) | 575 (8.0) |

**Table 2.** Absorption spectra maxima with molar extinction co-efficients in brackets / $M^{-1}$ $cm^{-1}$ $10^3$ for **L3** in DCM and **7**, **8**, and **9** in DMF.

### 4.3.1 Emission Studies

The room temperature emission studies of **L3** and complexes **7** – **9** are summarised in Table 3 and Figure 11. **L3** was found to yield no emission, in agreement with previous luminescence studies of functionalised TTF systems.[35] The observed emission in the studies of complexes **7** – **9** was found to be that of the chromophoric unit $Ru(R\text{-}bpy)_2$, as shown by the similarity of the emission maxima to those of $[Ru(R\text{-}bpy)_3]^{2+}$ for all three complexes.[36,37,38] This result suggests that the model of electron transfer processes outlined in Figure 1 may be an accurate representation for these complexes, as the two distinct units appear to retain their individual properties. It would be expected that the lifetime of these emissions would be substantially reduced relative to the tris-(R-bpy) complexes (100s of nanoseconds) as the TTF moiety should facilitate rapid electron transfer to the $Ru(R\text{-}bpy)_2$ moiety and result in quenching of the emission. These observations have been made previously for a ruthenium complex incorporating a TTF functionalised bipyridyl ligand.[19] The fact that emission is observed at all suggests that the timescale of the intramolecular electron transfer is longer than the intersystem crossing from the $^1$MLCT state to the $^3$MLCT state (which generally occurs on a sub-picosecond timescale)[39].

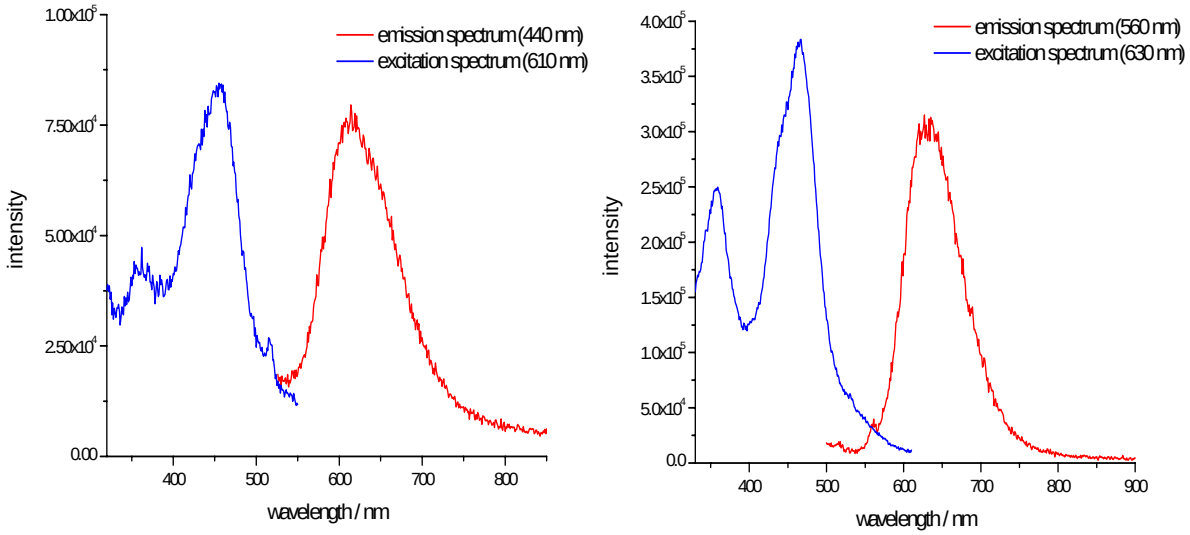


**Figure 11.** Emission and excitation spectra for **7** (left) and **8** (right) in ethanol, at room temperature with the corresponding excitation and emission wavelengths shown in brackets.

The excitation spectra for these complexes are much more defined than the observed absorption spectra. The excitation spectra are showing the transitions which are resulting in the emission. In this case they would be allowed transitions to $^{1}$MLCT which relax (*via* intersystem crossing) to the emissive $^{3}$MLCT states, the lack of overlap between the excitation and emission spectra is further evidence for emission from the triplet state. The absence of the broad absorption bands in the excitation spectra indicates that there are transitions which relax non-radiatively for these complexes. These may involve transitions within the TTF moiety or orbitals which are largely mixed *i.e.* both Ru and TTF in character.

Emission studies of complexes **7** - **9** were also carried out at 77 K in frozen glass ethanol solutions. These exhibit very similar emission and excitation spectra, however there is

greater resolution at lower temperature, especially for **8** which shows two sharp peaks at 77 K in place of a broad band at room temperature (Figure 12).

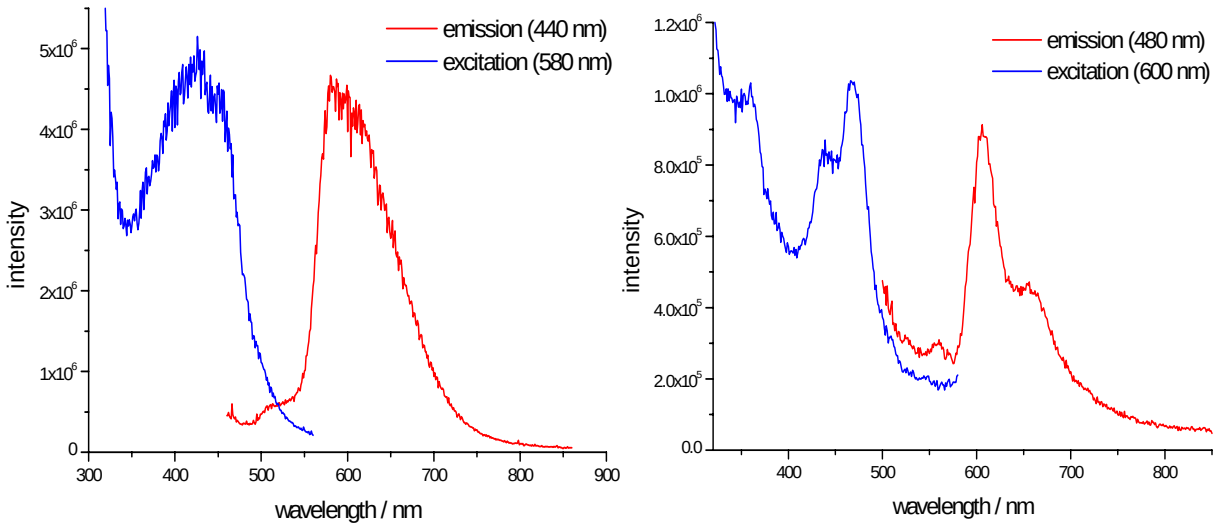


**Figure 12.** Excitation and emission spectra of **7** (left) and **8** (right) in rigid glass at 77 K, with corresponding excitation and emission wavelengths shown in brackets.

| Compound | Emission max / nm | |
|---|---|---|
| | 293 K | 77 K |
| **L3** | - | - |
| **7** | 620 | 600 |
| **8** | 630 | 610, 655 |
| **9** | 640 | 610, 660 |

**Table 3.** Emission spectra maxima for **L3** and complexes **7** – **9** at room temperature and 77 K, in ethanol.

## 4.4 Spectroelectrochemistry

The OTTLE studies of **L3** in 0.3 M $TBABF_4$/DCM showed very clear changes to the absorption spectra for the mono-oxidised and di-oxidised species (Table 4, Figure 13). The first oxidation results in the growth of visible region bands at 22000 and 12000 $cm^{-1}$ and the complete collapse of two of the UV bands as well as the decrease in intensity of the third UV band. The second oxidation results in the collapse of the two visible region bands and the growth of a more intense band at 14800 $cm^{-1}$. Two new bands were also observed in the UV region at 42600 and 34000 $cm^{-1}$. The two bands in the visible region for the mono-oxidised species must involve the resultant singly-occupied molecular orbital (SOMO) as they consequently collapse upon di-oxidation. It is likely that these transitions are intramolecular SOMO to lower unoccupied orbitals and/or HOMO-1 to SOMO.

It should be noted that these studies were also carried out in 0.1 M $TBABF_4$/DMF and showed irreversible behaviour with no isosbestic points during the oxidised species generation, suggesting degradation of the oxidised species in this more coordinating solvent.

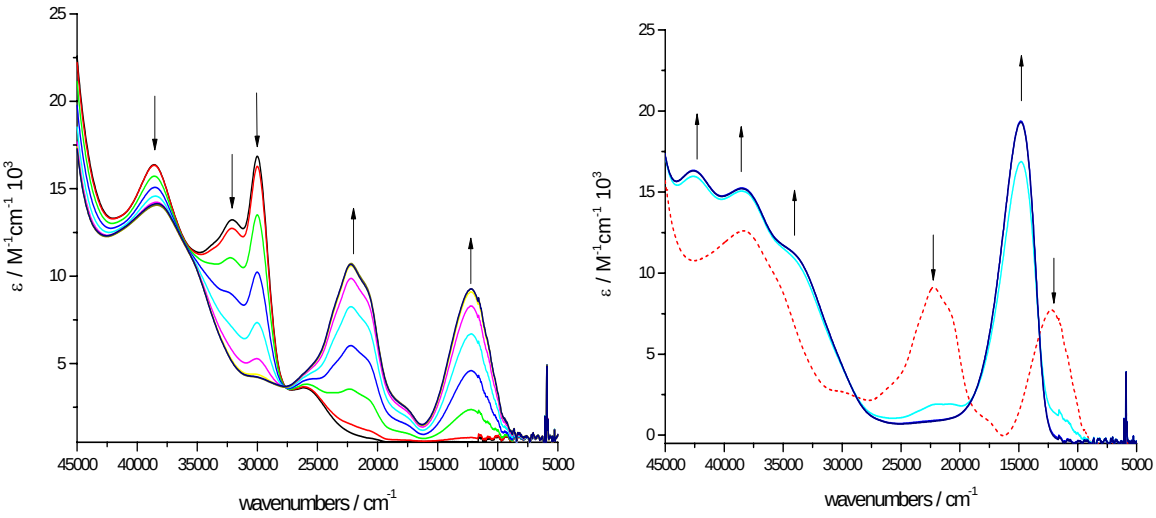


**Figure 13.** Oxidative OTTLE study of **L3** showing mono-oxidation (left) and di-oxidation (right) in 0.3 M $TBABF_4$/DCM, at -40 °C with applied potentials of + 0.85 and + 1.25 V respectively (*vs.* Ag/AgCl). Mono-oxidised spectrum is shown as a dashed line in right hand graph for clarity.

The oxidative OTTLE studies of **7** (Figure 14, Table 4) show the growth of a broad band between 9000 and 13000 $cm^{-1}$ after mono and di-oxidation. The intraligand band at 34000 $cm^{-1}$ also decreases in intensity after both oxidations. The main difference between the two is the behaviour of the visible region bands at 22000 and 30000 $cm^{-1}$. The mono-oxidised species shows a partial collapse of the highest energy visible band but no change in the low energy band. However, the di-oxidised species shows a complete collapse of the high energy band accompanied by a growth of the low energy band. The origins of the changes in absorption with oxidation are further discussed in conjunction with the oxidative OTTLE studies of **8**, below. It should be noted that the tri-oxidised species of **7** was also studied but was found to be unstable in both DMF and DCM.

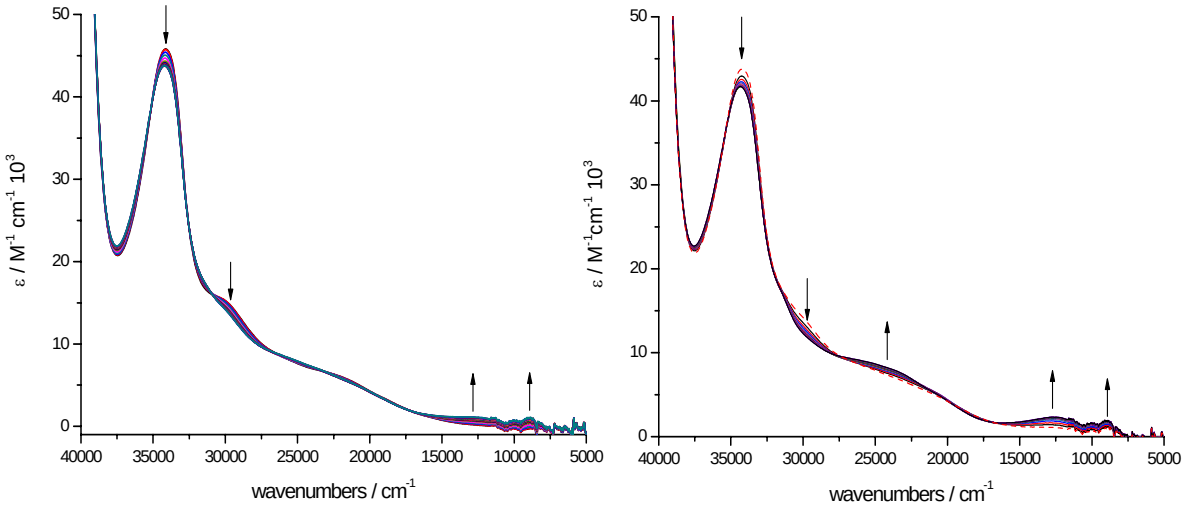


**Figure 14.** Mono-oxidation (left) and di-oxidation (right) of **7** in 0.3 M $TBABF_4$/DMF, with an applied potential of + 0.48 and + 0.64 V respectively (*vs.* Ag/AgCl). Mono-oxidised species shown as dashed red line in di-oxidation study.

The oxidations of **8** were studied in both DMF and DCM, to investigate the reversibility of the various processes (Figure 15, Figure 16). In both solvents the first and second oxidations were found to be fully reversible, however the third was only partially reversible in DMF and fully reversible in DCM.

The first two oxidations have similar effects on the absorption spectrum of **8**, showing the growth of a band at 9200 $cm^{-1}$, a decrease in intensity of the bipyridyl intraligand band at 32000 $cm^{-1}$ and the increase of the MLCT band at 23000 $cm^{-1}$. The main difference between the two spectra is the appearance of a second low energy band at 13000 $cm^{-1}$ for the di-oxidised species. The low energy bands may either be assigned to intraligand TTF transitions, as observed for **L3**, or to HOMO to LUMO transitions, as discussed further in Section 4.6.

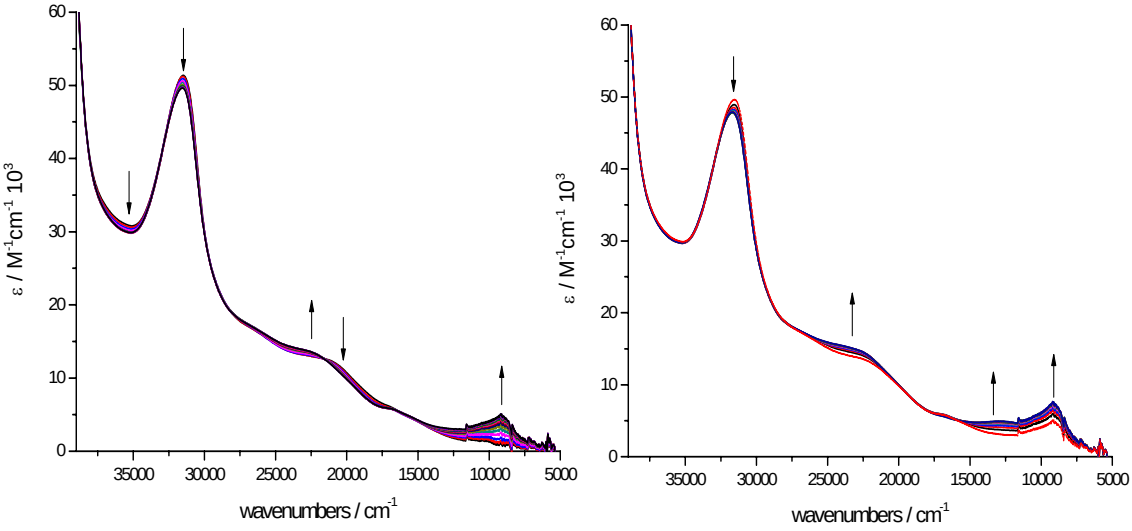


**Figure 15.** Oxidative OTTLE studies of **8** in 0.1 M $TBABF_4$/DMF showing mono-oxidised (left) and di-oxidised (right) species, with applied potentials of + 0.5 and + 0.68 V respectively (*vs.* Ag/AgCl). Mono-oxidised species shown as dashed line in right hand graph for clarity.

The tri-oxidised absorption spectrum shows a further growth in intensity of the low energy peaks at 14000 and 9200 $cm^{-1}$, however this is accompanied by the decrease in the MLCT band at 23000 $cm^{-1}$ and a slight broadening of the intraligand band. These are typical responses for a ruthenium oxidation,[40] albeit not as pronounced as for most other ruthenium bipyridyl complexes, and so this third oxidation was tentatively assigned to the ruthenium centre. The fact that the first two oxidations showed very similar responses and that they resulted in the growth rather than collapse of the band assigned as an MLCT suggests that these oxidations are not based on the ruthenium centre, and were tentatively assigned as TTF based oxidations.

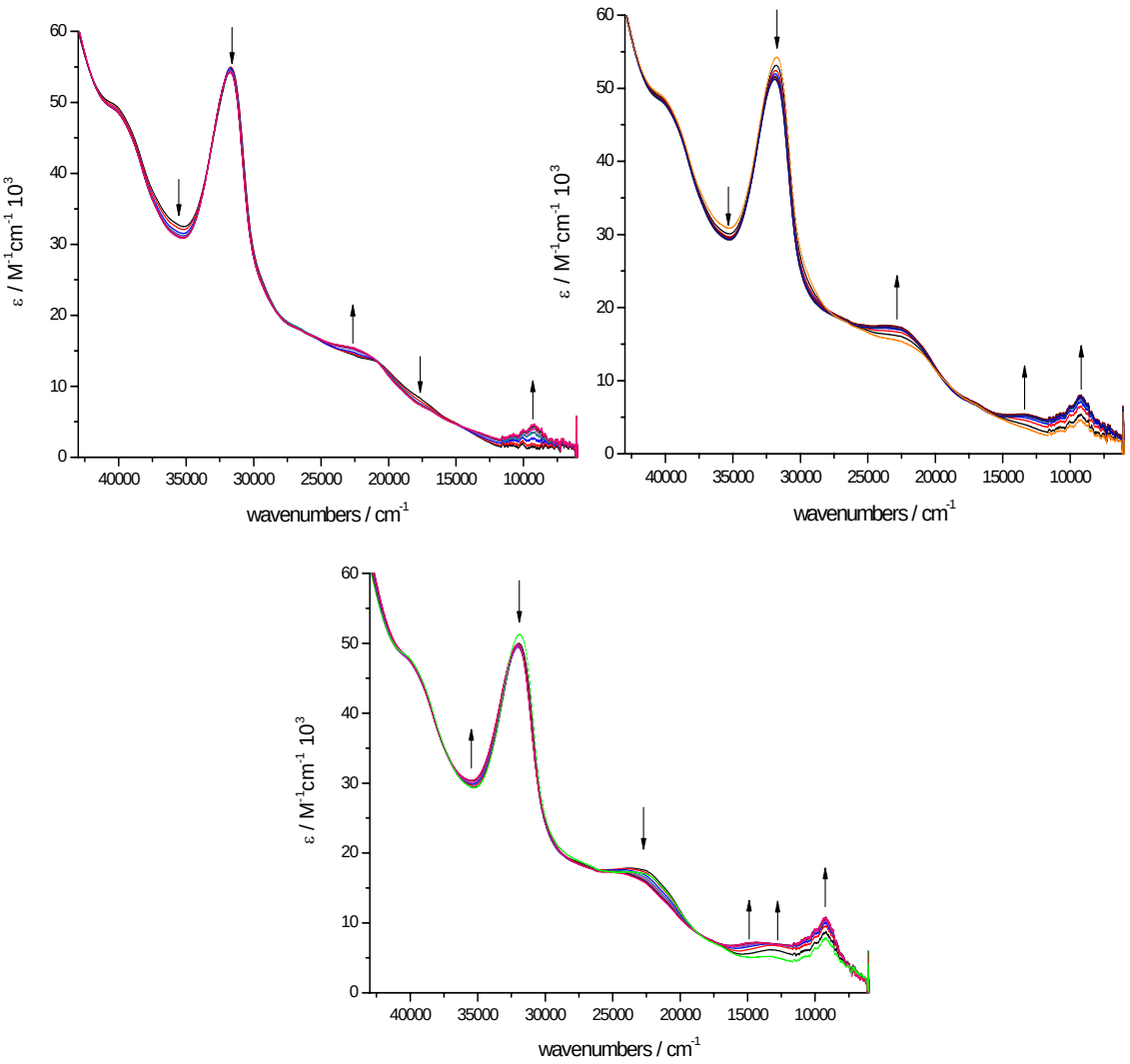


**Figure 16.** Oxidative OTTLE studies of **8** in 0.3 M $TBABF_4$/DCM, showing mono-oxidised (top left), di-oxidised (top right) and tri-oxidised (bottom), with applied potentials of + 0.5, + 0.68 and + 0.91 V respectively (*vs.* Ag/AgCl).

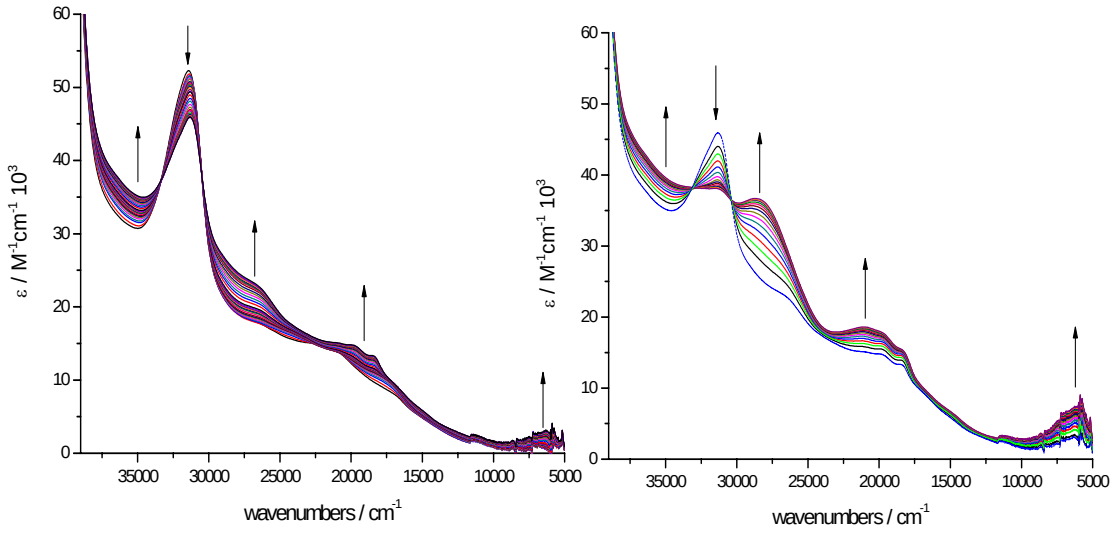


**Figure 17.** Reductive OTTLE studies of **8** in 0.1 M $TBABF_4$/DMF showing mono-reduced (left) and di-reduced (right) with applied potentials of – 1.15 V and – 1.4 V respectively (*vs.* Ag/AgCl). Mono-oxidised spectrum shown as dashed blue line in di-reduced hand graph for clarity.

The reductive OTTLE studies of **8** showed typical mono-reduced and di-reduced species for a ruthenium bipyridyl complex (Figure 17), with the partial collapse of the bipyridyl intraligand band at 31000 $cm^{-1}$ and the growth of three new bands at 6500, 19000 and 27000 $cm^{-1}$ on mono-reduction. The bipyridyl intraligand band further collapses upon di-reduction and continued growth of the three new π-π* bands was observed. These studies indicate that the LUMOs are located on the bipyridyl ligands as expected.

| Compound | Absorption / $cm^{-1}$ ($\varepsilon$ / $M^{-1}$ $cm^{-1}$ $10^3$) |
|---|---|
| $[L3]^+$ | 38300 (14.0), 30050 (4.2), 22200 (10.7), 12230 (9.2) |
| $[L3]^{2+}$ | 42650 (16.3), 38480 (15.2), 34024 (11.3), 14840 (19.4) |
| $[Ru(bpy)_2L3]^+$ | 8980 (1.2), 12900 (1.2), 21880 (6.1), 29690 (13.6), 34200 (43.7) |
| $[Ru(bpy)_2L3]^{2+}$ | 8980 (2.1), 12660 (2.4), 24200 (8.3), 34250 (41.7) |
| $[Ru(decbpy)_2L3]^+$ | 9240 (5.1), 22540 (13.8), 31540 (49.4) |
| $[Ru(decbpy)_2L3]^{2+}$ | 9190 (7.6), 12960 (4.9), 23880 (15.4), 31710 (47.8) |
| [b] $[Ru(decbpy)_2L3]^{3+}$ | 9170 (11.0), 14420 (7.2), 23720 (16.7), 32020 (46.4) |
| $[Ru(decbpy)_2L3]^-$ | 6475 (2.9), 18470 (13.5), 19840 (14.9), 26780 (23.3), 31300 (45.8), 34830 (35.1) |
| $[Ru(decbpy)_2L3]^{2-}$ | 6170 (7.4), 18380 (15.5), 21000 (18.7), 28550 (36.5), 31450 (38.1), 34790 (39.5) |

[b] Study carried out in 0.3 M $TBABF_4$/DCM.

**Table 4.** Absorption spectra maxima of electrochemically mono-oxidised and di-oxidised **L3**, mono-oxidised, di-oxidised, tri-oxidised, mono-reduced, di-reduced **8**, and mono-oxidised, di-oxidised and tri-oxidised **7**.

## 4.5 *In-situ* EPR

The mono-oxidation of **L3** resulted in the growth of a single peak with g = 2.0197. Inducing the second oxidation resulted in the collapse of this new peak. This is entirely as expected for a functionalised TTF, with the single uncoupled peak showing that the unpaired electron is located on one of the central rings surrounded by elements with a nuclear spin of zero, rather than the peripheral methyl thiol or cyanoethylthio groups where there are non-zero nuclear spin elements.

The EPR studies of **8** showed the growth of a single uncoupled peak upon inducing the first oxidation with g = 2.0191. With di-oxidation the peak collapses to yield an EPR silent species and there is no return of a signal upon tri-oxidation. This provides further evidence for the first oxidation being TTF based, as the generation of an uncoupled signal with a g-factor very similar to that of oxidised **L3** can only account for an unpaired electron being located on the TTF ligand. The studies do not discern between the nature of the second and third oxidations, however as the collapse of the peak could result from either the ruthenium or the second TTF based oxidation.

The lack of any observable signal with the oxidation of the ruthenium (whether it be the second or third) is not wholly unexpected. Ruthenium has two non-zero spin isotopes $^{99}$Ru and $^{101}$Ru, both with I = 5/2. It may be expected that upon oxidation of the ruthenium centre the resulting $d^5$ Ru(III) would be EPR active. This is often not the

case, however, as spin-orbit coupling leads to rapid relaxation due to the strong orbital contribution to the magnetic moment.

Overall these spectroelectrochemical studies have shown that this system has the potential to show long-lived charge-separated lifetimes in a DSSC as the HOMO appears to be located largely on the TTF ligand.

## 4.6 DFT Calculations

The level of theory and basis sets used for the following calculations are detailed in Chapter 2, Section 2.5. The calculated optimised structure of **8** showed a 'kinked' **L3** moiety with a torsion angle of 158.5 ° between C11-C13-S14-C15 (Figure 18). Whilst a crystal structure was not obtained of this complex to verify if this is a true representation of the system, the structure can be compared to the 54 examples in the Cambridge Crystallographic Database[41] of complexes where transition metals are directly bound to a TTF ligand. The majority of these structures are copper and nickel complexes, but there are also a number of platinum group metal complexes, namely platinum, palladium, iridium and one example of a rhodium structure. A comparison of the torsion angles on the TTF ligand for all monometallic structures in this search showed that all but three complexes had a torsion angle greater than 160°, those exceptions were two platinum and one gold complex. With examples of the 'kinked' TTF available it may be concluded that the calculated structure is a reliable representation of the system.

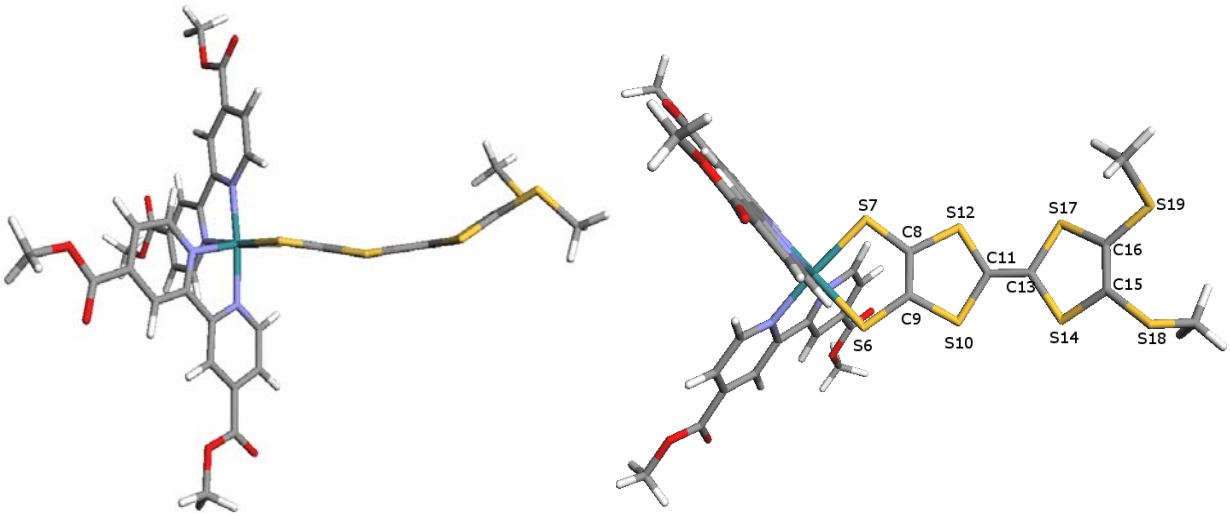


**Figure 18.** Optimised geometry of **8** in a DMF polarisable continuum model (left), with relevant atom labelling (right).

Computational calculations involving **8** also proved to be very informative about the nature of the numerous oxidations occurring with this complex. The calculated occupied orbitals (Figure 19, Table 5) relate very well to the experimentally observed phenomena. The HOMO and HOMO-1 show only a small contribution from the ruthenium centre with the majority of the orbital found to be localised on the TTF ligand. The HOMO-2 showed a much larger ruthenium contribution to the orbital with a smaller degree of TTF nature. These results agree very well with the spectroelectrochemical studies and once again suggest that the first oxidation is TTF in nature, which indicates that this system may show significantly increased charge-separation in a DSSC. The LUMO and further unoccupied orbitals were calculated to be largely based on the two bipyridyl ligands with a small contribution from the ruthenium, which also relates very well to the reductive OTTLE study conclusions.

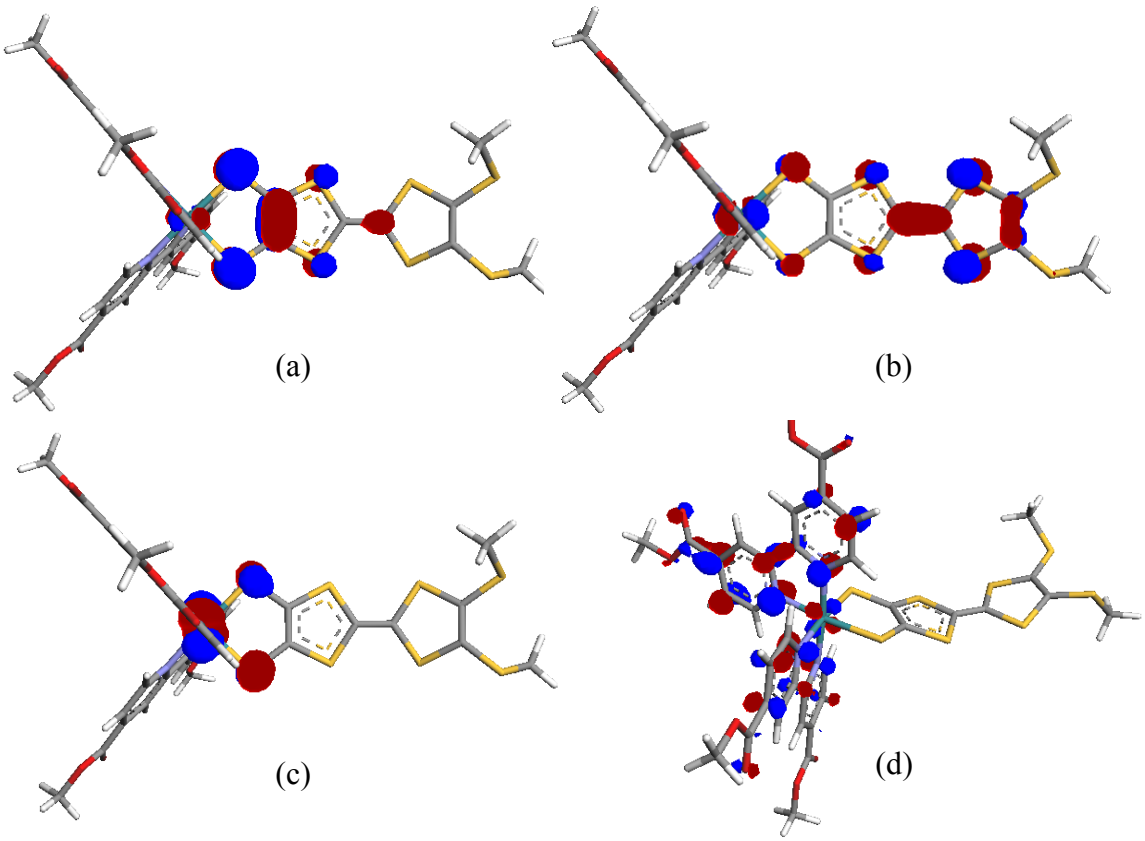


**Figure 19.** Calculated HOMO (a), HOMO-1 (b), HOMO-2 (c) and LUMO (d) of **8** using a DMF polarisable continuum model.

| Molecular orbital | Energy (eV) | % Ru | % decbpy | % TTF |
|---|---|---|---|---|
| LUMO+1 | -2.67 | 10.66 | 87.28 | 2.02 |
| LUMO | -2.75 | 7.75 | 90.11 | 2.12 |
| HOMO | -4.35 | 6.77 | 4.73 | 88.45 |
| HOMO-1 | -5.20 | 14.54 | 3.76 | 81.72 |
| HOMO-2 | -5.52 | 57.08 | 7.59 | 35.33 |

**Table 5.** Calculated energies and percentage contributions of Ru, decbpy, TTF for selected orbitals of **8** in DMF.

## 4.7 TD-DFT

To simulate the full absorption spectrum of **8**, 70 singlet-singlet transitions were calculated using the optimised geometry in a DMF polarisable continuum model (Figure 20). A summary of those transitions with significant oscillator strength can be found in Table 6. The lowest energy calculated transition was the HOMO-LUMO transition at 1100 nm. This was not observed in the experimental spectrum, presumably due to the poor orbital overlap between the HOMO, based on the TTF, and the LUMO, based on the bipyridyl ligand. The low probability of this transition was also indicated by the very low calculated oscillator strength of the transition.

The visible region absorption bands are relatively well reproduced, with the energies being quite similar to those observed experimentally. The intensities are however somewhat overestimated, as has been observed with the other systems in this work. Interestingly these transitions were calculated to have pure MLCT character, involving transitions from the HOMO-3 to unoccupied orbitals. This would suggest that the dye behaves as the separate chromophore and electron-donor system, as outlined in Figure 1, which agrees with the emission study results. Therefore, in a DSSC if the injection of an electron into the conduction band of $TiO_2$ occurs after MLCT then the resultant hole will be on the ruthenium centre. However, as the TTF moiety is easier to oxidise than the ruthenium, then intramolecular charge transfer can readily occur between the two units, shifting the location of the dye cation to the TTF ligand. The location of the hole further

from the surface of the $TiO_2$ should then lead to a significantly longer-lived charge-separated state. The higher energy visible band has significant contribution from transitions which originate from the TTF based HOMO, and so the poor orbital overlap may be contributing to the low molar extinction coefficient in this region of the observed absorption spectrum.

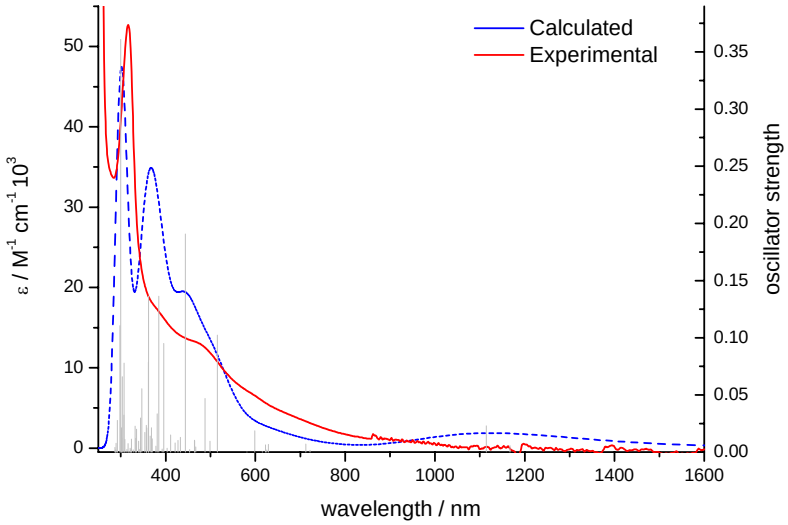


**Figure 20.** Gaussian convolution of calculated transitions (blue line), compared to experimental spectrum (red line), for **8** in DMF, both left axis. The calculated transitions are also shown relative to the calculated oscillator strength (grey columns), right axis.

| Excited state | Energy (nm) | | *f* | Character |
|---|---|---|---|---|
| | Calculated | Observed | | |
| **2** | 1114 | - | 0.023 | HOMO to LUMO (14%) **LLCT** (TTF-bpy) |
| | | | | HOMO to LUMO+1 (80%) **LLCT** (TTF-bpy) |
| **11** | 515 | 563 | 0.12 | HOMO-3 to LUMO (74%) **MLCT** (Ru-bpy) |
| **19** | 444 | 484 | 0.19 | HOMO-4 to LUMO+1 (48%) **MLCT** (Ru-bpy) |
| **27** | 385 | 400 | 0.14 | HOMO-3 to LUMO+3 (66%) **MLCT** |
| **33** | 362 | 400 | 0.14 | HOMO to LUMO+9 (34%) **LLCT** (TTF-bpy) |
| | | | | HOMO to LUMO+10 (31%) **LLCT** (TTF-bpy) |
| **63** | 300 | 317 | 0.36 | HOMO-10 to LUMO+1 (57%) |
| | | | | **bpy intraligand** |

**Table 6.** Summary of selected calculated excited state transitions, energies and character for **8** in DMF. Only those with oscillator strength greater than 0.1 are shown, with the exception of the HOMO-LUMO transition.

## 4.8 Solar Cell Measurements

The I-V measurements for **9** were somewhat disappointing, with very low efficiencies recorded (Figure 21, Table 7). Under the same conditions a DSSC sensitised with N719 achieved an efficiency of 2.65 %. The sensitisation of the $TiO_2$ film was satisfactory

with a dark brown film obtained after soaking the film overnight in a 0.5 mM 1:1 methanol/DMF solution. The absorption spectrum of the film resembled that of the dye in solution, indicating no degradation of the dye upon adsorption (Figure 21). Variation of the electrolyte to contain simply 0.6 M LiI/ 0.03 M $I_2$ showed no significant improvement, therefore an energy mismatch between the LUMO and the conduction band of the $TiO_2$ does not appear to be the cause of the low efficiency in this case. The failure of this dye to function efficiently in a DSSC is further discussed with respect to the TAS measurements in Section 4.9.

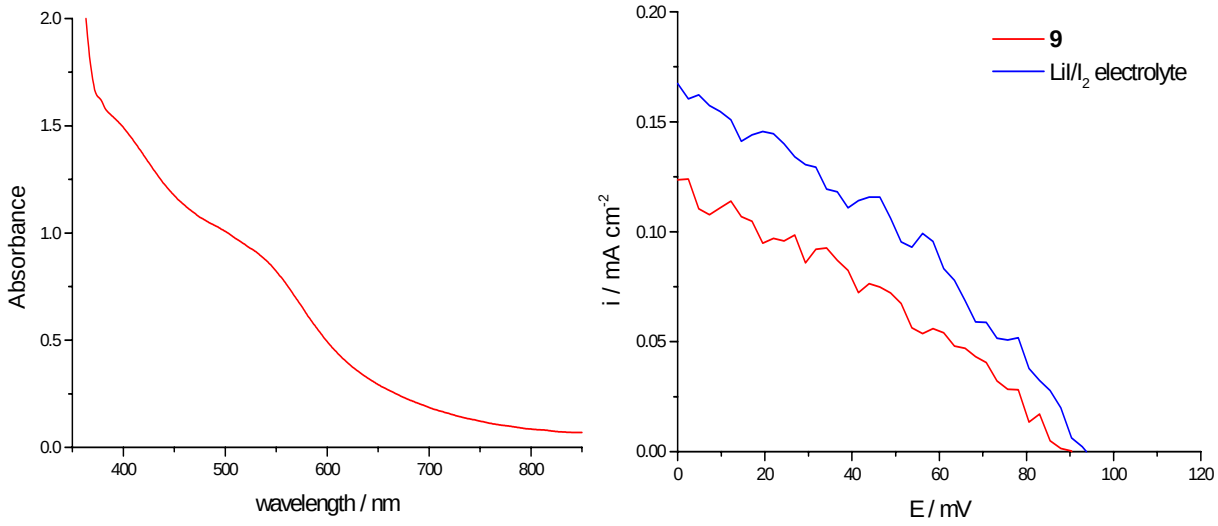


**Figure 21.** Absorption spectrum of $TiO_2$ film sensitised with **9** (left) and AM 1.5 (1000 $Wm^{-2}$) I-V characteristics for DSSCs sensitised with **9** (right).

| Cell | $V_{oc}$ (mV) | $I_{sc}$ (mA $cm^{-2}$) | ff | η (%) |
|---|---|---|---|---|
| **9** | 88 | 0.12 | 0.31 | 0.004 |
| **LiI/$I_2$ electrolyte** | 93 | 0.17 | 0.35 | 0.006 |
| **N719** | 737 | 6.87 | 0.53 | 2.65 |

**Table 7.** Short-circuit current, open-circuit voltage, fill factor and global efficiency for DSSCs sensitised with **9** and N719.

## 4.9 Transient Absorption Spectroscopy

The recombination and regeneration kinetics of the dye/$TiO_2$ system was of particular interest for **9** as transient absorption spectroscopy should provide definitive evidence of a long-lived charge-separated state. The clear growth of a band at ~ 1000 nm upon oxidation of **8**, observed in the OTTLE study, was used to investigate the charge-separated lifetime of the $TiO_2$ conduction band electron ($TiO_2|e^-$) and the dye cation hole ($d^+$) using transient absorption spectroscopy.

Using an excitation wavelength of 500 nm and a probe wavelength of 995 nm the charge-separated lifetime was studied using three different electrolytes: propylene carbonate (PC) only, propylene carbonate and lithium perchlorate and finally propylene carbonate and lithium iodide/iodine (Figure 22). This allowed both the recombination and regeneration kinetics to be investigated.

Initial results were very promising, with an extended lifetime observed during the recombination study using propylene carbonate only as the electrolyte. The measured half-life ($t_{1/2}$) was found to be very long-lived with a value of 20 ms, compared to a $t_{1/2}$ = 600 μs for N719, under the same conditions. The addition of $LiClO_4$ to the electrolyte had two effects: the amplitude of the signal increased and the dynamics of the system became more complex. There is still a long-lived signal, but in addition there is also a secondary rise and decay of the signal at longer time scales.

The study involving $LiI/I_2$ was found to have the same complex dynamics as the $LiClO_4$ recombination study, with only a small decrease in signal life-time, suggesting that the regeneration of this dye is particularly slow. The failure of the iodide to regenerate the neutral dye is likely to be the cause of the very low DSSC efficiency measured.

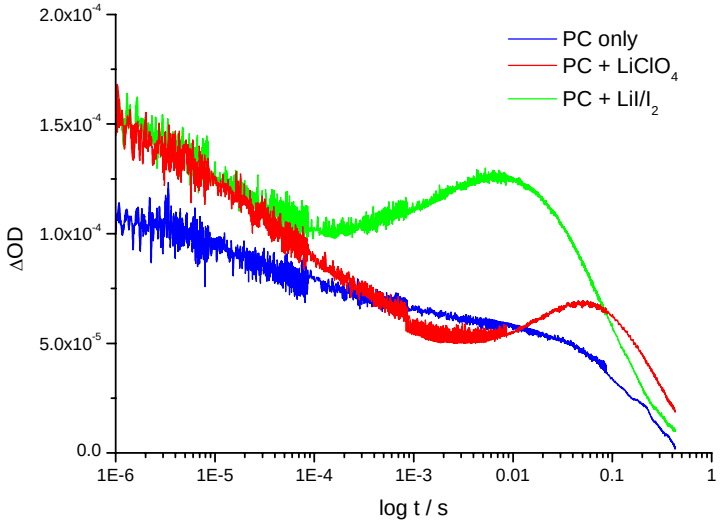


**Figure 22.** Transient absorption decay profiles for a $TiO_2$ film sensitised with **9**, using propylene carbonate, PC + $LiClO_4$ and PC + $LiI/I_2$ as electrolytes. The excitation wavelength was 500 nm and probe wavelength 995 nm.

To enable comparison of this system to the other dyes investigated in this thesis the kinetics were also investigated using a probe wavelength of 600 nm (Figure 23). Very similar behaviour was observed as for the study at 995 nm, with a long-lived signal observed in both the recombination and regeneration studies. The unusual kinetics are again observed with an initial negative transient response followed by an increase in ΔOD, a result of a larger difference between the initial probe laser intensity and the resultant intensity after dye cation formation. This means that initially the absorbance of the dye cation at 600 nm is lower than the neutral dye followed by an increase in absorption. The decrease in intensity is a result of the electron recombining/dye regeneration and the dye returning to the neutral state.

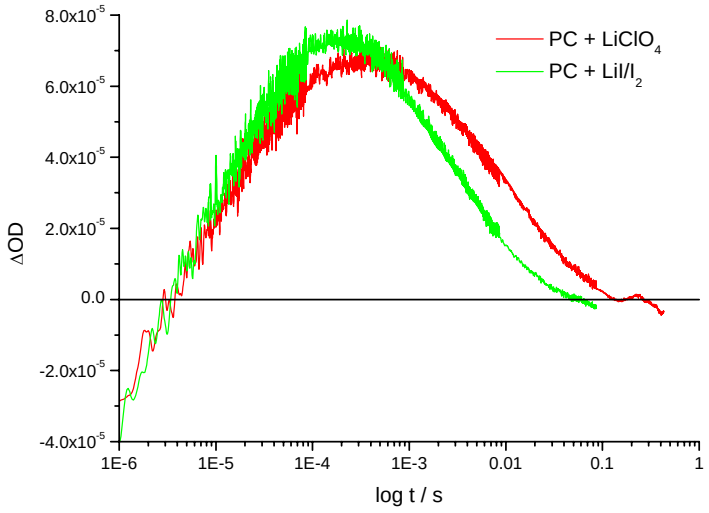


**Figure 23.** Transient absorption decay profiles for a $TiO_2$ film sensitised with **9**, using PC + $LiClO_4$ and PC + $LiI/I_2$ as the electrolyte. The excitation wavelength was 500 nm and probe wavelength 600 nm.

The first issue to address was whether the addition of these additives to the electrolyte was causing degradation of the dye in some form. The absorption spectra of the sensitised $TiO_2$ films were recorded upon changing the electrolyte composition, before and after irradiation (Figure 24). There was found to be no change in absorbance of the film, and no absorbance at ~ 1000 nm which would interfere with the TAS study and result in complex dynamics being observed. This also confirms that the species being observed involves the excited state of the dye or the dye cation specifically, and not the neutral form of the dye.

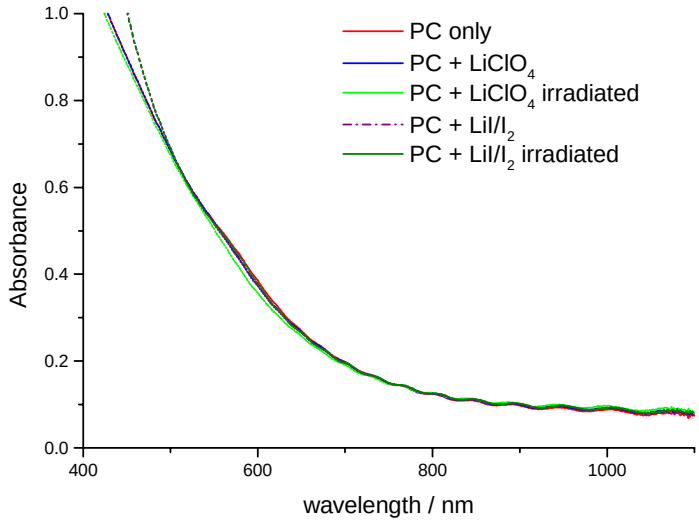


**Figure 24.** Absorption spectra of $TiO_2$ films sensitised with **9** with varying electrolytes, before and after TAS studies.

Another possibility is the formation of two oxidised species during the timescale of the study. For example, the $Ru^{3+}$ cation may be observed immediately after electron injection, followed by electron transfer from the TTF ligand to the ruthenium centre, resulting in a $TTF^{+\cdot}$ radical cation being observed (causing a rise in intensity). This is

highly unlikely however, as intramolecular electron transfer generally occurs on a much faster timescale.

A third theory involves the formation of a dye/electrolyte intermediate prior to electron recombination or dye regeneration, resulting in the increase in absorption due to a secondary species formation. In this instance the dye cation is formed, located on the TTF moiety as experimentally determined, and following this, an adduct is formed with the anions in the electrolyte. This was thought to be the most likely explanation for the complex dynamics and therefore further investigation of this theory was undertaken.

Evidence for such an intermediate has been presented recently, suggesting that the formation of a ruthenium bipyridyl cation/iodide intermediate is essential for the re-reduction of the dye. [42,43] The regeneration kinetics of N719 shows biphasic behaviour, whereby a fast phase involving the quenching of the dye cation is observed initially, followed by a slow phase with a long-lived signal. The initial fast phase was thought to be due to the reduction of the $[Ru(dcbpy)_2(NCS)_2]^+$ by iodide forming $I_2^-$ (Figure 25, Equation 1) and the second phase due to a long-lived $I_2^-$ and $TiO_2|e^-$, with the decay of this signal due to the dismutation of $I_2^-$ and interfacial charge recombination of $TiO_2|e^-$ with the redox couple (Figure 25, Equation 2).

$$(1) \qquad dye^+ + 2I^- \rightarrow dye + I_2^-$$

$$(2) \qquad 2I_2^- \rightarrow I^- + I_3^-$$

**Figure 25.** Processes involved in dye cation re-reduction to neutral dye.

The reduction of the oxidised dye (Equation 1) is believed to occur *via* formation of a $dye^+/I^-$ intermediate, although no unequivocal identification for the nature of this adduct exists. For **9** it may be the case that this intermediate formed with iodide is much more stable and hence the further reaction of the second iodide anion is very slow. The higher stability intermediate would result in the secondary rise in the TAS decay trace and also result in poor DSSC efficiency.

Further evidence for the formation of this stable intermediate upon addition of $ClO_4^-$ and $I^-$ is the observed increase in amplitude of ΔOD relative to the propylene carbonate only study. This increase in amplitude of the signal has previously been attributed to the formation of a $dye^+/I^-$ adduct upon studying in LiI. In a previous study the adduct formation was resolved at low iodide concentration showing an increase in ΔOD on the timescale $10^{-6}$ to $10^{-5}$ seconds, after this time the kinetics matched that of the higher iodide concentration studies. The exact nature of this adduct however could not be determined from this study.

In the present study, there may be a slower formation of a more stable intermediate between the anion and **9**, resulting in two signals superimposed on top of each other, which would account for both the initial higher ΔOD and the secondary rise in signal amplitude. Firstly the $TTF^+$ absorption is the dominant signal, with subsequent recombination resulting in a decrease in amplitude of this signal. However, with the formation of the $TTF^+$/anion adduct an increasing signal becomes apparent as the $TTF^+$ signal decreases below a certain level. The final decay in signal amplitude is ultimately

due to the recombination of the injected electron with the oxidised dye, rather than regeneration of the neutral dye *via* reduction by the iodide.

To investigate this theory, spectroelectrochemical studies were used to observe whether the dye was forming a distinctly different species in the presence of LiI. The mono-oxidised species was generated under standard OTTLE conditions in 0.1 M $TBABF_4$/DMF. Upon addition of 0.15 M LiI in DMF to the OTTLE cell, rapid regeneration of the neutral dye spectrum was observed. Under the long timescale of the scan used in the OTTLE study (approximately 2 minutes), no intermediate species was observed. This study does however prove that LiI will regenerate **9** as desired, but it is known from the TAS study that this does not occur faster than recombination *i.e.* below one second.

Attempts were made to bulk oxidise a solution of **8** and study the absorption spectrum after the addition of LiI using a stopped-flow set-up. It was hoped that this would allow the observation of the intermediate species absorption spectrum and potentially the kinetics of the adduct formation. However, the bulk oxidation of the dye using the technique of coulometry proved to be unsuccessful, even at low temperatures. This is possibly due to the instability of the oxidised product in large quantities.

A technique which should allow the observation of the secondary species absorption spectrum to be recorded is variable probe wavelength TAS. By focusing on one timescale and varying the probe wavelength, the varying intensity of the signal can be

used to gradually build up a picture of the oxidised dye. In the case of **9**, two separate species are predicted at two different timescales and hence by separately studying these two timescales the absorption spectra of these distinct species could be resolved. This work will be carried out in the near future.

## 4.10 Conclusions

This work has shown the successful synthesis and characterisation of a series of ruthenium bipyridyl complexes with a covalently linked TTF moiety. The absorption spectra of the complexes were found to be broad and with low molar extinction co-efficients for all derivatives, which was attributed to the additional transitions involving the TTF ligand as well as the expected MLCT. Whilst this low absorption is not ideal for use in a DSSC, the nature of the orbitals in this series proved to be very interesting. The HOMO was deduced to be largely TTF in nature *via* spectroelectrochemical and computational techniques. The HOMO-1 was not conclusively proven to be located on either the ruthenium centre or TTF *via* spectroelectrochemistry, but the computational work indicates the HOMO-1 to be largely TTF. The TD-DFT study showed the main origin of the low energy absorption band to be a ruthenium to bipyridyl ligand MLCT, suggesting that these dyes are acting as a separate chromophore and electron donor unit as desired, which was also indicated by the emission studies.

The sensitisation of $TiO_2$ by the acid derivative was successful and the function of this dye in a DSSC proved to be very informative. The efficiencies of the DSSCs were found to be extremely low (less than 0.01 %). Upon further investigation of the kinetics of recombination and regeneration *via* transient absorption spectroscopy, it was found that although there was the desired long-lived charge-separated state showing slow recombination, the regeneration of the dye was not efficient and therefore the recombination loss process is dominant. This slow reduction of the oxidised dye back to the neutral state by the iodide in the electrolyte shows the reason for the poor DSSC efficiency. The transient absorption spectroscopy study also indicated that there was the formation of a second species occurring, shown by a secondary rise in intensity in the decay trace. Attempts at further investigation and identification of this secondary species were hindered by the failure to generate the oxidised dye outwith the conditions used for an OTTLE study. However, it was observed that the dye could be regenerated by the iodide but only on a longer timescale than that of the recombination. The identification of the secondary species may lead to greater understanding of the mechanism of dye regeneration in a DSSC, which is still relatively unknown. For this reason further work will be undertaken in this area. In addition if further work is to be carried out on the use of **9** in a DSSC, particularly using solid-state non-iodide based electrolytes, then it would prove an interesting study to investigate the stability and performance of the systems with respect to the dye's alkyl chain length.

## 4.11 Synthesis

**L3** was prepared as described in the literature[44] and the ruthenium bipyridyl starting complexes as detailed in Chapter 2.

**2,3-bis(2-cyanoethylthio)-6,7-bis(methylthio)tetrathiafulvelene (L3).** CHN Calc. for $C_{14}H_{14}N_2S_8$: C 36.02, H 3.02, N 6.0, Found: C 36.69, H 3.34, N 5.11. $^1$H-NMR (DMSO, 250 MHz): δ 3.04 (t, $J_{HH}$ = 7, 4H), 2.72 (t, $J_{HH}$ = 6, 4H), 2.37 (s, 6H).

**Ru(bpy)$_2$(TTF-Me) (7).** $Ru(bpy)_2Cl_2$ (100 mg, 0.2 mmol) dissolved in methanol (10 ml) and silver nitrate (71 mg, 0.4 mmol) in water (1 ml) added. The mixture was refluxed for 1 hour and the resulting white silver chloride precipitate removed by centrifuge. TTF-Me (93 mg, 0.2 mmol) was suspended in tetrahydrofuran (5 ml), at 0 °C under nitrogen, and a 25 % tetramethylammonium hydroxide solution in methanol (250 μl, xs) added. The mixture was stirred under nitrogen at 0 °C for 20 minutes, followed by the removal of the solvent *in vacuo* and the resulting solid was redissolved in methanol (5 ml). The red ruthenium bipyridyl filtrate was then quickly added to the TTF-Me solution and the mixture stirred for 3 hours. The resulting brown product was collected by filtration. Yield: 61 mg (40 %). The crude product was further purified *via* a Sephadex LH-20 column using a 50:50 solution of methanol/dimethylformamide as the eluent. CHN Calc. for $C_{28}H_{28}N_4S_8Ru$: C 40.71, H 3.42, N 6.78, Found: C 40.86, H 2.99, N 6.57. +ve FAB-MS: m/z 772 ($M^+$). $^1$H-NMR (DMSO, 360 MHz): δ 10.68 (d,

$J_{HH}$ = 5, 2H), 9.75 (d, $J_{HH}$ = 8, 2H), 8.61 (t, $J_{HH}$ = 8, 2H), 8.10 (d, $J_{HH}$ = 8, 2H), 7.97 (t, $J_{HH}$ = 6, 2H), 7.80 (t, $J_{HH}$ = 6, 2H), 7.46 (d, $J_{HH}$ = 6, 2H), 7.34 (t, $J_{HH}$ = 7, 2H), 2.42 (s, 6H).

**Ru(decbpy)$_2$(TTF-Me) (8).** Ru(decbpy)$_2$Cl$_2$ (100 mg, 0.129 mmol) dissolved in methanol (10 ml) and silver nitrate (44 mg, 0.26 mmol) in water (1 ml) added. The mixture was refluxed for 1 hour and the resulting white silver chloride precipitate removed by centrifuge. TTF-Me (60 mg, 0.129 mmol) was suspended in tetrahydrofuran (5 ml), at 0 °C under nitrogen, and a 25 % tetramethylammonium hydroxide solution in methanol (120 µl, xs) added. The mixture was stirred under nitrogen at 0 °C for 20 minutes, followed by the removal of the solvent *in vacuo* and the resulting solid was redissolved in methanol (5 ml). The red ruthenium bipyridyl filtrate was then quickly added to the TTF-Me solution and the mixture stirred for 2 hours. The resulting brown product was collected by filtration. Yield: 67 mg (49 %). The crude product was further purified *via* a Sephadex LH-20 column using a 50:50 solution of methanol/dimethylformamide as the eluent. CHN Calc. for $C_{44}H_{46}N_4S_8O_8RuCl_8$: C 37.63, H 3.59, N 3.99, Found: C 37.78, H 2.56, N 4.23. +ve FAB-MS: m/z 1060 ($M^+$). $^1$H-NMR (DMSO, 360 MHz): δ 10.12 (d, $J_{HH}$ = 6, 2H), 9.14 (s, 2H), 8.95 (s, 2H), 8.27 (d, $J_{HH}$ = 6, 2H), 7.78 (d, $J_{HH}$ = 6, 2H), 7.5 (d, $J_{HH}$ = 6, 2H), 4.54 (q, $J_{HH}$ = 7, 2H), 4.37 (q, $J_{HH}$ = 7, 2H), 2.41 (s, 6H), 1.46 (t, $J_{HH}$ = 7, 3H), 1.32 (t, $J_{HH}$ = 7, 3H).

**Ru(dcbpy)$_2$(TTF-Me) (9).** Ru(decbpy)$_2$Cl$_2$ (100 mg, 0.129 mmol) dissolved in methanol (10 ml) and silver nitrate (44 mg, 0.26 mmol) in water (1 ml) added. The

mixture was refluxed for 1 hour and the resulting white silver chloride precipitate removed by centrifuge. The filtrate was treated with 0.1 M KOH (3 ml) and the mixture stirred for 15 mins. TTF-Me (60 mg, 0.129 mmol) was suspended in tetrahydrofuran (5 ml), at 0 °C under nitrogen, and a 25 % tetramethylammonium hydroxide solution in methanol (120 μl, xs) added. The mixture was stirred under nitrogen at 0 °C for 20 minutes, followed by the removal of the solvent *in vacuo* and the resulting solid was redissolved in methanol (5 ml). The base treated ruthenium bipyridyl filtrate was then quickly added to the TTF-Me solution and the mixture stirred for 2 hours. On acidification of the mixture with 1 M HCl (2 ml) a brown precipitate was collected by centrifugation. Yield: 64 mg (56 %). The crude product was further purified *via* a Sephadex LH-20 column using a 50:50 solution of methanol/dimethylformamide as the eluent. CHN Calc. for $C_{32}H_{26}N_4S_8O_{10}Ru$: C 39.05, H 2.66, N 5.69, Found: C 38.82, H 2.00, N 4.65. $^1$H-NMR (DMSO, 360 MHz): δ 10.06 (d, $J_{HH}$ = 6, 2H), 9.05 (s, 2H), 8.96 (s, 2H), 8.20 (d, $J_{HH}$ = 6, 2H), 7.72 (d, $J_{HH}$ = 6, 2H), 7.46 (d, $J_{HH}$ = 6, 2H), 2.36 (s, 6H).

## 4.12 References


[1] G. Will, J. Sotomayor, S.N. Rao, D. Fitzmaurice, *J. Mater. Chem.,* 1999, **9**, 2297-2299.

[2] J. Sotomayor, G. Will, D. Fitzmaurice, *J. Mater. Chem.,* 2000, **10**, 685-692.

[3] R. Argazzi, C.A. Bignozzi, T.A. Heimer, F.N. Castellano, G.J. Meyer, *J. Phys. Chem. B*, 1997, **101**, 2591-2597.

[4] R. Argazzi, C.A. Bignozzi, T.A. Heimer, F.N. Castellano, G.J. Meyer, *J. Am. Chem. Soc.*, 1995, **117**, 11815-11816.

[5] N. Hirata, J-J. Lagref, E.J. Palomares, J.R. Durrant, Md. K. Nazeeruddin, M. Grätzel, D. Di Censo, *Chem. Eur. J.*, 2004, **10**, 595-602.

[6] K. Peter, H. Wietasch, B. Peng, M. Thelakkat, *Appl. Phys. A*, 2004, **79**, 65-71.

[7] S.A. Haque, S. Handa, K. Peter, E. Palomares, M. Thelakkat, J.R. Durrant, *Angew. Chemie Int. Ed.*, 2005, **44**, 5740-5744.

[8] C.S. Karthikeyan, K. Peter, H. Wietasch, M. Thelakkat, *Sol. Energy Mater. Sol. Cells*, 2007, **91**, 432-439.

[9] S. Handa, H. Wietasch, M. Thelakkat, J.R. Durrant, S.A. Haque, *Chem. Commun.*, 2007, 1725-1727.

[10] K. Shankar, J. Bandara, M. Paulose, H. Wietasch, O.K. Varghese, G.K. Mor, T.J. LaTempa, M. Thelakkat, C.A. Grimes, *Nano Lett.*, 2008, **8**, 1654-1659.

[11] C.S. Karthikeyan, H. Wietasch, M. Thelakkat, *Adv. Mater.*, 2007, **19**, 1091-1095.

[12] J.N. Clifford, E. Palomares, Md.K. Nazeeruddin, M. Grätzel, J. Nelson, X. Li, N.J. Long, J.R. Durrant, *J. Am. Chem. Soc.*, 2004, **126**, 5225-5233.

[13] M.R. Bryce, *Chem. Soc. Rev.*, 1994, **20**, 355-390.

[14] M. Bendikov, F. Wudl, D.F. Perepichka, *Chem. Rev.*, 2004, **104**, 4891-4945.

[15] M. Mas-Torrent, C. Rovira, *J. Mater. Chem.*, 2006, **16**, 433-436.

[16] T. Enoki, A. Miyazaki, *Chem. Rev.*, 2004, **104**, 5449-5477.

[17] T. Jørgenson, T.K. Hansen, J. Becher, *Chem. Soc. Rev.*, 1994, **23**, 41-51.

[18] J. Becher, Z-T. Li, P. Blanchard, N. Svenstrup, J. Lau, M.B. Nielsen, P. Leriche, *Pure & Appl. Chem.*, 1997, **69**, 465-470.

[19] T. Devic, D. Rondeau, Y. Şahin, E. Levillain, R. Clérac, P. Batail, N. Avarvari, *Dalton Trans.*, 2006, 1331-1337.

[20] Q-Y. Zhu, Y. Liu, Y. Zhang, G-Q. Bian, G-Y. Niu, J. Dai, *Inorg. Chem.*, 2007, **46**, 10065-10070.

[21] N. Martinez Rivera, E.M. Engler, R.R. Schumaker, *Chem. Commun.*, 1979, 184-185.

[22] L.V. Interrante, K.W. Browall, H.R. Hart, I.S. Jacobs, G.D. Watkins, S.H. Wee, *J. Am. Chem. Soc.*, 1975, **97**, 889-890.

[23] T. Nakazono, M. Nakano, H. Tamura, G. Matsubayashi, *J. Mater. Chem.*, 1999, **9**, 2413-2417.

[24] Y. Suga, M. Nakano, H. Tamura, G. Matsubayashi, *Bull. Chem. Soc. Jpn.*, 2004, **77**, 1877-1883.

[25] Y. Ji, R. Zhang, Y-J. Li, J-L. Zuo, X-Z. You, *Inorg. Chem.*, 2007, **46**, 866-873.

[26] S. Campagna, S. Serroni, F. Puntoriero, F. Loiseau, L. De Cola, C.J. Kleverlaan, J. Becher, A.P. Sørenson, P. Hascoat, N. Thorup, *Chem. Eur. J.*, 2002, **8**, 4461-4469.

[27] C. Goze, S-X. Liu, C. Leiggener, L. Sanguinet, E. Levillain, A. Hauser, S. Decurtins, *Tetrahedron*, 2008, **64**, 1345-1350.

[28] C. Jia, S-X. Liu, C. Tanner, C. Leiggener, A. Neels, L. Sanguinet, E. Levillain, S. Leutwyler, A. Hauser, S. Decurtins, *Chem. Eur. J.*, 2007, **13**, 3804-3812.

[29] C. Goze, C. Leiggener, S-X. Liu, L. Sanguinet, E. Levillain, A. Hauser, S. Decurtins, *Chem. Phys. Chem.*, 2007, **8**, 1504-1512.

[30] R.R. Ruminski, B.F. Ermel, M.A. Hiskey, *Inorg. Chim. Acta*, 1986, **119**, 195-201.

[31] K. Natsuaki, M. Nakano, G. Matsubayashi, R. Arakawa, *Inorg. Chim. Acta,* 2000, **299**, 112-117.

[32] N. Svenstrup, K.M. Rasmussen, T.K. Hansen, J. Becher, *Synth.*, 1994, 809-812.

[33] D.L. Lichtenberger, R.L. Johnston, K. Hinkelmann, T. Suzuki, F. Wudl, *J. Am. Chem. Soc.*, 1990, **112**, 3302-3307.

[34] V. Gutmann, *Coord. Chem. Rev.*, 1967, **2**, 239.

[35] P.R. Ashton, V. Balzani, J. Becher, A. Credi, M.C.T. Fyfe, G. Mattersteig, S. Menzer, M.B. Nielsen, F.M. Raymo, J.F. Stoddart, M. Venturi, D.J. Williams, *J. Am. Chem. Soc.*, 1999, **121**, 3951-3957.

[36] K. Kalyanasundaram, *Coord. Chem. Rev.*, 1982, **46**, 159-244.

[37] J. Ferguson, E. Krausz, *J. Phys. Chem.*, 1987, **91**, 3161-3167.

[38] Md.K. Nazeeruddin, K. Kalyanasundaram, *Inorg. Chem.*, 1989, **28**, 4251-4259.

[39] N.H. Damrauer, G. Cerullo, A. Yeh, T.R. Boussie, C.V. Skank, J.K. McCusker, *Science*, 1997, **275**, 54-57.

[40] G. Wolfbauer, A.M. Bond, D.R. MacFarlane, *Inorg. Chem.*, 1999, **38**, 3836-3846.

[41] D.A. Fletcher, R.F. McMeeking, D.J. Parkin, *J. Chem. Inf. Comput. Sci.*, 1996, **36**, 746-749.

[42] I. Montanari, J. Nelson, J.R. Durrant, *J. Phys. Chem. B*, 2002, **106**, 12203-12210.

[43] J.N. Clifford, E. Palomares, Md.K. Nazeeruddin, M. Grätzel, J.R. Durrant, *J. Phys. Chem. C*, 2007, **111**, 6561-6567.

[44] K.B. Simonsen, N. Svenstrup, J. Lau, O. Simonsen, P. Mork, G.J. Kristensen, J. Becher, *Synth.*, 1996, 407-418.

# Chapter 5:

# Cu(*exo*$O_2$-cyclam) Ligand Dyes

## 5.1 Introduction

As outlined and discussed in Chapter 4 the use of a redox active ligand can lead to intramolecular charge transfer and a long-lived charge-separated state in a $TiO_2$/dye system. Another strategy for introducing this electron transfer capability is to have a polynuclear complex, where there is more than one metal centre present in the dye.

A number of examples of this class of dye exist in the literature which link a ruthenium polypyridyl complex to another platinum group metal complex such as Ru (II), Os (II), Re (I) or Rh (III) *via* a bridging ligand.[1,2,3,4,5,6] These systems are often referred to as heterosupramolecular triads when adsorbed on the surface of $TiO_2$ as the semiconductor becomes an active component in the system. A number of problems can arise with these types of sensitisers, for example if a flexible linker, *e.g.* bis-pyridylethane, is used to couple the two complexes it can be hard to control the orientation of the whole dye. This may lead to the resultant dye cation hole being closer to the surface than desired, and hence the long-lived charge-separated state is not achieved. In addition the size of these dyes are much larger than that of a mononuclear complex and can lead to poor pore filling on the $TiO_2$ and therefore low dye coverage, leading to a lower efficiency cell.[7] Despite these issues, efficient charge-separation has been achieved with polynuclear complexes and a long-lived state on the millisecond timescale has been observed for a trinuclear ruthenium complex.[8]

In this chapter the Cu(*exo*$O_2$-cyclam) ligand has been incorporated into a series of ruthenium polypyridyl complexes. This allowed investigation of polynuclear complexes which are smaller than the typical polynuclear systems containing two platinum group metal complexes. In addition ruthenium bipyridyl complexes with O-donor ligands have previously been shown to exhibit extended absorption ranges, as discussed in Section 3.1 of this work.

The ligand chosen for this study has previously been used within the group to investigate polynuclear complexes in the context of magnetic materials.[9,10,11] In these studies the Cu(*exo*$O_2$-cyclam) ligand was found to exhibit electronic communication between metal centres in trinuclear copper, cobalt, nickel, zinc, iron and manganese complexes. Numerous studies have also been carried out by other groups, particularly Tang *et al.*, incorporating this ligand into other heteropolynuclear complexes containing a wide range of first row transition metals and lanthanides, again yielding interesting magnetic properties. [12,13,14,15,16,17,18]

It was hoped that the possible communication between the copper (II) in the ligand and the ruthenium polypyridyl moiety could be exploited to control electron transfer within a DSSC, leading to a decrease in recombination of the injected electron with the oxidised dye, in a similar fashion to that described in Chapter 4. This study is also the first example of this ligand complexed to a metal outside the first row transition metals and lanthanide series, expanding the diversity of this functional ligand. The general formula

of the complexes synthesised is [Ru(4,4'-(R-bpy)$_2$(Cu(*exo*O$_2$-cyclam))][NO$_3$]$_2$, where R = H, $CO_2Et$ and $CO_2H$ (Figure 1).

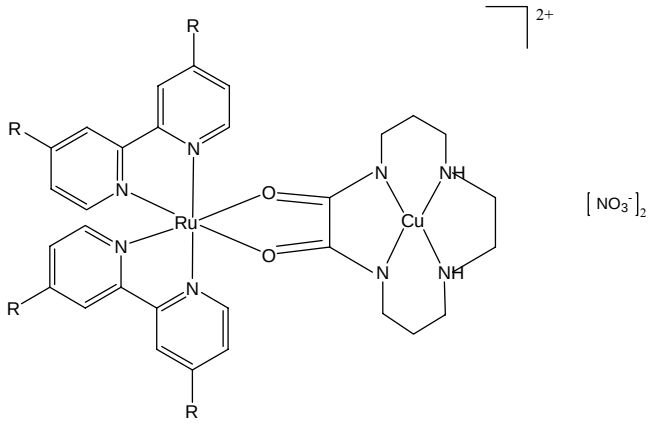


**Figure 1.** Structure of complexes **10** (R=H), **11** (R=$CO_2Et$) and **12** (R=$CO_2H$) synthesised with **L4**.

There are no existing DSSC studies with ruthenium polypyridyl moieties covalently attached to a copper complex. There are however several biological, sensor and electrochromic studies utilising complexes with both a ruthenium and copper moiety where the complexes have been fully characterised, showing evidence of communication between the ruthenium and copper centres. [19,20,21,22,23,24,25,26] These studies are further discussed with reference to the results obtained in this work.

## 5.2 Electrochemistry

In both DMF and DCM, **10** was found to have two oxidations, one reversible and one irreversible (Figure 2). Apart from the second oxidation showing greater definition in

DCM, there does not appear to be any solvent coordination observed in the electrochemistry, with the first oxidation being fully reversible in both solvents.

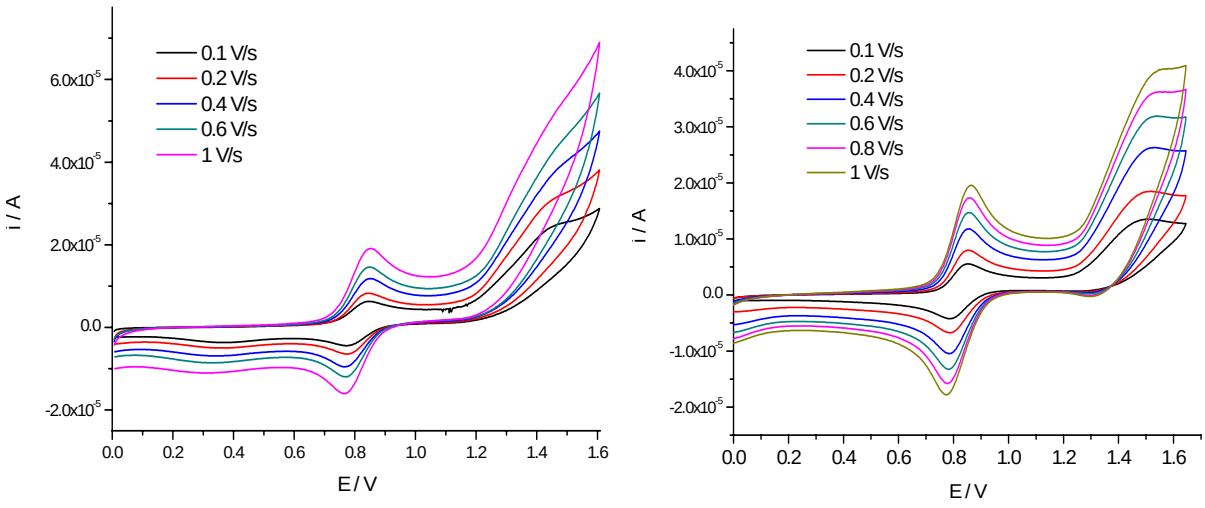


**Figure 2.** Cyclic voltammetry studies of **10** in 0.1 M $TBABF_4$/DMF (left) and 0.3 M $TBABF_4$/DCM (right), both at room temperature.

The electrochemistry of **11** in DMF (Figure 3) was found to exhibit unusual behaviour with respect to the oxidations. At slow scan rates there appear to be three distinct oxidations, with the first and third processes becoming more and less defined respectively with increasing scan rate. Further investigation of the electrochemistry at -40 °C still showed the presence of three oxidations, however there was very little change in the definition of the peaks with varying scan rate at this temperature. The reversibility of the first oxidation is also increased upon reducing the temperature suggesting that the rate constant for the decomposition of the oxidised species becomes smaller as the temperature is lowered. The second and third oxidations remain irreversible at low temperature.

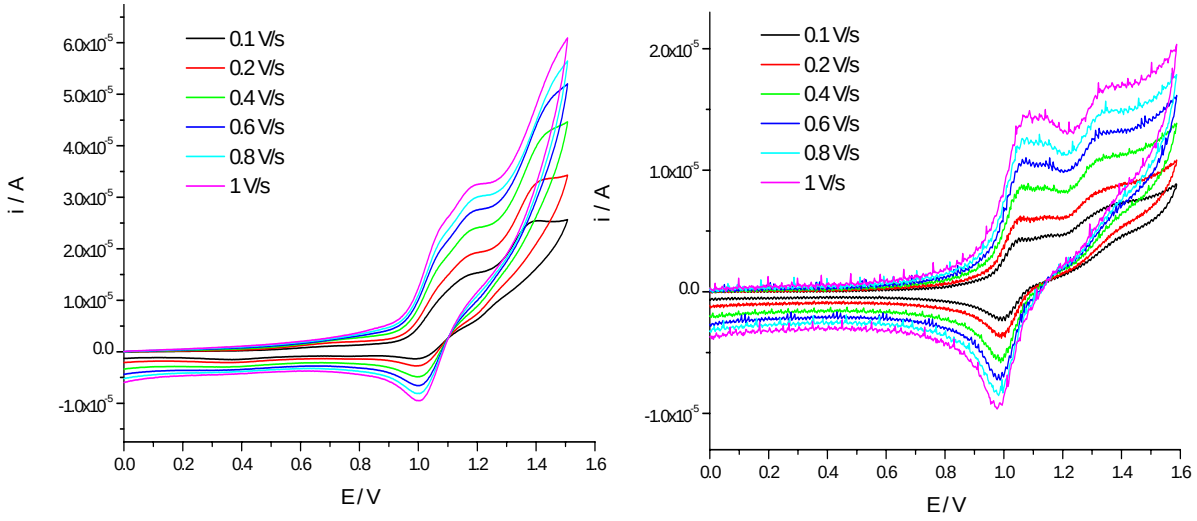


**Figure 3.** CV studies of **11** in 0.1 M $TBABF_4$/DMF at room temperature (left) and -40 °C (right).

To investigate if these phenomena were solvent dependent the electrochemistry of this complex was also studied in DCM (Figure 4). In this non-coordinating solvent the cyclic voltammogram and differential pulse voltammogram showed only two oxidations, the first reversible and the second irreversible. This is very strong evidence for solvent coordination playing a role upon oxidation of this complex. In the strongly coordinating solvent DMF, upon mono-oxidation of the dye a second oxidation very close in potential is observed, which is also seen to be less dominant with increasing reversibility of the first oxidation *i.e.* at lower temperature and faster scan rates. The fact that this second oxidation is not observed in DCM and that the first oxidation is seen to be fully reversible would agree with the solvent coordination theory. In addition the crystal structure of **10** (Section 5.6) has shown that the complex crystallises with two nitrate counter anions in the axial postions above and below the copper. It is reasonable to assume that solvent molecules could occupy these positions if the solvent is highly

coordinating. Further evidence of solvent coordination and investigation of the nature of the two oxidations are discussed in Section 5.4.

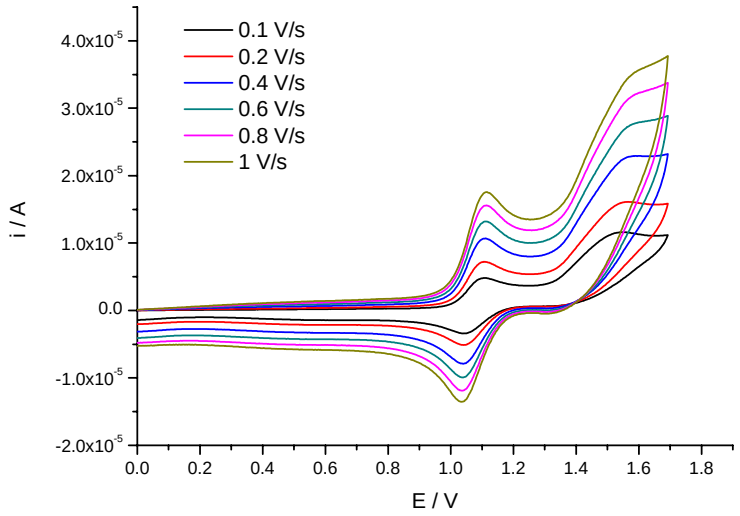


**Figure 4.** Cyclic voltammetry study of **11** in 0.3 M $TBABF_4$/DCM at room temperature.

The reductions seen for **10** and **11** were slightly more positive than for any of the previous dye series (Table 1, Figure 5, Figure 6). Assuming the first reduction to be that of the SOMO, which is presumably copper based, this observation is not unexpected. The second and third reductions for all three complexes in this series are more similar to the reduction potentials of the bipyridyl ligands seen for the other systems in this work. For complex **10** however these reductions shouldn't be attributed to the parent complex as the variation of scan rate shows a shift in the peak potential indicating an irreversible reduction process.

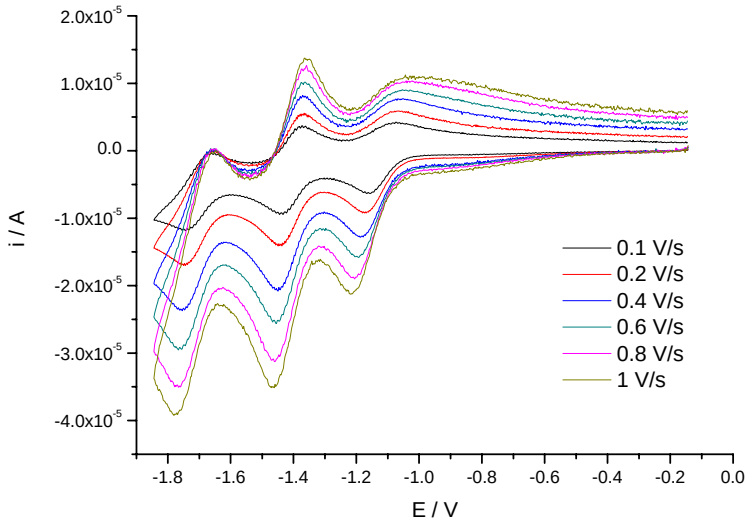


**Figure 5.** Reductive cyclic voltammetry study of **10** in 0.1 M $TBABF_4$/DMF, at room temperature.

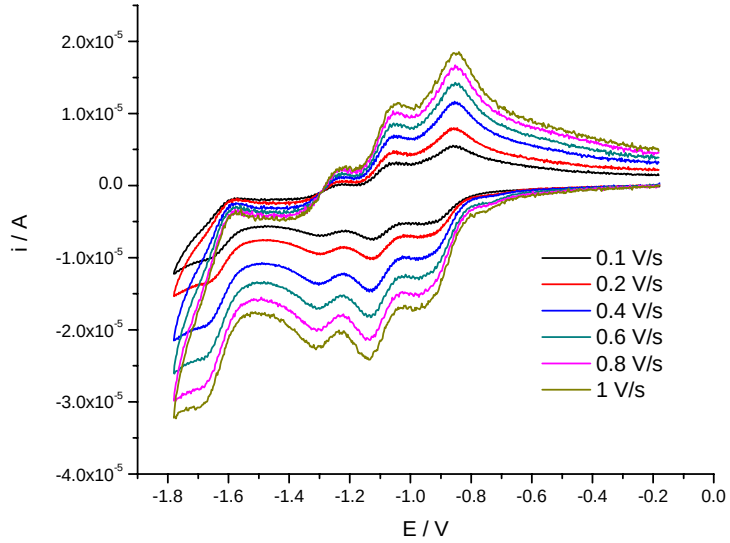


**Figure 6.** Reductive cyclic voltammetry study of **11** in 0.1 M $TBABF_4$/DMF, at room temperature.

The electrochemistry of Cu(*exo*$O_2$-cyclam) has been studied previously and was found to have one reversible oxidation at + 0.17 V (*vs.* Ag/AgCl). However, in a trinuclear complex $[Cu(Cu(exoO_2\text{-cyclam}))_2]^{2+}$ the macrocycle oxidation process was found to

shift to the more positive potential of + 0.5 V (*vs.* Ag/AgCl). [10] The shift from free ligand to complexed was thought to be the result of an increased positive charge density from the central Cu(II) ion. In comparison to the trinuclear copper complex the oxidation of the Cu(*exo*$O_2$-cyclam) in these ruthenium complexes, whether it be the first or second oxidation, has shifted to a more positive potential. This may be a result of having only one Cu(*exo*$O_2$-cyclam) ligand species bound to the central metal rather than two as in the trinuclear system.

| **Complex** | **$E_{1/2}^{ox}$ / V** | | **$E_{1/2}^{red}$ / V** | | | |
|---|---|---|---|---|---|---|
| **L4** | 0.17 [b] | | - | | | |
| **10** | 1.60 [a] | 0.76 | -1.15 [a] | -1.41 | -1.70 [a] | |
| **11** | 1.39 [a] | 1.17 | -0.92 | -1.13 | -1.25 | -1.70 [a] |
| **12** | 1.25 [a] | 1.04 [a] | -0.93 [a] | -1.21 [a] | -1.63 [a] | |

[a] Irreversible

[b] From reference 4 measured in 0.1 M $LiClO_4/CH_3CN$.

**Table 1.** Redox potentials of **L4**, **10**, **11** and **12** carried out in 0.1 M $TBABF_4$/DMF (*vs.* Ag/AgCl) at room temperature.

## 5.3 Absorption Spectroscopy

For all three dyes in this series, two visible region bands and one UV band were observed in DMF (Figure 7, Table 2). The energy of the absorption bands for **12** are

lower, and the molar extinction co-efficients significantly higher than for that of N719.[27] As discussed in Chapter 1, these properties can be advantageous when fabricating higher efficiency DSSCs as less dye will be required to yield comparable light harvesting efficiency, when comparing to N719 for example, and hence thinner cells can be made. These thinner cells can lead to decreased charge carrier recombination particularly in solid-state cells. The lower energy bands suggest that the use of the O-donor groups has resulted in a destabilisation of the Ru $t_{2g}$ orbitals resulting in a smaller HOMO-LUMO transition and an increased absorption range. Further discussion of the character of these bands can be found in Section 5.7: TD-DFT.

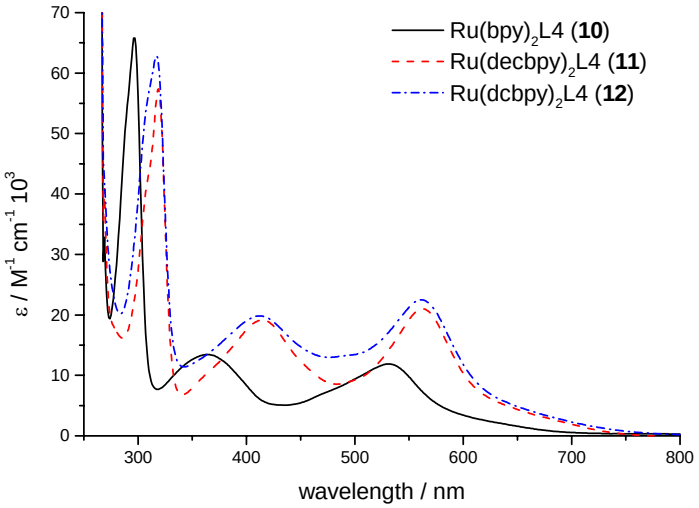


**Figure 7.** Absorption spectra of **10**, **11** and **12** in DMF.

| Complex | $\pi - \pi^*$/nm | MLCT/nm | |
|---|---|---|---|
| **10** | 297 (65.9) | 530 (10.1) | 365 (11.3) |
| **11** | 319 (61.4) | 561 (21.0) | 415 (19.1) |
| **12** | 317 (64.2) | 562 (22.2) | 413 (19.6) |

**Table 2.** Energy of transitions with molar extinction co-efficients in brackets / $M^{-1}cm^{-1}$ $10^3$ for **10**, **11** and **12** in DMF.

### 5.3.1 Emission Studies

Emission studies were carried out in ethanol at room temperature and 77 K for **10**, **11** and **12** (Figure 8, Table 3). No emission was observed at room temperature, even after de-gassing of the solution, however weak emission was observed at 77 K. The excitation and emission spectra for all complexes show a large Stokes shift indicating emission from a $^3$MLCT state. In addition the excitation spectra closely resemble the absorption spectra for each of the complexes, indicating that these transitions are largely MLCT in character, further discussed in Section 5.8.

In comparison to the other dye series investigated in this work the emission intensity for this series is around 100 times smaller, despite the similar solution concentration used across all studies. There are two possibilities for this decrease in emission intensity: firstly there may be a large degree of Cu-ligand character to the HOMO, resulting in the lowest energy excited state which is populated after excitation no longer being an

MLCT, and secondly the emission from the $^3$MLCT may be quenched by intramolecular electron or energy transfer to/from the copper ligand. The nature of the highest occupied molecular orbitals is further discussed in Section 5.8, however the intramolecular electron or energy transfer warrants further discussion at this point.

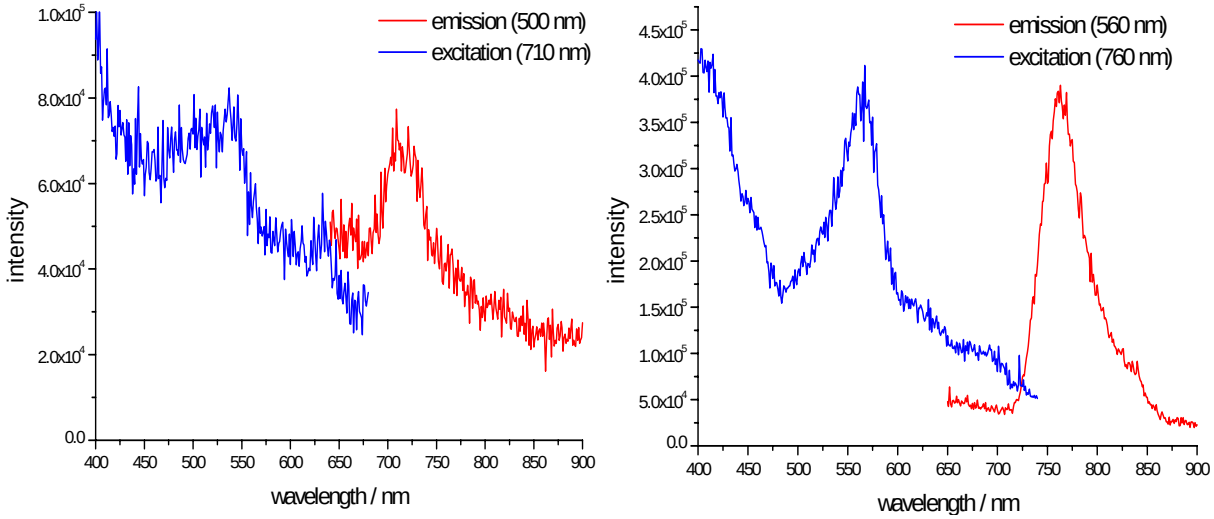


**Figure 8.** Excitation and emission spectra for complexes **10** (left) and **11** (right) at 77 K in ethanol with the corresponding excitation or emission wavelengths shown in brackets.

| Complex | Emission Max. / nm | |
|---|---|---|
| | 293 K | 77 K |
| **10** | - | 710 |
| **11** | - | 760 |
| **12** | - | 740 |

**Table 3.** Emission spectra maxima for complexes **10** – **12** in ethanol at room temperature and 77 K.

As mentioned in the introduction to this chapter, a number of polynuclear systems have been synthesised and characterised that contain a ruthenium polypyridyl moiety covalently attached to a copper system. In a number of these studies the emission of the ruthenium polypyridyl moiety was not preserved upon binding of copper (II), which was attributed to either electron transfer (eT) or energy transfer (ET) to/from the copper (II). In the former case the formation of a Ru(III)-Cu(I) or Ru(I)-Cu(III) transient species could occur. For the systems studied previously this possibility has been ruled out largely due to the Cu(I)/Cu(II) couple being very negative with respect to the Ru(II)/Ru(III) couple. This is likely to be the case for complexes **10** – **12** also, as the Cu(I)/Cu(II) occurs at approximately -1 V (*vs.* Ag/AgCl) compared to a Ru(II)/Ru(III) potential of > 0.7 V. However in contrast to the studies in the literature, the possibility of electron transfer from the Cu(II) to the Ru(II) may potentially occur in the present system due to the much more positive oxidation potential of the Cu(II)/Cu(III) redox couple, and is of course why **L4** was chosen for this particular study.

In general energy transfer can occur *via* two mechanisms: Förster's (a dipole-dipole interaction) or Dexter's (an electron exchange interaction). Dexter excitation transfer is a short range interaction and requires an orbital overlap of the donor and acceptor units,[28] which is shown to be true for complexes **10** – **12** in Section 5.7. Therefore it may be likely that the decreased emission intensity observed for these complexes is a result of energy transfer from the $^3$MLCT excited state to **L4**, possibly *via* a Dexter's energy transfer mechanism or indeed also *via* electron transfer.

This quenching process is unlikely to be a hindrance to the performance of **12** in a DSSC as the strong electronic coupling between the bipyridyl ligands and the $TiO_2$ conduction band leads to very rapid electron injection, on the pico to femtosecond timescale,[29,30] into the conduction band after excitation of an electron to the $^3$MLCT. Therefore the electron injection should be more likely to occur than the energy transfer from the MLCT to the copper excited state, provided that the ET occurs on a timescale longer than picoseconds. Further studies, such as femtosecond flash photolysis, are required to establish the exact mechanism and timescale of the fluorescence quenching in these complexes, this was however beyond the scope of this work.

## 5.4 Spectroelectrochemistry

The presence of two oxidations for these complexes required thorough investigation *via* spectroelectrochemical techniques in order to identify the character of these processes *i.e.* whether they are ruthenium or copper based. These findings could then be used to understand how the dye functions in a DSSC *i.e.* whether a long-lived charge-separated state would be expected.

Electrochemistry studies revealed **10** showed no signs of solvent coordination to the oxidised species and therefore the OTTLE study of this complex was only carried out in 0.1 M $TBABF_4$/DMF. An applied potential of 1 V (*vs.* Ag/AgCl) was used to induce the mono-oxidised species and showed a near complete collapse of the lowest energy CT

band, a partial collapse of the second CT band, a broadening of the bipyridyl intraligand band and finally the growth of a new bipyridyl intraligand band at 31500 $cm^{-1}$ (Figure 9, Table 4). All of these changes indicate that this oxidation is largely ruthenium in character as they are also observed upon oxidation of $Ru(bpy)_2Cl_2$. The di-oxidised species shows only minor changes relative to the mono-oxidised species with the further collapse of the low energy CT band, a small decrease in the intensity of the second CT, and a shift to lower energy of the broadened bipyridyl intraligand band combined with a small growth of the new intraligand band at 31500 $cm^{-1}$. Both studies were shown to be reversible back to the original dicationic spectrum by application of a reductive potential (-0.2 V *vs.* Ag/AgCl). The fact that the mono-oxidised and di-oxidised species have very similar absorption spectra leads to no firm conclusions about the identity of the oxidations. Further investigative work was carried out using *in-situ* EPR (Section 5.5).

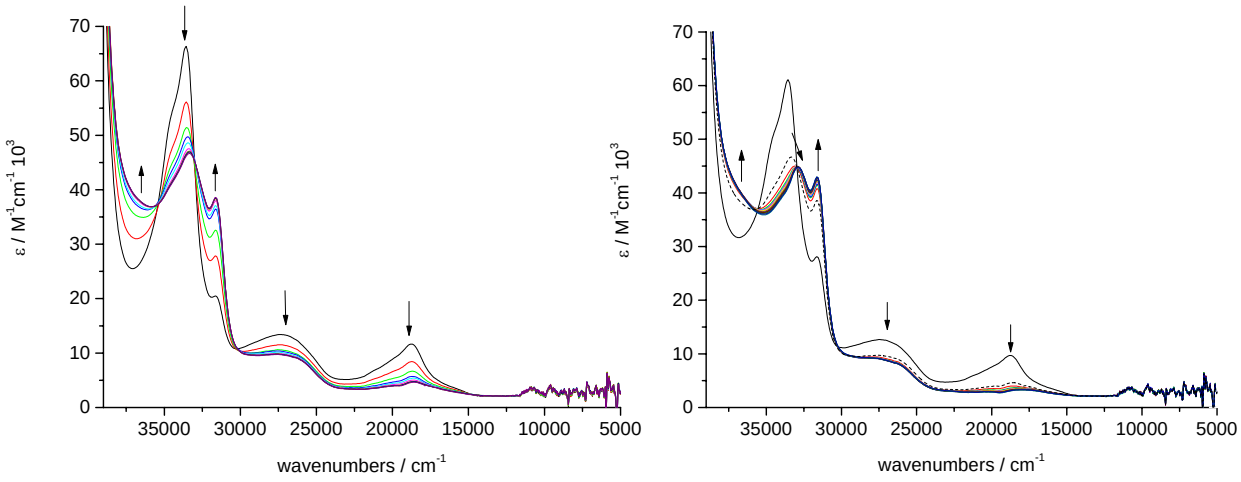


**Figure 9.** Oxidative OTTLE studies of **10** in 0.1 M $TBABF_4$/DMF with an applied potential of + 1 V (left) and + 1.6 V (right) *vs.* Ag/AgCl. The final mono-oxidised spectrum is shown as a dashed blue line in the right hand graph for clarity.

The electrochemical studies of **11** showed that solvent coordination may be an issue upon oxidation and so to investigate this further the OTTLE studies of this complex were carried out in both 0.1 M $TBABF_4$/DMF and 0.3 M $TBABF_4$/DCM.

The mono-oxidation of **11** in DMF showed very similar changes to **10** with the collapse of the CT bands and a broadening of the intraligand band in DMF (Figure 10). The study in DMF was however found to be only partially reversible with the regenerated spectrum being very similar to the original dicationic spectrum, yet slightly shifted to a higher energy and with a lower intensity. This may be indicative of the fact that the solvent coordination is not destructive (as is the case for other dye series studied cf. $Ru(decbpy)_2(NCS)_2$ for example, Chapter 3, Section 3.5) but is instead coordinating in the axial positions above and/or below the copper (II). This species could be envisaged to have a very similar absorption spectrum as was observed in this study.

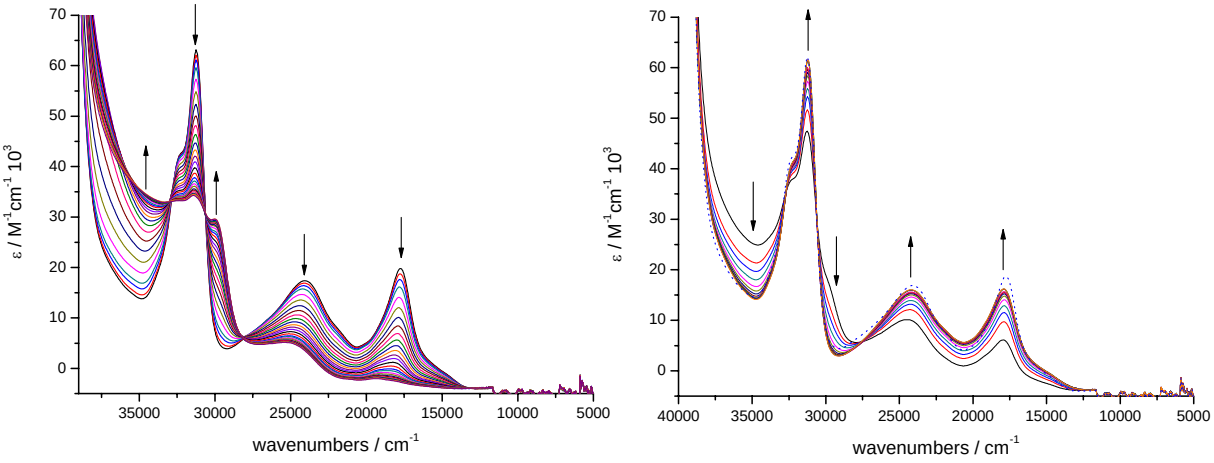


**Figure 10.** Mono-oxidation study of **11** in 0.1 M $TBABF_4$/DMF, with an applied potential of 1.25 V (*vs.* Ag/AgCl) (left) and reversibility study, with an applied potential of -0.2 V (*vs.* Ag/AgCl) (right). Dicationic dye spectrum shown as dashed line in reversibility study.

In order to draw more reliable conclusions about the oxidised species of this complex the OTTLE studies were also carried out in 0.3 M $TBABF_4$/DCM. Mono-oxidation showed the same observations as in the DMF study with the collapse of the CT bands and broadening of the intraligand (Figure 11, Table 4). This study was fully reversible back to the original spectrum, showing no evidence of solvent coordination, as expected from the electrochemistry studies. Di-oxidation showed only minor changes, as was observed for **10**, with the growth of a small band at 27000 $cm^{-1}$ and an increase in the second intraligand band at 30000 $cm^{-1}$. The di-oxidised study was also found to be reversible. Again these studies are not conclusive as to the identity of these oxidation processes and further work has been carried out using *in-situ* EPR.

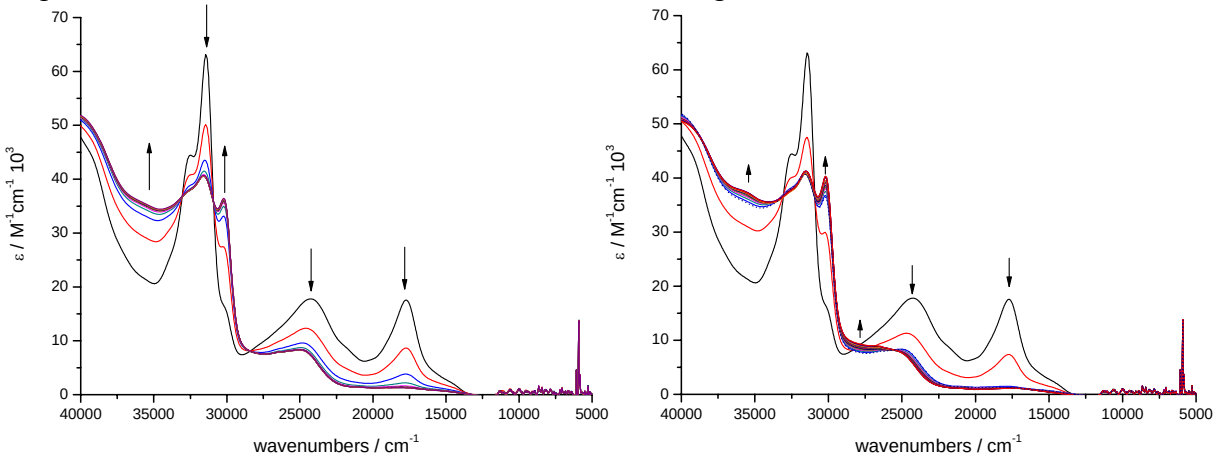


**Figure 11.** OTTLE studies of **11** in 0.3 M $TBABF_4$/DCM showing mono-oxidised, with an applied potential of 1.25 V (*vs.*Ag/AgCl) (left) and di-oxidised species with an applied potential of 1.7 V (*vs.* Ag/AgCl) (right). Mono-oxidised spectrum shown as dashed line in di-oxidised study.

The reductive OTTLE studies of **11** were carried out in 0.1 M $TBABF_4$/DMF (Figure 12, Table 4). The mono-reduction showed a decrease in intensity and slight shift to lower energy of the MLCT bands and a broadening of the bipyridyl intraligand band.

This indicates that the initial reduction is not a bipyridyl based orbital process as it would be for a typical ruthenium bipyridyl complex, but rather is a reduction of the copper (II). This observation also agrees with the reductive electrochemistry study where the first reduction occurred at a less negative potential than would be expected for a bipyridyl ligand and hence was assigned as a copper reduction (Section 5.2). This can also be rationalised in terms of TD-DFT results and this point is further discussed in Section 5.8.

The di-reduced study on the other hand showed typical changes in absorption that would be expected for a bipyridyl based orbital. This includes the decrease in intensity of the band at 31000 $cm^{-1}$ and the growth of bands at 28000, 22000 and 6500 $cm^{-1}$. Both the mono-reduced and di-reduced studies were fully reversible.

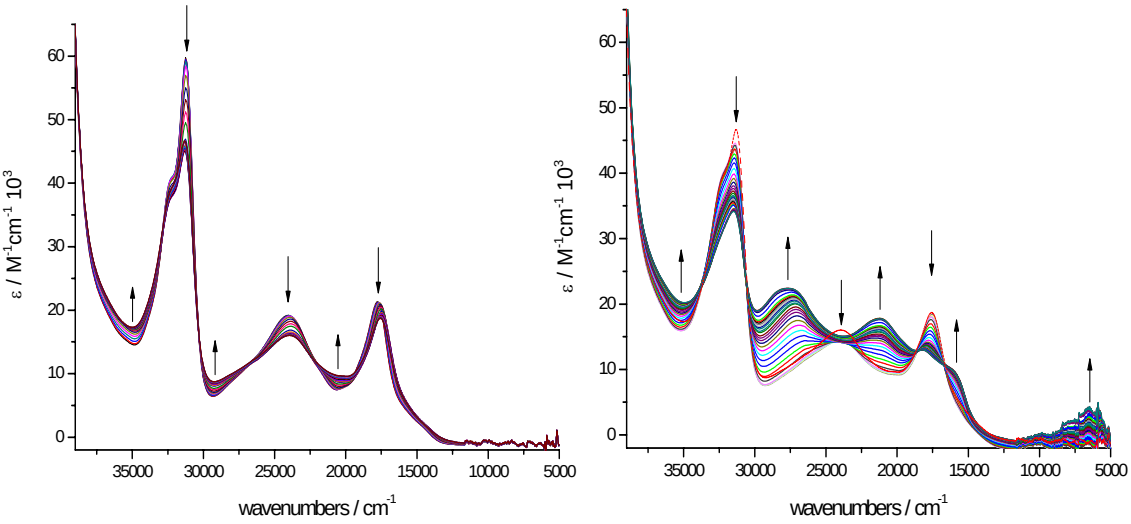


**Figure 12.** Reductive OTTLE studies in 0.1 M $TBABF_4$/DMF of **11** showing mono-reduced (left) and di-reduced (right), with applied potentials of -1 V and -1.2 V (*vs.* Ag/AgCl) respectively. Final mono-reduced spectrum shown as dashed line in right-hand graph.

| Complex | Energy / $cm^{-1}$ ($\varepsilon$ / $M^{-1}cm^{-1}$ $10^3$) |
|---|---|
| [a][Ru(bpy)$_2$(Cu(*exo*O$_2$-cyclam))]$^{3+}$ | 33300 (46.6), 31600 (38.6), 27400 (9.7), 18600 (4.6) |
| [a][Ru(bpy)$_2$(Cu(*exo*O$_2$-cyclam))]$^{4+}$ | 32950 (42.1), 31600 (41.4), 27000 (8.7) |
| [b][Ru(decbpy)$_2$(Cu(*exo*O$_2$-cyclam))]$^{3+}$ | 31600 (40.6), 30200 (36.5), 25000 (8.3), 17800 (1.3) |
| [b][Ru(decbpy)$_2$(Cu(*exo*O$_2$-cyclam))]$^{4+}$ | 31500 (41.3), 30200 (40.3), 27400 (9.1), 25100 (7.8), 17400 (1.1) |
| [a][Ru(decbpy)$_2$(Cu(*exo*O$_2$-cyclam))]$^{1+}$ | 31300 (45.0), 23975 (16.0), 17575 (18.7) |
| [a][Ru(decbpy)$_2$(Cu(*exo*O$_2$-cyclam))] | 31500 (34.1), 27700 (22.4), 21225 (17.8), 16050 (9.8), 6500 (4.2) |

[a] Studied in 0.1 M $TBABF_4$/DMF.

[b] Studied in 0.3 M $TBABF_4$/DCM.

**Table 4.** Summary of energies and molar extinction co-efficients of absorption bands for mono- and di-oxidised **10** and **11** and mono- and di-reduced **11**.

## 5.5 In-situ EPR

Due to the presence of the paramagnetic copper (II) ion in these dyes it was possible to record EPR spectra without first inducing any redox processes. This technique should definitively prove the presence of the SOMO on the copper (II) centre as this ion has a very distinctive EPR signal with a nuclear spin of 3/2.

The room temperature EPR spectrum of **10** in 0.3 M $TBABF_4$/DCM shows four peaks, which are preserved upon cooling to 253 K. The presence of this signal shows the coupling of the unpaired electron in the dye to the copper (II) ligand. The g-factor for this complex was 2.13, with a hyperfine splitting value of 125 G. Inducing the first oxidation results in the loss of this signal and produces no observable EPR signal. The second oxidation also results in no observable EPR active species formed. Both studies were reversible, with the re-growth of the copper (II) signal upon re-reduction.

The room temperature EPR spectrum of **11** in 0.3 M $TBABF_4$/DCM also shows a clear copper (II) signal, and again this is preserved upon cooling to 253 K. The g-factor for this complex was 2.09 and a hyperfine splitting value of 75 G. The fact that this value is lower than that seen for **10** suggests the SOMO is more declocalised away from the copper in this case. Both the mono-oxidised and di-oxidised species show no clear EPR signal, however the copper (II) signal is once again regenerated upon re-reduction.

The only conclusion that can be drawn from this series of experiments is that the unpaired electron is coupled to the copper (II) on the macrocycle ligand. The fact that this signal disappears on oxidation may be a result of either copper or ruthenium oxidation. Removal of an electron from a copper based orbital would obviously remove the coupling to copper (II). However, the signal may equally be lost upon oxidation of the ruthenium, as strong exchange coupling could occur between the two metal centres which would lead to rapid relaxation and no signal being observed. Further discussion of this point can be found in Section 5.8. The lack of an observable ruthenium EPR

signal, as previously discussed in Chapter 4, leaves the nature of the oxidations ambiguous at this stage.

## 5.6 X-ray Diffraction (XRD)

Single crystals of **10** were grown, by Russell Johnstone during his undergraduate final year project, using vapour diffusion of methanol into a saturated solution of **10** in DMF. The complex crystallised in the space group C2/c with four molecules per unit cell (Figure 13, Table 5). The two nitrate counter anions were shown to be weakly co-ordinated to the axial positions of the copper (II), at a distance of 2.646 Å, exhibiting typical Jahn-Teller distorted six-coordinate geometry around the copper (II).

The packing diagram shows the formation of centrosymmetric dimers interacting through π-stacking of one of the bipyridyl ligands in each complex, with an interplanar separation of 3.19 Å. The copper centres on adjacent molecules were found to be shielded from one another by the organic ligands, counterions and solvent molecules resulting in the shortest intermolecular Cu…Cu distance being 7.610 Å. Further details of bond lengths and angles can be found in Table 6.

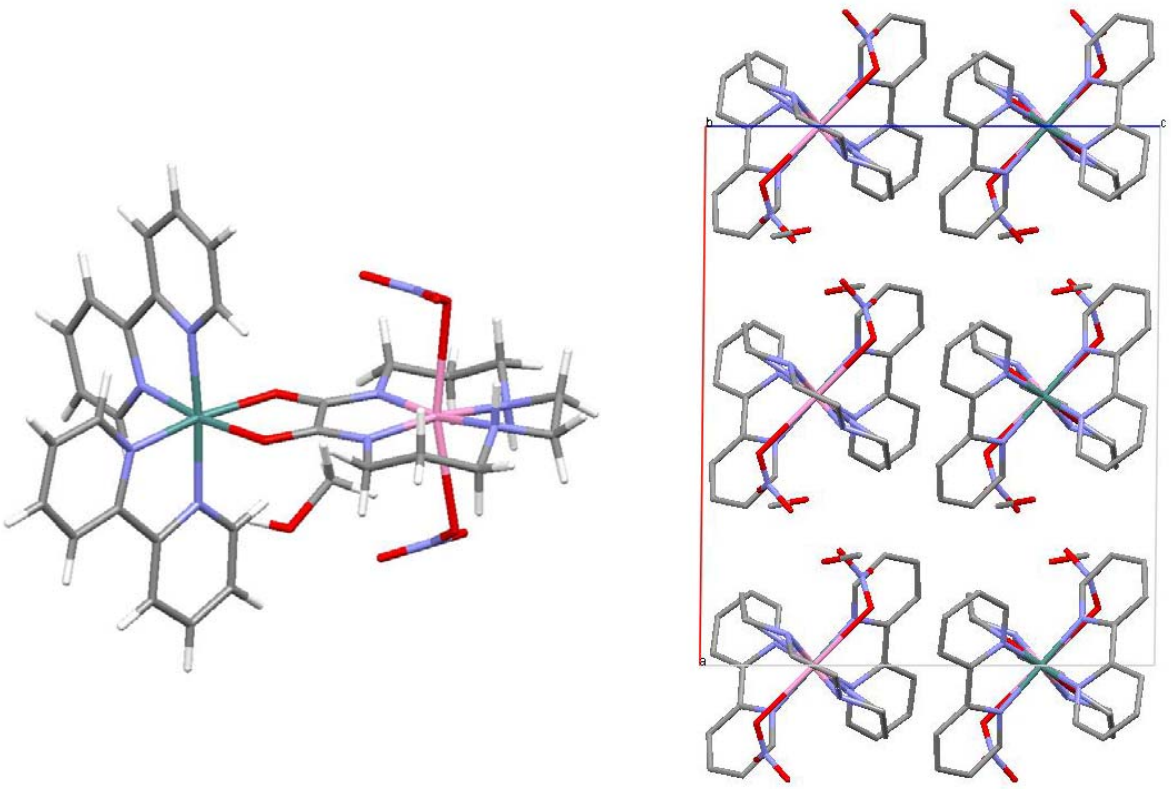

**Figure 13.** X-ray crystal structure of **10** showing the axially co-ordinated nitrate ions above and below the copper (II) ion (left). Packing diagram (right) as viewed along the b-axis, in this case solvent and hydrogen atoms have been omitted for clarity. Carbon atoms are shown in grey, nitrogen in blue, oxygen in red, hydrogen in white, copper in pink and ruthenium in teal.

As previously mentioned, this structure is the first example of **L4** being used as a ligand for a second-row transition metal, despite numerous examples of first-row and lanthanide complexes, and clearly shows the potential of **L4** as a functional ligand for a wider range of metals. Ruthenium complexes incorporating chelating oxygen-donor ligands are also somewhat rare with only seven examples present in the Cambridge Structural Database prior to this work.[31]

| Chemical Formula | $C_{32}H_{42}N_{10}O_{10}CuRu$ |
|---|---|
| $M_r$ | 891.36 |
| T / K | 150 |
| Lattice type | Monoclinic |
| Space group | C2/c |
| a / Å | 17.399(5) |
| b / Å | 13.501(4) |
| c / Å | 14.678(5) |
| V / $Å^3$ | 3448.0(18) |
| $\beta$ / ° | 90.611(15) |
| Z | 4 |
| λ | 0.71073 |
| Reflections collected | 11017 |
| Unique | 3127 |
| $R_1$ ($I > 2\sigma I$) | 0.0873 |
| $wR_2$ | 0.1016 |
| GoF | 1.0608 |

**Table 5.** Crystallographic data for **10**.

## 5.7 DFT Calculations

The details for the computational work carried out on **11** can be found in Chapter 2, Section 2.4.1. Whilst a crystal structure of **11** was not obtained, the calculated geometry

could be compared to the bond lengths and angles obtained for the free ligand (**L4**) and complex **10** crystal structures. A comparison of selected parameters (Table 6, Figure 15) shows that the optimised structure, using a DMF polarisable continuum model, has a very good resemblance to that seen in these crystal structures, with most bond lengths and angles in good agreement. The main difference between the two ruthenium complex structures is the angle around the copper, with a more asymmetric nature in the calculated structure relative to the XRD structure (Figure 14). This may be due to the presence of the nitrate anions in the XRD structure, and the fact that the calculation is attempting to compensate for the vacant coordination sites by making the centre less planar.

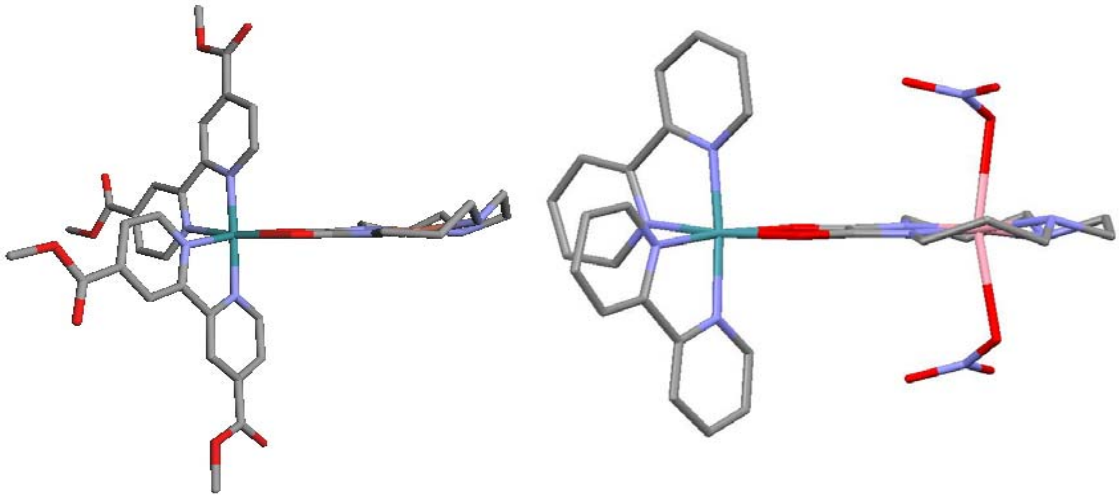

**Figure 14.** DFT calculated structure (left) and XRD structure (right) showing difference in angle around the copper (II) centre between the two systems. Hydrogen atoms and solvent molecules have been omitted for clarity.

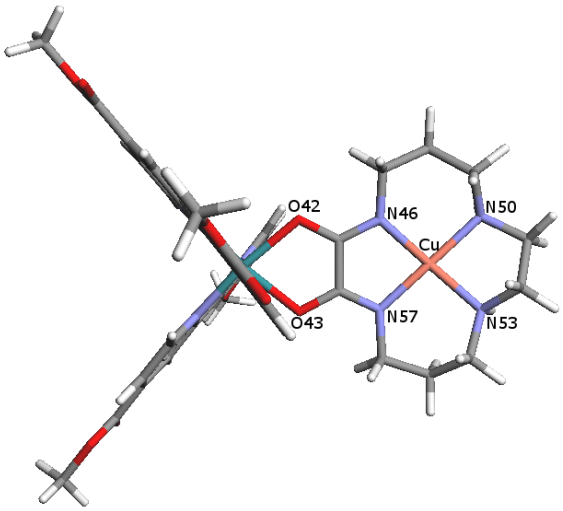


**Figure 15.** Selected atom labels for calculated optimised geometry of **11** in DMF.

| **Parameter** | **11** | **L4** [a] | **10** |
|---|---|---|---|
| Cu-N(46) | 1.967 | 1.9410(16) | 1.914 |
| Cu-N(57) | 1.962 | 1.9544(16) | 1.914 |
| Cu-N(50) | 2.029 | 2.0082(16) | 1.945 |
| Cu-N(53) | 1.999 | 2.0300(17) | 1.945 |
| Cu…Ru | 5.440 | - | 5.291 |
| Ru-O(42) | 2.133 | - | 2.082(5) |
| Ru-O(43) | 2.135 | - | 2.083 |
| N(46)-Cu-N(57) | 84.76 | 83.87(7) | 84.61 |
| N(46)-Cu-N(53) | 168.38 | 177.15(7) | 171.26 |
| N(57)-Cu-N(53) | 96.02 | 96.06(7) | 95.84 |
| N(46)-Cu-N(50) | 95.50 | 94.78(7) | 95.84 |
| N(57)-Cu-N(50) | 176.85 | 161.49(8) | 171.26 |
| N(53)-Cu-N(50) | 84.36 | 86.18(7) | 85.05 |

[a] Values obtained from reference 13.

**Table 6.** Comparison of selected parameters from calculated optimised geometry of **11** with crystal structures of **L4** and **10**. Bond lengths are reported in Å and angles in degrees.

Due to the paramagnetic nature of this system an unrestricted calculation was performed, meaning that the alpha and beta electrons are treated separately generating two sets of one electron orbitals. To verify the absence of spin contamination the spin-squared operator was confirmed to be within 10 % of 0.75. The unpaired electron location was deduced by comparing the energies of the two sets of orbitals and also by calculating a spin density, which shows the difference between the alpha and beta densities (Figure 16). The lone electron was found to be located on the copper centre, as shown from the positive density (blue shaded area) in the spin difference map. The alpha HOMO orbital was determined to be the SOMO, as the population analysis of this orbital also matches that of the beta LUMO orbital.

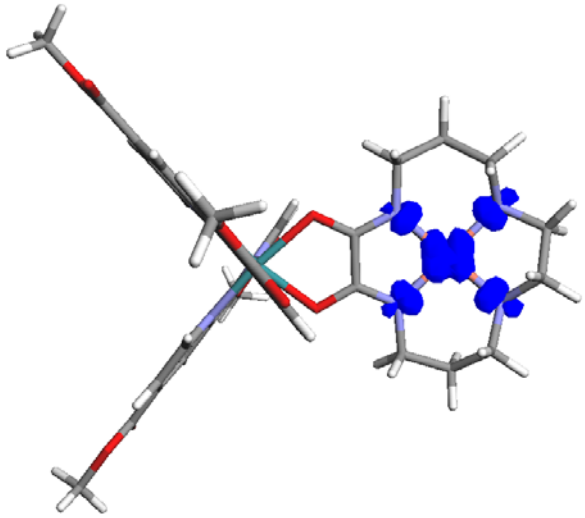

**Figure 16.** Spin difference isosurface of **11**, showing the difference between the alpha and beta densities.

The energies of the HOMO (which is more accurately described as the SOMO) and HOMO-1 orbitals were calculated to be very similar, with only a 0.07 eV difference.

The SOMO was found to be largely based on the ruthenium centre with a small degree of Cu(*exo*$O_2$-cyclam) character (Figure 17, Table 7), whereas the HOMO-1 showed significant delocalisation of the orbital over the Cu(*exo*$O_2$-cyclam). From the *in-situ* EPR studies it was expected that the location of the unpaired electron would be at least partially on the copper (II). This appears to have been recreated by these calculations with a small copper ligand contribution to the SOMO, however a much larger copper contribution was calculated for the HOMO-1. These calculations may also indicate the possibility that upon oxidation the dye cation hole may be significantly delocalised over the macrocycle ligand and hence will be further from the $TiO_2$ surface.

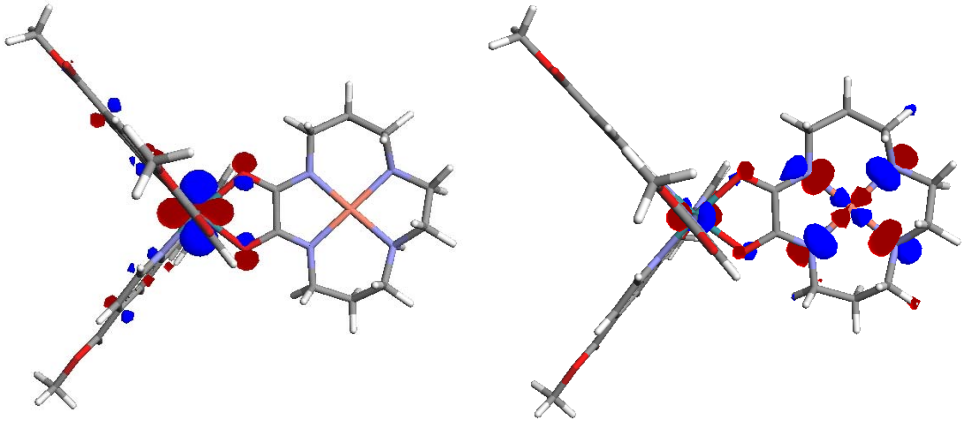

**Figure 17.** Calculated alpha HOMO (left) and alpha HOMO-1 (right) of **11** using a DMF polarisable continuum model.

| MO | α-Energy / eV [a] | % Ru | % decbpy | % Cu(*exo*$O_2$-cyclam) |
|---|---|---|---|---|
| LUMO | -3.198 (-3.201) | 7.09 | 91.79 | 1.1 |
| SOMO | -6.068 | 68.40 | 18.59 | 13.02 |
| HOMO-1 | -6.139 (-6.064) | 20.94 | 6.9 | 72.17 |
| HOMO-2 | -6.261 (-6.216) | 57.03 | 16.24 | 26.73 |
| HOMO-3 | -6.27 (-6.247) | 47.04 | 12.52 | 40.43 |

[a] β-energy shown in brackets

**Table 7.** Energies and percentage contributions of Ru, decbpy and Cu(*exo*$O_2$-cyclam) for selected alpha electron molecular orbitals.

## 5.8 TD-DFT

The calculated absorption spectrum of **11** was obtained *via* TD-DFT using the optimised geometry in a DMF polarisable continuum model, with 110 singlet transitions calculated in order to simulate the full spectrum. The Gaussian convolution of the calculated transitions shows two absorption bands at 419 and 503 nm (Figure 18, Table 8). The character of the low energy band was found to consist mostly of HOMO-2 to LUMO excitation. This transition is a mixed ruthenium/Cu(*exo*$O_2$-cyclam) to bipyridyl charge transfer. The other main contributor to this band is a LLCT from the Cu(*exo*$O_2$-cyclam) to the bipyridyl ligand from the HOMO-1 to LUMO+1 orbital.

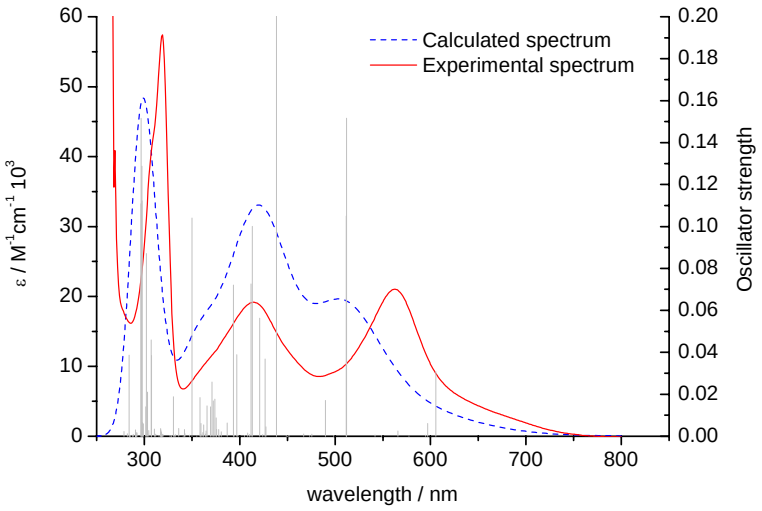


**Figure 18.** Gaussian convolution of calculated transitions (blue dashed line), compared to experimental spectrum (red line), for **11** in DMF, both left axis. The calculated transitions are also shown relative to the oscillator strength (grey columns), right axis.

The second band at 419 nm was shown to be largely MLCT in character with a SOMO to LUMO+2 transition. Transitions from the SOMO to LUMO were calculated to be at 688 and 605 nm, *i.e.* of lower energy than the observed bands, however the transitions also have small oscillator strengths (less than 0.0001), hence the fact that they do not contribute to the calculated spectrum.

| Excited state | Energy (nm) Calculated | Observed | *f* | Character |
|---|---|---|---|---|
| **12** | 512 | 561 | 0.152 | HOMO-2 to LUMO (67%) **MLCT**<br>HOMO-1 to LUMO+1 (43%) **LLCT** (Cu-bpy) |
| **24** | 439 | 415 | 0.207 | HOMO to LUMO+2 (84%) **MLCT** |
| **95** | 297 | 319 | 0.152 | HOMO-7 to LUMO (22%) **intraligand** (bpy)<br>HOMO-7 to LUMO+1 (27%) **intraligand** (bpy)<br>HOMO-4 to LUMO+3 (29%) **LLCT**<br>(Cu-bpy) |

**Table 8.** Summary of selected calculated excited state transitions, energies and character for **11** in DMF, with oscillator strength greater than 0.1.

These calculations certainly do not solve the debate as to whether the first or second oxidation is copper in origin, however if they are indeed an accurate picture of the MOs of this system then they do explain why the spectroelectrochemical studies were not conclusive. With the lowest energy absorption band calculated to have a mixed origin, showing significant MLCT and LLCT character, the oxidation of either the copper or the ruthenium would result in the collapse of this band. In addition the oxidation of the ruthenium may result in rapid intramolecular charge transfer from the copper (II) due to the fact that the SOMO and HOMO-1 are very close in energy. This would result in the loss of the copper (II) signal in the *in-situ* EPR study. Further to this, the fact that there is such a large contribution of the copper (II) to the highest occupied orbitals may be the

reason for the observed low emission intensity for this dye series. This may be cause by rapid intramolecular charge-transfer quenching the emission from the MLCT state or alternatively this may be due to the significant LLCT character resulting in non-radiative decay pathways.

## 5.9 Solar Cell Measurements

A 0.5 mM methanol dye bath was used to adsorb **12** onto the $TiO_2$ film. A deeply coloured maroon film was obtained and the absorption spectrum is very similar to that seen in solution with a peak at 550 nm (Figure 19). There is also a very gradual increase in absorption from 800 nm, showing a significant increase in absorption range relative to N719.

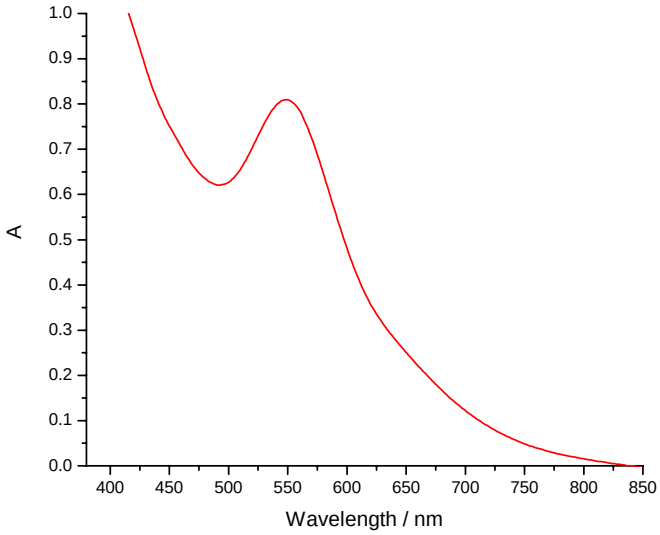


**Figure 19.** Absorption spectrum of **12** adsorbed on $TiO_2$ film.

### 5.9.1 IPCE

IPCE curves for this system show a clear correlation to the absorption spectrum of the dye in solution with peaks seen at 545 nm and 400 nm of 13.7% and 14.2% respectively, for the 1 $cm^2$ active area cell containing the default electrolyte (Figure 20). This result was somewhat lower than expected as the sensitised $TiO_2$ films were very deeply coloured. Dye desorption studies were carried out, after the solar cell measurements were completed, by soaking the films in 0.1 M KOH allowing a quantitative assessment of the concentration of adsorbed dye on the film using absorption spectroscopy. These showed the expected high concentration of dye on the surface and no evidence for poor pore filling which may be expected with the larger dye systems. Therefore the low IPCE results must be the result of another issue, further discussed below.

Attempts were therefore made to increase the efficiency of the devices sensitised with **12**. Possible causes of low efficiency were thought to be: i) the wrong orientation of the dye on the surface *i.e.* the dye lying flat on the $TiO_2$ meaning the dye cation hole would be closer than desired, ii) dye aggregation or iii) that the bipyridyl based unoccupied orbital is not at a sufficiently high energy in order to inject into the conduction band of the $TiO_2$. These problems were briefly investigated by variation of cell parameters, dye bath concentration and electrolyte additives (Figure 20). The variation in conditions are summarised in Table 9. Due to time restrictions the IPCE curves for some cells were only measured over a short wavelength.

| Cell | Dye bath concentration / mM | Anion | Electrolyte [a] | Cell Area / $cm^2$ | $TiO_2$ treatment |
|---|---|---|---|---|---|
| **A** | 0.5 | Nitrate | 1 | 1 | - |
| **B** | 0.05 | Nitrate | 1 | 1 | - |
| **C** | 0.5 | Nitrate | 2 | 1 | - |
| **D** | 0.5 | Nitrate | 1 | 0.3 | $TiCl_4$, blocking layer |
| **E** | 0.5 | $BPh_4$ | 1 | 1 | - |
| **F** | 0.5 | Acetate | 1 | 1 | - |

[a] Electrolyte 1 constituents: 0.6 M 1-methyl-3-propylimidazolium iodide (PMII), 0.03 M $I_2$, 0.1 M guanidinium thiocyanate, 0.5 M tert-butyl pyridine (TBP) in acetonitrile/valeronitrile; Electrolyte 2 constituents: 0.6 M LiI, 0.03 M $I_2$.

**Table 9**. Summary of variation in parameters for DSSCs sensitised with **12**.

Cell B, sensitised using a dilute dye bath, resulted in a film which was less highly coloured with the resulting IPCE being significantly lower with a peak at 2.95%. Cell C, containing the simplified electrolyte, was found to have a slightly increased IPCE at 560 nm of 15.48%. The reduction in the active area size to 0.3 $cm^2$ plus the addition of a compact $TiO_2$ blocking layer and $TiCl_4$ treatment, cell D, resulted in a dramatic improvement, showing a maximum of 31 % (further details on cell optimisation conditions can be found in Chapter 3, Section 3.7).

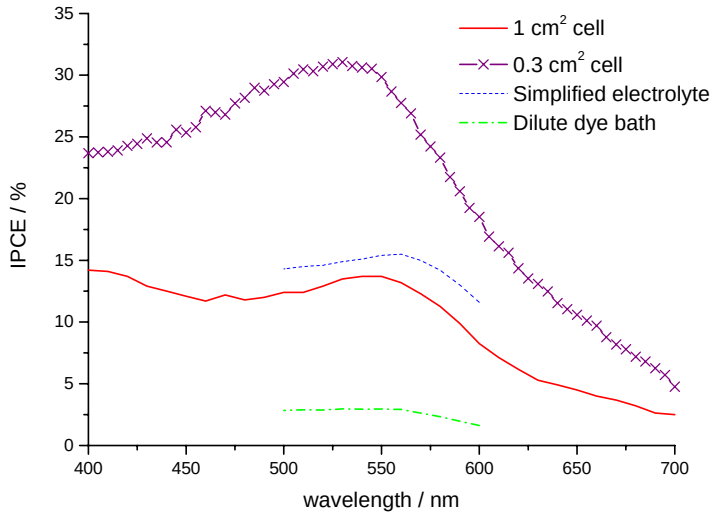


**Figure 20.** IPCE curves for DSSCs sensitised with **12**.

### 5.9.2 I-V Measurements

The current-voltage curves for each cell correlate well to the trend seen in the IPCE study with cell D having the highest overall efficiency of 2.55 % (Figure 21, Table 10). It should be noted however that under the same conditions a 0.3 $cm^2$ cell sensitised with N719 gave an efficiency of 6.4 %. The short-circuit current was seen to increase dramatically for cell C relative to cell A, upon removing the TBP and guanidinium thiocyanate from the electrolyte (Figure 21). This increase may indicate that a mismatch between the bipyridyl based unoccupied orbital of the dye and the conduction band of the $TiO_2$ was a contributing factor to the low injection efficiency in this case. It is thought that the TBP and guanidinium thiocyanate additives reduce the dark current by

co-adsorption to the surface of the $TiO_2$, resulting in effective screening between the $TiO_2$ and the electrolyte.[32] This adsorption is also thought to cause a negative-shift of the conduction band edge, which in turn increases the open circuit voltage and short-circuit current for cells sensitised with N719.[33,34] However if the energy of the bipyridyl unoccupied orbital is not sufficient for injection, then by removing the additives the conduction band energy may drop down to a level whereby injection is more efficient, hence the increase in photocurrent. The open circuit voltage for cell C was also seen to decrease dramatically from 560 mV, for cell A, to 300 mV. This is likely to be due to the resultant decrease in energy difference between the Fermi level of the $TiO_2$ and the redox electrolyte, which defines this parameter, rather than a result of any effect from the dye. Ideally the electrolyte would subsequently be optimised for this system to maximise the overall efficiency of the cell but due to time restrictions this was not possible. The dilute dye bath cell was seen to be the least efficient cell due to the low short-circuit current measured. This is likely a result of the decreased concentration of dye present on the surface of the $TiO_2$.

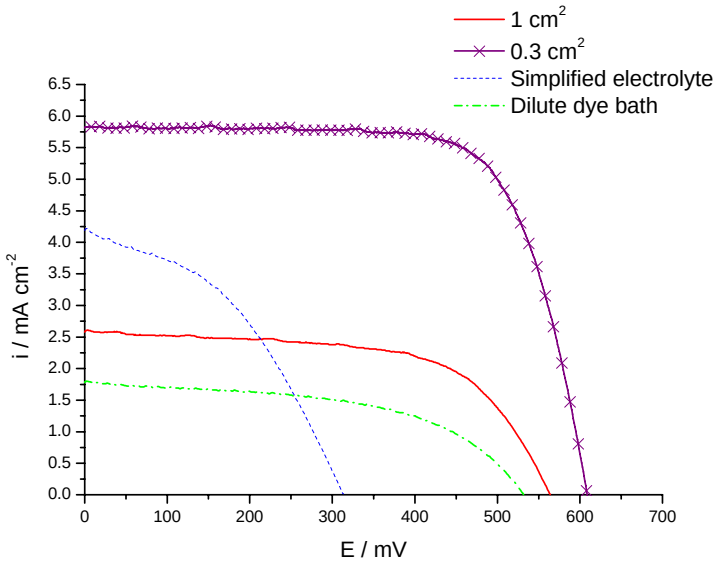


**Figure 21.** AM 1.5 (1000 $Wm^{-2}$) IV characteristics for DSSCs sensitised with **12**, under varying conditions.

Investigation of the incorrect dye orientation, *i.e.* the dye lying flat on the surface of the $TiO_2$ with the dye cation hole in close proximity (rather than at right angles with the hole further away) was attempted by addition of strongly coordinating anions such as acetate to a dye bath containing the tetraphenylborate salt. It was important to use the non-coordinating tetraphenylborate salt (rather than the nitrate salt of **12**) to ensure that this anion would be displaced upon addition of a more coordinating anion to the dye bath. These studies however did not prove fruitful with cells made with both the tetraphenylborate and acetate salts yielding very poor photocurrents and hence low efficiencies (Figure 22). It is possible that the failure of the tetraphenylborate anions to cancel out the dicationic charge of the dye results in this poor cell performance, whereas with the nitrate salt these anions coordinate strongly and this is not the case. The acetate

salt however was shown to have a significantly decreased dye concentration (Figure 22), which would result in the observed lower photocurrent. This may be due to the adsorption of acetate to the $TiO_2$ surface in preference to the dye. These studies may also indicate that the nitrate anion is important for the function of this dye in a DSSC.

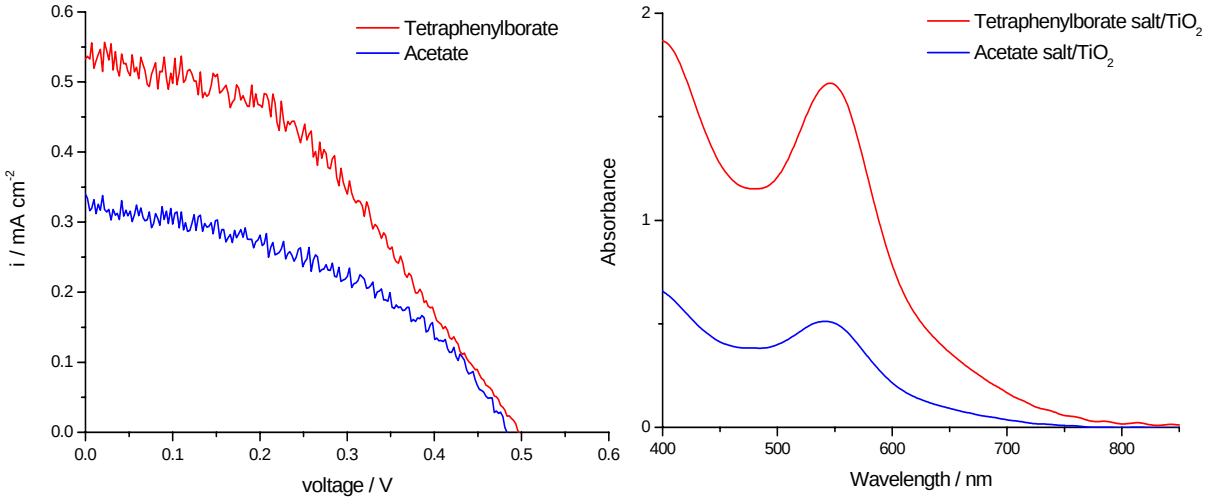


**Figure 22.** IV curves of DSSCs (left) and absorption spectra (right) of $TiO_2$ films sensitised with tetraphenylborate and acetate salts of **12**.

Finally, despite the high molar extinction co-efficients and possible increased charge separation with **12**, the IPCE and global efficiencies of DSSCs sensitised with this dye may ultimately be limited by the fluorescence quenching caused by ET or eT from the $Ru(dcbpy)_2$ moiety to the Cu(II), as discussed in Section 5.3.1. Although this theory is still unproven until the timescale of this ET has been fully investigated.

| Cell | $V_{oc}$ (mV) | $I_{sc}$ (mA $cm^{-2}$) | ff | η (%) |
|---|---|---|---|---|
| **A** | 564 | 2.58 | 0.61 | 0.89 |
| **B** | 532 | 1.78 | 0.53 | 0.50 |
| **C** | 314 | 4.19 | 0.42 | 0.55 |
| **D** | 608 | 5.84 | 0.72 | 2.55 |
| **E** | 496 | 0.54 | 0.41 | 0.11 |
| **F** | 483 | 0.33 | 0.42 | 0.07 |
| **N719** | 637 | 5.37 | 0.62 | 2.12 |

**Table 10.** IPCE maxima, short-circuit current, open-circuit voltage, fill factor and overall AM 1.5 one-sun (1000 $Wm^{-2}$) efficiency of DSSCs sensitised with **12** and N719.

## 5.10 Transient Absorption Spectroscopy

Through measuring the time it takes the injected electron in the conduction band to recombine with the oxidised dye, the location of the dye cation hole and hence whether the copper (II) is playing the intended role in the system can be studied further. Due to the small magnitude of the conduction band electron signal (at 1000 nm) with this dye, and the fact that there is no clear dye cation absorption band, as shown in the OTTLE studies, the bleach signal *i.e.* the decrease in absorption of the ground state absorption spectrum, was monitored (Figure 23).

The study carried out with the propylene carbonate (PC) only present was used to investigate the recombination dynamics in the system and was found to have a recombination lifetime of 772 μs. However, with the addition of the $LiClO_4$ this decreased to a 95 μs lifetime. The purpose of the $LiClO_4$ was to try to increase the electron injection into the conduction band to enable a study of the conduction band electrons to be made, and whilst the signal at 1000 nm did not significantly increase, the resulting small increase in electrons in the conduction band can result in fewer empty trap sites, leading to electrons recombining with the oxidised dye on a shorter timescale. The regeneration dynamics study with the $LiI/I_2$ electrolyte showed the expected faster decay with a half-life of 20 μs showing that the dye is being regenerated by the redox electrolyte as desired.

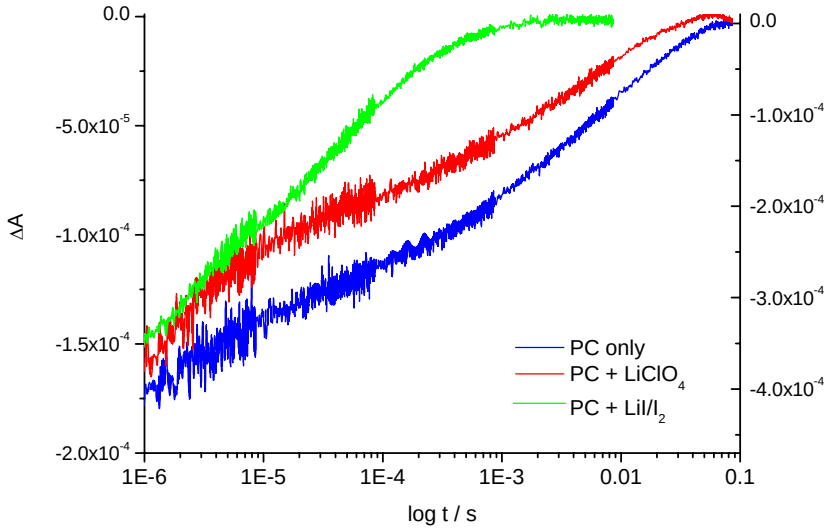


**Figure 23.** Transient decay traces for **12**/$TiO_2$ film with propylene carbonate (PC) only electrolyte, PC + $LiClO_4$ (both left axis) and PC + $LiI/I_2$ (right axis). Excitation wavelength was set to 500 nm and probe at 600 nm.

The absorption spectrum of the sensitised film was recorded after each addition of new electrolyte and also after the TAS study was completed (Figure 24). There is no change in absorbance and peak position (530 nm) with both the propylene carbonate and $LiClO_4$ electrolytes, even after irradiation. However, upon addition of the $LiI/I_2$ containing electrolyte a clear red-shift of the peak occurs and continues to occur after irradiation. The spectrum recorded the after 24 hours showed a further shift of the peak to the red, with a value of 555 nm. This change in absorption of the dye would also result in the significant increase in magnitude of the TAS signal (right axis, Figure 23). The reason for the increase in signal is due to the difference between the neutral and oxidised dye spectrum becoming larger. There should however be no change in the dynamics and therefore the studies in different electrolytes can still be compared with confidence.

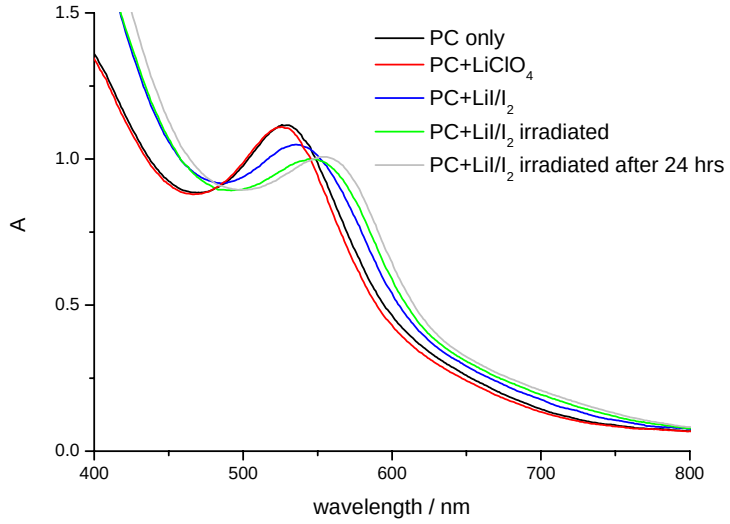


**Figure 24.** Absorbance spectra of **12** sensitised $TiO_2$ films covered with propylene carbonate electrolyte containing no additives, $LiClO_4$ and $LiI/I_2$ before and after irradiation.

## 5.11 Stability Studies

The reason for the change in the absorption band is of more concern. There is the possibility that there is some sort of ion exchange occurring where the nitrates coordinated to the copper (II) are displaced by LiI, $I_2$ or $I_3^-$ resulting in the absorption band shift. Another issue may be the loss of the copper (II) ligand to the electrolyte. If either of these is the case then the long-term stability of a DSSC sensitised with **12** will be severely affected. However, there is a possibility that this problem may be avoided through the use of solid-state electrolytes, which do not contain iodide.

Solution absorption studies of **11** in DMF with sequential addition of the LiI, $I_2$ and LiI/$I_2$ were attempted but showed no correlation to the changes observed in the TAS study. This may be due to the fact that the anion coordination/copper (II) ligand loss involves the excited state or oxidised form of the dye.

Under prolonged irradiation (AM 1.5 light of 1000 W/$m^2$), cells sensitised with **12** were also found to increase in efficiency with time (Figure 25). As well as this the absorption spectrum of the film was observed to show a blue-shift of the low-energy absorption maximum. These observations again indicate the low stability of the system upon prolonged exposure to light, particularly in the presence of LiI/$I_2$ electrolyte. It should also be noted that a prolonged irradiation experiment undertaken with a cell sensitised with N719 showed no efficiency variation with time.

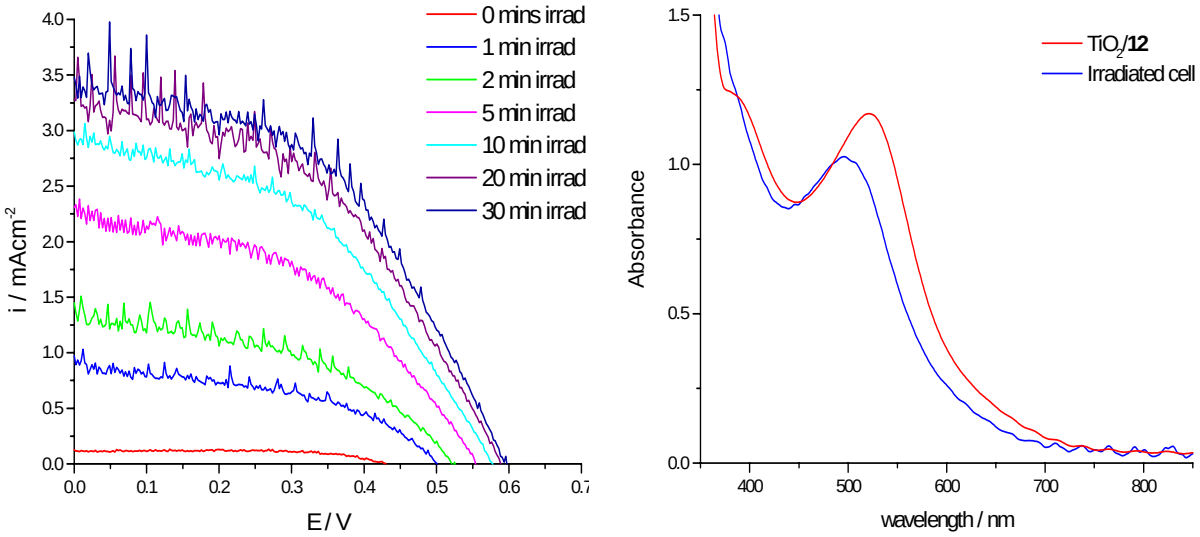


**Figure 25.** IV curves for a cell sensitised with **12** (left) showing variation of efficiency with time and absorption spectrum of $TiO_2$ film sensitised with **12** (right) before and after prolonged irradiation.

In an attempt to determine if the absorption spectrum variation was a result of the Cu(*exo*$O_2$-cyclam) ligand falling off the complex, the technique of ICP-OES (inductively coupled plasma – optical emission spectroscopy) was used to investigate the copper concentration of several solutions made up using both irradiated and non-irradiated cells. The electrolyte was washed off the electrodes into a separate solution by soaking the films in acetonitrile for 5 minutes and the dye was desorbed from the $TiO_2$ surface by soaking in 0.1 M KOH for 5 minutes. It was hoped that the observation of copper in the electrolyte solutions of the irradiated cells, and not in the non-irradiated cells, would show evidence for this degradation mechanism. However, the solutions used all showed negative values of copper concentration indicating that the error bars of the experiment are larger than the concentrations trying to be observed.

## 5.12 Conclusions

The synthesis and characterisation of the series of dyes Ru(R-bpy)$_2$(Cu(*exo*O$_2$-cyclam)), where R=H, $CO_2Et$ and $CO_2H$, has been successfully achieved. The absorption range and molar extinction co-efficients of the dyes were significantly increased relative to N719, yielding $TiO_2$ films sensitised up to 800 nm for the acid derivative (**12**). This is in keeping with previous work showing that O-donor ligands, such as acetylacetonato, can be successfully employed to yield lower energy absorption maxima. The electrochemical studies of the dyes showed initial evidence of the redox-activity of the ligand being retained in the complex with the presence of two oxidations. Spectroelectrochemical studies proved inconclusive as to the nature of the two oxidations however, with the OTTLE studies indicating the possibility of significant contribution from the ruthenium (II) centre, as evidenced by the collapse of the CT bands upon mono-oxidation. On the other hand, the *in-situ* EPR studies suggested a significant copper (II) contribution as evidenced by the collapse of the copper (II) EPR signal upon mono-oxidation. Further investigation *via* hybrid DFT calculations showed the two highest occupied orbitals to be very close in energy (0.07 eV apart) with one being largely ruthenium and the other largely copper based. In conjunction with TD-DFT these calculations revealed that the ambiguity in the spectroelectrochemical studies may arise from the similarity in energy of the highest MOs. As both the OTTLE and *in-situ* EPR may be likely to show the same result whether the oxidation was ruthenium or copper based.

The DSSCs sensitised with **12** showed a relatively high efficiency of 2.55 % when using a small active area cell (0.3 $cm^2$). There was however evidence for an energy mismatch between the conduction band of the $TiO_2$ and the bipyridyl based unoccupied orbital. Hence further work may be required to optimise the electrolyte constituents so as to maximise the efficiency by finding the best trade-off between the short-circuit current and the open-circuit voltage. The transient absorption studies showed the dye to be functioning correctly in the cell with the regeneration occurring on a faster timescale than the recombination dynamics. Interestingly the recombination half-life was not as long-lived as would have been hoped for this system. This may be a result of some of the dyes being wrongly orientated on the surface of the $TiO_2$, perhaps caused by an interaction between the copper (II) and surface bound anions, resulting in efficient transfer of an electron from the $TiO_2$ to the oxidised dye. It would appear that this is not a major orientation as both the TAS and solar cell measurements suggest the cells sensitised with this dye can yield siginficant efficiencies. There was also evidence of the dye being unstable in the presence of the liquid redox electrolyte, which may be caused by the displacement of the nitrate anions around the copper or the leaching of the copper (II) ligand into the electrolyte. Experiments to investigate which degradation mechanism was operating in this case were inconclusive.

To conclude, this study has provided the first evidence of the Cu(*exo*$O_2$-cyclam) ligand, widely used for first row transition metal and lanthanide complexes in magnetic applications, being complexed to a second row transition metal. This may open up

further research in the area of magnetic materials. The use of this ligand has also been successful in extending the light harvesting ability of the dye as desired.

## 5.13 Synthesis

Synthesis of the Cu(*exo*$O_2$-cyclam) ligand was carried out according to previously published methods [9,10] and the ruthenium starting materials as described in Chapter 2.

**Cu(*exo*$O_2$-cyclam).** CHN Calc. for $C_{10}H_{18}N_4O_2Cu$: C 41.44, H 6.26, N 19.33, Found: C 41.58, H 6.61, N 18.75.

**[Ru(bpy)$_2${Cu(*exo*$O_2$-cyclam)}][$NO_3$]$_2$ (10).** Synthesis as described in reference 11. $Ru(bpy)_2Cl_2$ (377 mg, 0.78 mmol) was dissolved in methanol (25 ml) and silver nitrate (240 mg, 1.41 mmol) in water (3 ml) was added. The mixture was stirred at room temperature for 1 hour under nitrogen and in reduced light, and the resulting precipitate removed by filtration. To the red solution was added Cu(*exo*$O_2$-cyclam) (226 mg, 0.78 mmol) and the mixture stirred for 1 hour. After filtration the filtrate was concentrated to 5 ml and propan-2-ol (20 ml) added. The solution was stored at 5 °C overnight and the resulting precipitate collected by filtration. Yield: 351 mg (53 %). CHN Calc. for $C_{30}H_{38}N_{10}O_{10}CuRu$: C 41.7, H 4.4, N 16.23, Found: C 41.25, H 3.70, N 15.69. +ve FAB-MS: m/z 765 $(M\text{-}NO_3)^+$, 702 $(M\text{-}2NO_3)H^+$, 413 $(Ru(bpy)_2)^+$, 351 $(M\text{-}2NO_3)^{2+}$.

**[Ru(decbpy)$_2${Cu(*exo*O$_2$-cyclam)}][NO$_3$]$_2$ (11).** Ru(decbpy)$_2$Cl$_2$ (100 mg, 0.129 mmol) was dissolved in methanol (10 ml) and silver nitrate (44 mg, 0.26 mmol) in water (1 ml) was added. The mixture was refluxed for 1 hour, in the dark, under $N_2$. The resultant precipitate (silver chloride) was removed by centrifugation. To the solution Cu(*exo*O$_2$-cyclam) (38mg, 0.129 mmol) was added as a solid and the mixture stirred under $N_2$ and in dark, overnight. The solution was filtered and the filtrate concentrated on a rotary evaporator, diethyl ether was layered on top and the flask placed in fridge. The resulting maroon precipitate was collected by filtration. The crude product was furthered purified *via* a Sephadex LH-20 column using methanol as the eluent, collecting the main purple band. Yield: 98 mg (68 %), CHN Calc. for $C_{42}H_{54}N_{10}O_{18}RuCu$: C 43.81, H 4.73, N 12.16, Found: C 43.50 H 4.05 N 11.81, +ve FAB-MS: m/z 1054 ($M^+$-$NO_3$), 990 ($M^+$-2$NO_3$)H, 702 (Ru(decbpy)$_2^+$).

**[Ru(dcbpy)$_2${Cu(*exo*O$_2$-cyclam)}][NO$_3$]$_2$ (12).** Ru(decbpy)$_2$Cl$_2$ (100 mg, 0.129 mmol) was dissolved in methanol (10 ml) and silver nitrate (44 mg, 0.26 mmol) in water (1 ml) was added. The mixture was refluxed for 1 hour, in the dark, under $N_2$. The resultant precipitate (silver chloride) was removed by centrifugation. 0.1 M KOH (3 ml) was added and the solution stirred for 15 minutes. To this solution Cu(*exo*O$_2$-cyclam) (38mg, 0.129 mmol) was added as a solid and the mixture stirred under $N_2$ and in dark, overnight. The product was precipitated by the addition of 1 M $HNO_3$ (2 ml), the resulting maroon precipitate was further purified *via* a Sephadex LH-20 column using water as the eluent, collecting the main purple band. Yield: 19 mg (16 %), CHN Calc.

for $C_{34}H_{44}N_{10}O_{22}RuCu$: C 36.81, H 3.99, N 12.63, Found: C 35.66 H 3.09 N 12.72, -ve ESI-MS: m/z 439 ($M^{2+}$-$2NO_3$).

## 5.14 References


[1] C.A. Bignozzi, R.A. Argazzi, C.J. Kleverlaan, *Chem. Soc. Rev.,* 2000, **29**, 87-96.

[2] Md.K. Nazeeruddin, P. Liska, J. Moser, N. Vlachopoulos, M. Grätzel, *Helv. Chim. Acta,* 1990, **73**, 1788-1803.

[3] C.A. Bignozzi, J.R. Schoonover, F. Scandola, *Prog. Inorg. Chem.*, 1997, **44**, 1-95.

[4] A.C. Lees, C.J. Kleverlaan, C.A. Bignozzi, J.G. Vos, *Inorg. Chem.,* 2001, **40**, 5343-5349.

[5] B. Gholamkhass, K. Koike, N. Negishi, H. Hori, T. Sano, K. Takeuchi, *Inorg. Chem.*, 2003, **42**, 2919-2932.

[6] C. Chiorboli, S. Fracasso, F. Scandola, S. Campagna, S. Serroni, R. Konduri, F.M. Macdonnell, *Chem. Commun.*, 2003, 1658-1659.

[7] Md. K. Nazeeruddin, M. Grätzel, *Comp. Coord. Chem. II*, 2003, **9**, 719-758.

[8] Y. Xu, G. Eilers, M. Borgström, J. Pan, M. Abrahamsson, A. Magnuson, R. Lomoth, J. Bergquist, T. Polívka, L. Sun, V. Sundström, S. Styring, L. Hammarström, B. Åkermark, *Chem. Eur. J.*, 2005, **11**, 7305-7314.

[9] L. Cronin, A.R. Mount, S. Parsons, N. Robertson, *Dalton Trans.,* 1999, 1925-1927.

[10] L. Cronin, P.A. McGregor, S. Parsons, S. Teat, R.O. Gould, V.A. White, N.J. Long, N. Robertson, *Inorg. Chem.,* 2004, **43**, 8023-8029.

[11] V.A. White, R.D.L. Johnstone, K.L. McCall, N.J. Long, A.M.Z. Slawin, N. Robertson, *Dalton Trans.*, 2007, 2942-2948.

[12] H-Z. Kou, B.C. Zhou, S. Gao, R-J. Wang, *Angew. Chemie Int. Ed.,* 2003, **42**, 3288-3291.

[13] J-K. Tang, Y. Ou-Yang, H-B. Zhou, Y-Z. Li, D-Z, Liao, Z-H. Jiang, S-P. Yan, P. Cheng, *Cryst. Growth. and Design,* 2005, **5**, 813-819.

[14] J-K. Tang, S-F. Si, L-Y. Wang, D-Z. Liao, Z-H. Jiang, S-P. Yan, P. Cheng, X. Liu, *Inorg. Chem. Commun.*, 2002, **5**, 1012-1015.

[15] J-K. Tang, S-F. Si, E-Q. Gao, D-Z. Liao, Z-H. Jiang, S-P. Yan, *Inorg. Chim. Acta.,* 2002, **332**, 146-152.

[16] J-K. Tang, L-Y. Wang, L. Zhang, E-Q. Gao, D-Z. Liao, Z-H. Jiang, S-P. Yan, P. Cheng, *J. Chem. Soc. Dalton Trans.,* 2002, 1607-1612.

[17] J-K. Tang, Y-Z. Li, Q-L. Wang, E-Q. Gao, D-Z. Liao, Z-H. Jiang, S-P. Yan, P. Cheng, L-F. Wang, G-L. Wang, *Inorg. Chem.*, 2002, **41**, 2188-2192.

[18] H-Z. Kou, B.C. Zhou, R-J. Wang, *Inorg. Chem.,* 2003, **42**, 7658-7665.

[19] M. Osawa, H. Sonoki, M. Hoshino, Y. Wakatsuki, *Chem. Lett.*, 1998, 1081-1082.

[20] B. Geißer, R. Alsfasser, *Eur. J. Inorg. Chem.*, 1998, 957-963.

[21] B. Geißer, R. Alsfasser, *Dalton Trans.*, 2003, 612-618.

[22] N. Onozawa-Komatsuzaki, R. Katoh, Y. Himeda, H. Sugihara, H. Arakawa, K. Kasuga, *Bull. Chem. Soc. Jpn.,* 2003, **76**, 977-984.

[23] D. Bruce, M.M. Richter, *Analyst*, 2002, **127**, 1492-1494.

[24] A. Hazell, R. Hazell, C.J. McKenzie, L.P. Nielsen, *Dalton Trans.*, 2003, 2203-2208.

[25] S.C. Rawle, P. Moore, N.W. Alcock, *Chem. Commun.*, 1992, 684-687.

[26] F. Bolletta, I. Costa, L. Fabbrizzi, M. Licchelli, M. Montalti, P. Pallavicini, L. Prodi, N. Zaccheroni, *Dalton Trans.*, 1999, 1381-1385.

[27] Md.K. Nazeeruddin, A. Kay, I. Rodicio, R. Humphry-Baker, E. Müller, P. Liska, N. Vlachopoulos, M. Grätzel, *J. Am. Chem. Soc.*, 1993, **115**, 6382-6390.

[28] P. Suppan, *Chemistry and Light,* Royal Society of Chemistry, 1994.

[29] B. Wenger, M. Grätzel, J-E. Moser, *J. Am. Chem. Soc.*, 2005, **127**, 12150-12151.

[30] S.A. Haque, E. Palomares, B.M. Cho, A.N.M. Green, N. Hirata, D.R. Klug, J.R. Durrant, *J. Am. Chem. Soc.*, 2005, **127**, 3456-3462.

[31] D.A. Fletcher, R.F. McMeeking, D.J. Parkin, *J. Chem. Inf. Comput. Sci.*, 1996, **36**, 746-749.

[32] M. Grätzel, *J. Photochem. Photobiol. A: Chem.,* 2004, **164**, 3-14.

[33] X. Yin, H. Zhao, L. Chen, W. Tan, J. Zhang, Y. Weng, Z. Shuai, X. Xiao, X. Zhou, X. Li, Y. Lin, *Surf. Interface Anal.*, 2007, **39**, 809-816.

[34] H. Kusama, H. Orita, H. Sugihara, *Sol. Energy Mater. Sol. Cells*, 2008, **92**, 84-87.

# Chapter 6:

# Conclusions and Future Work

Overall this work has shown the potential of ligand variation to enhance a number of parameters in a DSSC. The use of the strongly-electron donating S-donor ligands resulted in higher molar extinction co-efficients for both series and for the di-anionic **L1** a large increase in absorption range was also observed. Despite these advantageous features the efficiencies of the DSSCs were significantly lower than those obtained for N719. The low efficiency for **3** was attributed to the cyano group of **L1** binding to the $TiO_2$ in addition to the acid groups of the bipyridyl ligand.

The investigation of increased charge-separated states using redox-active systems as ligands yielded mixed results. The series incorporating **L3** showed extremely long-lived charge-separation with a recombination half-life of milliseconds. This was shown to be a direct result of the HOMO being located largely over the TTF ligand. The dyes synthesised with **L4** however did not show conclusive evidence for the HOMO being located on the ligand and the charge-separated life-time was not extended past that of a ruthenium centred HOMO. Although the DSSCs made with this dye did achieve the highest efficiency cells of all four series. The performance of these cells did, however, vary under prolonged light irradiation, suggesting either dye degradation or counter anion exchange.

Optimisation of the DSSCs, using the liquid iodide/triiodide electrolyte, sensitised with the dyes synthesised in this work can be achieved by variation of the electrolyte additives. By empirically altering the concentration of additives such as cheno, TBP and guanidinium thiocyanate the $V_{oc}$ and $I_{sc}$ values can be maximised to achieve the full

potential of the dyes. Further improvement of efficiencies can be achieved by several different $TiO_2$ treatments, *e.g.* compact $TiO_2$ blocking layer, scattering layers and $TiCl_4$ treatment. The reduction in size of the active area of the cell can lead to more efficient charge extraction and hence a better fill factor, typical sizes used for high efficiency cells are 0.3 and 0.1 $cm^2$.

Investigation of the use of solid-state electrolytes, such as spiro-OMeTAD, would be of particular interest with these systems. Dyes **9** and **12** showed some sensitivity to the iodide/triiodide liquid electrolyte and therefore the use of spiro-OMeTAD may improve the efficiencies of the DSSCs sensitised with these dyes. Indeed the higher extinction co-efficient for **12** will be useful as this will mean no loss in light harvesting for the thinner $TiO_2$ films, required when using spiro-OMeTAD. A comparison of the stability of these solid-state cells relative to the liquid electrolyte cells may also indicate the mechanism of degradation which affected the efficiencies after prolonged irradiation. The long-lived charge-separated state for **9** could also be a distinct advantage when using spiro-OMeTAD, as this should reduce charge recombination in the DSSC (a common problem for these cells, due to the slow dye regeneration). Increasing the alkyl chain length on the TTF ligand may also be advantageous for use in a solid-state cell, as this will increase the wettability of the electrolyte to the $TiO_2$/dye surface.

Of particular interest is the interaction of **9** with the iodide/triiodide electrolyte. The efficiency of the DSSCs sensitised with this dye were extremely low. The TAS measurements suggested a strong interaction resulting in an unusually long [$dye^+$,$I^-$]

intermediate, which would result in inefficient dye regeneration and a low efficiency. Isolation of this adduct may result in a greater understanding of the mechanism of dye regeneration (still a relatively ill-understood area), hence further work in this area is essential for future dye development. Investigation of the adduct by further TAS studies, such as measuring difference absorption spectra at the two timescales which appear to have different species being observed. This difference absorption spectrum focuses on one timescale and records the intensity of the TAS signal. The probe wavelength is then varied, allowing an absorption spectrum of the transient species to be built up. Two different absorption spectra should be obtained at the two timescales and therefore this should show further evidence for some sort of intermediate formation.

For all complexes investigated in this work further investigation of the luminescence properties is required to enable a greater understanding of their properties. Luminescence lifetimes and quantum yields may shed light on the interesting emission observed for the dye series incorporating **L1**, **L3** and **L4**.

Finally, the use of S-donor and redox-active ligands has proved an advantageous approach to dye design and warrants further investigation. There are numerous possibilities and several advantages to be explored using these ligand classes. For example, introducing further conjugation into the ligands should result in a further increase in the molar extinction co-efficients.

# Publications

# Binuclear and trinuclear complexes of *exo*$O_2$-cyclam†‡§

**Vivienne A. White,[a] Russell D. L. Johnstone,[b] Keri L. McCall,[b] Nicholas J. Long,[a] Alexandra M. Z. Slawin[c] and Neil Robertson*[b]**

***Received 25th January 2007, Accepted 20th April 2007***
***First published as an Advance Article on the web 10th May 2007***
**DOI: 10.1039/b701166k**

Complexes of the ligand 2,3-dioxo-1,4,8,11-tetraaza-cyclotetradecane (*exo*$O_2$-cyclam) have been prepared of formula $[M^1\{M^2(exoO_2\text{-cyclam})\}_2][BPh_4]_2$ where $M^1M^2$ = CoCo (**3**), ZnZn (**4**), MnCu (**5**), FeCu (**6**), CoCu (**7**), NiCu (**8**), ZnCu (**9**), and $[(bipy)_2Ru\{Cu(exoO_2\text{-cyclam})\}][NO_3]_2$ (**10**). Complex **10** crystallised in the space group *C*2/*c* and shows Jahn–Teller distorted Cu(II) with axial nitrate ligands. The {Cu(*exo*$O_2$-cyclam)} moiety chelates to the Ru with Ru–O distances of 2.082(5) Å. Complexes **5–10** show a Cu(II)/Cu(III) redox process and additional metal-centred (**6**, **8**, **10**) processes and ligand-centred (**10**) processes. The electrochemical and UV-Vis spectroelectrochemical study of **10** suggested two closely-spaced oxidations based on the Cu and Ru centres which suggests that substituted derivatives of **10** will be of interest for enhanced charge separation in dye-sensitised solar cells. Magnetic susceptibility measurements revealed dominant antiferromagnetic coupling within the trinuclear species **3**, **5–8**. Complex **10** showed Curie–Weiss behaviour with weak intermolecular interactions.

## Introduction

Multimetallic transition metal complexes offer an important route for the preparation of magnetic materials,[1] development of catalytic reagents,[2] models of metalloenzymes,[3] study of solar-cell dyes[4] and in the construction of metallosupramolecular architectures.[5] In such systems interaction between different metal centres is a key feature and ligand units that can induce and control this are therefore of great importance. We and others have previously reported the synthesis and characterization of cyclam-based macrocyclic ligands that incorporate *cis*-exogenous oxygen atoms (hereafter referred to as *exo*$O_2$) arranged for chelation to a metal atom external to the macrocyclic ring.[6–8] These macrocycles incorporate an oxamide-based bis-bidentate linker with deprotonatable amides and are related to amino acid based ligands.[9] Although bis-amide macrocycles have been widely studied[10–12] generally as precursors to saturated macrocycles (by reduction), only a small minority of those reported contain *cis* amides and the use of exogenous binding groups as bidentate linkers has been seldom utilized for the formation of multinuclear systems in macrocyclic chemistry.[13]

Our reports of *exo*$O_2$ macrocycles as ligands have stimulated much further work involving synthesis of heteropolynuclear complexes and assemblies.[14] Such macrocycles have tremendous potential to form novel functional materials as illustrated by the variety of systems developed from the related open chain oxamido analogues, including multinuclear complexes[15–19] and coordination polymers,[16,18–20] giving for example ferromagnetic complexes and ferrimagnetic chains. The extension of this approach to macrocyclic complexes offers the possibility to exploit the greater control over ligand selectivity, greater structural rigidity of the ligand framework and greater thermodynamic and kinetic stability typical of macrocyclic complexes.

We report the synthesis of a series of multinuclear complexes using the ligand 2,3-dioxo-1,4,8,11-tetraaza-cyclotetradecane (*exo*$O_2$-cyclam) (Fig. 1), along with the electrochemical, magnetic, EPR, structural and spectroelectrochemical characterisation of products.

## Results and discussion

### Synthesis of new complexes

Studies to date of multinuclear complexes involving the ligand *exo*$O_2$-cyclam have included binuclear species of first-row transition metals, mixed transition-metal–lanthanide complexes and coordination polymers with transition metals and lanthanides.[14] Apart from our early report of the trinuclear Cu(II) species (**2**) however, there has been little further study of this readily-prepared class of trinuclear molecules. We therefore report here the systematic synthesis and study of a series of seven new (homo and hetero) trinuclear complexes (**3–9**). These include the first examples of metals other than Cu(II) within the macrocyclic cavity, namely the Co(II) and Zn(II) trinuclear complexes **3** and **4**. (We also were able to obtain samples of mononuclear Co(II) and Zn(II) analogues of **1** as shown by mass spectrometry, however we were unable to obtain these in pure form.) We also report the synthesis, structural characterisation and spectroelectrochemical investigation of a novel binuclear Ru–Cu complex (**10**). Ligand **1** has, to the best of our knowledge, not previously been used to complex a transition metal outwith the first row, despite the considerable importance of heavier transition metals such as Ru

[a]*Department of Chemistry, Imperial College, London, UK SW7 2AZ*
[b]*School of Chemistry, University of Edinburgh, King's Buildings, Edinburgh, UK. E-mail: neil.robertson@ed.ac.uk; Fax: +44 1316504743; Tel: +44 1316504755*
[c]*School of Chemistry, University of St Andrews, North Haugh, St Andrews, UK KY16 9ST*

† The HTML version of this article has been enhanced with colour images.
‡ CCDC reference number 634705 (complex **10**). For crystallographic data in CIF or other electronic format see DOI: 10.1039/b701166k
§ Electronic supplementary information (ESI) available: Additional synthetic details and EPR and magnetic data. See DOI: 10.1039/b701166k

 

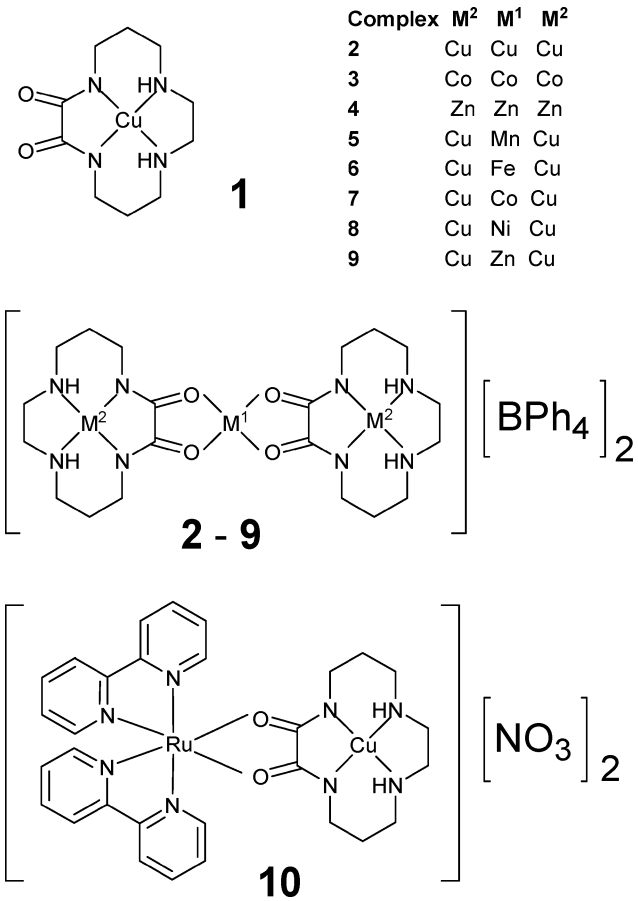


**Fig. 1** Complexes **1** and **2** have been reported by us previously.[7] Complexes **3–10** are new to this work.

due to the exploitation of their photophysical properties in, for example, solar energy conversion.[4]

Complexes **5–10** were all prepared by treating the appropriate metal salt with the mononuclear Cu(II) precursor (**1**) in an analogous manner to the synthesis of **2** although we used $[BPh_4]^-$ as the added counterion due to difficulties obtaining pure products with smaller counterions such as $[BF_4]^-$. The homotrinuclear complexes **3** and **4** were prepared by reaction of the precursor *exo*$O_2$-cyclam ligand with the appropriate Co(II) or Zn(II) salt. All complexes were shown to be pure by elemental analysis (except **4**) and their identity verified by mass spectrometric measurements in addition to the electronic characterisation outlined below. The remaining presence of uncomplex macrocycle in the synthesis of **4** suggests a poorer affinity of the macrocycle for Zn(II).

### X-Ray structure of CuRu

Numerous attempts were made to obtain X-ray quality crystals of each of the trinuclear complexes, however this was without success. We found that the best purity for these complexes was achieved by preparing $[BPh_4]^-$ salts due to low solubility in the reaction solution and reduced contamination with salt impurities. It may be that consistent use of the large organic counterion on grounds of product purity was a poor choice for sample crystallinity, hampering our efforts towards growing single crystals or obtaining highly-crystalline powders. Although the difficulty in obtaining X-ray structures for the trinuclear complexes was an impediment, the electrochemical and magnetic characterisation (see below) was fully consistent with the anticipated trinuclear character observed for our previously reported structure of **2**[7] and for the reported structures of the related trinuclear macrocyclic systems involving a modified Cu-cyclam with *cis*-exogenous oxygen atoms coordinated to other metals such as Co(II) and Ni(II).[21]

In contrast to the trinuclear complexes, crystals of the binuclear CuRu species (**10**) were readily grown by vapour diffusion of methanol into a DMF solution of the complex. The complex crystallises in the space group $C2/c$ with four molecules per unit cell. The structure shows the expected chelation of the *exo*-oxygen groups of the Cu-cyclam moiety to the Ru centre (Fig. 2) with the asymmetric unit comprising half of the molecule and a two-fold rotation axis lying along the Cu–Ru axis. The Ru $\cdots$ O distances are 2.082(5) Å leading to a Cu $\cdots$ Ru distance of 5.29(1) Å. The Cu–N bond lengths are found to be 1.945(8) Å and 1.913(6) Å to the amine and amide nitrogens respectively, slightly shorter than the corresponding distances for **2**. The two nitrate counterions are weakly coordinated to the axial positions of the Cu(II) at a distance of 2.645(8) Å to give a characteristic Jahn–Teller distorted, six-coordinate geometry around Cu(II).

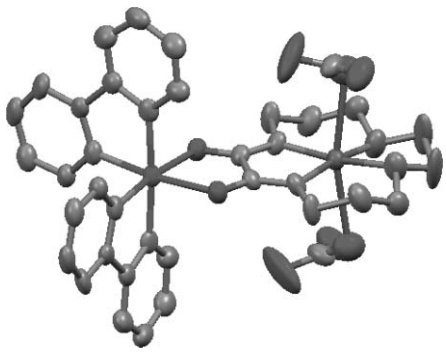

**Fig. 2** Single-crystal X-ray structure of **10** with probability ellipsoids set at 50%. Figure prepared using the program Mercury.[22]

The molecules pack to form centrosymmetric dimers interacting through π-stacking of one of the bipy ligands on each complex with an interplanar separation of 3.19(1) Å. The Cu centres however are effectively well separated from those in adjacent molecules by the organic ligands, counterions and solvent molecules such that the shortest intermolecular Cu $\cdots$ Cu distance is 7.61(1) Å.

As indicated above, this appears to be the first example of [Cu(*exo*$O_2$-cyclam)] (**1**) used as a ligand for a second-row transition metal. The hard oxygen donor atoms have likely encouraged the initial work with **1** (and also work with related ligands) to focus on the first row or lanthanides, however this work clearly shows the potential of **1** as a functional ligand for a wider range of metals. However, complexes of the form $[(bipy)_2RuL]$, where L is a chelating oxygen-donor ligand remain relatively rare, and a search of the Cambridge Structural Database shows only seven examples structurally characterised prior to this work.[23]

### Electrochemical and spectroelectrochemical studies

The cyclic voltammetry of complexes **3–9** was studied in $CH_3CN$ over the range +1.5 to −1.75 V. In addition, due to the irreversible oxidation observed for $BPh_4^-$ at +0.75 V, the $BF_4^-$ salts of **3–9** were

**Table 1** Electrochemical properties through cyclic voltammetry of **3–10** in $CH_3CN$ (**3–9**) or DMF at 250 K (**10**) *versus* SCE showing $E_{1/2}$/V with oxidation/reduction peak separation in parentheses. The macrocyclic Cu(II/III) process has been assigned as indicated and the other columns indicate any additional processes to less positive or more positive potential. For **10**, the oxidation at 0.73 V was resolved into two peaks through differential pulse voltammetry

| | | Cu(II/III) | |
|---|---|---|---|
| **1**[6] | | 0.62 (65) | |
| **2**[6] | | 1.08 | 1.36 |
| **3** | | — | |
| **4** | | — | |
| **5** | | 1.37 (159) | |
| **6** | −0.76 | 1.16 (270) | |
| **7** | | 0.98 (155) | |
| **8** | 0.61[a] | 1.05 (58) | |
| **9** | | 0.86 (203) | |
| **10** | −1.72, −1.47 | 0.73 (150) | |

[a] Obscured by $BPh_4^-$ and only observed for $BF_4^-$ salt in DMF.

studied (in DMF due to poor solubility in $CH_3CN$). Complex **10** was studied as the nitrate salt. The precursor mononuclear complex **1** shows a reversible oxidation at +0.77 V and complex **2** shows two reversible oxidations at 1.08 and 1.36 V, the former assigned as oxidation of the macrocyclic Cu(II). As anticipated each complex **5–10** also displays a process that can be assigned to oxidation of the Cu(II) centres in the macrocycle (Table 1, Fig. 3) which was observed in each case to be chemically reversible, although not always electrochemically reversible. In each case, the Cu(II/III) process was more positive for the trinuclear complexes in comparison with the mononuclear species (**1**) which is in keeping with the donation of electron density from the Cu-macrocycle moiety to another metal.

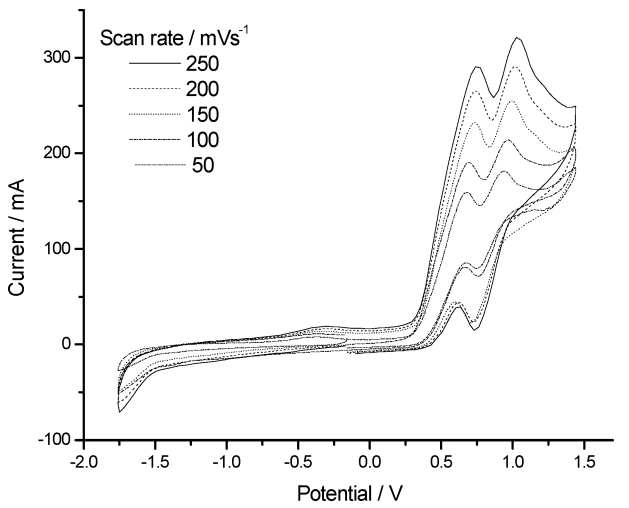


**Fig. 3** Cyclic voltammograms of $[Zn\{Cu(exoO_2\text{-cyclam})\}_2][BPh_4]_2$ (**9**) showing irreversible oxidation of $BPh_4^-$ and reversible oxidation of Cu(II).

Among the trinuclear species, additional redox processes were observed only for complexes **6** and **8**, the former tentatively assigned as reduction to Fe(0) and the latter as oxidation to Ni(III). Neither the trinuclear Zn(II) complex **4** nor the analogous Co(II) complex **3** were redox active within the electrochemical window. Complex **10** shows two reductions assigned as based on the bipyridyl ligands as is expected for Ru complexes containing these moieties. Oxidation of **10** showed only one peak in the cyclic voltammogram (Table 1), however differential pulse voltammetry revealed two peaks at 0.65 and 0.77 V which we assign, by analogy with related complexes, as sequential oxidation of the Ru(II) and the Cu(II) centres although it is not possible to distinguish the order of these processes.

Complex **10** is related to species that have previously been utilised in solar energy conversion using dye-sensitised solar cells.[4] The most effective dyes in such systems are based on Ru–polypyridyl complexes and the inclusion of an additional electron donating fragment has also proven important as it can lead to enhanced charge-separation within the dye following charge injection into nanoporous $TiO_2$ from the photoinduced dye excited state. Complex **10** represents a model system for such a dye as it lacks only the carboxylate functionalities typically attached to the bipyridyl ligands to anchor the dye to the metal oxide surface. Due to this additional point of interest for **10**, we explored the spectroelectrochemical characterisation using *in situ* UV-Vis-nearIR spectroscopy of the oxidised form to give insight into the nature of the frontier orbitals.

The UV-Vis spectrum of **10** shows peaks at 297 nm (33675 $cm^{-1}$, 42000 $M^{-1}$ $cm^{-1}$), 357 nm (28000 $cm^{-1}$, 6200 $M^{-1}$ $cm^{-1}$), 501 nm (19950 $cm^{-1}$, 5700 $M^{-1}$ $cm^{-1}$) and a shoulder at 526 nm (19000 $cm^{-1}$, 5100 $M^{-1}$ $cm^{-1}$) (Fig. 3). By analogy with related Ru(II) complexes bearing two bipyridyl groups the first of these is assigned as intrabipy π to π* and the bands at 357 and 501 nm to MLCT processes from the metal-based HOMO-1 and HOMO respectively. In addition, the precursor complex **1** shows a transition at 520 nm (8000 $M^{-1}$ $cm^{-1}$) so the low-energy shoulder at 526 nm in **10** can be assigned as a transition within the Cu(II) component of the molecule.

Electrochemical oxidation of **10** at +1.0 V and 253 K is accompanied by clean and reversible conversion between the reduced and oxidised forms as evidenced by good isosbestic points (Fig. 4) and the ready conversion of the product back to show the starting spectrum upon re-reduction. It is expected that both the Ru(II) and the Cu(II) centres will undergo oxidation based on the cyclic voltammetry results and we were unable to obtain clean conversion to the first oxidised product due to the close spacing of the two processes. Lowering of intensity for the bands at 33675 $cm^{-1}$, 28000 $cm^{-1}$ and 19950 $cm^{-1}$ is consistent with spectral changes observed for oxidation of the analogous

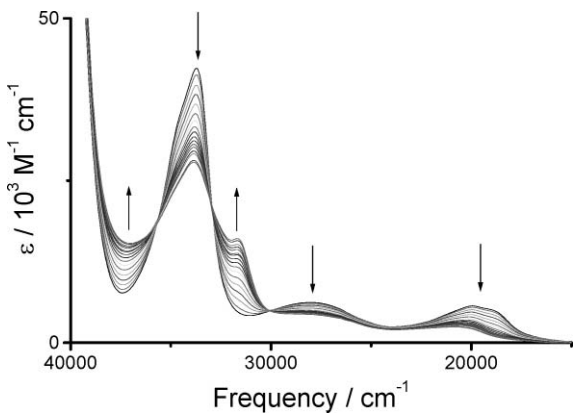


**Fig. 4** Spectroelectrochemical study of **10** upon oxidation at +1.0 V at 253 K.

complex $[Ru(bipy)_2Cl_2]$. Likewise the growth of bands around 37000 $cm^{-1}$ and at 31650 $cm^{-1}$ are also in keeping with oxidation of $[Ru(bipy)_2Cl_2]$ and together this is taken as evidence for the oxidation of the Ru centre in complex **10**. In addition, the shoulder at 19000 $cm^{-1}$ also reduced in intensity upon oxidation. Although, no spectrum of oxidised **1** is available for comparison due to low solubility at reduced temperatures, the large perturbation in oxidised **10** to a band assigned as arising from the Cu(II) component of the molecule is taken as evidence that this moiety has also been oxidised.

To be of optimum use in a dye-sensitised solar cell, it is desirable for a molecule related to **10** that the Cu(II) centre is oxidised before Ru(II) such that a Ru(III) centre generated following photoinduced charge-transfer to $TiO_2$ is followed by electron transfer from Cu(II) to Ru(III) to maximise charge separation. The useful analogue of **10** for this purpose will possess additional electron-withdrawing carboxy groups on the bipy ligands (to facilitate binding to $TiO_2$) and this will typically lead to a more positive oxidation potential for the Ru(II) centre. This suggests the possibility of enhanced charge separation of such a dye in a dye-sensitised solar cell and will be the subject of future investigations.

### Magnetic properties

The powder EPR spectrum for mononuclear complex **1** (see ESI, Fig. S1(a))§ was found to show a broad signal centred around $g = 2.05$ consistent with Cu(II) in an approximately square-planar or axially-distorted environment.[13] In acetonitrile, a complicated pattern was observed corresponding to more than one Cu(II) species, possibly due to some axial coordination to the metal from solvent or counterion species. A similar solution spectrum for the Zn(II) centred complex **9** was observed (see ESI, Fig S1(b)).§ Complexes **3**, **6**, **7** and **8** were all EPR silent, possibly due to coupling between the metal centres leading to rapid relaxation.

Magnetic susceptibility data were recorded for complexes **3**, **5–8** and **10** in the range 2–300 K and corrected for diamagnetic contribution using Pascal's constants (see ESI, Fig. S2–S7).§ Complex **10** has only one paramagnetic metal centre and these molecules are well separated in the crystal structure, hence the observed compliance with the Curie–Weiss law with the Curie constant ($C$) close to the value expected for one unpaired electron and a low Weiss constant ($\theta$). Data were recorded on more than one sample of each complex **3**, **5–8** as the $BPh_4^-$ salt and were found to be consistent between samples. Data for the $BF_4^-$ salts were found to be qualitatively comparable but are not reported due to the poorer purity of these salts. Although an X-ray structure is available only for **10**, the presence in **3** and **5–8** of large counterions to separate the complexes and the dominant coupling anticipated through the macrocyclic linker is expected to lead to magnetic behaviour determined primarily by intra-complex couplings. Accordingly, all the complexes showed no indication of any peak or inflection in the low temperature data that might correspond to long-range magnetic order. Above 100 K, complexes **3**, **5–7** showed Curie–Weiss behaviour with a linear plot of $1/\chi_{mol}$ against $T$ and a large negative Weiss constant, consistent with intramolecular antiferromagnetic coupling (Table 2). The observed Curie constants showed a generally quite poor correspondence with the expected values (equivalent to the theoretical value of $\chi T$ at high temperature), perhaps due to the limited temperature range over which the fits could be attempted. In keeping with the large negative values of Weiss constant, calculated values of $\chi T$ decreased steadily with temperature for all the complexes, consistent with antiferromagnetic interactions between the central metal and the macrocyclic metal in the complexes. The spin state of the central metal could be verified from the limiting values of $\chi T$ at room temperature (rt) and low temperature. For the Co(II) complex **7**, $S = 1/2$ for the central Co(II) was also considered (theoretical $\chi T$ at room temperature of 1.13 emu K $mol^{-1}$), however this was not consistent with the fit to the trinuclear model below. Deviations from expected values may also arise from inter-trimer interactions and anisotropy of the metal centres.

Data were fit with the appropriate expressions derived using Kambe's method[24] and the Hamiltonian $\hat{\mathbf{H}} = -2JS_M(S_{Cu1} + S_{Cu2})$ (M = Mn, Fe, Co) or $\hat{\mathbf{H}} = -2JS_{Co}(S_{Co1} + S_{Co2})$ (**3**) based on isotropic coupling, an average $g$ value close to 2 and assuming zero coupling between the two terminal Cu(II) or Co(II) centres in the trinuclear complexes. The latter assumption is supported by the lack of such coupling observed in **2**[7] and the lack of any improvements to fits in this work using a model that allowed for this interaction. Values of temperature-independent paramagnetism of the order $10^{-4}$ emu $mol^{-1}$ were used, taken from literature values.[24]

Similar Mn(II), Fe(II), Co(II) and Ni(II) complexes coupled to Cu(II) *via* an oxamide bridge have been reported in the literature using the analogous open chain ligand oxpn and related macrocyclic ligands. A summary of coupling constants between

**Table 2** Magnetic properties of complexes[a]

| | $C$/emu K $mol^{-1}$ | $\theta$/K | $\chi T$(rt)/emu K $mol^{-1}$ | $\chi T$(min)/emu K $mol^{-1}$ | $J/cm^{-1}$ | $g$ |
|---|---|---|---|---|---|---|
| **2**[6] | | | | | −364 | |
| **3** | 1.46 | −144 | 1.02 (1.13) | 0.43 (0.38) | −43 | 2.05 |
| **5** | 6.34 | −143 | 4.38 (5.13) | 1.52 (1.88) | −23 | 1.98 |
| **6** | 7.05 | −338 | 3.30 (3.75) | 0.81 (1) | −34 | 2.00 |
| **7** | 2.19 | −41 | 1.91 (2.63) | 0.40 (0.38) | −26 | 2.00 |
| **8** | 0.32 | −0.5 | 0.32 (0.75) | 0.16 (0) | — | — |
| **10** | 0.39 | −3.3 | | | | |

[a] $C$/emu K $mol^{-1}$ and $\theta$/K derived from Curie–Weiss fit above 100 K. $\chi T$(min) gives the lowest value reached which for each was at <40 K. Theoretical, spin-only values are given in parentheses where spin of the central metal is assumed to be $S = 1/2$ Cu(II), $S = 3/2$ Co(II), $S = 5/2$ Mn(II), $S = 2$ Fe(II) or $S = 0$ Ni(II). $J/cm^{-1}$ and $g$ were obtained from fit to trinuclear isotropic exchange model over whole temperature range using the above spins for the central metal. For **6** and **7**, $g$ was fixed at 2.00. Fit to the trinuclear model for **8** with Ni(II) $S = 1$ was attempted, however the fit did not model the data appropriately since the model predicts a non-magnetic ground state which was not observed.

**Table 3** Example literature values in $cm^{-1}$ of oxamide-bridged exchange-coupling where Cu(II) is complexed by the nitrogen-donors and the other metal complexed by the oxygen donors. All values show antiferromagnetic coupling and are compared with the values obtained for **5–7**

| Cu(II)–Mn(II) | Cu(II)–Fe(II) | Cu(II)–Co(II) | Cu(II)–Ni(II) |
|---|---|---|---|
| −13.9,[14] −14,[18] −19.8,[25] −25.6[26] | −30.8,[6c] −28.7[6c] | −28.1[21] | −42.9,[21] −47.5,[27] −52.5,[14] −63.9,[28] −67.4,[28] −48,[18] −98.7[16] |
| −23 (**5**) | −34 (**6**) | −26 (**7**) | — (**8**)[a] |

[a] No fit obtained.

the M(II) coordinated by the *exo*$O_2$ unit and the Cu(II) by the nitrogen atoms is given in Table 3. For complexes **3**, **5**, **6** and **7**, $\chi T$ values at low and high temperature were generally consistent with expected values and acceptable fits were obtained to the trinuclear model, giving $J$ values comparable with the literature precedent (Table 3).

The largest deviations from anticipated values of $\chi T$ were observed for the Ni(II) complex **8**. For this complex the low-temperature and high-temperature values of $\chi T$ were not in good agreement with the assumption of either $S = 0$, expected for square-planar Ni(II), or $S = 1$, expected for tetrahedral or axially-coordinated Ni(II). A fit to the Curie–Weiss model yielded a value of Curie constant that could not be readily rationalised. Also, no fit could be achieved to the isotropic trinuclear model assuming $S = 1$ since this predicts a non-magnetic ground state which was not observed. The EPR-silent nature of **8** contrasts with **9** (Fig. S1(b))§ where the central metal is Zn(II) $S = 0$, which may suggest that the Ni(II) plays a more complex role than as a simple diamagnetic linker. However, the Ni(II) also does not act as a simple $S = 1$ centre and the nature of the behaviour is not clear at present.

## Conclusions

This study has led to a number of conclusions regarding the complexing behaviour of the ligand *exo*$O_2$-cyclam which has recently received much attention. Firstly, we have isolated complexes of this ligand where it contains metals other than Cu(II) (*i.e.* Co(II) and Zn(II)) within the macrocyclic cavity, which we believe to be the first examples of this nature. The ready binding of these metals and our failure to isolate analogous complexes with Mn(II), Fe(II) or Ni(II) may be explained by the similarity in ionic radius of Cu(II) (73 pm), Co(II) (74 pm) and Zn(II) (74 pm), in contrast with the other metals studied (Mn(II) 0.83/0.67 (hs/ls); Fe(II) 0.78/0.61 (hs/ls); Ni(II) 0.69). The series of trinuclear complexes with paramagnetic metals bridged by the oxamido moiety shows antiferromagnetic coupling between the central and macrocyclic metals and in each case electrochemical investigation showed oxidation of the Cu(II) macrocyclic centres. Overall, the capabilities of the Cu(II)–macrocycle fragment as a "complex-as-ligand" unit has been established in this and other work by ourselves and others. It can be used to clip on to a wide variety of other transition metal centres to introduce unpaired electrons and redox activity into the unit.

We have taken initial steps to exploit this by preparing complex **10** where the Cu(II) fragment may act as an additional electron-donor unit to the Ru–polypyridyl fragment, of interest in charge-separation, solar energy conversion and possibly also in catalysis. To the best of our knowledge, this is the first example where the use of **1** as a ligand has been extended to a 2nd-row transition metal. Electrochemical and spectroelectrochemical studies suggests closely-spaced oxidations of the Cu(II) and Ru(II) centres with values that are suitable for further studies in preparing species that can show large charge separation. Further work will focus on preparing and testing solar-cell dyes related to complex **10** and other routes to exploit **1** as a functional ligand.

## Experimental

Cyclic voltammograms were recorded in dry $CH_3CN$ or dimethylformamide with 0.1 M $TBABF_4$ supporting electrolyte using a Pt disc working electrode, $Ag/Ag^+$ reference electrode and Pt-mesh counter electrode. After each experiment the reference was calibrated against the ferrocene/ferrocenium couple and results here are reported against SCE. For the spectroelectrochemistry study, the quartz cell used was 0.5 mm thick, the working electrode a Pt/Rh gauze, counter electrode a Pt wire and the reference electrode Ag/AgCl. A Perkin-Elmer Lambda 9 spectrophotometer, linked to a PC running UV-Winlab software was used to record the spectra. The sample was studied at 253K in 0.1M $TBABF_4$–DMF. EPR spectra were obtained for solution samples in $CH_3CN$ on a Bruker ER200D X-band spectrometer and magnetic susceptibility data were recorded on a Quantum Design MPMS2 SQUID magnetometer over the range 2–300 K.

### Crystal data for 10·2$CH_3OH$, $C_{32}H_{42}N_{10}O_{10}CuRu$

$M_r = 891.36$, monoclinic, space group $C2/c$, $a = 17.399(5)$, $b = 13.501(4)$, $c = 14.678(5)$ Å, $\beta = 90.611(15)°$, $V = 3448.0(18)$ Å$^3$, $Z = 4$, $\lambda = 0.71073$, 11017 reflections were measured of which 3122 were unique. The structure was solved using SIR92[29] and refined on $F$ using 2310 reflections ($I > 2\sigma(I)$) using Crystals[30] and converged to $R_1 = 0.0873$ ($I > 2\sigma(I)$) and $wR_2 = 0.1016$ (all data) GoF = 1.0608.

### [Co{Co(*exo*$O_2$-cyclam)}$_2$][$BPh_4$]$_2$ (3)

Cobalt(II) chloride (39 mg, 0.3 mmol) and 2,3-dioxo-1,4,8,11-tetraazacyclotetradecane (46 mg, 0.2 mmol) were dissolved under $N_2$ in degassed methanol (3 mL) added *via* syringe and suba seal to give a deep green solution. Degassed distilled water (1 mL) was added and the mixture turned a deep red overnight. Sodium tetraphenyl borate (68.5 mg, 0.2 mmol) in degassed methanol (2 mL) was added causing immediate precipitation. The solution was removed by cannular filtration and the solid washed with degassed distilled water (2 × 3 mL) *in situ* and dried under vacuum. The product was dissolved in minimal dry acetonitrile, cannular filtered and the solvent removed under vacuum to yield a deep red glassy powder (117 mg, 0.93 mmol, 93%). Calculated for $C_{68}H_{76}N_8O_4B_2Co_3$: C 64.44, H 6.00, N 8.83%. Found: C 64.31,

 

H 6.02, N 9.04%. (+ve FAB) $m/z$: 856 (M + CoL)$^+$, 628 (M)$^+$, 570 (M − Co)$^+$, 286 (M − $LCo_2$)$^+$ (L = *exo*$O_2$-cyclam). IR (KBr, cm$^{-1}$): (3607m, 3490m), 3403m br, 3232m, 3057w, 2983m, 2360m, 2015w, 1698m, 1648s, 1444w, 1383s, 1356m, 1224w, 1078m, 1032w, 914m. UV (acetone, nm ($\varepsilon$/M$^{-1}$ cm$^{-1}$)): 334 (3438), 519 (396).

### [Zn{Zn(*exo*$O_2$-cyclam)}$_2$][$BPh_4$]$_2$ (4)

Zinc(II)nitrate (89 mg, 0.3 mmol) in methanol (20 mL) was added slowly drop-wise to 2,3-dioxo-1,4,8,11-tetraazacyclotetradecane (48 mg, 0.2 mmol) in a mixture of distilled water (10 mL) and methanol (5 mL) with stirring. No colour change was observed. After stirring for a further 24 h the volume was reduced by half. Sodium tetraphenyl borate (68.45 mg, 0.2 mmol) in methanol (2 mL) was added causing an immediate white precipitate. The solution was removed by cannular filtration and the solid washed with distilled water (2 × 5 mL) then dried to yield a white powder (85 mg, 0.07 mmol, 66%) containing the product and uncomplexed ligand. [(+ve FAB) $m/z$: 645 (M)$^+$, 583 (M − Zn)$^+$, 519 (M − 2Zn)$^+$, 356 (M − LZn)$^+$, 229 (L)$^+$]. IR (KBr, cm$^{-1}$): (3560m), 3402m br, 3229m, 3056w, 2922m, 2362m, 1685s, 1621s, 1446w, 1383s, 1359m, 1181m, 1085m, 1058m, 934m.

### [Mn{Cu(*exo*$O_2$-cyclam)}$_2$][$BPh_4$]$_2$ (5)

Cu[2,3-dioxo-1,4,8,11-tetraazacyclotetradecane] (20 mg, 0.07 mmol, 2 equiv.) was dissolved in distilled water (2.5 mL). Manganese(II) dichloride (4.4 mg, 0.035 mmol, 1 equiv.) in distilled water (2 mL) was then added drop-wise over 15 min. A purple to pink colour change was observed. The mixture was allowed to stand for at least 1 h and sodium tetraphenyl borate (24 mg, 0.07 mmol, 2 equiv.) in methanol (1 mL) added in portions over 10 min causing immediate precipitation. After standing for *ca.* 30 min, the precipitate was filtered off, washed with distilled water (4 × 3 mL) *in situ* and blown under a strong stream of nitrogen. The product was then washed off the filter with acetonitrile (~5 mL). The acetonitrile was removed and the product dried under vacuum to yield a purple glassy powder (35 mg, 0.028 mmol, 79%). Calculated for $C_{68}H_{80}N_8O_6B_2Cu_2Mn$: C 62.34, H 6.11, N 8.56%. Found: C 62.31, H 5.78, N 8.68.%. (+ve FAB) $m/z$: trace 923 (M + CuL)$^+$, 633 (M)$^+$, trace 344 (M − (CuL)$^+$, 290 (M − LCuMn)$^+$ (L = *exo*$O_2$-cyclam). IR (KBr, cm$^{-1}$): 3411s br, 3230m, 3051w, 2361m, 1695w, 1616m 1613s, 1441w, 1384m, 1083w, 1014w, 934m, 734m, 706m, 668m, 613s. UV (acetone, nm ($\varepsilon$/M$^{-1}$ cm$^{-1}$)): 328 (1351), 350 (769), 413.5 (246), 502.5 (187).

### [Fe{Cu(*exo*$O_2$-cyclam)}$_2$][$BPh_4$]$_2$ (6)

Cu[*exo*$O_2$-cyclam] (20 mg, 0.07 mmol, 2 equiv.), iron(II) chloride (7 mg, 0.033 mmol, 1 equiv.), and sodium tetraphenyl borate (24 mg, 0.07 mmol, 2 equiv.) were reacted and purified as described for compound **5** to yield a yellow-brown glassy powder (37 mg, 0.027 mmol, 82%). Calculated for $C_{68}H_{76}N_8O_4B_2Cu_2Fe$: C 64.15, H 5.97, N 8.80%. Found: C 64.09, H 5.88, N 8.93%. (+ve FAB) $m/z$: 924 (M + CuL)$^+$, 634 (M)$^+$, 345 (M − (CuL)$^+$, 290 (M − LCuFe)$^+$ (L = *exo*$O_2$-cyclam). IR (KBr, cm$^{-1}$): 3412s br, 3233m, 3052m, 1699m, 1616s, 1477w, 1428m, 1384m, 1350w, 1086w, 1014w, 934m, 880m, 812m, 737m, 706, 668m, 612s. UV (acetone, nm ($\varepsilon$/M$^{-1}$ cm$^{-1}$)): 382 (2452), 459 (517), 509 (357).

### [Co{Cu(*exo*$O_2$-cyclam)}$_2$][$BPh_4$]$_2$ (7)

Cu[2,3-dioxo-1,4,8,11-tetraaza-cyclotetradecane] (20 mg, 0.07 mmol, 2 equiv.), cobalt(II) perchlorate (12.8 mg, 0.035 mmol, 1 equiv.), and sodium tetraphenyl borate (24 mg, 0.07 mmol, 2 equiv.) were reacted and purified as described for compound **5** to yield a deep red purple glassy powder (38 mg, 0.03 mmol, 86%). Calculated for $C_{68}H_{76}N_8O_4B_2Cu_2Co$: C 63.99, H 5.96, N 8.78%. Found: C 64.02, H 6.09, N 8.59%. (+ve FAB) $m/z$: trace 929 (M + CuL)$^+$, 638 (M)$^+$, 290 (M − LCuCo)$^+$ (L = *exo*$O_2$-cyclam). IR (KBr, cm$^{-1}$): 3413s br, 3231m, 3054m, 2934w, 2443w, 1614s, 1446m, 1384m, 1352w, 1088m, 1032w, 990w, 736m, 706m, 612s. UV (acetone, nm ($\varepsilon$/M$^{-1}$ cm$^{-1}$)): 332 (1924), 488 (251).

### [Ni{Cu(*exo*$O_2$-cyclam)}$_2$][$BPh_4$]$_2$ (8)

Cu[2,3-dioxo-1,4,8,11-tetraazacyclotetradecane] (20 mg, 0.07 mmol, 2 equiv.), nickel(II) nitrate (10.2 mg, 0.035 mmol, 1 equiv.), and sodium tetraphenyl borate (24 mg, 0.07 mmol, 2 equiv.) were reacted and purified as described for compound **5** to yield a pink-purple glassy powder (37 mg, 0.029 mmol, 83%). Calculated for $C_{68}H_{76}N_8O_4B_2Cu_2Ni$: C 64.02, H 5.96, N 8.79%. Found: C 63.71, H 5.96, N 8.53%. (+ve FAB) $m/z$: 636 (M)$^+$, 347 (M − (CuL)$^+$, 290 (M − LCuNi)$^+$ (L = *exo*$O_2$-cyclam). IR (KBr, cm$^{-1}$): 3414s br, 3232m, 3054m, 2850m, 2361w, 2343w, 1637m, 1616s, 1448m, 1426m, 1384s, 1088m, 1032w, 990m, 736m, 708s, 668m, 613s. UV (acetone, nm ($\varepsilon$/M$^{-1}$ cm$^{-1}$)): 330 (1432), 502 (212).

### [Zn{Cu(*exo*$O_2$-cyclam)}$_2$][$BPh_4$]$_2$ (9)

Cu[2,3-dioxo-1,4,8,11-tetraazacyclotetradecane] (29 mg, 0.1 mmol, 2 equiv.), zinc(II) chloride (6.8 mg, 0.05 mmol, 2 equiv.), and sodium tetraphenyl borate (34 mg, 0.035 mmol, 2 equiv.) were reacted and purified as described for compound **5** to yield a purple glassy powder (60 mg, 0.047 mmol, 94%). Calculated for $C_{68}H_{80}N_8O_6B_2Cu_2Zn$: C 61.93, H 6.07, N 8.50%. Found: C 61.83, H 6.03, N 8.37%. (+ve FAB) $m/z$: trace 934 (M + CuL)$^+$, 644 (M)$^+$, 354 (M − (CuL)$^+$, 290 (M − LCuZn)$^+$ (L = *exo*$O_2$-cyclam). IR (KBr, cm$^{-1}$): 3416m br, 3205m, 3054m, 2931m, 2850m, 2343w, 1607s, 1446m, 1426m, 1352s, 1088m, 1032w, 990w, 736m, 706s, 668m, 612s. UV (acetone, nm ($\varepsilon$/M$^{-1}$cm$^{-1}$)): 336 (390), 506 (160).

### [(Bipy)$_2$Ru{Cu(*exo*$O_2$-cyclam)}][$NO_3$]$_2$·2$H_2O$ (10)

[Ru(bipy)$_2$$Cl_2$]·2$H_2O$ (377 mg, 0.78 mmol) was dissolved in degassed methanol (25 mL) under $N_2$ and to this $AgNO_3$ (240 mg, 1.41 mmol in water (3 mL) was added. The resulting dark red solution was stirred for 1 h and the white AgCl precipitate was removed by filtration under $N_2$. To the red solution was added Cu(*exo*$O_2$-cyclam) (226 mg, 0.78 mmol) and stirring continued for 1 h. After filtration, the volume was reduced to 5 mL, propan-2-ol (20 mL) added and the solution stored at around 5 °C overnight. This yielded a brown precipitate (351 mg, 0.41 mmol, 53%). Calc. for $C_{30}H_{38}N_{10}O_{10}CuRu$, C 41.7; H 4.4; N 16.23%; Found C 41.25, H 3.70, N 15.69%. (+ve FAB) $m/z$: 765 (M − $NO_3^-$)$^+$, 702 (M − 2$NO_3^-$)H$^+$, 476 (M − **1**$NO_3^-$)$^+$, 413 (Ru(bipy)$_2$)$^+$, 351 (M − 2$NO_3^-$)$^{2+}$, 289 (**1**)$^+$. UV (DMF, nm ($\varepsilon$/M$^{-1}$ cm$^{-1}$)): 297 (42000), 357 (6200), 501 (5700), 526 (shoulder, 5100).

## Acknowledgements

We thank the EPSRC (DTA) and EPSRC (Supergen Excitonic Solar Cells) for financial support.

## Notes and references

1 O. Kahn, *Molecular Magnetism*, VCH Publishers Inc., Weinheim, 1993; O. Kahn, *Adv. Inorg. Chem.*, 1995, **43**, 179; O. Kahn, *Acc. Chem. Res.*, 2000, **33**, 647; K. S. Murray, *Adv. Inorg. Chem.*, 1996, **43**, 261; M. Zhao, C. Stern, A. G. M. Barrett and B. M. Hoffman, *Angew. Chem., Int. Ed.*, 2003, **42**, 462; S. L. J. Michel, B. M. Hoffman, S. Baum and A. G. M. Barrett, *Prog. Inorg. Chem.*, 2001, **20**, 473; S. Mohanta, K. K. Nanda, R. Werner, W. Haase, A. K. Mukherjee, S. K. Dutta and K. Nag, *Inorg. Chem.*, 1997, **36**, 4656.

2 I. O. Fritsky, R. Ott, H. Pritzkow and R. Krämer, *Chem.–Eur. J.*, 2001, **7**, 1221.

3 S. Torelli, C. Belle, I. Gautier-Luneau and J. L. Pierre, *Inorg. Chem.*, 2000, **39**, 3526.

4 N. Robertson, *Angew. Chem., Int. Ed.*, 2006, **45**, 2338; C. A. Bignozzi, R. Argazzi and C. J. Kleverlaan, *Chem. Soc. Rev.*, 2000, **29**, 87.

5 G. Seeber, B. M. Kariuki and L. Cronin, *Chem. Commun.*, 2002, 2912.

6 (*a*) R. Tripier, O. Siri, F. Rabiet, F. Denat and R. Guillard, *Tetrahedron Lett.*, 1999, **40**, 79; (*b*) J. Chen, D.-Z. Liao, Z.-H. Jiang and S.-P. Yan, *J. Coord. Chem.*, 2005, **58**, 787; J.-K. Tang, O.-Y. Yan, H.-B. Zhou, Y.-Z. Li, D.-Z. Liao, Z.-H. Jiang, S.-P. Yan and P. Cheng, *Cryst. Growth Des.*, 2005, **5**, 813; (*c*) E.-Q. Gao, G.-M. Yang, J.-K. Tang, D.-Z. Liao, Z.-H. Jiang and S.-P. Yan, *Polyhedron*, 1999, **18**, 3643; (*d*) R. Tripier, F. Denat, R. Guilard and H. Ledon, *Fr. Pat.*, FR 2810035 A1, 2001; (*e*) F. Kou, S. Zhu, H. Lin, K. Ma and Y. Chen, *Polyhedron*, 1997, **16**, 741.

7 L. Cronin, P. A. McGregor, S. Parsons, S. Teat, R. O. Gould, V. A. White, N. J. Long and N. Robertson, *Inorg. Chem.*, 2004, **43**, 8023; L. Cronin, A. R. Mount, S. Parsons and N. Robertson, *J. Chem. Soc., Dalton Trans.*, 1999, 1925.

8 V. A. White, N. J. Long and N. Robertson, *Org. Biomol. Chem.*, 2005, **3**, 4268.

9 M. R. McDonald, W. M. Scheper, H. D. Lee and D. W. Margerum, *Inorg. Chem.*, 1995, **34**, 229.

10 L. Siegfried and T. A. Kaden, *Helv. Chim. Acta*, 1984, **67**, 29.

11 P. Chautemps, G. Gellon, B. Morin, J. L. Pierre, C. Provent, S. M. Refaif, C. G. Beguin, A. Elmarzouki, G. Serratrice and E. Saintaman, *Bull. Soc. Chim. Fr.*, 1994, **131**, 434; L. Fremond, E. Espinosa, M. Meyer, F. Denat, R. Guilard, V. Huch and M. Veith, *New J. Chem.*, 2000, **24**, 959.

12 E. Kimura, Y. Kurogi, T. Tojo, M. Shionoya and M. Shiro, *J. Am. Chem. Soc.*, 1991, **113**, 4857; E. Kimura, *Tetrahedron*, 1992, **48**, 6175.

13 E.-Q. Gao, W.-M. Bu, G.-M. Yang, D.-Z. Liao, Z.-H. Jiang, S.-P. Yan and G.-L. Wang, *J. Chem. Soc., Dalton Trans.*, 2000, 1431.

14 H.-Z. Kou, B. C. Zhou, S. Gao and R.-J. Wang, *Angew. Chem., Int. Ed.*, 2003, **42**, 3288; J.-K. Tang, S.-F. Si, L.-Y. Wang, D.-Z. Liao, Z.-H. Jiang, S.-P. Yan, P. Cheng and X. Liu, *Inorg. Chim. Acta*, 2003, **343**, 288; J.-K. Tang, S.-F. Si, L.-Y. Wang, D.-Z. Liao, Z.-H. Jiang, S.-P. Yan, P. Cheng and X. Liu, *Inorg. Chem. Commun.*, 2002, **5**, 1012; J.-K. Tang, S. F. Si, E.-Q. Gao, D.-Z. Liao, Z.-H. Jiang and S.-P. Yan, *Inorg. Chim. Acta*, 2002, **332**, 146; J.-K. Tang, L.-Y. Wang, L. Zhang, E.-Q. Gao, D.-Z. Liao, Z.-H. Jiang, S.-P. Yan and P. Cheng, *J. Chem. Soc., Dalton Trans.*, 2002, 1607; J.-K. Tang, Y.-Z. Li, Q.-L. Wang, E.-Q. Gao, D.-Z. Liao, Z.-H. Jiang, S.-P. Yan, P. Cheng, L.-F. Wang and G.-L. Wang, *Inorg. Chem.*, 2002, **41**, 2188; H.-Z. Kou, B. C. Zhou and R.-J. Wang, *Inorg. Chem.*, 2003, **42**, 7658; Y. Ouyang, L.-H. Yu, D.-Z. Liao, Z.-H. Jiang and S.-P. Yan, *J. Coord. Chem.*, 2005, **58**, 1361; J.-K. Tang, O.-Y. Yan, H.-B. Zhou, Y.-Z. Li, D.-Z. Liao, Z.-H. Jiang, S.-P. Yan and P. Cheng, *Cryst. Growth Des.*, 2005, **5**, 813; J.-K. Tang, Q.-L. Wang, S.-F. Si, D.-Z. Liao, Z.-H. Jiang, S.-P. Yan and P. Cheng, *Inorg. Chim. Acta*, 2005, **358**, 325; J.-K. Tang, Q.-L. Wang, E.-Q. Gao, J.-L. Chen, D.-Z. Liao, Z.-H. Jiang, S.-P. Yan and P. Cheng, *Helv. Chim. Acta*, 2002, **85**, 175.

15 A. Escuer, R. Vicente, J. Ribas, R. Costa and X. Solans, *Inorg. Chem.*, 1992, **31**, 2627.

16 C. Benelli, A. C. Fabretti and A. Giusti, *J. Chem. Soc., Dalton Trans.*, 1993, 409; O. Kahn, Y. Journaux and J. Sletten, *Inorg. Chem.*, 1986, **25**, 439.

17 T. Sanada, T. Suzuki and S. Kaizaki, *J. Chem. Soc., Dalton Trans.*, 1998, 959.

18 N. Fukita, M. Ohba, T. Shiga, H. Okawa and Y. Ajiro, *J. Chem. Soc., Dalton Trans.*, 2001, 64.

19 O. Kahn, *Prog. Inorg. Chem.*, 1995, 179.

20 J. L. Sanz, B. Cervera, R. Ruiz, C. Bois, J. Faus, F. Lloret and M. Julve, *J. Chem. Soc., Dalton Trans.*, 1996, 1359.

21 S.-B. Wang, R.-F. Li, G.-M. Yang, D.-Z. Liao, Z.-H. Jiang and S.-P. Yan, *Inorg. Chim. Acta*, 2005, **358**, 2595.

22 C. F. Macrae, P. R. Edgington, P. McCabe, E. Pidcock, G. P. Shields, R. Taylor, M. Towler and J. van de Streek, *J. Appl. Crystallogr.*, 2006, **39**, 453–457.

23 D. A. Fletcher, R. F. McMeeking and D. J. Parkin, *J. Chem. Inf. Comput. Sci.*, 1996, **36**, 746.

24 E. Sinn and C. M. Harris, *Coord. Chem. Rev.*, 1969, **4**, 391.

25 E.-Q. Gao, G.-M. Yang, D.-Z. Liao, Z.-H. Jiang, S.-P. Yan and G.-L. Wang, *Transition Met. Chem.*, 1999, **24**, 244.

26 S.-B. Wang, G.-M. Yang, D.-Z. Liao and L.-C. Li, *Inorg. Chem.*, 2004, **43**, 852.

27 E.-Q. Gao, D.-Z. Liao, Z.-H. Jiang and S.-P. Yan, *Polyhedron*, 2001, **20**, 923.

28 E.-Q. Gao, J.-K. Tang, D.-Z. Liao, Z.-H. Jiang, S.-P. Jan and G.-L. Wong, *Helv. Chim. Acta*, 2001, **84**, 908.

29 A. Altomare, M. Cascarano, C. Giacovazzo and A. Guagliardi, *J. Appl. Crystallogr.*, 1994, **26**, 343.

30 P. W. Betteridge, J. R. Carruthers, R. I. Cooper, K. Prout and D. J. Watkins, *J. Appl. Crystallogr.*, 2003, **36**, 1487.

 

# Spectroscopic, electrochemical and computational study of Pt–diimine–dithiolene complexes: rationalising the properties of solar cell dyes†

**Elaine A. M. Geary,[a] Keri L. McCall,[a] Andrew Turner,[a] Paul R. Murray,[a] Eric J. L. McInnes,[b] Lorna A. Jack,[a] Lesley J. Yellowlees[a] and Neil Robertson*[a]**

***Received 2nd January 2008, Accepted 22nd April 2008***
***First published as an Advance Article on the web 29th May 2008***
**DOI: 10.1039/b719789f**

A series of [Pt(II)(diimine)(dithiolate)] complexes of general formula [Pt{X,X′-$(CO_2R)_2$-bpy}(mnt)] (where X = 3, 4 or 5; R = H or Et, bpy = 2,2′-bipyridyl and mnt = maleonitriledithiolate), have been spectroscopically, electrochemically and computationally characterised and compared with the precursors [Pt{X,X′-$(CO_2R)_2$-bpy}$Cl_2$] and X,X′-$(CO_2R)_2$-bpy. The study includes cyclic voltammetry, *in situ* EPR spectroelectrochemical studies of fluid solution and frozen solution samples, UV/Vis/NIR spectroelectrochemistry, hyrid DFT and TD-DFT calculations. The effect of changing the position of the bpy substituents from 3,3′ to 4,4′ and 5,5′ is discussed with reference to electronic changes seen within the different members of the family of molecules. The performance of the mnt complexes in dye-sensitised solar cells has been previously described and the superior performance of [Pt{3,3′-$(CO_2R)_2$-bpy}(mnt)] is now explained in terms of decreased electronic delocalisation through twisting of the bipyridyl ligand as supported by the EPR and computational results.

## Introduction

Complexes of Pt(II) with polypyridyl ligands have been widely studied due to properties including redox activity, solvatochromism and luminescence.[1,2] In most cases, ligands on the Pt centre can be readily varied, allowing for manipulation of the molecular and electronic properties of these complexes making them useful as model systems for the study of many physical properties. In recent years square-planar Pt(II) coordination complexes have also been studied for their potential use in the area of dye-sensitised solar cells (DSSCs)[3–6] and in solar to chemical energy conversion.[7] In a DSSC, a dye molecule is adsorbed on to the surface of a semiconductor (usually $TiO_2$). Upon illumination with visible light, the photo-excited dye injects an electron into the conduction band of the semiconductor, which is supported on a transparent electrode. The dye is re-reduced by a redox couple (typically $I^-/I_3^-$), which in turn is regenerated at the counter electrode, thus completing the circuit.[8]

The dye molecule in a DSSC requires a linker moiety which attaches the dye to the surface of the semiconductor[9] and in the large majority of studies this has been the (4,4′-$CO_2H)_2$-bpy ligand (bpy = 2,2′-bipyridyl). The 4,4′-substituted carboxylic acid groups on the bpy bind to the surface of the semiconductor allowing electron transfer from the excited dye molecule to the semiconductor. This electron transfer reaction is facilitated by the interaction of the π* orbital on the substituted bpy with the 3d orbital manifold of the conduction band of the $TiO_2$.

An attractive feature of [Pt(diimine)(dithiolene)] complexes is the ease with which the HOMO and LUMO of the molecule can be separately tuned. Over the past two decades, Eisenberg *et al.* have systematically studied the electrochemistry and luminescence of a range of these molecules by sequentially changing the substituents on the diimine and dithiolene components.[2] This has shown that the excited state energies can be tuned by up to 1 eV. Such studies have demonstrated that the LUMO on [Pt(II)(diimine)(dithiolate)] complexes is located on the diimine functionality and the HOMO is a mixture of Pt(d) and S(p) orbital character. The visible charge-transfer transition for these molecules is therefore assigned as a MMLL′CT (mixed metal–ligand to ligand charge transfer) from the Pt/S HOMO to the diimine based LUMO.[1,2,10] These previous studies have focussed almost exclusively on complexes with 4,4′-disubstitued diimine ligands.[1,2,10]

We have recently reported the synthesis and study in DSSCs of a series of [Pt(II)(diimine)(dithiolate)] complexes, that bind to the semiconductor surface through a bpy ligand substituted with carboxylic acid groups at the positions, 3,3′, 4,4′ and 5,5′ respectively. The solar-energy conversion efficiencies of the resulting complexes were studied and interestingly showed the 3,3′-disubstituted bpy molecule to be the most efficient sensitiser of those tested.[6] In marked contrast, studies of Ru–bpy dyes (the most efficient class of sensitiser) in DSSCs have focussed almost entirely

[a]*School of Chemistry, University of Edinburgh, King's Buildings, Edinburgh, UK EH9 3JJ. E-mail: neil.robertson@ed.ac.uk; Fax: +44 1316504743; Tel: +44 1316504755*
[b]*School of Chemistry, University of Manchester, Oxford Road, Manchester, UK M13 9 PL*

† Electronic supplementary information (ESI) available: Table S1: UV/Vis of oxidised and reduced species; Fig. S1–S4: UV/Vis spectra of **2a**$^{0/1-}$, **2b**$^{0/1-/2-}$, **2c**$^{0/1-/2-}$, **2c**$^{0/1+}$; Fig. S5–S7: EPR of **1b**$^{1-}$, **2c**$^{1-}$, **1b**$^{1-}$ (frozen); Tables S2 and S3: frontier orbital energies of **2a**, **3a**; Table S4: calculated contribution of ring C and N atoms to the LUMO of **1c**, **2c**, **3c**; Table S5: calculated frontier orbital energies of **1b**, **1c**, **2c**, **3c**; Fig. S8–S17 representations of frontier orbitals of **2a**, **3a**, **2c**, **3c**, **1b**; Table S6: comparison of calculated and experimental structure of **1c**; Table S7: calculated energies and % contributions of HOMO and LUMO for **1b**, **1c**, **2c**, and **3c**; Tables S8–S10: TD-DFT results for **1c**, **2c**, **3c**; Fig. S10: TD-DFT results for **2c**, **3c**. See DOI: 10.1039/b719789f

on 4,4′-substitution. We are only aware of one Ru dye involving 3,3′-$(CO_2H)_2$-bpy ligands that has been studied in DSSCs and this showed slightly poorer results than the analogous Ru complex with 4,4′-$(CO_2H)_2$-bpy ligands.[11] Presumably, the slightly poorer performance is the reason for the lack of further interest, however our results on Pt complexes suggest that 3,3′-$(CO_2H)_2$-bpy ligands are worth revisiting.

Following this discovery, the aim of the current work is to greatly extend our understanding of the electronic properties of [Pt{X,X′-$(CO_2Et)_2$-bpy}(mnt)] (X = 3, 4 or 5; mnt = maleonitriledithiolate) by systematic electronic characterisation of each member of this family and comparison with related precursors, (Fig. 1) using UV/Vis/NIR spectroelectrochemistry, *in situ* EPR spectroelectrochemistry and DFT calculations. In particular, this allows insight into the bpy based LUMO which influences not only the photophysical and electronic properties of the molecules, but also the coupling to $TiO_2$ and consequent electronic properties of the composite system. We have reported some initial work on the UV/Vis/NIR spectroelectrochemistry of **1c–3c**[6] in our original study and this is incorporated here in the discussion.

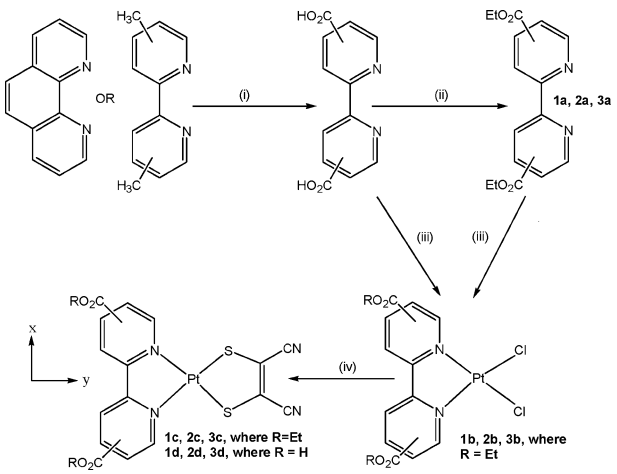


**Fig. 1** Synthesis of members of the family of [Pt{X,X′-$(CO_2R)_2$-bpy}(mnt)]. (i) $KMnO_4$(aq.), 120 °C/HCl; (ii) $EtOH/H_2SO_4$, 115 °C; (iii) $K_2PtCl_4$, 125 °C; (iv) $Na_2$(mnt), RT (140 °C for **2c**). The principle axis system for the EPR analysis is also shown with the *z*-axis perpendicular to the molecular plane.

## Results and discussion

### (i) Electrochemistry

The electrochemistry of the [Pt{X,X′-$(CO_2Et)_2$-bpy}(mnt)] family (**1c–3c**), the related [Pt{X,X′-$(CO_2Et)_2$-bpy}$Cl_2$] precursor molecules (**1b–3b**) and the corresponding uncoordinated bpy ligands (**1a–3a**) was studied by cyclic voltammetry in a solution of 0.1 M $TBABF_4$ in DMF at 293 K. Redox potentials for all processes are listed in Table 1.

The electrochemical properties show various trends which are common within each of the 3,3′, 4,4′ and 5,5′ motifs. In each case the free bpy ligand shows either one or two reductions within the solvent window. On binding to the Pt centre, the reduction potentials significantly shift to more positive values due to the stabilisation of the LUMO after complexation of the free ligand to the Pt metal. On substitution of the two chloride ligands with the mnt ligand, each [Pt{X,X′-$(CO_2Et)_2$-bpy}(mnt)] complex (**1c**, **2c** and **3c**) shows two fully reversible reductions, the potentials of which remain similar to those of their respective [Pt{X,X′-$(CO_2Et)_2$-bpy}$Cl_2$] precursors (Fig. 2), particularly for the first reduction. This shows that there is only a small effect on the LUMO of the complex after substitution of the chloride ligands for mnt, consistent with assignment of the LUMO as bpy based.[2]

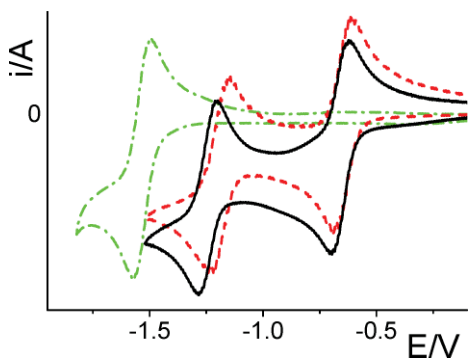


**Fig. 2** Cyclic voltammogram showing reduction processes for **2a** (dash–dot green), **2b** (solid black) and **2c** (dashed red) in 0.1 M $TBABF_4$–DMF at 293 K and scan rate 0.1 V $s^{-1}$.

In addition, each of the [Pt{X,X′-$(CO_2Et)_2$-bpy}(mnt)] complexes (**1c**, **2c** and **3c**) shows one irreversible oxidation at a similar

**Table 1** Redox potentials of the [Pt{X,X′-$(CO_2Et)_2$-bpy}(mnt)] family and related precursor molecules and ligands[a]

| No. | Compound | $E_2$/V | $E_1$/V | $E_{ox}$/V |
|---|---|---|---|---|
| **1a** | 3,3′-$(CO_2Et)_2$-bpy | — | −1.84 | — |
| **1b** | [Pt{3,3′-$(CO_2Et)_2$-bpy}$Cl_2$] | −1.27 | −0.61 | — |
| **1c** | [Pt{3,3′-$(CO_2Et)_2$-bpy}(mnt)] | −1.20 | −0.59 | 1.35∗ |
| **1d** | [Pt{3,3′-$(CO_2H)_2$-bpy}(mnt)] | −1.05∗ | −0.69∗ | 1.27∗ |
| **2a** | 4,4′-$(CO_2Et)_2$-bpy | — | −1.53 | — |
| **2b** | [Pt{4,4′-$(CO_2Et)_2$-bpy}$Cl_2$] | −1.25 | −0.67 | — |
| **2c** | [Pt{4,4′-$(CO_2Et)_2$-bpy}(mnt)] | −1.20 | −0.65 | 1.39∗ |
| **2d** | [Pt{4,4′-$(CO_2H)_2$-bpy}(mnt)] | −1.19 | −0.82∗ | 1.27∗ |
| **3a** | 5,5′-$(CO_2Et)_2$-bpy | −1.61 | −1.23 | — |
| **3b** | [Pt{5,5′-$(CO_2Et)_2$-bpy}$Cl_2$] | −1.03 | −0.53 | — |
| **3c** | [Pt{5,5′-$(CO_2Et)_2$-bpy}(mnt)] | −0.99 | −0.52 | 1.41∗ |
| **3d** | [Pt{5,5′-$(CO_2H)_2$-bpy}(mnt)] | −1.16 | −0.69∗ | 1.27∗ |

[a] * irreversible, § quasi reversible reduction.

potential to each other, consistent with location of the HOMO on the dithiolate moiety.

Reduction of the free ligand becomes harder in the order {5,5′-$(CO_2Et)_2$-bpy}, {4,4′-$(CO_2Et)_2$-bpy}, {3,3′-$(CO_2Et)_2$-bpy}, since the electron-withdrawing groups at the 5,5′ position of the bpy provide greater stabilisation of the monoanion than substituents at the 4,4′ or 3,3′ positions.[12] The electrochemistry of [Pt{5,5′-$(CO_2Et)_2$-bpy}(mnt)] (**3c**) shows both reductions at the least negative potential of the series **1c–3c**, as expected,[12] however the first reduction potential ($E_1$) of [Pt{3,3′-$(CO_2Et)_2$-bpy}(mnt)] (**1c**) occurs at less negative potential than that of [Pt{4,4′-$(CO_2Et)_2$-bpy}(mnt)] (**2c**) which is in contrast with the reduction potentials of the free ligands **1a** and **2a**. The crystal structure of [Pt{3,3′-$(CO_2Et)_2$-bpy}(mnt)] previously reported by us[6] shows a significant torsion angle (30.7°) between the two pyridine rings of the bpy moiety while [Pt(II)(bpy)(dithiolate)] complexes with substituents at the 4,4′ positions have much smaller torsion angles *e.g.* 0.68° for a di-Me substituted bpy,[13] and 12.69° for a di-tBu substituted bpy[14] (the biggest for any 4,4′-disubstituted bpy). This suggests that the structural differences between the 3,3′ and 4,4′ disubstituted molecules influence their relative electrochemical responses and this results in the first reduction of **1c** being intermediate between that of **2c** and **3c**. For each of the molecules studied, the separation of the first and second reduction is between 0.36 V and 0.66 V. This is associated with the spin pairing energy of the two added electrons in the same orbital (*vide infra*).

The electrochemistry of the carboxylic acid substituted complexes (**1d**, **2d** and **3d**) shows broadly similar oxidation and reduction potentials to those of the ester-substituted complexes (**1c**, **2c** and **3c**), suggesting that the more-soluble ester species used for convenience in the further studies below are good models for the acid derivatives used in DSSCs.

### (ii) Spectroelectrochemistry

UV/Vis/NIR spectroelectrochemistry of reduced **1c**, **2c** and **3c** was reported in our prior work[6] and in this work we have also studied the spectroelectrochemistry of the corresponding species **1a**,**b**, **2a**,**b** and **3a**,**b** as well as oxidations of **1c**, **2c** and **3c**, which were observed to be chemically reversible at −60 °C (observed absorptions are tabulated in the ESI, Table S1, Fig. S1–S4†). Electrochemical reduction to the monoanionic and dianionic species for **1a–c**, **2a–c** and **3a–c** show similar trends. For the complexes **1–3b** and **1–3c**, similar bands appeared compared with the free ligands **1–3a** consistent with the reduction electron locating on the bpy ligand. Spectral features of the reduced, substituted bpy ligands in turn were similar to the unsubstituted $bpy^{1-}$.[15] Upon oxidation of **1c**, **2c** and **3c**, each of the spectra show similar features (*e.g.* Fig. S4†). On generation of the $\mathbf{1c}^{1+}$, $\mathbf{2c}^{1+}$ and $\mathbf{3c}^{1+}$, the peaks associated with the π–π* transition of the coordinated bpy shift to lower energy. This has previously been shown in a study of $[Ru(bpy)_3]^{3+}$ and $[Ir(bpy)_3]^{3+}$ where the π–π* transition of the coordinated bpy shifted to lower energy as the positive charge on the complex was increased.[16,17] In the monooxidised species, the decrease in intensity of the peak at 19 000 $cm^{-1}$, which has already been assigned as a MMLL′CT peak from the mnt moiety, is consistent with the site of oxidation as based at least in part on the mnt motif.

### (iii) EPR in fluid solution

*In situ* EPR spectroelectrochemistry was performed on each member of the [Pt{X,X′-$(CO_2Et)_2$-bpy}(mnt)] series (**1c**, **2c**, **3c**) and comparison made where possible with the precursor species **1a**,**b**, **2a**,**b** and **3a**,**b**. Data observed were broadly comparable to previous studies of related complexes.[18]

#### (a) Reduced 3,3′-$(CO_2Et)_2$-bpy ligand and complexes ($\mathbf{1a}^{1-}$, $\mathbf{1b}^{1-}$, $\mathbf{1c}^{1-}$)

Reduction of **1c** in a solution of 0.1 M $TBABF_4$ in DMF at 233K gives an EPR active solution of $\mathbf{1c}^{1-}$. The coupling to the ligand nuclei is best resolved at 293 K (Fig. 3) and the coupling constants for $\mathbf{1c}^{1-}$ are presented, alongside those of $\mathbf{1b}^{1-}$ (Fig. S5†) in Table 2. Coupling is observed to the Pt centre, two ring N atoms and two ring H atoms. These are most likely to be the hydrogens in the 5,5′ positions as this has previously been shown to be the most electronically important position.[12] This assignment is supported by DFT calculations (*vide infra*) that show the LUMO of the neutral complex to have a much higher contribution from the ring carbons in the 5-position than any of the other carbon atoms of

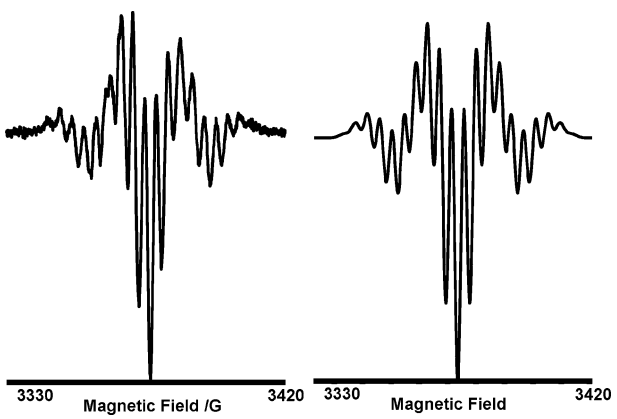


**Fig. 3** Left: 2nd derivative EPR spectrum of $\mathbf{1c}^{1-}$ in 0.1 M $TBABF_4$–DMF at 293 K. Right: simulated spectrum using parameters given in Table 2.

**Table 2** EPR data for $\mathbf{1b}^{1-}$ and $\mathbf{1c}^{1-}$ in 0.1 M $TBABF_4$ in DMF at 293 K. All hyperfine coupling constants given in G with $10^{-4}$ $cm^{-1}$ in parenthesis. Δ = linewidth

| | $\mathbf{1b}^{1-}$ | $\mathbf{1c}^{1-}$ | $\mathbf{2b}^{1-}$ | $\mathbf{2c}^{1-}$ | $\mathbf{3b}^{1-}$ | $\mathbf{3c}^{1-}$ |
|---|---|---|---|---|---|---|
| $a_{iso}$ (H × 2) | 3.7 (3.4) | 4.0 (3.7) | | | | |
| $a_{iso}$ (N × 2) | 3.7 (3.4) | 4.0 (3.7) | | | | |
| $a_{iso}$ (Pt) | 45.5 (42.2) | 42.0 (39.2) | 59.5 (54.9) | 56.0 (52.1) | 39 | 36 |
| Δ | 4.1 | 4.3 | | | | |
| *g* | 1.997 | 2.001 | 1.988 | 1.994 | 1.994 | 1.967 |

the ring (Table S4†). On introduction of another electron to each complex and formation of $\mathbf{1b}^{2-}$ and $\mathbf{1c}^{2-}$ respectively, the signal collapses as the second electron enters the same orbital as the first and they spin pair. The similarities between the spectra of $\mathbf{1b}^{1-}$ and $\mathbf{1c}^{1-}$ are consistent with the reduction electron entering an orbital primarily located on the derivatised bpy motif analogous to the results found in the UV/Vis/NIR spectroelectrochemistry experiments. We were unable to obtain the spectrum for $\mathbf{1a}^{1-}$ due to poor stability in the reduced form.

### (b) Reduced 4,4′-$(CO_2Et)_2$-bpy ligand and complexes ($\mathbf{2a}^{1-}$, $\mathbf{2b}^{1-}$, $\mathbf{2c}^{1-}$)

*In situ* reduction of the ligand (**2a**) gives an EPR active solution (Fig. 4) with coupling constants listed in Table 3. The reduction electron couples strongly to the ring nitrogen and to one ring hydrogen on each pyridine ring. Again, the ring hydrogen atoms that show strong coupling can be assigned as those in the 5-position through DFT calculations that show the carbons in these positions give much the largest contribution to the LUMO of the neutral compound compared with the other ring carbons (Table 3).

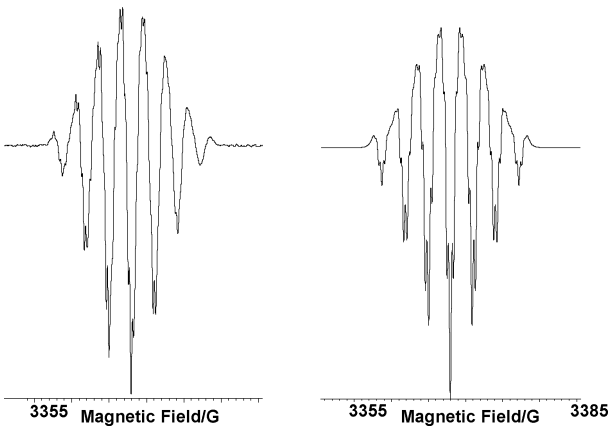


**Fig. 4** Left: EPR spectrum of $\mathbf{2a}^{1-}$ in 0.1 M $TBABF_4$–DMF at 233 K. $E_{gen} = -1.85$ V. Right: simulated EPR spectrum of $\mathbf{2a}^{1-}$ using parameters given in Table 3.

The solution EPR of $\mathbf{2b}^{1-}$ at 233 K in solution of 0.1 M $TBABF_4$ in DMF shows a broad line with two $^{195}Pt$ satellites and any coupling to the ligand nuclei for this species remains unresolved at a range of temperatures. This is analogous to the *in situ* EPR spectroelectrochemistry results for the related complex $\mathbf{2c}^{1-}$. As was the case for $\mathbf{1b}^{2-}$ and $\mathbf{1c}^{2-}$, on introduction of another electron to form both $\mathbf{2b}^{2-}$ and $\mathbf{2c}^{2-}$ the signals collapse as the second electron enters the same orbital as the first and they spin pair forming a diamagnetic species.

### (b) Reduced 5,5′-$(CO_2Et)_2$-bpy ligand and complexes ($\mathbf{3a}^{1-}$, $\mathbf{3b}^{1-}$, $\mathbf{3c}^{1-}$)

The *in situ* EPR spectrum of the $\{5,5'\text{-}(CO_2Et)_2\text{-bpy}\}^{1-}$ ligand ($\mathbf{3a}^{1-}$) shows coupling of the reduction electron to the two ring nitrogen atoms, and two sets of two ring hydrogen atoms assigned as shown in Table 3. It is of note in this case that no large coupling to ring hydrogens occurs since the most electronically important 5-positions contain the ester substituents rather than H-atoms.

The solution EPR of $\mathbf{3b}^{1-}$ at 273 K in solution of 0.1 M $TBABF_4$ in DMF shows coupling of the reduction electron to the $^{195}Pt$ nucleus. Any coupling to the ligand nuclei for this species remains unresolved at a range of temperatures similar to the results found for $\mathbf{2b}^{1-}$. Again in this case the EPR spectrum of $\mathbf{3c}^{1-}$ is analogous to the *in situ* EPR spectrum for the related dichloride complex $\mathbf{3b}^{1-}$ which shows a similar magnitude of the coupling of the reduction electron to the Pt nucleus.

### (iv) EPR in frozen solutions

On cooling to 173 K rhombic X-band EPR spectra were obtained for $\mathbf{1b}^{1-}$, $\mathbf{1c}^{1-}$ and $\mathbf{2c}^{1-}$ and, following spectral simulation, the parameters obtained are listed in Table 4. For all compounds, the average of $g_1 + g_2 + g_3$ is in good agreement with $g_{iso}$. The small shift in $g_{iso}$ from the free electron value, $g_e$ of 2.0023 suggests that there is only a small admixture of metal orbitals in the SOMO and that the reduction electron is therefore based mainly on the bpy ligand. These results reiterate the findings of the

**Table 3** EPR coupling constants for $\mathbf{2a}^{1-}$ and $\mathbf{3a}^{1-}$ in 0.1 M $TBABF_4$–DMF at 233 K. All hyperfine coupling constants given in G. $\Delta$ = linewidth. For comparison, the calculated percentage contribution to the LUMO from the ring carbon and nitrogen atoms for the neutral compounds is given, with the position of the atom on the bipy ring shown in parentheses

| Parameter | $\mathbf{2a}^{1-}$ | %LUMO | $\mathbf{3a}^{1-}$ | %LUMO |
|---|---|---|---|---|
| $a_{iso}$ (H × 2) | 3.45 | 13.41 (5-position) | 0.90 | 5.89 (4-position) |
| $a_{iso}$ (H × 2) | 0.42 | 0.11 (6-position) | — | 1.88 (6-position) |
| $a_{iso}$ (H × 2) | 0.40 | 0.10 (3-position) | 0.41 | 3.78 (3-position) |
| $a_{iso}$ (N × 2) | 2.90 | 12.75 | 1.30 | 5.62 |
| $\Delta$ | 0.56 | | 0.69 | |
| $g$ | 2.004 | | 2.003 | |

**Table 4** EPR parameters of compounds in 0.1 M $TBABF_4$–DMF at 173 K. The $A_{iso}$ values are taken from solution spectra. Nominal $A_3$ values of 20 G were used in the simulations as these are not resolved. The $A_3$ values in the table are calculated as $3A_{iso} - (A_1 + A_2)$. $W_{1\text{–}3}$ refer to linewidths

| Compound | $g_{iso}$ | $g_1$ | $g_2$ | $g_3$ | $A_{iso}/cm^{-1}$ | $A_1/cm^{-1}$ | $A_2/cm^{-1}$ | $A_3/cm^{-1}$ | $W_1$/G | $W_2$/G | $W_3$/G |
|---|---|---|---|---|---|---|---|---|---|---|---|
| **1b** | 1.9975 | 2.038 | 2.012 | 1.972 | $42.2 \times 10^{-4}$ | $44 \times 10^{-4}$ | $60 \times 10^{-4}$ | $23 \times 10^{-4}$ | 5 | 7 | 18 |
| **1c** | 2.0014 | 2.033 | 2.019 | 1.975 | $39.2 \times 10^{-4}$ | $40 \times 10^{-4}$ | $49 \times 10^{-4}$ | $29 \times 10^{-4}$ | 5 | 7 | 18 |
| **2c** | 1.994 | 2.044 | 2.025 | 1.936 | $52.1 \times 10^{-4}$ | $55 \times 10^{-4}$ | $64 \times 10^{-4}$ | $37 \times 10^{-4}$ | 8 | 8 | 20 |

UV/Vis/NIR spectroelectrochemical study whereby the reduction electron locates itself on the bpy motif. In each case, coupling was resolved to the $^{195}$Pt nucleus for each of the *g*-components but no further splittings to ligand nuclei were resolved. Experimental and simulated spectra are shown in Fig. 5 and 6 and S7.† Previous studies have shown that the singly-occupied orbital in related complexes is of $b_2$ symmetry assuming $C_{2v}$ point symmetry with metal contributions to the singly occupied orbital consisting of $5d_{yz}$ and $6p_z$ contributions. (The principle axes are defined as shown in Fig. 1.[18]) The contribution of these orbitals to the SOMO can be determined using eqn (1)–(3).[18,19]

$$A_{xx} = A_s - (4/7)P_d a^2 - (2/5)P_p b^2 \quad (1)$$

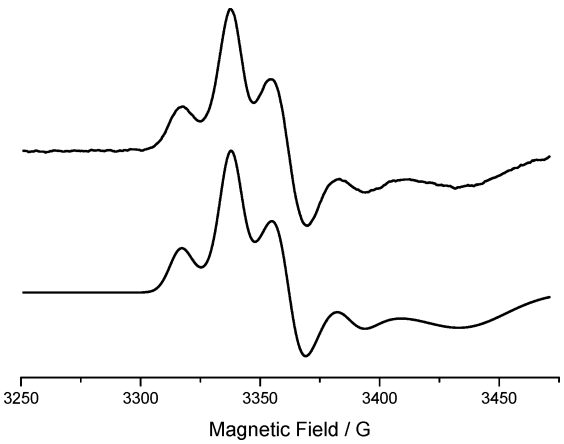


**Fig. 5** EPR spectrum of $\mathbf{1c}^{1-}$ in a solution of 0.1 M $TBABF_4$ in DMF at 173 K. $E_{gen} = -2.0$ V. Simulated spectrum shown beneath.

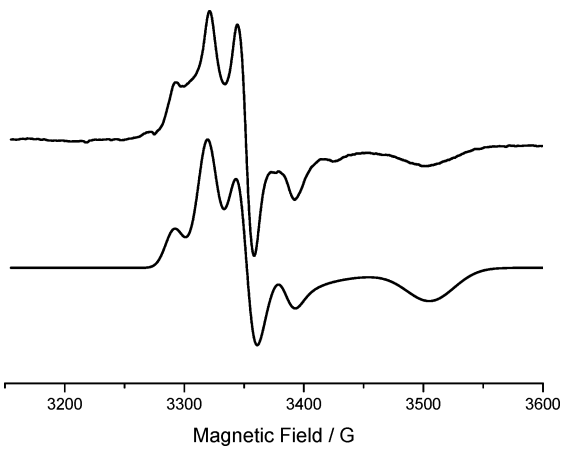


**Fig. 6** EPR spectrum of $\mathbf{2c}^{1-}$ in a solution of 0.1 M $TBABF_4$ in DMF at 173 K. $E_{gen} = -1.15$ V. Simulated spectrum shown beneath.

$$A_{yy} = A_s - (2/7)P_d a^2 - (2/5)P_p b^2 \quad (2)$$

$$A_{zz} = A_s + (2/7)P_d a^2 + (4/5)P_p b^2 \quad (3)$$

The parameters $a^2$ and $b^2$ are respectively the contribution of $5d_{yz}$ and $6p_z$ to the SOMO, $P_d$ and $P_p$ are the electron nuclear dipolar coupling parameters for platinum 5d and 6p electrons respectively and $A_s$ is the isotropic Fermi contact term. Using calculated values $P_d = 0.0549$ cm$^{-1}$ and $P_p = 0.0402$ cm$^{-1}$,[20] we can derive values for $a^2$ and $b^2$ (Table 5).

This allows us to compare the effects of mnt substitution for two chloride ligands by examination of the values for $\mathbf{1b}^{1-}$ and $\mathbf{1c}^{1-}$. It is apparent that a reduction in Pt contribution to the SOMO occurs in the mnt complex $\mathbf{1c}^{1-}$ and this may be associated with greater electron delocalisation in the latter consistent with the extended conjugation of the mnt. Likewise, we can compare the influence of altering the ester groups from the 4,4′ to the 3,3′-positions ($\mathbf{2c}^{1-}$ and $\mathbf{1c}^{1-}$). The former shows a noticably higher Pt contribution to the SOMO. This may be rationalised in terms of a better overlap between the bpy and the Pt orbitals for the 4,4′-derivative due to greater planarity across the molecules, whereas the twist in the bpy ligand of the 3,3′-analogue reduces the orbital overlap of the bpy ligand with the Pt centre.

### (v) DFT calculations and discussion

To further interpret the electronic character of these complexes, hybrid density functional theory (DFT) calculations were performed on **1b**, **1c**, **2a**, **2c**, **3a** and **3c** (see Experimental section for details). Plots of the isosurfaces and calculated energies of the HOMO, LUMO, HOMO − 1 and LUMO + 1 orbitals can be found in Fig. 7 (**1c**) and in the ESI (Fig. S8–S17†). A comparison of selected

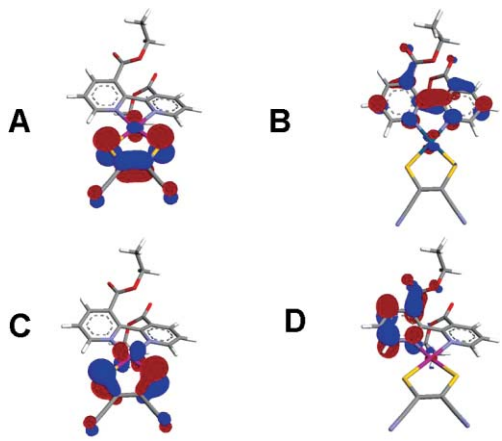


**Fig. 7** (A) Calculated HOMO of **1c**. (B) Calculated LUMO of **1c**. (C) Calculated HOMO − 1 of **1c**. (D) Calculated LUMO + 1 of **1c**.

**Table 5** Platinum $5d_{yz}$ and $6p_z$ admixtures and total contribution to the SOMO of the anions determined by EPR, compared with hybrid-DFT calculations of the Pt contribution to the LUMO and to the HOMO of the neutral complexes

| | $a^2$ | $b^2$ | Total Pt SOMO (EPR) | | Total Pt LUMO (calc.) | Total Pt HOMO (calc.) |
|---|---|---|---|---|---|---|
| $\mathbf{1b}^{1-}$ | 0.034 | 0.050 | 0.084 | **1b** | 0.078 | 0.429 |
| $\mathbf{1c}^{1-}$ | 0.019 | 0.023 | 0.042 | **1c** | 0.058 | 0.118 |
| $\mathbf{2c}^{1-}$ | 0.019 | 0.073 | 0.092 | **2c** | 0.083 | 0.106 |
| | | | | **3c** | | 0.111 |

angles and bond distances from the calculated structure of **1c** and the XRD structure shows that the calculated structure is very close to that experimentally observed, Table S6.† All calculations are consistent with the HOMO based largely on the mnt moiety and the LUMO largely based on the bpy moiety (Table S7†) as previously reported, with a larger total contribution of Pt orbitals to the HOMO than to the LUMO (Table 5) for **1c**, **2c** and **3c**.[1,2,10] For the dichloride **1b**, the Pt contribution to the HOMO is seen to be much larger than for the three mnt-complexes in keeping with the capacity of the dithiolene ligand to enhance delocalisation of the frontier orbitals in the complex. We also observe that the Pt contribution to the LUMO in **1b**, **1c** and **2c** matches the trend for the Pt contribution to the SOMO determined from the EPR results. In fact, there is also a reasonable match with the absolute values however, although gratifying, this may be fortuitous and it is the reproduction of the trend that is most significant.

The noticable difference in the Pt contribution to the LUMO/SOMO of **1c**/**1c**$^{1-}$ compared with **2c**/**2c**$^{1-}$ is likely to be due to the non-planar character of the former caused by the steric hindrance at the 3,3′-positions and we can therefore surmise that this causes poorer overlap with the Pt orbitals. Furthermore, the computational results show clear evidence of the consequences of this non-planarity in the LUMO and LUMO + 1 orbitals (Fig. 7). In particular, the latter orbital is localised on one of the pyridyl rings of the ligand only, in complete contrast to the corresponding orbital for the planar **2c** (Fig. S13†) which is distributed over the whole bpy ligand.

Time-dependant density functional theory (TD-DFT) calculations were carried out for **1c**, **2c** and **3c** in the presence of DMF. This method has been previously used on similar platinum–diimine–dithiolate systems to great effect with the results showing a remarkable similarity to experimental observations.[21,22] A summary of relevant calculated transitions for each complex can be found in Tables S8–S10† and figures showing the calculated transitions relative to the observed absorption spectrum are shown in Fig. 8 and S18.† The calculated composition of the lowest energy transition for all three complexes was found to be 70% HOMO–LUMO and MMLL′CT in nature as expected. The calculated energy was slightly underestimated, by an average of 1660 cm$^{-1}$, for all three complexes. It should be noted that the inclusion of solvent in these calculations is essential, as has been observed previously in similar systems,[23] as the TD-DFT studies carried out under vacuum vastly underestimated the energy of the MMLL′CT by ~12000 cm$^{-1}$. The highest energy transitions were identified as bpy intraligand transitions and calculated to be no more than

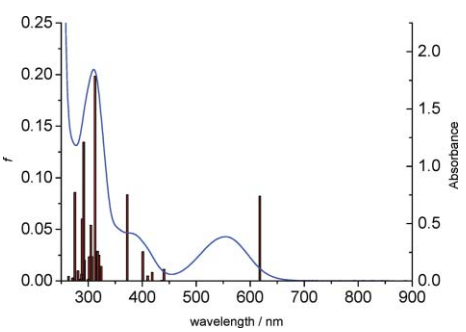


**Fig. 8** Calculated TD-DFT results shown as a bar chart (left axis) relative to the observed absorption spectrum (right axis) in DMF of **1c**.

900 cm$^{-1}$ from those observed. The relative size of the oscillator strengths match the relative intensities of the observed spectra well, with the bpy intraligand transitions being the most intense and the two CT bands being of a similar magnitude to one another. Lastly, the observed trend in the energy of the HOMO–LUMO transitions was reproduced with **1c** being the lowest and **2c** being the highest.

In our prior work we determined that **1c** showed a better solar-to-electric power-conversion efficiency than **2c** (and much better than **3c**).[6] In particular this arose from a higher open-circuit voltage for a cell using **1c** which was explained by the longer charge recombination time (between electrons in the $TiO_2$ and the oxidised dye) that was determined for this complex.[6] This charge-recombination is known as a key loss process and its inhibition is one of the widely-studied approaches to dye design for DSSCs.[24]

The results presented in this work suggest that the longer-lived charge-separated state for complex **1c** on $TiO_2$ is related to the non-planar geometry of the complex. We have shown, by the lower contribution of the Pt orbitals to the SOMO/LUMO of **1c** compared with **2c** as shown by EPR/DFT studies, that this reduces the electronic coupling between the bpy ligand and the Pt(mnt) fragment of the dye as well as reducing the electronic coupling across the bpy ligand itself. According to the electrochemical and spectroelectrochemical results, the positive charge density on the oxidised dye is located largely on the mnt ligand and this conclusion is supported by DFT calculation of the HOMO location on the neutral complexes. The poorer electron delocalisation across the dye in the case of **1c** will then lead to poorer electronic communication between the cation on the dye and electrons in the $TiO_2$ giving a longer-lived charge-separated state.

Interestingly, the observation of significantly poorer photovoltaic performance using **3c** is also consistent with this analysis. The electrochemical and EPR results in this work and previous ENDOR results demonstrate that the 5,5′-positions on the bpy are the most strongly electronically coupled to the ring. Thus, the poor performance of **3c** may in part be explained by enhanced charge recombination *via* strong electronic communication from the $TiO_2$ to the positive charge on the oxidised dye *via* the acid groups in the 5-position of the bpy.

## Conclusions

This work contains the first detailed spectroelectrochemical (UV/Vis/NIR and EPR) and DFT study on a family of [Pt(diimine)(dithiolate)] dyes and their synthetic precursors. These molecules are important in their relevance to the area of solar cell dyes and also more generally for their optical and electronic functionality. The optically transparent thin layer electrode (OTTLE) and *in situ* EPR experiments confirm previous investigations which assign the location of the bpy based LUMO, although they also demonstrate partial involvement of the metal centre in the LUMO as indicated by coupling of the reduction electron to the Pt nucleus, supported by computational results. Trends in the OTTLE study of the mnt dyes indicate that in general the location of the reduction electron is similar within the 3,3′, 4,4′ and 5,5′ motifs.

Most significantly, the EPR and DFT studies provide a rationale for the superior performance of the 3,3′-substituted bpy-complex over the 4,4′-substituted bpy counterpart in DSSCs. This provides

 

important guidance in the optimisation of such solar cell dyes in future studies and we suggest that the focus in the DSSC field on 4,4′-bipy ligands with almost no investigation of 3,3′-bipy may be a missed opportunity for dye enhancement.

## Experimental

The synthesis of each compound **1–3(a–d)** has previously been reported.[6] Electrochemical studies were carried out using a DELL GX110PC with General Purpose Electrochemical System (GPES), version 4.8, software connected to an autolab system containing a PGSTAT 20 potentiostat. The technique used a three electrode configuration, with a 0.5 mm diameter Pt disc working electrode, a Pt rod counter electrode and an Ag/AgCl (saturated KCl) reference electrode against which the ferrocenium/ferrocene couple was measured to be +0.55 V. The supporting electrolyte was 0.1 M tetrabutylammonium tetrafluoroborate ($TBABF_4$), solvent was dry, degassed DMF and concentration of compound approximately 1 mmol.

OTTLE measurements were taken using a quartz cell of 0.5 mm, a Pt/Rh gauze working electrode, an Ag/AgCl reference electrode and a Pt wire counter electrode. UV-Vis spectra were recorded on a Perkin-Elmer Lambda 9 spectrophotometer, controlled by a Datalink PC, running UV/Winlab software. 0.1 M $TBABF_4$ was used as the supporting electrolyte in all cases.[25]

All *in situ* EPR spectra were recorded on an X-band Bruker ER200D-SCR spectrometer, connected to a Datalink 486DX PC running EPR Acquisition System, version 2.42 software. *In situ* EPR experiments were electrogenerated using a BAS CV-27 voltammograph. Variable temperature work was carried out using a Bruker ER111VT variable temperature unit. In some cases, solution spectra were recorded at reduced temperature to ensure long-term stability of the reduced species. All $g$ values were corrected to 2,2′-diphenyl-1-picrylhydrazyl with $g_{\text{literature}} = 2.0036 \pm 0.0002$. Spectra were simulated by manipulation of parameters until a satisfactory reproduction of experimental spectra was obtained, assuming couplings to the following nuclei: $^{195}$Pt ($I = \frac{1}{2}$, 33.8% abundance), $^{1}$H ($I = \frac{1}{2}$, 100% abundance) and $^{14}$N ($I = 1$, 100% abundance). Since each of these gives a different combination of nuclear spin (hence splitting) and natural abundance, no ambiguity in nuclear types arises in the simulations.

Density functional theory calculations of all complexes were performed using either the Gaussian 03 program package[26] or the GAMESS-UK package.[27] The starting structure was input using the builder program Arguslab and default convergence conditions of Gaussian 03 were used. The Becke three parameters hybrid exchange and the Perdew–Wang 1991 correlation functionals (B3PW91) were used.[28,29] For the platinum atom the Hay–Wadt VDZ($n$+1)ECP was used[30] with the other atoms described by 6-31G*.[31] The optimised structures were verified as minima on the potential energy surface by the absence of negative values in the frequency calculations. TD-DFT calculations were carried out in the presence of a polarisable continuum model (PCM) DMF[32] solvation field, with the first 25 singlet transitions calculated.

## Acknowledgements

We thank the University of Edinburgh Christina Miller fund and the EPSRC Excitonic Solar Cells Supergen Consortium for financial support and we thank the EPRSC Multifrequency EPR National Service.

## Notes and references

1 S. D. Cummings and R. Eisenberg, *J. Am. Chem. Soc.*, 1996, **118**, 1949.
2 M. Hissler, J. E. McGarrah, W. B. Connick, D. K. Geiger, S. D. Cummings and R. Eisenberg, *Coord. Chem. Rev.*, 2000, **208**, 115.
3 E. A. M. Geary, N. Hirata, J. Clifford, J. R. Durrant, S. Parsons, A. Dawson, L. J. Yellowlees and N. Robertson, *Dalton Trans.*, 2003, 3757.
4 A. Islam, H. Sugihara, K. Hara, L. Pratap Singh, R. Katoh, M. Yanagida, Y. Takahashi, S. Murata and H. Arakawa, *New J. Chem.*, 2000, **24**, 343.
5 A. Islam, H. Sugihara, K. Hara, L. P. Singh, R. Katoh, M. Yanagida, Y. Takahashi, S. Murata, H. Arakawa and G. Fujihashi, *Inorg. Chem.*, 2001, **40**, 5371.
6 E. A. M. Geary, L. J. Yellowlees, L. A. Jack, I. D. H. Oswald, S. Parsons, N. Hirata, J. R. Durrant and N. Robertson, *Inorg. Chem.*, 2005, **44**, 242.
7 J. Zhang, P. Du, J. Schneider, P. Jarosz and R. Eisenberg, *J. Am. Chem. Soc.*, 2007, **129**, 7726.
8 M. K. Nazeeruddin and M. Graetzel, *Comprehensive Coordination Chemistry II*, ed. J. A. McCleverty and T. J. Meyer, Elsevier Science, Amsterdam, 2004, vol. 9, p. 719.
9 E. Galoppini, *Coord. Chem. Rev.*, 2004, **248**, 1283; N. Robertson, *Angew. Chem., Int. Ed.*, 2006, **45**, 2338.
10 W. Paw, S. D. Cummings, M. A. Mansour, W. B. Connick, D. K. Geiger and R. Eisenberg, *Coord. Chem. Rev.*, 1998, **171**, 125.
11 P.-H. Xie, Y.-J. Hou, T.-X. Wei, B.-W. Zhang, Y. Cao and C.-H. Huang, *Inorg. Chim. Acta*, 2000, **308**, 73; Y.-J. Hou, P.-H. Xie, B.-W. Zhang, Y. Cao, X.-R. Xiao and W.-B. Wang, *Inorg. Chem.*, 1999, **38**, 6320.
12 L. Jack, Ph.D. Thesis, University of Edinburgh, 2003.
13 J. M. Bevilacqua and R. Eisenberg, *Inorg. Chem.*, 1994, **33**, 2913.
14 B. W. Smucker, J. M. Hudson, M. A. Omary and K. R. Dunbar, *Inorg. Chem.*, 2003, **42**, 4714.
15 E. Koenig and S. Kremer, *Chem. Phys. Lett.*, 1970, **5**, 87.
16 V. T. Coombe, G. A. Heath, A. J. MacKenzie and L. J. Yellowlees, *Inorg. Chem.*, 1984, **23**, 3423.
17 G. A. Heath, L. J. Yellowlees and P. S. Braterman, *Chem. Commun.*, 1981, 287.
18 E. J. L. McInnes, R. D. Farley, C. C. Rowlands, A. J. Welch, L. Rovatti and L. J. Yellowlees, *J. Chem. Soc., Dalton Trans.*, 1999, 4203.
19 P. H. Rieger, *J. Magn. Reson.*, 1997, **124**, 140.
20 E. J. L. McInnes, R. D. Farley, S. A. MacGregor, K. J. Taylor, L. J. Yellowlees and C. C. Rowlands, *J. Chem. Soc., Faraday Trans.*, 1998, 2985.
21 C. J. Adams, N. Fey, M. Parfitt, S. J. A. Pope and J. A. Weinstein, *Dalton Trans.*, 2007, 4446–4456.
22 C. Makedonas and C. A. Mitsopoulou, *Eur. J. Inorg. Chem.*, 2006, 2460–2468; C. Makedonas, C. A. Mitsopoulou, F. J. Lahoz and A. I. Balana, *Inorg. Chem.*, 2003, **42**, 8853.
23 A. Vlček Jr. and S. Záliš, *Coord. Chem. Rev.*, 2007, **251**, 258–287.
24 N. Hirata, J.-J. Lagref, E. J. Palomares, J. R. Durrant, M. K. Nazeeruddin, M. Grätzel and D. Di Censo, *Chem.–Eur. J.*, 2004, **10**, 595.
25 E. Alessio, S. Daff, M. Elliot, E. Iengo, L. A. Jack, K. G. Macnamara, J. M. Pratt and L. J. Yellowlees, Spectroelectrochemical techniques, *Trends Mol. Electrochem.*, 2004, 339.
26 M. J. Frisch, G. W. Trucks, H. B. Schlegel, G. E. Scuseria, M. A. Robb, J. R. Cheeseman, J. A. Montgomery, Jr., T. Vreven, K. N. Kudin, J. C. Burant, J. M. Millam, S. S. Iyengar, J. Tomasi, V. Barone, B. Mennucci, M. Cossi, G. Scalmani, N. Rega, G. A. Petersson, H. Nakatsuji, M. Hada, M. Ehara, K. Toyota, R. Fukuda, J. Hasegawa, M. Ishida, T. Nakajima, Y. Honda, O. Kitao, H. Nakai, M. Klene, X. Li, J. E. Knox, H. P. Hratchian, J. B. Cross, V. Bakken, C. Adamo, J. Jaramillo, R. Gomperts, R. E. Stratmann, O. Yazyev, A. J. Austin, R. Cammi, C. Pomelli, J. Ochterski, P. Y. Ayala, K. Morokuma, G. A. Voth, P. Salvador, J. J. Dannenberg, V. G. Zakrzewski, S. Dapprich, A. D. Daniels, M. C. Strain, O. Farkas, D. K. Malick, A. D. Rabuck, K. Raghavachari, J. B. Foresman, J. V. Ortiz, Q. Cui, A. G. Baboul, S. Clifford, J. Cioslowski, B. B. Stefanov, G. Liu, A. Liashenko, P. Piskorz, I. Komaromi, R. L. Martin, D. J. Fox, T. Keith, M. A. Al-Laham, C. Y. Peng, A. Nanayakkara, M. Challacombe, P. M. W. Gill, B. G. Johnson,

W. Chen, M. W. Wong, C. Gonzalez and J. A. Pople, *GAUSSIAN 03 (Revision C.02)*, Gaussian, Inc., Wallingford, CT, 2004.
27 GAMESS-UK is a package of *ab initio* programs. See: http://www.cfs.dl.ac.uk/gamess-uk/index.shtml:M. F. Guest, I. J. Bush, H. J. J. van Dam, P. Sherwood, J. M. H. Thomas, J. H. van Lenthe, R. W. A. Havenith and J. Kendrick, The GAMESS-UK electronic structure package: algorithms, developments and applications, *Mol. Phys.*, 2005, **103**, 719–747.
28 J. P. Perdew, J. A. Chevary, S. H. Vosko, K. A. Jackson, M. R. Pederson, D. J. Singh and C. Fiolhais, *Phys. Rev. B*, 1993, **48**.
29 J. P. Perdew, K. Burke and Y. Wang, *Phys. Rev. B*, 1996, **54**, 16533.
30 P. J. Hay and W. R. Wadt, *J. Chem. Phys.*, 1985, **82**, 299.
31 M. M. Francl, W. J. Pietro, W. J. Hehre, J. S. Binkley, M. S. Gordon, D. J. Defrees and J. A. Pople, *J. Chem. Phys.*, 1982, **77**, 3654.
32 E. S. Boes, P. R. Livotto and H. Stassen, *Chem. Phys.*, 2006, **331**, 142.

 

# Appendix

# Conferences Attended

- European Conference on Hybrid and Organic Solar Cells – Paris, June 2006 (Poster)
- RSC Supramolecular and Coordination Chemistry Discussion Group – Belfast, December 2006 (Poster)
- ScotChem Materials Chemistry – Heriot-Watt, March 07 (Poster + flash presentation)
    - 1st prize poster award
- ScotChem Computational Chemistry – St. Andrews, April 2007 (Poster)
- RSC Industry Tour – Cambridge, June 2007 (Poster)
    - 3rd prize poster award
- International Symposium of Photophysics and Photochemistry of Coordination Compounds – Dublin, July 2007 (Poster)
- Universities of Scotland Inorganic Conference – Edinburgh, September 2007 (Poster and Organiser)
- Scottish Regional Dalton Meeting – Heriot-Watt, April 2008 (Poster)
- Coordination Chemistry/Inorganic Reaction Mechanisms Discussion Group Meeting – Edinburgh, June 2008 (Poster)

## Training Courses

- Science Communication in Action – October 2005 to February 2006
- NMR Spectroscopy of Small Molecules – June 2007
- Mass Spectrometry: Principles and Practise in the 21st Century – April 2008